NASA Technical Memorandum 100711

Relationships of Earthquakes (and Earthquake-Associated Mass Movements) and Polar Motion as Determined by Kalman Filtered, Very-Long-Baseline-Interferometry Group Delays

Joseph R.M. Preisig

October 1988

NASA

NASA Technical Memorandum 100711

Relationships of Earthquakes (and Earthquake-Associated Mass Movements) and Polar Motion as Determined by Kalman Filtered, Very-Long-Baseline-Interferometry Group Delays

Joseph R.M. Preisig
Goddard Space Flight Center
Greenbelt, Maryland

National Aeronautics and
Space Administration

**Information Management
Division**

1988

PREFACE

A Kalman filter was designed to yield optimal estimates of geophysical parameters from (observed) VLBI group delay data. The geophysical parameters are the polar motion components, adjustments to nutation in obliquity and longitude, and a change in the length of day parameter. VLBI clock parameters and atmospheric zenith delay parameters were simultaneously estimated with the geophysical parameters. The right ascension and declination of the VLBI (radio) sources, and VLBI site positions were kept at a priori values. The primary source of VLBI group delay observations was the 1984-85 IRIS (International Radio Interferometric Surveying) data set consisting of day long VLBI observing sessions (at five day intervals). The Kalman filter limits subjectivity in VLBI data analysis.

The scientific objective of Kalman filtering the VLBI group delay data was to examine the relationship between earthquakes and associated mass movements, and the Chandler wobble of the earth. The Kalman filter produces precise estimates of polar motion over time intervals of one day or less. The estimated polar motion results were deconvolved to produce excitation functions versus time. Changes in the earth's inertia tensor due to earthquakes and associated mass movements may be seen in the observed excitation

functions. The excitation signatures of the preceding mass movements may appear as Heaviside step functions or other manifestations. Such excitation studies have been made in the past using less precise polar motion data; one objective of this research was to characterize excitation signatures associated with earthquakes more exactly using contemporary data.

Several great earthquakes occurred during 1984-86, all with magnitudes (M_S) approaching 8.0 or above. Excitation functions were calculated at five day intervals around the time of the 1985 great Chilean and 1985 great Mexican earthquakes. The excitation results were produced for a 45 day window surrounding the epoch of each main event. The observed excitations were compared with theoretical excitation (elastic dislocation) values calculated by Chao and Gross (1987).

Changes (ramps) in excitation are strongly correlated with the time of the 1985 great Mexican earthquake, but the changes in excitation are not statistically significant. The excitation formal errors are typically 0.5 milliarcseconds. The observed excitation magnitude and direction are very close to being in accord with the theoretical estimates.

Two steps are observed in the x-component of excitation twenty days prior to the 1985 great Chilean earthquake and

roughly twenty days after. The step magnitudes are 1.5 mas and 0.8 mas, respectively. The net excitation is 2.4 mas in a direction 7.1 degrees East longitude. This is significant. The observed excitation is thirteen times larger than the theoretical value. The theoretical excitation direction is 110 degrees East longitude. These Chilean results are similar to the findings of Chao and Gross (1985) for the great 1977 Sumba earthquake.

Finally, IRIS polar motion data are deconvolved near the time of the great 1986 Taiwan earthquake. A step of 3.8 +/- 0.5 mas in the (observed) x-component of excitation begins directly after the Taiwan main shock. Such a step is very significant. All of the preceding results indicate that earthquakes and associated mass movements play a larger role in the excitation of the Chandler wobble than elastic dislocation theory (alone) predicts. More observations are needed before the earthquake excitation level can be accurately estimated.

The earthquake related excitations may arise from: 1. the main shock; 2. (pre- and post-seismic) movements of lithospheric slabs during subduction; 3. viscous relaxation (post-seismic) of the asthenosphere near the earthquake region; 4. (pre-seismic) lithospheric flexure (bowing) near subduction zones like that of Chile; 5. Aseismic fault slip. Subduction (zones where most earthquakes occur) appears to have a significant role in excitation of the Chandler wobble.

ACKNOWLEDGEMENTS

NASA grant 240-5084-A supported much of my work in geophysics, image processing, and Very-Long-Baseline Interferometry; especially acknowledged is the support and research freedom extended by the NASA Graduate Student Researchers Program. I thank my Ph.D. mentor, Dr. Francis Wu, who was instrumental in getting me started in Kalman filtering of VLBI group delay data.

Much of the VLBI computing and analysis work presented in this dissertation was performed at the NASA Goddard Space Flight Center (Greenbelt, Maryland). Dr. Chopo Ma of the VLBI analysis team was my principal advisor, and I thank him and Lily Liu for their assistance, as well as Jim Ryan for introducing me to VLBI data analysis. I thank the Goddard VLBI team (including NASA, SAR, and Interferometrics, Inc. for their assistance in this undertaking.

Additionally, Dr. Goran Lundqvist helped the work greatly with scientific and programming advice; polar motion and Kalman filtering aid was rendered by Dr. Tom Herring (Center for Astrophysics, Cambridge, Massachusetts), Dr. Ben Chao (NASA-GSFC), and Dr. Richard Gross (Los Alamos National Laboratory).

CONTENTS

Chapter I.

INTRODUCTION

The Chandler wobble is a polar motion of fourteen month period; specifically it is manifested as an angular displacement between an axis fixed to a stationary geometric pole on the surface of the earth and the spin axis of the earth. Since the discovery of the wobble in 1891 (Chandler, 1891), the sources of its excitation have been extensively investigated without great success. J. Milne (1893) was one of the first to suspect some relation between polar motion and earthquakes.

Extensive variation of latitude data have been recorded and analyzed to examine the driving source of the fourteen month wobble. More recently, theoretical elastic-dislocation models have been developed to determine if earthquakes can indeed drive Chandler wobble. Unfortunately, variation of latitude observations taken with zenith telescopes or other conventional optical techniques are not very precise; and elastic-dislocation models, while explaining immediate fault zone behavior fairly well, do not begin to model extensive mass movements associated with earthquakes or the inelastic behavior of the earth. This work examines the degree to which earthquakes and related mass movements excite the Chandler

wobble.

Fortunately, we are not at an impasse in addressing this question. In the last two decades several techniques have been developed which more precisely measure the polar motion of the earth. These include Lunar Laser Ranging (LLR), Satellite Laser Ranging (SLR - via the LAGEOS satellite), and Very Long Baseline Interferometry (VLBI). VLBI is currently able to measure the components of polar motion with an optimum precision of 0.5 milliarcseconds (Robertson, 1985). Since VLBI observing sessions span typically one to two days, one can readily study earth orientation on time scales up to these lengths. Using many day-long VLBI data sets, one can examine polar motion over time periods of weeks to years. This study looks at polar motion on time scales of several hours to several months.

VLBI parameters such as polar motion components or baseline lengths (the chord distance between two points on the earth's surface) have been estimated in the past from least squares analysis (Clark et al., 1985). A more powerful technique for parameter estimation is Kalman filtering/smoothing, and a major aspect of the work presented here is the application of Kalman filtering to VLBI observations to produce optimal estimates of VLBI parameters.

The intent of this work is to investigate relationships between earthquakes (and associated mass movements) and the Chandler wobble of the earth using VLBI data. Some

questions to be addressed are: To what degree do earthquakes excite the Chandler wobble of the earth?; Does the Chandler wobble trigger earthquakes?; Do the movements of lithospheric slabs decoupled (from lithospheric plates) by earthquakes excite the Chandler wobble?; To what degree does unsteady bowing (lithospheric flexure) at ocean trenches excite the Chandler wobble of the earth? VLBI polar motion estimates appear to be approaching sufficient precision and temporal resolution to begin answering the preceding questions in some detail.

The arrangement of the chapters in this work follows. In Chapter II polar motion fundamentals will be presented, while Kalman filtering and smoothing will be introduced in Chapter III. An introduction to Very Long Baseline Interferometry will be given in Chapter IV, and a review of research into the relationships of earthquakes and Chandler wobble will be presented in Chapter V. In Chapter VI, a Kalman filter will be developed which produces polar motion parameter estimates from VLBI group delay data. Filter optimization and operation will be explained in Chapter VII and VIII. Results and conclusions will be presented in Chapters IX and X.

Chapter II.

THE EQUATIONS OF POLAR MOTION

It is now appropriate to define some parameters of earth orientation and rotation. Consider that the earth is rotating with some angular velocity with respect to a quasi-inertial reference frame. The earth does not rotate at a constant angular velocity, and as such, there are changes in the length of day. In addition to rotational variations, there are small amplitude oscillations of the earth in directions orthogonal to the earth's mean rotation axis. The Chandler wobble makes up a part of these oscillations which are otherwise known collectively as polar motion. Chandler wobble differs from nutation because it is not a forced motion due to interactions of the earth with other planets, moons or stars (Stacey, 1977).

The polar motion of the earth is made up of at least three motions: the Chandler wobble, the annual wobble and a secular trend in the polar motion. "The [Chandler] wobble results from rotation of the Earth about an axis that departs slightly from its axis of greatest moment of inertia." (Stacey, 1977). The Chandler wobble manifests itself as an oscillatory angular displacement between the spin axis and axis of greatest moment of inertia of the earth;

the period of oscillation is roughly fourteen months.

Superimposed on the Chandler wobble is a wobble of a twelve-month period, the annual wobble; the annual wobble is driven by interactions of the oceans and atmosphere with the earth. The remaining component of polar motion discussed here is the secular trend. The secular trend is a long term drift in polar motion; it has a drift amplitude of several milliarcseconds per year (Morabito and Eubanks, 1985). The secular trend appears to be driven by isostatic rebound of the earth after unloading by glacial melting (after ice ages). More details about polar motion can be found in Lambeck (1980).

The changes in length of day alluded to previously can be measured by comparing time as kept using atomic time standards to time found astronomically (by looking at the rotational position of the earth with respect to quasars (these quasi-stellar objects define a quasi-inertial reference frame) or other stars). The latter time entity is known as sidereal time. The difference between atomic clock time and astronomical time is typically used to characterize changes in length of day.

A type of astronomically-based time scale (like sidereal time) commonly used in VLBI work is UT1 (Universal Time). The atomic clock time scales, UTC (Coordinated Universal Time) and TAI (International Atomic Time), are also used in the VLBI community. TAI differs from UTC by leap seconds which are introduced into UTC by the Bureau Inter-

nationale de l'Heure (BIH - a world time keeping agency). Leap seconds are corrections added into UTC to keep UTC within one second of time determined from earth rotation rate (Sullivan, 1984). The quantities UT1-UTC and UT1-TAI describe changes in the length of day. For further information about such time scales, please refer to Kaplan (1981) and Ma (1978).

The mathematical development which describes polar motion and rotation is now presented. Following the treatment (with modifications) of Munk and MacDonald (1960), Conservation of Angular Momentum is used to describe the wobble and rotation of the earth

$$N = \frac{dL}{dt} + \omega \times L. \qquad (II.1)$$

N represents the torques acting on the earth, L is the total angular momentum of the earth, and ω is the angular velocity of the earth. We are concerned with the motion of the coordinate system x_i (where i=1,2,3) which rotates with angular velocity ω with respect to the inertial system X_i. x_i and X_i are coincident at some reference epoch.

It is now helpful to separate the total angular momentum L into two parts

$$L_i = C_{ij}(t)\omega_j + l_i(t). \qquad (II.2)$$

$C_{ij}(t)$ is the inertia tensor and $l_i(t)$ represents a relative

angular momentum term. The components of C can be expressed as

$$C_{ij} = \int_V \rho\,(x_k x_k \delta_{ij} - x_i x_j)\,dV \qquad (II.3)$$

where ρ is the density of the object of concern, V is the volume, and δ_{ij} is the Kronecker delta. The relative angular momentum components are given by

$$l_i = \int_V \rho\,\epsilon_{ijk}\,x_j\,u_k\,dV, \qquad (II.4)$$

where ϵ_{ijk} is the Levi-Civita symbol, and u_k is the component of velocity with respect to the x_i-system.

Substitution of (II.2) into (II.1) gives the Liouville equation

$$N = \frac{d}{dt}\,(C\omega + l) + \omega x (C\omega + l). \qquad (II.5)$$

Simplified versions of equation (II.5) will now be formed to determine elementary equations of motion for Chandler wobble and changes in the length of day.

One can also describe the Chandler wobble as a normal mode of the earth (Smith, 1977; Smith and Dahlen, 1981) and can use elastic-gravitational normal mode theory to characterize its behavior. It is an interesting note that Dahlen suggests "We could really say the Chandler wobble was just like every other normal mode if it were excited

principally by earthquakes, but that does not appear to be the case."

Perturbation theory is applied to the Liouville equation (II.5) to simplify it. For the case of polar motion and earth rotation in which movements of figure axes and rotation pole (and fluctuations in spin rate) are small with respect to the reference coordinate system x_i, the following perturbation scheme works well

$$\begin{aligned} C_{11} &= A + c_{11}, \quad C_{22} = A + c_{22}, \quad C_{33} = C + c_{33} \\ C_{12} &= c_{12}, \quad C_{13} = c_{13}, \quad C_{23} = c_{23} \\ \omega_1 &= \Omega m_1, \quad \omega_2 = \Omega m_2, \quad \omega_3 = (1+m_3)\Omega. \end{aligned} \tag{II.6}$$

In this model, A, A and C are the initial (pre-deformation) moments of inertia of the earth with C being the largest moment. c_{ij} are the perturbations to the inertia tensor. Clearly if all perturbations c_{ij} go to zero , we are left with an axi-symmetric earth of major moment of inertia C and equal minor moments A. This makes sense and is a fair approximation to the geometry of the real earth.

The angular velocities $\omega = (\omega_1, \omega_2, \omega_3)$ are written as perturbations of the mean angular velocity of the earth, Ω. ω_1 and ω_2 will be trivial if m_1 and m_2 go to zero, but ω_3 is generally of order Ω; this is intuitively gratifying, considering that one desires an earth which continues to rotate at some nearly constant angular velocity, regardless of the perturbations applied.

Substituting definitions (II.6) into the Liouville

equation (II.5), neglecting products and squares of perturbations and other small terms, one arrives at the following simplified Liouville equations

$$\frac{\dot{m}_1}{\sigma_r} + m_2 = \Phi_2 \quad ; \quad \frac{\dot{m}_2}{\sigma_r} - m_1 = -\Phi_1 \tag{II.7}$$

$$\dot{m}_3 = \dot{\Phi}_3 \tag{II.8}$$

where

$$\begin{aligned}
\Omega^2(C-A)\Phi_1 &= \Omega^2 c_{13} + \Omega\dot{c}_{23} + \Omega l_1 + \dot{l}_2 - N_2 \\
\Omega^2(C-A)\Phi_2 &= \Omega^2 c_{23} - \Omega\dot{c}_{13} + \Omega l_2 - \dot{l}_1 + N_1 \\
\Omega^2 C\Phi_3 &= -\Omega^2 c_{33} - \Omega l_3 + \Omega\int_0^t N_3\, dt',
\end{aligned} \tag{II.9}$$

where the dot indicates differentiation of the designated variable with respect to time, and $\sigma_r = ((C - A)\Omega)/A$ is a frequency parameter of the wobble. The r subscript denotes that a "rigid" earth is being modelled. Equations (II.7) are very simplified descriptions of the Chandler wobble; they do not model: the effects of an elastic earth on wobble; the lack of participation of the core in wobble; the effects of oceans; solid-fluid interactions at the core-mantle boundary, etc. For further explanations about the preceding effects, please consult Lambeck (1980), Smith and

Dahlen (1981) and Dickman (1982).

Equations (II.7) govern the polar motion of our earth model, while equation (II.8) characterizes earth rotation. m_1 , m_2 are the parameters typically measured and used to describe polar motion. The excitation functions Φ_1 , Φ_2 , Φ_3 are not simple, and their earthly sources are even more difficult to pin down. The atmosphere and earthquakes are possible sources of excitation, for example.

The coordinate system first conventionally used for polar motion measurements was that defined by the International Latitude Service (ILS), an organization which made polar motion observations. The x_3 (polar) axis of the ILS system (determined from the mean latitudes of five ILS observatories from 1900-1905) is called the Conventional International Origin (CIO). The x_1 and x_2 axes are oriented along the Greenwich meridian and 90 degrees West meridian, respectively, thereby completing the triad. By convention, m_1 is taken along the $+x_1$ direction and m_2 is in the $-x_2$ direction.

This is a good opportunity to illustrate how the effect of an earthquake would appear in measured polar motion results. It is common to express the components of wobble (m_1, m_2) as a complex number: $m = m_1 + i\, m_2$ (also $\Phi = \Phi_1 + i\Phi_2$). An equation for polar motion as a function of modified excitation function terms is presented in Munk and MacDonald (1960)

$$m(t) = \exp(i\sigma_0 t)\{m_0 - i\sigma_0 \int_{-\infty}^{t} \psi(\tau)\exp(-i\sigma_0\tau)d\tau\}, \qquad (II.10)$$

where m_0 is complex (m_0=initial wobble amplitude), and σ_0 is a wobble frequency term. ψ and σ_0 are modifications of Φ and σ_r, which account for the fact that the elastic earth deforms in response to its rotation. Thus the complex equation (II.7) for a rigid earth, $\dot{m} = i\sigma_r(m-\Phi)$ can be extended to the case of an elastic earth $\dot{m} = i\sigma_0(m - \psi)$, where m, Φ and ψ are complex (Munk and Mac Donald, 1960; Lambeck, 1980).

One can model the earthquake excitation ψ as a Heaviside step function, JH(t),

$$JH(t) = \begin{cases} 0 , & t<0 \\ J , & t\geq 0 \end{cases} \qquad (II.11)$$

where J is a complex constant. The step function is useful as an approximation of the earthquake excitation function because mass movements associated with the release of elastic energy during a seismic event should occur in a time short compared with the period of the Chandler wobble (Mansinha and Smylie, 1970). The earthquake occurs at time t=0. Thus for $t < 0$

$$m(t) = m_0 \exp(i\sigma_0 t) \qquad (II.12)$$

and for $t \geq 0$

$$m(t)=m_0\exp(i\sigma_0 t) + J(1-\exp(i\sigma_0 t)). \qquad (11.13)$$

There is no change in rotation pole position at t=0 since m(t) is continuous. However, the pole about which the polar motion is taking place (the secular pole) does change as does the radius of the polar motion about this new pole, and thus m has a change in curvature.

The effect of a hypothetical earthquake and its associated mass shift on polar motion is shown in Figure 1, taken from Mansinha and Smylie (1970). A kink occurs in the path of the pole at the time of the earthquake, and the radius of the polar motion about the secular pole may also change. The kink is not a step discontinuity in the polar motion, even though the excitation function is discontinuous. It has been difficult to resolve kinks in existing polar motion data (Haubrich, 1970). It may be possible with Kalman filtered VLBI data in coincidence with a sufficiently large earthquake. The application of Kalman filtered VLBI data to the study of earthquake excitation of Chandler wobble is the central theme of this work.

The Chandler wobble is driven by some mechanism (or mechanisms) and one would expect such an oscillation to be damped by other physical processes. Likely damping processes include mantle anelasticity and "... a non-equilibrium oceanic response to wobble." (Dickman, 1986; see also Smith and Dahlen, 1981). The Chandler wobble quality factor, Q, which is used to characterize Chandler wobble (fractional)

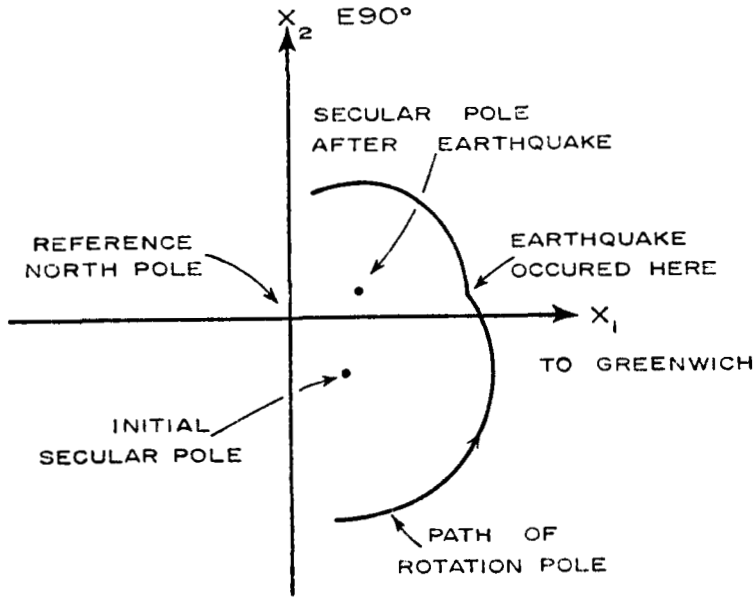

Fig. 1. The effect of a sudden mass shift on the pole path and secular pole. A step function in excitation has been assumed. (From Mansinha and Smylie, 1970).

energy dissipation, has been estimated by various techniques to be in a (preferred) range of 30 to 170 (Dickman, 1986).

The value of Q is directly proportional to how long it would take to damp out the Chandler wobble. A Q of 100 corresponds to a damping time of roughly 38 years. The excitations applied to the earth must be sufficient to drive the Chandler wobble to observed excitation levels, and one must account for losses in the driven earth system, due to damping mechanisms, when one is trying to evaluate the excitation sources.

Chapter III.

KALMAN FILTERING AND SMOOTHING

This section describes the merits and structures of Kalman filters and smoothers. Since the time of Gauss, scientists and engineers have used least squares analysis of measurements to provide best estimates of parameters of interest. Least squares is applicable when the statistics of an observable of interest are stationary. Data are handled en masse and a single set of parameter estimates and their statistical uncertainties is produced by the least squares analysis. This procedure works wonderfully for instructional physics-laboratory excercises in which one measures the dimensions of say, a metal block; but it leaves something to be desired in cases where dimensions are changing in time, such as finding optimal estimates of the distance and velocity of a rocket which has just been launched. The Kalman filter algorithm was formulated in early 1960's (Kalman, 1960; Kalman and Bucy, 1961) to deal with such situations.

A Kalman filter is a recursive optimal estimator for parameters of interest. Rather than forcing statistical moments of observables to be stationary, the filter uses the modelled physical dynamics of a given problem to provide

optimal estimates of parameters of concern in the time domain. However, how optimal a parameter estimate turns out is dependent on the accuracy and completeness of the physical models employed in the filter. In general, measurements are handled sequentially, and from a series of measurements, the Kalman filter gives a series of parameter estimates in time. For instance, in tracking a rocket each range measurement input into a Kalman filter will produce an optimal estimate of distance and velocity of the rocket from the filter shortly thereafter. This process can continue in a recursive manner until the payload has returned to earth.

It should be noted that Kalman filters are limited in application to systems which satisfy the assumptions on which such a filter is based. The main assumption is that the Kalman filter be applied to systems which can be modelled as (mathematically) Markov processes (for details see Jazwinski (1970)). In addition, Kalman filters are particularly useful in describing stochastic processes such as white noise, random walks and integrated random walks. The filter may fail when other stochastic behavior operates; in such cases other optimal estimation techniques should be sought.

The criteria for how optimal a Kalman filter is, are now defined. The optimal estimates of the filter or smoother should be unbiased, of minimum variance and consistent; that is, the estimates should achieve the true value of a parameter as the number of measurements increases (Gelb,

1974). The meanings of unbiased and minimum variance are evident.

Before too much confusion is introduced by use of the words filter and smoother, let each be defined. A filter can produce estimates actively during the time over which data are being taken. A smoother is generally applied to data after the data have already been taken. Pictorial definitions of filtering, smoothing and prediction are displayed in Figure 2 (Gelb, 1974). Both Kalman filters and smoothers will be developed in this work.

It is instructive to begin by looking at the more familiar least squares analysis. An attempt will be made to follow the mathematical notation of Jazwinski (1970). In this dissertation (especially for Kalman filter notation) capital Roman letters represent matrices and small Roman letters are used to denote vectors. One can describe the linear measurement process of an experiment by the following equation

$$y = M x + v \qquad \text{(III.1)}$$

where y, x and v are column vectors and M is a matrix. In the equation above y is a (m by one) vector of measurements made in an experiment, x is a (n by one) vector of the parameters to be estimated (the ultimate results of an experiment) and M is a matrix (m by n) of factors (partial derivatives if the problem is non-linear) relating the

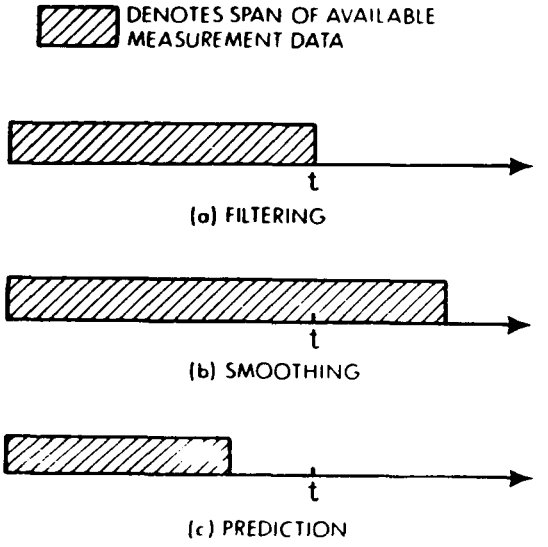

Fig. 2. Three Types of Estimation Problems (estimate desired at time t). (From Gelb et al., 1974).

measurements to the parameters. v is a (m by one) vector of measurement "noise" or uncertainty. n and m are positive integers.

An optimal, minimum variance estimate of x, namely $\hat{x}$, is desired. Using the method of Gelb et al. (1974), one finds $\hat{x}$ by calculating the value of x that minimizes the scalar cost function (net squared estimation error), J

$$J = (y - M\hat{x})^T(y-M\hat{x}) \qquad \text{(III.2)}$$

where the raised-T denotes matrix transpose. The result of this procedure is

$$\hat{x} = (M^T)^{-1}M^T y . \qquad \text{(III.3)}$$

The -1 exponent refers to inversion of the matrix in parentheses. Thus, the sum of the squares of the $(y - M\hat{x})$ elements has been minimized in accordance with the definition that the optimal estimate be of minimum variance. Equation (III.3) gives the best estimate of x for the case of unweighted least squares only.

Equation (III.1) is very close in form to the measurement equation of the Kalman filter. The discrete form of the Kalman filter is taken (as modified) from Jazwinski (1970). More complete descriptions of the filter can be found in Jazwinski (1970), Gelb et al. (1974) and Brown (1983). The equations which comprise the Kalman filter algorithm are

derived in Appendix I. The Kalman filter measurement equation is

$$y_k = M(k)x_k + v_k \qquad \text{(III.4)}$$

where y_k, $M(k)$, x_k and v_k are the same as for the least squares variables, except that the indices k refer to the time at which the observation was made. Consequently, $time(k+1)=t_{k+1}$ is the observation epoch directly and temporally after $time(k)=t_k$. For Kalman filtering, the time interval $t_{k+1} - t_k$ does not have to be equal to the previous interval $t_k - t_{k-1}$. All (III.4) describes is the measurement of data vector y_k, which is related to the parameter vector x_k, with the noise vector v_k influencing the measurement process at the observation time t_k.

In contrast to least squares analysis, an assumption of stationarity is not required in the Kalman filter. Rather, the dynamical variations in the parameter x_k are modeled using the state vector model (Jazwinski, 1970)

$$x_{k+1} = \Phi(k+1,k)x_k + \Gamma(k)w_k \qquad \text{(III.5)}$$

x_{k+1} is the parameter at time t_{k+1} and x_k is the parameter at time t_k. $\Phi(k+1,k)$ is an (n by n) state transition matrix describing the deterministic variation in x going from time t_k to t_{k+1}. w_k is the state vector which models stochastic variations in x, and $\Gamma(k)$

is the matrix which relates w_k to x. Equation (III.5), as posed, thus models both the deterministic and stochastic dynamic variations of x in time.

For completeness, the properties of the "noises" v_k, w_k are defined to be as follows (Jazwinski, 1970), where E{*} is the expectation value of *

$$E\{w_k\} = 0 \quad , \quad E\{v_k\} = 0;$$

$$E\{w_k w_l^T\}=Q(k)\delta_{kl}, \; E\{v_k v_l^T\}=R(k)\delta_{kl} \qquad \text{(III.6)}$$

$$\text{and } R(k)>0.$$

Again δ_{kl} is a Kronecker delta, Q(k) is a system noise covariance and R(k) is a measurement noise covariance. The first four relations suggest that w_k and v_k are zero-mean, non-stationary white noise processes. The fact that R(k)>0 helps to assure that the Kalman filter does not diverge as it is applied. Equations (III.4), (III.5) and (III.6) are the system model of the discrete Kalman filter.

$\hat{x}(k|k)$ and P(k|k) are the Kalman filter analogs to average values and variances of parameters in least squares analysis. K(k+1) is the gain of a Kalman filter and is quite similar to the gain of an electronic amplifier. The notation (k|k), (k+1|k) which follows many of the Kalman filter symbols merits explanation. The (k|k) notation is simply that of conditional probability. $\hat{x}(k|k)$ is the optimal estimate of x at time t_k conditioned on the

information in the previous measurements through y_k. $\hat{x}(k+1|k)$ is an optimal estimate at time t_{k+1} of the state parameter x based on the information of measurements y_k; since measurement y_{k+1} is not included in the measurement y_k, $\hat{x}(k+1|k)$ amounts to a prediction of of the estimate x at time t_{k+1} based only on measurements through $y=y_k$. The notation is similar for error covariance P. Also, a small k in single parentheses following a variable, (k), denotes that the Kalman variable is at time t_k.

The operational steps for a discrete Kalman filter are (Jazwinski, 1970)

(1) Store the state of the filter $[\hat{x}(k|k), P(k|k)]$; (III.7) where $P(k|k)$ is the error covariance of $\hat{x}(k|k)$.

(2) Project the filter state forward in time (a prediction step)

$$\hat{x}(k+1|k) = \Phi(k+1,k)\hat{x}(k|k) \qquad \text{(III.8)}$$

(3) Project the error covariance matrix forward in time (another prediction step)

$$P(k+1|k)=\Phi(k+1,k)P(k|k)\Phi^{T}(k+1,k)+\Gamma(k)Q(k+1)\Gamma^{T}(k) \qquad \text{(III.9)}$$

(4) Determine the Kalman filter gain matrix, K

$$K(k+1)=P(k+1|k)M^{T}(k+1)\{M(k+1)P(k+1|k)M^{T}(k+1) \quad \text{(III.10)}$$
$$+R(k+1)\}^{-1}$$

(5) Combine measurement information y_{k+1} with the projected state $\hat{x}(k+1|k)$ to form the optimal state estimate at time t_{k+1}

$$\hat{x}(k+1|k+1)=\hat{x}(k+1|k)+K(k+1)\{y_{k+1}-M(k+1)\hat{x}(k+1|k)\} \quad \text{(III.11)}$$

(6) Update the error covariance matrix

$$P(k+1|k+1)=\{I-K(k+1)M(k+1)\}P(k+1|k)\{I-K(k+1)M(k+1)\}^{T} \quad \text{(III.12)}$$
$$+ K(k+1)R(k+1)K^{T}(k+1)$$

(7) Go to the next time step by setting k=k+1, and return to step (1) of this procedure. (III.13)

Filter steps (1)-(7) are now explained. $\hat{x}(k|k)$ and $P(k|k)$ are the most recent estimates of the state vector and its error covariance. They are stored in step (1). If one is just starting the Kalman filter $\hat{x}(k|k)=x_0$ and $P(k|k)=P_0$, where x_0 is the vector of initial state conditions and P_0 is the initial condition of the error covariance. Usually x_0 and P_0 can be crude guesses of x and P or they can be based on a priori information. If one has no a priori knowledge of the value of parameter x, one should specify P_0 to be very large as an approximation to infinity. In filter steps (2) and (3), one uses the deterministic state transition matrix

$\Phi(k+1,k)$ and the stochastic system (process) noise covariance $Q(k+1)$ to predict (project forward in time) the state of the system in the future, $\{\hat{x}(k+1|k), P(k+1|k)\}$. This procedure relies on accurate system modelling (equation III.5) to achieve consistent estimates. The filter utilizes all the physical information about the system to estimate state values and their uncertainty in the near future, i.e. the next time epoch t_{k+1}. $\Phi = I$ (I is an identity matrix) means that $x_{k+1} = x_k$ is constant in time (if no random forcing is assumed), and $Q = 0$ implies that the parameter vector x_k being estimated is strictly deterministic.

In step (4) the gain matrix is computed. Clearly the gain combines the predicted covariance of the estimates $P(k+1|k)$ and the measurement noise covariance $R(k+1)$. The gain is the multiplier which determines how much the predicted parameter estimate $\hat{x}(k+1|k)$ will be adjusted when the next parameter estimate $\hat{x}(k+1|k+1)$ is made.

Finally, the updated parameter estimate $\hat{x}(k+1|k+1)$ and covariance $P(k+1|k+1)$ are calculated in steps (5) and (6) of the filter. These are the best estimates of x and P for time step t_{k+1}. In step (5), $[y_{k+1} - M(k+1)\hat{x}(k+1|k)]$ is a quantity called the "innovation" which reflects the difference between measured data y_{k+1} and the modeled prediction of what the observation should be. Compare the innovation with the measurement equation (III.4). Step (5) modifies the predicted parameter estimate $\hat{x}(k+1|k)$ by adding to it the product of

the gain and the innovation. Thus, the final state estimate at some time includes the most recent measurement information. Filter step (6) and its meaning are more complex than step (5). If the gain were zero, P(k+1|k+1) would simply be equal to its predicted value P(k+1|k). At the end of the filtering process, k is set to k+1 and the recursive filter loop begins again, and continues until the last measurement is processed.

It is apparent that a matrix inversion is required in step (4) of the filter, and one would like to avoid such inversions if at all possible. Inversions take time to do and may fail computationally. In the case of application of the Kalman filter to VLBI delay data, matrix inversion can be avoided if VLBI delays are the only measurements utilized in y. The concept of a VLBI delay will be described shortly. It is sufficient to know that the delay is indeed the primary observable in VLBI data acquisition. Thus, for VLBI delay analysis, y_k becomes a scalar (m=1), and the matrix inversion of filter step (4) becomes a simple division.

However, multiple delays are usually measured at a given time t_k, presenting another barrier to avoiding the inversion ($m \neq 1$). An "iterative" approach for handling multiple measurements is cryptically outlined in Jazwinski (1970). To implement this, one must first model the measurement noises v_k as uncorrelated. This allows one to process each delay at t_k in a one-at-a-time fashion through the

filter loop. Then, one proceeds through steps (1)-(7) for a single delay, and thereby y_k is now most definitely a scalar. The procedure for avoiding the inversion follows.

During the first run at time t_k through steps (1)-(7), the state transition matrix $\Phi(k+1,k)$ and system noise covariance $Q(k+1)$ use their values as normally calculated (as calculated using the non-iterative Kalman filter). However, upon completing this iteration, the time step is not increased from k to k+1. Rather, the filter is forced to stay at time t_k. Now the second measurement at time t_k is filtered (steps (1)-(6)), but $\Phi(k+1,k)$ is set to identity (I) and Q(k) is given zero value. This is because, while the filter is iterating within multiple delay data at time t_k, the state vector x should not change deterministically (thus Φ = I) nor stochastically (thereby Q = 0). Once all the delays at time t_k have been filtered, the logic of this paragraph is repeated at time t_{k+1}, and so on. The iterative filter can thereby loop through uncorrelated measurement data without the added need of calling an inversion subprogram into use.

The linear Kalman filter outlined in equations (III.7)-(III.13) works well for linear physical problems. The procedure which makes the Kalman filter suitable for non-linear applications is termed "linearization" and while many authors do not describe it in the literature because linearization supposedly is widely known, it will be outlined briefly here for completeness.

Continuous (as opposed to discrete) non-linear system equations analogous to the linear system equations (III.4) and (III.5) from Jazwinski (1970) are

$$y(t_k) = h(x(t_k);t_k) + v_k \qquad \text{(III.14)}$$

$$\text{and} \quad \frac{dx_t}{dt} = f(x_t,t) + G(t)w_t. \qquad \text{(III.15)}$$

$y(t_k)$ is the continuous measurement vector, $h(x(t_k),t_k)$ is a non-linear measurement function and v_k is the measurement noise. x_t is the continuous parameter vector, $f(x_t,t)$ is the non-linear state dynamics function and w_t is a white Gaussian noise of zero mean. $G(t)$ is the matrix which relates the white noise vector to the parameter vector.

Equation (III.14) can be linearized by proposing the existence of a reference measurement $\bar{y}(t_k) = h(\bar{x}(t_k),t_k)$, where the bars over y and x denote reference values. In essence, one assumes reference values $\bar{y}$ and $\bar{x}$ which approximate the non-linear behavior of y and x. Subtracting the reference value $\bar{y}$ from both sides of equation (III.14), one finds

$$y(t_k)-\bar{y}(t_k)=h(x(t_k),t_k)-h(\bar{x}(t_k),t_k)+v_k \qquad \text{(III.16)}$$

If one defines the variation in the measurement $y(t_k)$ from the reference value $\bar{y}(t_k)$ as

$$\delta y(t_k) \equiv y(t_k) - \bar{y}(t_k) \qquad \text{(III.17)}$$

and then assumes that the difference between actual and reference measurement functions can be represented by the first term of a Taylor series expansion

$$h(x(t_k);t_k) - h(\bar{x}(t_k),t_k) \approx \frac{\partial h_i(\bar{x}(t_k),t_k)}{\partial x_j}\,\delta x(t_k) \qquad \text{(III.18)}$$

where $$\delta x_t \equiv x_t - \bar{x}(t), \qquad \text{(III.19)}$$

then the new measurement perturbation equation is

$$\delta y(t_k) = M\{t_k;\bar{x}(t_k)\}\delta x(t_k) + v_k, \qquad \text{(III.20)}$$

and $$M\{t_k;\bar{x}(t_k)\} \equiv \frac{\partial h_i(\bar{x}(t_k);t_k)}{\partial x_j} \; . \qquad \text{(III.21)}$$

The variation in measurements $\delta y(t_k)$ is related to the variations in parameters $\delta x(t_k)$ by the matrix of partials M. In awesome fashion, the non-linear equation (III.14), which describes behavior of the total measurement $y(t_k)$, has been converted to an equation of Kalman filter measurement form (see equation III.4). Equation (III.20) deals not with the total measurement $y(t_k)$, but with the variation in the measurement $\delta y(t_k)$. Also equation (III.20) is already in discrete form.

Linearization of equation (III.15) is somewhat more

difficult. The reference value in x is given as

$$\frac{d\bar{x}(t)}{dt} = f(\bar{x}(t),t). \qquad \text{(III.22)}$$

Subtracting (III.22) from (III.15) one finds

$$\frac{d}{dt}(x_t-\bar{x}(t)) = f(x_t,t) - f(\bar{x}_t,t)+G(t)w_t. \qquad \text{(III.23)}$$

Employing definition (III.19), the relation

$$f(x_t,t)-f(\bar{x}(t),t)\approx\frac{\partial f_i(\bar{x}(t),t)}{\partial x_j}\,\delta x_t \qquad \text{(III.24)}$$

and defining

$$F\{t;\bar{x}(t)\} \equiv \frac{\partial f_i(\bar{x}(t),t)}{\partial x_j} \qquad \text{(III.25)}$$

(Jazwinski, 1970), one finds

$$\frac{d(\delta x_t)}{dt} = F\{t;\bar{x}(t)\}\delta x_t + G(t)w_t. \qquad \text{(III.26)}$$

(III.26) is still a continuous state equation and must be converted to discrete form. Details of the discretization procedure occur later in this work and will not be given here. The discrete version of (III.26) is (Jazwinski,1970)

$$\delta x(t_{k+1}) = \Phi(t_{k+1},t_k;\bar{x}(t_k))\delta x(t_k) + w(t_{k+1}) \qquad \text{(III.27)}$$

Equation (III.27) bears no small resemblance to equation (III.5), but now the x variation, δx, is being modeled as opposed to x-total.

The state equations (III.20) and (III.27) are very much like (III.4) and (III.5). It can be shown (Jazwinski, 1970) that

$$\hat{x}(t_k|t_k)=\bar{x}(t_k) + \delta\hat{x}(t_k|t_k) \qquad \text{(III.28)}$$

and that the covariances of x and δx are identical. The preceding facts allow one to use the linear Kalman filter (steps (1)-(7)) to optimally estimate parameter variations and the covariance of these variations for the system of linearized equations (III.20) and (III.27). This linearization scheme will work as long as the approximations in (III.18) and (III.24) hold true. One may have difficulty applying steps (1)-(7) to a strongly non-linear physical system, and other more sophisticated forms of filters such as the extended Kalman filter and adaptive Kalman filter may be needed (Jazwinski, 1970). Fortunately, the Very Long Baseline Interferometry (VLBI) state and measurement system equations are only weakly non-linear (Ryan, 1984) and steps (1)-(7) are very applicable.

The last segment of the Kalman filtering and smoothing chapter is devoted to the latter topic. VLBI parameters are not estimated in real time, and data from VLBI observing sessions are available for analysis only long after a

session is concluded. Thus it would make more sense to smooth VLBI delay data instead of only filtering it.

The "fixed-interval" smoother is the Kalman smoother of interest here. It is applied to a total data span of fixed duration, typically one day long in the case of VLBI observations. The time interval between data points is not necessarily constant. The following development of the smoother is adapted from Brown (1983). This fixed-interval smoother was developed by Rauch, Tung and Striebel (1965).

Consider a data set containing N+1 points. One applies the Kalman filter (steps (1)-(7)) in a forward direction (time progressing in a natural sense). As the process continues, the optimal filter estimates $\hat{x}(k|k)$, $\hat{x}(k+1|k)$ and the associated error covariances $P(k|k)$, $P(k+1|k)$ are stored in memory locations for use in the smoother. The need to store the estimates and covariances may limit the applicability of the smoother to problems whose x and P values can be accomodated in available computer memory. As the last datum is handled by the Kalman filter, the fixed-interval smoother is turned on. The smoother traverses the data set in a backward time progression. The smoother then smoothes the stored optimal estimates and error covariances. The filtering step is a forward pass through the data, and the smoothing step is a backward pass through the data.

The first smoothing step uses the last estimates from the filter, $[\hat{x}(N|N), P(N|N)]$, as initial conditions in the following algorithm. The smoother gain A(k) is first calcu-

lated

$$A(k) = P(k|k)\Phi^{T}(k+1,k)P^{-1}(k+1|k) \qquad \text{(III.29)}$$

Next the smoother optimal estimate and error covariance are calculated

$$\hat{x}(k|N) = \hat{x}(k|k) + A(k)\{\hat{x}(k+1|N)-\hat{x}(k+1|k)\} \qquad \text{(III.30)}$$

$$P(k|N) = P(k|k) + A(k)\{P(k+1|N)-P(k+1|k)\}A^{T}(k) \qquad \text{(III.31)}$$

where k = N-1, N-2, ...,0. Equations (III.29)-(III.31) are the complete, discrete, fixed-interval smoother algorithm. The smoother has no prediction steps like the Kalman filter; all the data which are to be processed are left from the filter. Another point is that the optimal estimates $\hat{x}(k|N)$, $P(k|N)$ are undeniably the result of smoothing since estimates at time t_k are based on N observations, as is indicated by the algorithm. Also note that a matrix inversion is present in the gain calculation, and that it cannot be avoided by iterative handling of the measurements as was possible in filtering. The state transition matrix Φ should be calculated as was done for the iterative Kalman filter, but note that the smoother traverses the filter estimates in reverse time order.

The smoother state parameter estimate $\hat{x}(k|N)$ is some modification of the filter estimates $\hat{x}(k|k)$ by a factor

employing the product of smoother gain A(k) with some differential variable, which is the difference of a filter estimate and a smoother estimate, $[\hat{x}(k+1|N) - \hat{x}(k+1|k)]$. The smoother covariance P(k|N) is calculated similarly to $\hat{x}(k|N)$, with slight additional complexity because P(k|N) is a matrix, not a vector like $\hat{x}(k|N)$. While the smoother involves fewer calculational steps than the filter, practical difficulties arise because one must store filter information for smoothing, and one cannot avoid performing matrix inversions while recursively smoothing.

The smoothing estimates $[\hat{x}(k|N), P(k|N)]$ should generally be more precise than the filter estimates, $[\hat{x}(k|k), P(k|k)]$. Figure 3 illustrates how the mean square error estimates of a Kalman filter and smoother may compare. Smoothing results in a smaller mean square estimation error than either forward or backward filtering alone, but as always there is a concomitant loss of resolution. In this work, the forward filter used with the VLBI group delay data will be iterative and linearized as has been described herein. The smoother will also deal with linearized variables and will be of the fixed-interval type producing optimal estimates of parameters of geophysical interest.

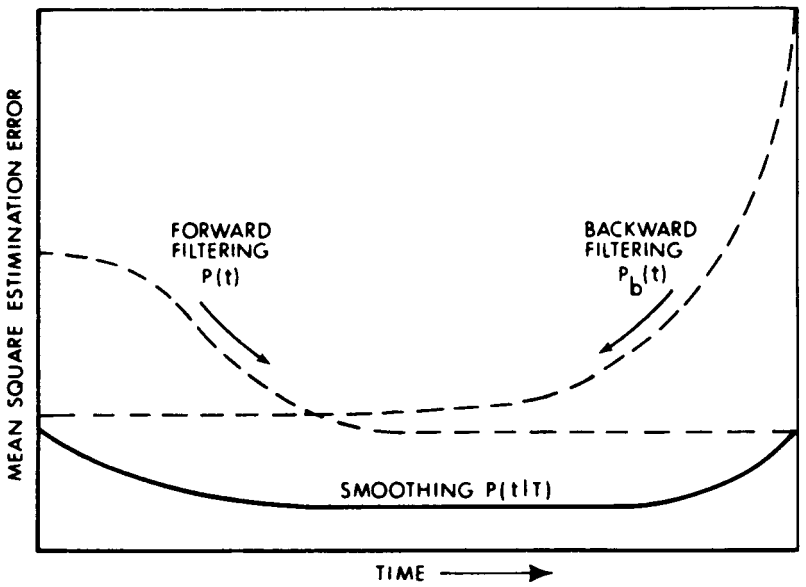

Fig. 3. Advantage of Performing Optimal Smoothing (From Gelb et al., 1974). The abscissa is time (progressing) during the measurement process. T is the total measurement interval (in time). The smoothing estimates are the result of optimal combination of the forward and backward filter estimates; this fact explains why the mean square estimation error increases during smoothing for times at the end of the measurement interval.

Chapter IV.

FUNDAMENTALS OF VERY LONG BASELINE INTERFEROMETRY

Very Long Baseline Interferometry (VLBI) was a child of the 1960's, matured in the 1970's and is producing results in the 1980's. It is a radio astronomy technique which provides very precise values of parameters of astronomical, geodetic and geophysical interest. Using VLBI, distances between two points on the surface of the Earth can be measured to a precision of several centimeters over a length of thousands of kilometers. Positions of quasi-stellar objects (quasars) in space can be determined to about one mas, which is a factor of 10 to 100 better than other current astronomical techniques. With VLBI, one can look at contemporary plate tectonic motions instead of several-million-year averages. Earth orientation angles and rotation rate can also be found to high precision. This chapter describes VLBI in some detail, so that one can understand the technique and its associated complexities. Many other reviews on VLBI are available in the theses and papers generated by the East Coast VLBI Group (U.S.A). For example, see Robertson (1975), Ma (1978), Herring (1983) and Lundqvist (1984).

Much of the VLBI work which is germane to geodesy, plate tectonics, and tectonic plate stability is performed under

the auspices of the NASA Crustal Dynamics Project (CDP). VLBI measurements will be regularly made via the CDP until at least the year 1990. VLBI is occurring between points on the North American continent, Hawaii, Japan, Europe, Kwajalein, etc. The majority of these observations are carried out by groups affiliated with the East Coast (U.S.A.) VLBI group or NGS (National Geodetic Survey).

Earth orientation VLBI measurements are carried out at least once every five days by the IRIS (International Radio Interferometric Surveying) network with stations in Massachusetts, Florida, Texas, Sweden and Germany. The measurements of the IRIS network have effectively been carried out since early 1984. The IRIS data set of 1984-85 will be the primary object of analysis of this research work.

Simply put, VLBI is an interferometric experiment over a very long baseline (or baselines), which is usually a line between two surficial points on Earth of length up to about 10,000 kilometers. The signals for the interferometry are radio wavelength and are generated by quasars and other distant radio sources. A radio signal arriving at the earth from such a source can be well approximated as a plane wave. The radio signals can be received by radio antennas and recorded with precise time information. If the respective arrival times at several antennas of a given wavefront from a radio source can be determined, then one can find the difference in arrival time at one station with respect to

another.

This difference in arrival time is called the delay, and results from one VLBI antenna being closer to the source of the plane wave than the other antenna. The delay provides information on the distance between the two stations, and on the orientation of the baseline with respect to the source. "The technique can be likened to the manner in which two blind people far apart on a beach can learn the direction from which waves are coming. If they recorded the exact time when each wave reached the toes of each observer they could determine the angle of its arrival." (Sullivan, 1984). They might also begin to know the distance between themselves after the arrival of many waves. Of course the previous thoughts are severely simplified.

The simple geometry of a single baseline delay measurement is shown in Figure 4 (Ma, 1978). The baseline B connects the two VLBI stations and S is the unit vector pointing from earth to the radio source. D is the distance most directly associated with the delay being measured; an incoming plane wave traverses distance D during the delay time. The plane wave arrives first at station one, which is the VLBI station closest to the source. The plane wave then arrives at station two. The radio signals are recorded independently on tape recorders at each station. A clock, usually a hydrogen maser time and frequency standard, is used to determine the time of plane wave arrival at each station. The tapes from each station are

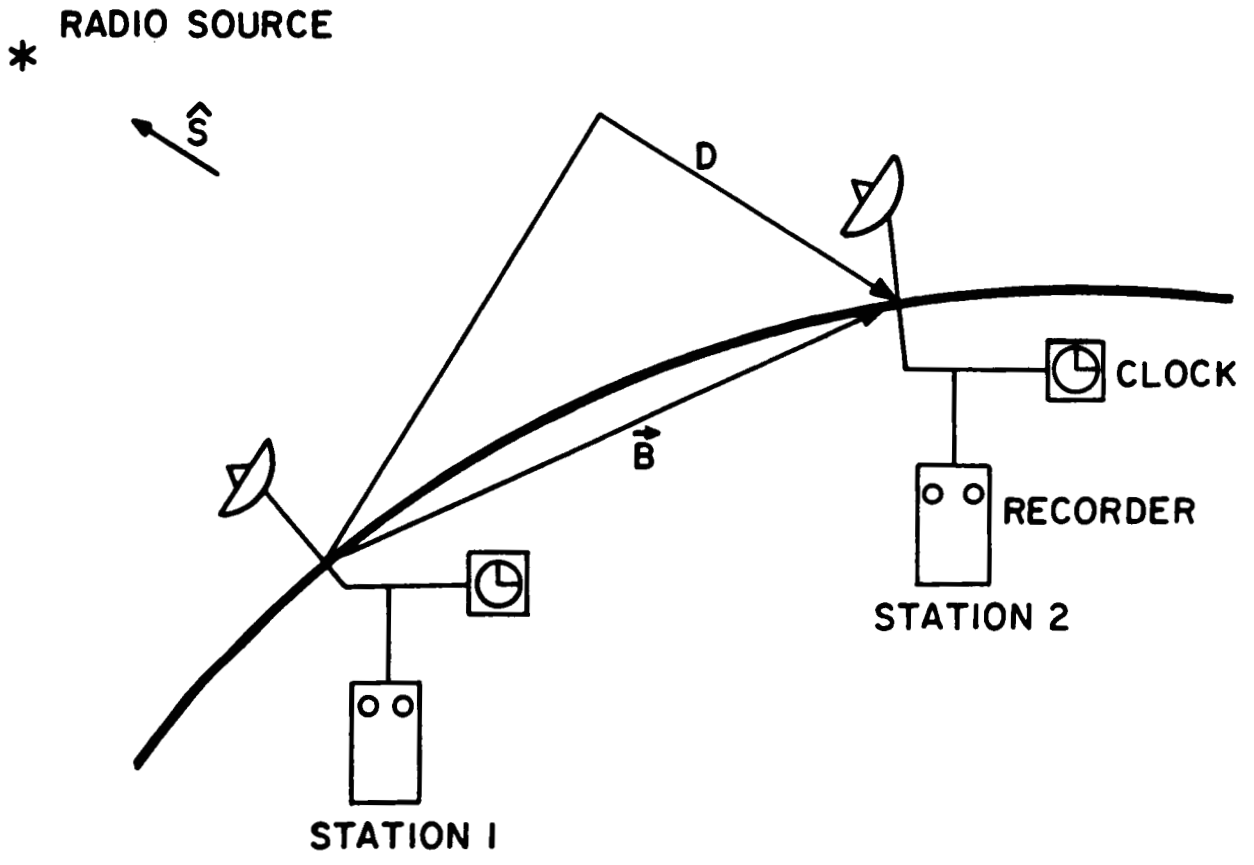

Fig. 4. Basic VLBI geometry (from Ma, 1978).

sent to a "correlator" where the delay between the arrival times is found precisely. VLBI differs from connected-element interferometry in that the endpoints of the interferometer are not connected electrically. A maser at each VLBI station provides time information on the data tapes to permit comparison of signal arrivals long after an experiment is run.

The geometrical delay, T_g, associated with the station geometry (see Figure 4) is

$$T_g = \frac{-B \cdot S}{c} \qquad (IV.1)$$

where c is the velocity of the plane wave and the dot denotes a dot product of two vectors. The geometrical delay is simply the distance D travelled by the plane wave between the two stations divided by wave velocity. The angle between vectors B and S can be estimated using relation (IV.1).

While the fundamental physics of VLBI is trivial, real world phenomena make VLBI modelling complex. The earth rotates as each delay measurement is made; so the VLBI observation geometry is not constant in time. The geometric delay changes temporally, and the motions of the stations cause Doppler shifts of the incoming radio signals. The earth wobbles with annual and fourteen-month periods, and precession and nutation occur. The earth is not rigid in general, and effects of earth and ocean tides on VLBI

observations must be modelled. The incoming radio waves traverse the ionosphere and troposphere, and propagation through these media affects the measured delays greatly. Most of these effects are well described in Ma (1978), Robertson (1975) and Lundquist (1984).

Herring et al. (1985) give a very clear description of several coordinate systems used in VLBI work and how one transforms a vector (such as a VLBI baseline vector) between the coordinate systems. The reference time epoch used in VLBI research is based on the year 2000, and is known as J2000.0. The time epoch formerly used in VLBI work was 1950. The notation of Herring et al. (1985) differs somewhat from that used in this dissertation. b_i is B_{2000} herein; b_t (Herring) is $B_{terrestrial}$ herein. The polar motion components x_p and y_p are x_{BIH} and y_{BIH} herein. The mean obliquity of data (ϵ_0 Herring) is given herein as ϵ. Little else is different. The passage from Herring et al. (1985) follows.

> In this appendix we discuss in detail the rotation matrices which are used in our analysis to transform between 'crust-fixed' and inertial coordinate systems. Our terrestrial coordinate system is defined by a set of site coordinates which would be invariant with time if there were no tectonic motions of the VLBI sites. From these site coordinates we compute the vectors between the sites, b_c, in the crust-fixed coordinate system. For the central epoch of each observation (typical duration 100-400 seconds), we compute the displacements of the sites due to the solid earth tides using the algorithms discussed in Herring et al. 1981. These displacements are added to b_c to yield $b_t = b_c + u_e$, where u_e is the (three dimensional) earth tide displacement computed from a planetary ephemeris of the sun and the moon, and the Love numbers h=0.609 and l=0.085. (We assume zero phase lag.) We now

apply a sequence of rotations to the coordinate system in which b_t is given to determine the coordinates of the baseline in inertial space, b_i. This sequence of rotations is:

$$b_i = PNSW\ b_t. \qquad (A.1)$$

We now discuss each of these rotations. We give firstly the expression used in evaluating the elements of the rotation matrices. We then discuss the physical significance of the transformations. In our discussion we will use the standard rotation matrices (Goldstein 1950, p. 109):

$$R_X(\xi) = \begin{pmatrix} 1 & 0 & 0 \\ 0 & C & S \\ 0 & -S & C \end{pmatrix}, \quad R_Y(\xi) = \begin{pmatrix} C & 0 & -S \\ 0 & 1 & 0 \\ S & 0 & C \end{pmatrix},$$

$$R_Z(\xi) = \begin{pmatrix} C & S & 0 \\ -S & C & 0 \\ 0 & 0 & 1 \end{pmatrix},$$

where $C = \cos\xi$, and $S = \sin\xi$, and ξ is the argument of the rotation.

We discuss the rotations in the order in which they are performed. The W matrix is given by:

$$W = R_X(-y_p)R_Y(x_p), \qquad (A.2)$$

where x_p and y_p describe the pole position (see later discussion) with the sign convention used by the BIH. The S matrix is given by:

$$S = R_Z(-GAST), \qquad (A.3)$$

where GAST is Greenwich apparent sidereal time given by:

$$GAST = GMST_0 + [d(GMST)/d(UT)]\ UT1 + \Delta\psi\cos\epsilon, \qquad (A.4)$$

where $GMST_0$ is Greenwich mean sidereal time at 0 hr UT, d(GMST)/d(UT) is the derivative of GMST with respect to universal time, UT (Aoki 1984), and $\Delta\psi\cos\epsilon$ is the 'equation of the equinoxes' with $\Delta\psi$ being the total nutation in longitude of date and ϵ being the true obliquity of date. The N matrix is given by

$$N = R_X(-\epsilon_0)R_Z(-\Delta\psi)R_X(\epsilon_0+\Delta\epsilon), \qquad (A.5)$$

where ϵ_0 is the mean obliquity of date, and $\Delta\psi$ and $\Delta\epsilon$ are the nutation angles computed from the IAU 1980 nutation series (Wahr 1981, Seidelmann 1982). The P matrix is given by

$$P = R_z(\zeta_a)R_y(-\theta_a)R_z(z_a) \ , \qquad (A.6)$$

where ζ_a, θ_a, and z_a are the standard arguments for precession (Lieske et al. 1977).

We now discuss the meaning of the transformations given above. The W rotation moves the pole T of the terrestrial coordinate system to the pole R of an intermediate coordinate system (see Figure A.1)[Fig. 5]. The pole R is approximately coincident with the pole of the instantaneous rotation axis (we discuss later in the appendix the specific definition of R). The S matrix rotates the coordinate system about the R pole. The combined PN matrix moves the pole R to the pole I which would be fixed in inertial space if the arguments of all of the transformations were correct. If we use the IAU [International Astronomical Union] 1980 nutation series in the evaluation of N, the PNSW transformation is not exactly correct because we perform the sidereal rotation about the R pole rather than about the earth's instantaneous rotation axis, R^*. However, the R^* pole moves relative to the crust with approximately a diurnal period under the action of the external luni-solar torques and, hence, in addition to the W transformation (whose arguments are assumed to change slowly compared to the diurnal period), we would need to apply another transformation, the diurnal-polar-motion (DNP) transformation (Kinoshita et al. 1979). Through second order in the separation of R and R^* (maximum separation 25 mas), this latter technique yields the same transformation as the technique of rotating about R (see discussions in Kinoshita et al. 1979 and Seidelmann 1982). Consequently, the axis for which the nutations are calculated is one which would be fixed relative to the crust of the earth if the earth were not undergoing free motion. This axis is the axis of figure of the Tisserand mean outer surface, or simply, the 'body axis' (Wahr 1981). The interpretation of x_p and y_p is more complicated than that for the nutation angles because the polar motion is composed of two types of motion: the free motion (Chandler wobble), and the forced motion (which has an approximately annual period and is due to interactions between the solid earth and the atmosphere/ocean system).

Herring et al. (1985) make corrections to the 1980 IAU Nutation Theory. A clear account of the physics of

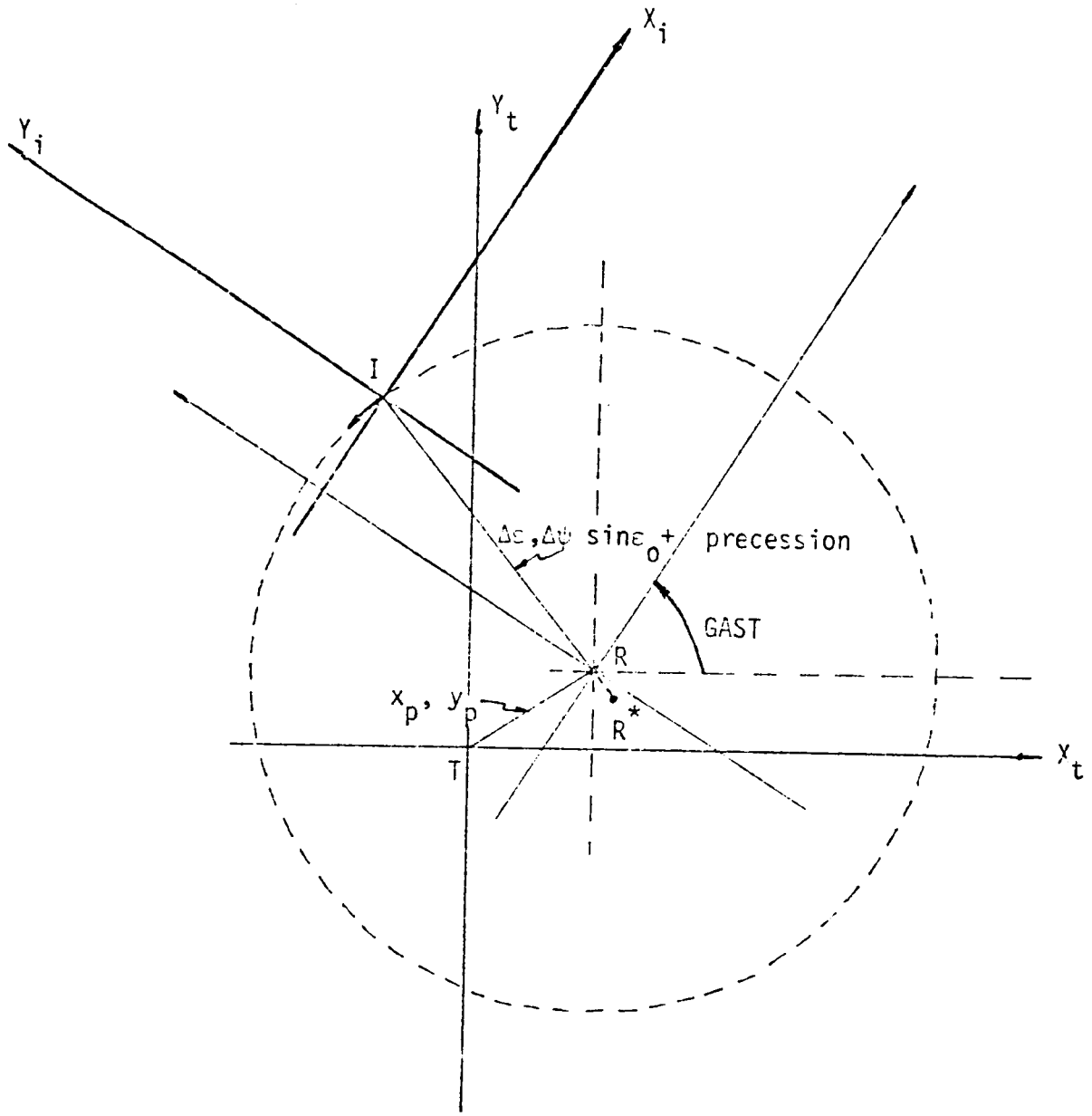

Fig. 5. The geometry of the various poles used in the transformation from the 'crust-fixed' coordinate system to the inertial coordinate system. The figure is not to scale. The separations of various poles are: T and R≈ 300 mas, R and I≈ 9,000 mas (due to nutation) plus≈ 0.1 degree (due to precession), and R and R* ≈25 mas. (From Herring et al., 1985).

precession and nutation can be found in Stacey (1977).

Now that the various transformation matrices and reference frames have been formulated, one should have sufficient courage and background to be exposed to the actual delay expression, which differs from the simple geometrical delay T_g (IV.1), due to Doppler and rotation effects etc. It is (Robertson, 1975)

$$\tau = \tau_0 - \dot{R}\cdot\{R_2 - R_1\} - \{\ddot{R}\cdot R_2 + \dot{R}\cdot\dot{R}_2\}\tau_0 + (\dot{LPT})\tau_0 \qquad (IV.2)$$

where

$$\tau_0 = (R_1 - R_2)\cdot S - \{(\dot{R}+\dot{R}_2)\cdot S\}\{(R_1 - R_2)\cdot S\}\{1 - (\dot{R}+\dot{R}_2)\cdot S\} \qquad (IV.3)$$
$$-(1/2)\{(\ddot{R}+\ddot{R}_2)\cdot S\}\{(R_1 - R_2)\cdot S\}^2 + \tau_A .$$

The variables of (IV.2) and (IV.3) are defined here (Ma, 1978)

τ = the delay (usually in nanoseconds)

R = solar system barycentric position of the earth's center

R_1 = geocentric position of station one (see Figure 4)

R_2 = geocentric position of station two

S = unit vector directed from earth to source

τ_A = propagation media delay

LPT = Long Period Terms (explained in Ma, 1978).

Dots over variables indicate differentiation with respect to coordinate time. Dots between variables denote dot products. Expressions for the delay rate, τ, are not quoted here because

they will not be used in this work; the delay rate equations can be found in Ma (1978). The value of the velocity of light is set to unity (c=1) in expressions (IV.2) and (IV.3).

From (IV.2) and (IV.3) it is evident that the delay τ is directly proportional to the simple geometrical delay (IV.1), which is $(R_1 - R_2)\cdot S$, because baseline length B $= R_2 - R_1$. Also the delay is directly proportional to the propagation media delays, τ_A, which makes sense. Equations (IV.2) and (IV.3) include terms resembling velocities $(\dot{R},\dot{R}_1,\dot{R}_2)$ and accelerations $(\ddot{R},\ddot{R}_1,\ddot{R}_2)$ which are due to a Taylor expansion procedure in the derivation of the delay. For the details see Robertson (1975). Equations (IV.2) and (IV.3) are approximations which neglect terms of order less than 10^{-15} seconds in delay (Robertson, 1975). This approximation is reasonable because group delay residual standard deviations are generally on the order of 100 picoseconds or less.

Relatively little has been said about the general method of determining the observed delay. For the moment, let the group delay be designated by the symbol Δt. τ will be used again later to represent the group delay. The delay between plane radio wave arrivals at two VLBI stations can simply be expressed as (Shapiro and Knight, 1970)

$$c\Delta t = n\lambda + \delta\lambda;\ 0 \leq \delta\lambda < \lambda. \qquad \text{(IV.4)}$$

where c is the velocity of the radio waves, n is an integer,

λ is the wavelength of the radio wave of concern, and $\delta\lambda$ is some fraction of a wavelength. Note that the case of a non-dispersive radio wave is being treated here. Clearly, the propagation distance, $c\Delta t$, between two stations can be thought of as a combination of integral and fractional wavelengths, as (IV.4) suggests. Using the relation $f = c/\lambda$, where f is frequency, one can convert (IV.4) to

$$2\pi f \Delta t = 2\pi n + \Phi \qquad \text{(IV.5)}$$

where Φ, the phase, is given by $\Phi = (2\pi\delta\lambda)/\lambda$.

Differentiating (IV.5) with respect to frequency, one can readily find (Shapiro and Knight, 1970)

$$\frac{d\Phi}{df} = 2\pi\Delta t. \qquad \text{(IV.6)}$$

Thus if one has phase information as a function of radio frequency, one can readily determine the group delay, Δt. The slope of the phase vs. frequency determines the group delay. VLBI observations are commonly made at multiple frequencies within two wide bands of radio frequency known as (Lundquist, 1984) S-band (2.3 GigaHertz) and X-band (8.4 GigaHertz). The multiple frequencies within each band are given in Lundqvist (1984). The technique of determining group delays from phase observations at multiple frequencies within wide radio bands is called "frequency synthesis". The technique is due to Rogers (1970). The reason for

making VLBI observations in both the S and X bands will be explained subsequently.

From (IV.6) one can derive an expression for the error in the group delay, $\delta\Delta t$ (Shapiro and Knight, 1970)

$$\delta\Delta t \approx \frac{\delta\Phi}{2\pi(f_{max}-f_{min})} \qquad \text{(IV.7)}$$

$\delta\Phi$ is the error in the phases Φ and f_{max}, f_{min} are the maximum and minimum frequencies enclosing the frequency synthesis bandwidth (Shapiro and Knight, 1970). From (IV.7) it is evident that the error in the delay, $\delta\Delta t$, is independent of the baseline length between two VLBI antennas.

There is considerable work done in preparing and executing a VLBI experiment, so it will be instructive to describe the process. The logistics of the experiment, such as equipment and personnel dispatching, etc., will not be mentioned. More than two stations usually participate in an experiment. The station antennas observe, in unison, about ten or more radio sources sequentially up to a total of 200 scans in 24 hours. In NASA Crustal Dynamics Program experiments, observation schedules are designed using the GSFC program SKED with the guidance of a VLBI scientist, and these schedules are sent in advance to the participating VLBI stations. Schedules must advise each VLBI station when to start and stop viewing a source, and these observational time limits must reflect the times when a given source is visible

at each station. Sources must be scanned long enough to produce acceptable interference fringes. There are many other complexities not addressed here.

The signals received at an antenna are stepped down from radio to 2 MHz baseband frequencies and the resulting signals are stored on tapes. Each tape also has time information from the station maser. Once the experiment is completed, all the tapes are sent to a correlator location. Crustal Dynamics Project tapes are sent to the Haystack (Massachusetts) correlator. The correlation process and much of what else goes on in VLBI experiments are described in Ma (1978). The observed delay for each baseline at each scan is the ultimate output of the correlator.

The delays are then sent on tape to an analysis team, such as the VLBI group at Goddard Space Flight Center (GSFC). Theoretical delays for each baseline are calculated using the program CALC. The theoretical delays are used as reference values in a linearization scheme similar to that of equation (III.17) and are based on a priori station positions, quasar positions, UT1/polar motion values, etc. The difference between the observed delay and the theoretical delay is called the delay residual. Typically group delay residuals are analyzed, but phase delay information is available.

The delay residuals are used to solve (either by least squares analysis or Kalman filtering/smoothing) for adjustments to the a priori parameter values of station positions,

earth orientation angles, clock variations etc. The estimation program at GSFC is called SOLVE, and generally a SOLVE solution requires several hours or more of analyst time to process a single VLBI experiment. Much of the analyst's time is used deciding polynomials to approximate the clock variations (arising from station maser behavior and other physical phenomena) seen in VLBI residual data. One goal of this work is to see if a Kalman filter can solve for clock variations in the time domain with limited analyst intervention, thus reducing analyst effort and also eliminating the subjectivity of analyst clock modelling. VLBI solution results generated by SOLVE are transferred into various data bases, one of which is openly available to geophysicists and astronomers. Outside users can use the information to study current plate tectonics, crustal block stability, earth rotation and orientation, or radio source structure and position.

The conversion of delay residual information to VLBI parameters of physical interest generally progresses towards solutions with better fits. Many SOLVE analysis sessions are required before solutions achieve stable form. In early (initial) solutions, BIH rapid service (preliminary) UT1 and polar motion values are used as a priori reference parameters. Later, final values of UT1 and polar motion are taken from the BIH Circular D. Meteorological information for calibrating the atmospheric delays in the observed delays is included in SOLVE runs as soon as it is available.

If the physical models in CALC or SOLVE are improved, new computer runs are made with updated versions of the software. The process continues until a solution fit cannot be improved, currently less than 50 picoseconds RMS group delay residual error.

There are some physical phenomena which grossly affect delay data. The models used by the East Coast VLBI group to minimize the effects of these phenomena on delays are described below. These include: the ionospheric correction, "clock" models, cable calibration, and various atmospheric models. This section is intended as a brief and contemporary explanation; some other phenomena affecting delay values, such as antenna axis offset, are not covered in this work, and generally can be found in Ma (1978).

It was mentioned previously that VLBI delay data are taken in two frequency bands, the S and X radio bands. This is done to remove the effects of the ionosphere on the delay. Charged particles are present in the ionosphere and delay incident VLBI signals. Delay due to passage of VLBI signals through the ionosphere (T_{ion}) is frequency dependent and can be modelled via the relation (Ma, 1978)

$$T_{ion} = k/f^2, \qquad \text{(IV.8)}$$

where k is a constant and f is the observing frequency of the band of interest.

Following Ma (1978), if τ_1 and τ_2 are the group delays

observed at frequencies f_1 and f_2 (for instance, at X and S band) and τ_{actual} is the actual group delay with ionospheric delay removed, then one can write

$$\tau_1 = \tau_{actual} + k/f_1^2 \qquad \text{(IV.9)}$$

$$\tau_2 = \tau_{actual} + k/f_2^2 \qquad \text{(IV.10)}$$

Since τ_1, τ_2, f_1 and f_2 are known for a VLBI experiment, while k and τ_{actual} are unknown, there are two equations and two unknowns. One can solve for k and τ_{actual}. With some slight algebraic manipulation

$$k = \frac{(\tau_1 - \tau_2)(f_1)^2(f_2)^2}{(f_2)^2 - (f_1)^2} \qquad \text{(IV.11)}$$

and

$$\tau_{actual} = \tau_1 - \frac{(\tau_1 - \tau_2)}{1 - (f_1/f_2)^2} \qquad \text{(IV.12)}$$

τ_{actual} is a single delay deduced from observations at two frequency bands and is relatively free from any ionospheric delay contribution.

Once a radio signal has penetrated the earth's ionosphere, it must traverse the atmosphere. As the VLBI signal passes through the atmosphere, the refractive index of the medium increases, and the path of the plane wave is no longer straight. Ideal and actual radio signal paths through the atmosphere are illustrated in Figure 6 (Lundqvist,1984;

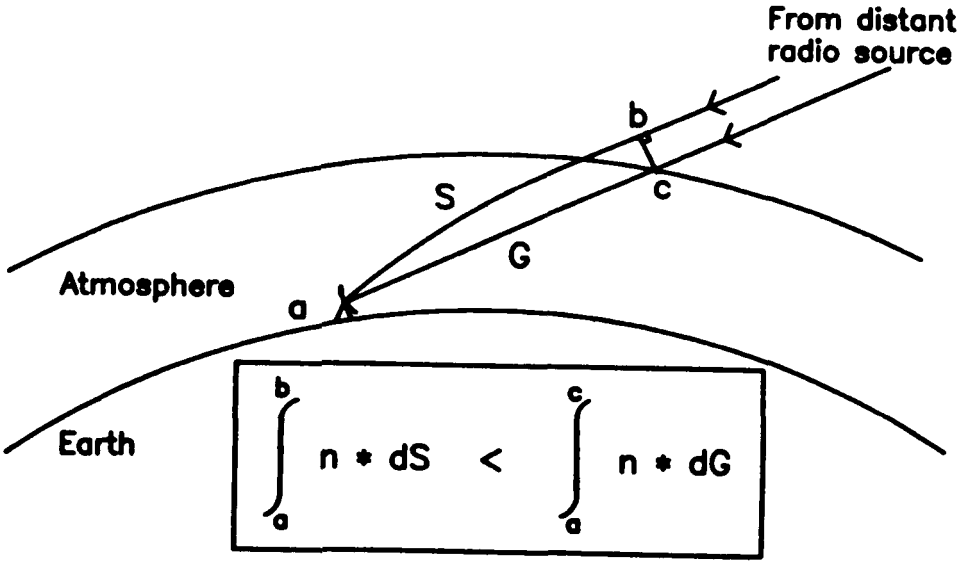

Fig. 6. The signal from the distant radio source will propagate along the path S, instead of the geometrically shorter path G, to the antenna at the surface of the earth due to the increasing refractive index down through the atmosphere (From Elgered, 1983; Lundqvist, 1984).

Elgered, 1983). Clearly the actual curved path travelled by the radio wave is longer than the ideal straight path that would be taken if the earth had no atmosphere; thus there is a delay associated with the propagation of a VLBI signal through the atmosphere due to additional path length. The atmospheric delay is roughly due to a dry component, from the air in the atmosphere, and a wet component, from water vapor in the atmosphere (an approximate description).

The additional path length due to the dry component, L_d, is given by (Moran, 1976; Ma, 1978)

$$L_d = 77.6 \frac{R}{mg} P_0 \quad \text{(cm)}, \qquad \text{(IV.13)}$$

where

R = 8.3144×10^7 erg/mole = universal gas constant

g = acceleration of gravity (at station) - cm/sec^2

m = molecular weight of dry air = 28.966

P_0 = dry air pressure (millibars).

It is much more difficult to estimate the wet component path length because of the highly inhomogeneous distribution of atmospheric water vapor. Consider that the determination of the moisture content in the atmosphere plays a large role in weather prediction, which is problematic at best. One might then appreciate the task of estimating the wet component path length faced in VLBI. The wet component path length depends on the amount of water vapor in the direction of the radio source being observed. A means of determining

the wet delay observationally using a Water Vapor Radiometer (WVR) will be set forth later. The wet component path length is roughly ten to fifteen percent of the dry component path length (Ma, 1978).

Even if directly observed atmospheric delay information is available, one normally adjusts the atmosphere delay in the zenith direction at each VLBI station. A priori atmospheric delays can be determined using barometric pressure (air column height) calculations or they can be set at atmospheric delay values from previous VLBI experiments. It is desirable to determine atmospheric path delays independently of VLBI measurements by using WVR's or radiosondes, but until recently this has rarely been done.

Several scaling equations relating zenith delay to actual path delay are, or will be, commonly used by East Coast VLBI analysis teams. The first is due to C.C. Chao (1972), and is a modified cosecant function (Elgered and Lundqvist, 1984)

$$L(EL) = \frac{L_Z}{\sin(EL) + \dfrac{0.00143}{\tan(EL) + 0.0445}}, \qquad \text{(IV.14)}$$

where L(EL) is the path length at the elevation angle EL and where L_Z is the zenith path length. Elevation angles are measured relative to the horizon, so that the EL of zenith equals 90 degrees. The Chao model constants were found by best least-square fits to radiosonde profile ray-tracing results (Elgered and Lundqvist, 1984). The Chao model only

requires elevation angle and zenith delay length for application, so it is generally applied to VLBI observations in which no ancillary meteorological data were recorded.

A more sophisticated mapping function is due to Marini (1974) for elevation angles greater than ten degrees (Elgered and Lundqvist, 1984)

$$L = \frac{1}{f(lat,h)} \frac{(A+B)}{\sin(EL) + \frac{B}{(A+B)(\sin(EL)+0.015)}} \quad (cm) \qquad \text{(IV.15)}$$

where

$A = (2.277 \times 10^{-3}) \times (P + (1255/T + 0.05) \times e)$

$B = (2.644 \times 10^{-3}) \times \exp(-0.14372 \times h)$

h = height of station above sea level (kilometers)

lat = station latitude

$f(lat,h) = 1.0 - (0.0026 \times \cos(2\ lat)) - (0.00031 \times h)$

e = water vapor partial pressure (millibars)

P = total pressure (mbar)

T = absolute temperature (K)

Obviously meteorological data must be recorded at the VLBI observing station in order to apply the Marini model. If meteorological data are available, the Marini model is generally used in preference over the Chao model for atmospheric delay calibration. However, VLBI analysts are free to choose the atmospheric model that allows the best least squares fit in the delay residuals.

Davis et al. (1985) give a newer relation between zenith

path length and path length at a specific elevation

$$L(EL) = \frac{L_z}{\sin(EL) + \dfrac{a_1}{\tan(EL) + \dfrac{a_2}{\sin(EL) + a_3}}} \qquad \text{(IV.16)}$$

where a_1, a_2, a_3 are again determined from best fits to ray tracings. This mapping function gives much better results than the Chao and Marini models, especially at elevation angles below about ten degrees (Davis et al., 1985).

As was suggested earlier, it would seem better to observe atmospheric delay directly, and remove it from VLBI data, than to find the zenith atmospheric delay from VLBI data. Since the dry part of the delay is readily determined, it is only necessary to measure the contribution of the wet atmospheric delay at elevation. The wet delay can be calculated by inverting brightness temperatures observed at 22 GHz and 31 GHz using water vapor radiometers (Clark et al., 1985; Resch et al., 1984). Brightness temperature is a quantity which characterizes the radiation given off by a black body using Planck's radiation law; in this instance microwave radiometers scan the radiation given off by the atmosphere. The water vapor radiometer technique relies on the fact that a water vapor resonant absorption line exists at 22 GHz, but not at 31 GHz. Thus the integrated water vapor content along some elevation angle can be estimated from the brightness temperature results. Several water

vapor radiometers are being tested at Crustal Dynamics Project (CDP) VLBI stations and should see active duty in the next several years.

Since WVR data have rarely been available in the past, it would be useful if some means could be discovered to retrieve wet atmospheric delay results directly from VLBI observations, so that VLBI data taken in the past decade could yield better results. Using a Kalman filter, Davis et al. (1985) were able to estimate wet atmospheric delays as a function of time (at each VLBI observation). These atmospheric delays, formed by Kalman filtering VLBI delay data only, match well (aside from slight biases) WVR atmospheric delay results observed independently of the VLBI delays.

VLBI delay observations also include the effects of "clock" variations. Such clock variations are time-like signals which are superimposed on VLBI delay signals; the clock variations are separated from VLBI signals through least squares or Kalman filter analysis. Differential clock variations between stations add directly into the observed VLBI delays, and are principally due to three sources: maser time (and frequency) variability, phase calibration and cable calibration signal failures.

The maser at a VLBI station is used as a time and frequency standard. A precise frequency standard is needed to step the incoming radio signals down to video frequencies suitable for recording. The hydrogen masers are typically stable to one part in 10^{14} in time, with hoped-for

improvement by one or two orders of magnitude as supercooled maser cavities come into operation. However, masers behave less well if their environment is not thermally controlled or if they are not isolated from other ills such as stray magnetic fields. The nuisance signal put into a VLBI delay by two masers at each end of a given baseline is the relative time difference between the masers. Most of the time difference between masers is a "ramp" function in time (otherwise known as a "rate"). Such a constant change in maser time as a function of time is due to an offset in the frequency of each maser, and can also be observed in a controlled laboratory environment. More often than not, any non-linearities visible in a maser-maser intercomparison are due to electronics external to the masers; the masers are indeed stable to one part in 10^{14} in time (Chiu, 1984).

Laboratory maser behavior indicates that "clock" fine structure irregularities usually seen imposed on the dominant clock rate trend are created by phase calibrator signal variations or other changes in signal path. The phase calibrator at a VLBI station generates pulses from the station frequency standard and injects them into the main signal path at the feed horn of the receiver. The phase calibrator pulses then follow the same signal path as the quasar signals until their recording on magnetic tape in video format. The purpose of the phase calibration is to correct for retardation and dispersion in the cable and electronics as the signal passes from feed to recorder. "The

arrival time associated with a signal is derived directly from the phase calibrator injected with that signal [the signal from maser to phase calibrator]." (Ma, 1978)

Unluckily, the electrical reference signal passing from the station frequency standard to the phase injector is also carried by cable, and is subject to environmental, dispersive and retardation effects, thus changing measured delay values. Care must be taken to maintain the integrity and physical dimensions of the maser-to-phase injector cable. Several members of the East Coast VLBI group are currently working to minimize phase calibrator (and associated) variability affecting the total VLBI delays. Such variability ultimately shows up in VLBI delay residual data. Cable calibration techniques are used to control the effects of thermal expansion and cable stretching on the length of the cable running from the station frequency standard to the VLBI receiver(s).

Together, maser time fluctuations, phase and cable calibration related alterations, and other jumps are referred to as "clock" variations by the VLBI analyst. Clock variations must be removed from VLBI delay data in order to obtain reliable astronomical and geophysical results. This is done within the VLBI program SOLVE with considerable analyst intervention. The analyst looks at delay residuals plotted as a function of time. (Note that the process being described here takes place only for least squares analysis, not in Kalman filtering/smoothing.)

Trends in the residuals are usually apparent, and the analyst tries to fit the delay residual plot with a polynomial (or polynomials) of the form

$$T_C = a_0 + a_1 t + a_2 t^2 + \ldots + A \sin(\Omega t) + B \cos(\Omega t) \quad \text{(IV.17)}$$

where T_C is the clock polynomial, a_0, a_1, a_2,..., A, B are constants which are evaluated in SOLVE to provide the best least-squares fit to the delay residuals, t is some measure of the time during the observing session, and Ω is the diurnal rotation frequency of the earth. Sinusoidal (diurnal) behavior is sometimes observed in the residual plots, and this can be fitted using the constants A and B.

Sometimes one cannot fit a single polynomial to the clock variability (on a single baseline) for a given data set. The analyst then may divide the data set into several time intervals; residuals in each interval of the experiment are then fit with a clock polynomial of their own. Clock polynomial analysis becomes very subjective and time-consuming. The value of a Kalman filtering/smoothing approach is thus clear; one does not have to divide a given data set into small time intervals for analysis.

The statistics of the delay residuals are found when the clock polynomials are included in the SOLVE least squares solution. These statistics are useful in judging the goodness of clock (and general) fit of a solution. Least squares data analysis continues until the data fit is good;

i.e. approaches levels consistent with contemporary data.

I now present the parameters of particular interest to this work, and how the measurement partial derivatives of these parameters are calculated for use in the Kalman filter/smoother. The partial derivatives are the components of M(k) in equation (III.4). The parameters of primary interest in this research are: the components of earth wobble, x and y (m_1, m_2 are freely interchanged with x,-y herein); the change in length of day, (UTC - UT1); the Kalman filter clock offset and rate terms, τ_c and τ_{cr}; the atmospheric wet zenith path delay parameters, L_z, and adjustments to the nutations in obliquity and longitude, $\Delta\epsilon$ and $\Delta\psi$. The clock coefficients and atmospheric parameters are clearly "nuisance" parameters in a study of polar motion, but the clock and atmospheric delays must be accurately modelled to give reliable and precise earth orientation results.

Partial derivatives for polar motion and earth rotation are formulated by combining equations (IV.1) and (A.1) (Ma, 1978)

$$T_g = \frac{-B_{2000} \cdot S_{2000}}{c} = \frac{-(PNSWB_{terr}) \cdot S_{2000}}{c} \qquad \text{(IV.18)}$$

where the 2000 and terr subscripts denote the J2000 and terrestrial reference frames, respectively. The source unit vector S is in the J2000 reference frame. (The spin matrix, S, and the source vector, S_{2000}, are not the same

entity.) The partials of the delay with respect to the polar motion parameters are found by differentiating equation (IV.18) with respect to x_{BIH} and y_{BIH} (as modified from Lundqvist, 1984)

$$\frac{\partial \tau}{\partial(x_{BIH}, y_{BIH})} = -(1/c)\left(PNS \frac{\partial W}{\partial(x_{BIH}, y_{BIH})} B_{terr} \right) \cdot S_{2000} \qquad (IV.19)$$

The partials of the wobble matrix W with respect to x_{BIH} and y_{BIH} are (Ma, 1978)

$$\frac{\partial W}{\partial x_{BIH}} = R_x(y_{BIH}) \frac{\partial R_y(x_{BIH})}{\partial x_{BIH}} \qquad (IV.20)$$

and

$$\frac{\partial W}{\partial y_{BIH}} = \frac{\partial R_x(y_{BIH})}{\partial y_{BIH}} R_y(x_{BIH}). \qquad (IV.21)$$

The partial derivatives of the nutation matrix with respect to the nutation in obliquity and longitude can be readily arrived at using equation (A.5)

$$N = R_x(-\epsilon) R_z(-\Delta\psi) R_x(\epsilon+\Delta\epsilon) \qquad (IV.22)$$

and differentiating IV.22 with respect to the obliquity angle

$$\frac{\partial N}{\partial(\Delta\epsilon)} = R_x(-\epsilon) R_z(-\Delta\psi) \frac{\partial R_x(\epsilon+\Delta\epsilon)}{\partial(\Delta\epsilon)}, \qquad (IV.23)$$

where

$$R_X(\epsilon+\Delta\epsilon) = \begin{pmatrix} 1 & 0 & 0 \\ 0 & \cos(\epsilon+\Delta\epsilon) & \sin(\epsilon+\Delta\epsilon) \\ 0 & -\sin(\epsilon+\Delta\epsilon) & \cos(\epsilon+\Delta\epsilon) \end{pmatrix} \qquad (IV.24)$$

Then

$$\frac{\partial N}{\partial(\Delta\epsilon)} = R_X(-\epsilon)R_Z(-\Delta\psi) \begin{pmatrix} 0 & 0 & 0 \\ 0 & -\sin(\epsilon+\Delta\epsilon) & \cos(\epsilon+\Delta\epsilon) \\ 0 & -\cos(\epsilon+\Delta\epsilon) & -\sin(\epsilon+\Delta\epsilon) \end{pmatrix} \qquad (IV.25)$$

We proceed similarly for the nutation in longitude

$$\frac{\partial N}{\partial(\Delta\psi)} = R_X(-\epsilon)\frac{\partial R_Z(-\Delta\psi)}{\partial\Delta\psi} R_X(\epsilon+\Delta\epsilon), \qquad (IV.26)$$

where

$$R_Z(-\Delta\psi) = \begin{pmatrix} \cos(-\Delta\psi) & \sin(-\Delta\psi) & 0 \\ -\sin(-\Delta\psi) & \cos(-\Delta\psi) & 0 \\ 0 & 0 & 1 \end{pmatrix} \qquad (IV.27)$$

so

$$\frac{\partial N}{\partial\Delta\psi} = R_X(-\epsilon) \begin{pmatrix} -\sin\Delta\psi & -\cos\Delta\psi & 0 \\ \cos\Delta\psi & -\sin\Delta\psi & 0 \\ 0 & 0 & 0 \end{pmatrix} R_X(\epsilon+\Delta\epsilon). \qquad (IV.28)$$

The partial derivative of the delay with respect to the

length of day parameter is approximated in a manner similar to the wobble partials

$$\frac{\partial \tau}{\partial (UTC-UT1)} = -(1/c) \left(PN \frac{\partial S}{\partial (UTC-UT1)} WB_{terr} \right) \cdot S_{2000} \quad (IV.29)$$

The partial derivative of S with respect to the time offset, UTC - UT1, is given by (Ma, 1978)

$$\frac{\partial S}{\partial (UTC-UT1)} = \begin{pmatrix} -\sin(GAST) & \cos(-GAST) & 0 \\ -\cos(GAST) & -\sin(-GAST) & 0 \\ 0 & 0 & 0 \end{pmatrix} \frac{d(GMST)}{d(UT)}, \quad (IV.30)$$

where GAST is Greenwich Apparent Sidereal Time.

Atmospheric and clock partial derivatives are found differently than the earth orientation measurement partials. The effect of the atmospheric path delay, τ_A, on the total delay (τ) of a specific baseline is (Ma, 1978)

$$\tau_A = \frac{L(2) - L(1)}{c} \quad (IV.31)$$

where L(1) and L(2) are atmospheric path lengths at VLBI stations (1) and (2). Recall that station (1) is closer in distance to the source under observation than station (2) at the time the delay is measured. Ma (1978) gives the partial of VLBI delay with respect to atmospheric path length in his dissertation.

The partial derivative of delay with respect to the clock offset parameter may be difficult to understand at this moment.

The meaning of the model should become clear later on. The observed delay τ includes clock offset effects, $\tau \propto a_0$. Then the measurement partial is simply

$$\frac{\partial \tau}{\partial a_0} = \pm 1, \qquad \text{(IV.32)}$$

where the sign is determined as in the subprogram MARTL (a modified form of the subroutine PARTL) within the analysis program SOLVE. The expression (IV.32) is the partial derivative for use with the Kalman filter/smoother, and is also the partial used in estimating the clock offset constant, the first term in the least squares clock polynomial (IV.17). The Kalman filter clock rate partial is assumed to be zero; this is an overly simple clock rate partial which models the clock ramp to be zero during a VLBI measurement. Such an assumption is only valid (to a fair degree) because VLBI measurements on a given source take place over a short time (roughly five to ten minutes). The primary partial derivatives used herein for Kalman filter VLBI analysis have thus been explained.

Chapter V.

EARTHQUAKES AND THE CHANDLER WOBBLE (A REVIEW)

The main thrust of this work is to clarify whether earthquakes are a significant excitation source of the Chandler wobble of the earth. Apparently, other mechanisms may be able to drive the wobble, such as atmospheric mass movements or core-mantle coupling, but the literature relevant to these phenomena will not be widely explored here (see Wilson et al., 1976 and Barnes et al., 1983). Literature concerning earthquake excitation of the Chandler wobble will be examined.

Interest in the effects of earthquakes on polar motion in the late 1960's led to the organization of a NATO Advanced Study Institute on "Earthquake Displacement Fields and the Rotation of the Earth" (Mansinha, Smylie and Beck, 1970), which was held in 1969. The edited volume based on this conference provides a good historical basis for any earthquake-excitation polar motion study. Prior to 1965, the changes in the earth's inertia tensor due to earthquakes were thought to be inadequate to excite Chandler wobble. Press (1965) demonstrated that mass displacements during a great earthquake extend over distances much further than were thought previously. Perhaps, since more mass is

involved in earthquakes than was previously thought, wobble may be excited by the larger associated inertia tensor changes.

An example of the involvement of mass at distance from a large earthquake and its effect on Chandler wobble is given by Stacey (1977). He considers an exemplary inertia tensor change for maintaining the Chandler wobble to be about 1.3×10^{28} kg-m^2, and considers that great earthquakes, such as that of 1964 in Alaska, may be the prime movers of the Chandler wobble. The inertia tensor change due to an Alaskan-like earthquake is found (Stacey, 1977) by approximating the earthquake geometry by two blocks of dimensions 800 km x 200 km x 200 km, and density 3000 kg/m^3, separated by a mean distance of 200 km, and displaced by 22 meters. The resulting inertia tensor change computed using the simple earthquake model is 8.5×10^{26} kg-m^2, which obviously falls short of Stacey's excitation requirement of 1.3×10^{28} kg-m^2.

However, if mass displacements at larger distances are included in the calculation of the perturbation of the inertia, Stacey (1977) states that the inertia tensor change due to the earthquake and associated mass movements is on the order of the required moment adjustment, 1.3×10^{28} kg-m^2. Thereby a great earthquake event might be able to significantly excite the Chandler wobble. Still, many geophysicists are not convinced that a great earthquake, occuring once or twice per decade, is sufficient to maintain

the Chandler wobble, though even they are not very sure of the time required for the Chandler wobble to damp out (Stacey, 1977).

More compelling evidence in support of the forcing of Chandler wobble by earthquakes was given by Mansinha and Smylie (1970) at the NATO Advanced Study Institute. Recall that Figure 1 depicts the modification of the Chandler wobble pole path due to a sudden mass shift in the earth. The rotation pole orbits about a shifted secular pole after excitation, with the orbital radius generally of different magnitude than prior to excitation. Mansinha and Smylie (1970) exploit the fact that a "kink" (change in curvature) is generated in the polar motion path due to a mass shift and try to correlate kinks in real data with large earthquakes, of Magnitude M > 7.5. The polar motion data (with annual wobble component removed) were from the BIH and ILS-IPMS (International Polar Motion Service) for the years 1957.0 to 1968.0.

The procedure by which kinks in the data are revealed is now described. If polar motion is continuous, the rotation pole moves through angle α in δ days with respect to the "mean pole", with angle α given by (Mansinha and Smylie, 1970)

$$\alpha = \frac{2\pi}{438} \times \delta, \qquad (V.1)$$

where 438 is their approximate period in days of the Chandler

wobble. A kink due to a shift in mass will disrupt the observed continuous polar motion. Mansinha and Smylie (1970) start their analysis, say at 1957.0, and fit a curve between two pole positions of the BIH data set (the analysis is done independently for ILS-IPMS data). ILS-IPMS and BIH measurements are made at regular time intervals. After the first arc is constructed between the two points, the arc is extended by assuming the same circular path (a predictive step) to approximate the next BIH datum. The predicted datum location on an x-y polar motion plot is then compared with the actual BIH datum location. If the prediction falls within some acceptance distance, a, of the actual BIH datum, no "kink" in the data has been observed, and a new arc is fitted to the three BIH data points in order to continue the comparison procedure between actual and predicted data (Mansinha and Smylie, 1970). The acceptance distance, a, is proportional to the error in the BIH measurements (a has centi-arcsecond units).

If the actual BIH polar motion position is further from the predicted datum than the acceptance distance "a", a break or "kink" in the pole path has been detected (Mansinha and Smylie, 1970). A new arc is now created using the aberrant BIH datum as a starting point and the comparison process continues again. The breaks found in the ILS-IPMS and BIH data were then compared against ($M > 7.5$) earthquake event times for 1957.0 to 1968.0 (Mansinha and Smylie, 1970), and random probability criteria were used to determine if the

breaks and the earthquakes were correlated. "For a = 0.015, 12 out of 22 earthquakes fall within ±10 days of a break and 17 out of 22 earthquakes fall within ±20 days of a break. The corresponding values of RP [random probability] are 1.3×10^{-3} and 1.6×10^{-3} respectively." (Mansinha and Smylie, 1970). The random probability function used in the study (cumulative binomial distribution) was (Mansinha and Smylie, 1970)

$$RP = \sum_{j=k}^{n} \binom{n}{j} p^j (1-p)^{n-j}. \qquad (V.2)$$

"The elementary probability p is the probability of a date, drawn at random, falling within ω [ω= correlation window; = 2δ] of a break [kink] and is given by the proportion of time axis of the total span of 11 years that is occupied by segments ω wide on each side of a break." (Mansinha and Smylie, 1970). Results are for BIH data sampled every ten days. Considering that only 22 large events occurred during the 11 year data span, and that 17 out of 22 earthquakes fall within ±20 days of a break, one might be inclined to believe that the polar motion breaks and earthquakes are well correlated.

Unfortunately, the study by Mansinha and Smylie (1970) may have been ahead of its time, although the method has a simple and believable mathematical basis. The polar motion data used in the analysis was only sampled at ten-day intervals, which leaves much to be desired in time resolution.

Also, Mansinha and Smylie (1970) note that the uncertainty of the polar motion data was on the order of ten milliarc-seconds, which is much larger than present-day uncertainties. However, current VLBI polar motion data sets do not approach the length (11 years) of the BIH and ILS-IPMS data used by Mansinha and Smylie. As a final point, Morabito and Eubanks (1985) intercompare ILS-IPMS polar motion data with concurrent polar motion component estimates determined by VLBI, satellite laser ranging and lunar laser ranging techniques and find differences between modern data and ILS-IPMS data of 50.3 milliarcseconds rms in the X component of wobbble and 23.3 milliarcseconds rms in the Y component; these differences are primarily due to seasonal variations in the ILS-IPMS data, but considerable differences still exist even after the seasonal variations are removed from the data. Morabito and Eubanks (1985) state that "These results indicate that any geophysical conclusions derived from ILS data should be interpreted with caution." The intercompared data spanned 1976-1979. Morabito and Eubanks' warning should be strongly heeded. Nevertheless, the work of Mansinha and Smylie (1970) was preeminent, and acted as a first step in contemporary Chandler wobble excitation research.

Dahlen (1973) uses a SNREI ("... spherically symmetric non-rotating Earth which is in hydrostatic equilibrium and has an isotropic elastic constitutive relation."- Smith, 1974) Earth model to calculate the pole shifts due to the

1960 Chilean and 1964 Alaskan earthquakes. The changes in the product of inertia components C_{13}, C_{23} (which are of primary interest in polar motion excitation-- see equations II.7 and II.9) of the earth model due to an earthquake at colatitude θ_0 and longitude Φ_0 are (Dahlen, 1973)

$$\begin{aligned}\Delta C_{13}=&M_0\{\tilde{\Gamma}_1(h)[[\sin2\alpha\sin\delta\cos\lambda+1/2\cos2\alpha\sin2\delta\sin\lambda)\\ &x\sin2\theta_0\cos\Phi_0-2(1/2\sin2\alpha\sin2\delta\sin\lambda-\cos2\alpha\sin\delta\cos\lambda)\\ &x\sin\theta_0\sin\Phi_0]+\tilde{\Gamma}_2(h)[-\sin2\delta\sin\lambda\sin2\theta_0\cos\Phi_0]\\ &+\tilde{\Gamma}_3(h)[(\sin\alpha\cos2\delta\sin\lambda-\cos\alpha\cos\delta\cos\lambda)\cos2\theta_0\cos\Phi_0\\ &+(\sin\alpha\cos\delta\cos\lambda+\cos\alpha\cos2\delta\sin\lambda)\cos\theta_0\sin\Phi_0]\}\end{aligned} \qquad (V.3)$$

$$\begin{aligned}\Delta C_{23}=&M_0\{\tilde{\Gamma}_1(h)[(\sin2\alpha\sin\delta\cos\lambda+1/2\cos2\alpha\sin2\delta\sin\lambda)\\ &x\ \sin2\theta_0\sin\Phi_0+2[1/2\sin2\alpha\sin2\delta\sin\lambda-\cos2\alpha\sin\delta\cos\lambda)\\ &x\ \sin\theta_0\cos\Phi_0+\tilde{\Gamma}_2(h)[-\sin2\delta\sin\lambda\sin2\theta_0\sin\Phi_0]\\ &+\tilde{\Gamma}_3(h)[\sin\alpha\cos2\delta\sin\lambda-\cos\alpha\cos\delta\cos\lambda)\cos2\theta_0\sin\Phi_0\\ &-(\sin\alpha\cos\delta\cos\lambda+\cos\alpha\cos2\delta\sin\lambda)\cos\theta_0\cos\Phi_0],\end{aligned} \qquad (V.4)$$

where h is the earthquake depth, δ is earthquake dip, α is the strike, λ is the slip angle and M_0 is the scalar moment of the earthquake. $\tilde{\Gamma}_1(h)$, $\tilde{\Gamma}_2(h)$, and $\tilde{\Gamma}_3(h)$ are canonical functions of depth computed for the SNREI Earth model under consideration; details about them can be found in Dahlen (1973). Clearly the product of inertia perturbations ΔC_{13} and ΔC_{23} of equations (V.3) and (V.4) are directly proportional to the seismic moment M_0 of a given earthquake; thus ΔC_{13} and ΔC_{23} are critically

dependent on moment determinations.

The pole shifts due to ΔC_{13} and ΔC_{23} are calculated by Dahlen (1973) for the 1960 Chilean and 1964 Alaskan earthquakes, and are compared with pole path shifts as seen in BIH polar motion data (Smylie and Mansinha, 1968). Dahlen (1973) finds that his theoretical polar motion shifts are an order of magnitude less than those observed by Smylie and Mansinha (1968), although the pole path shift directions determined with each method are in agreement. Noise contamination is blamed by Dahlen (1973) as the phenomenon which precludes observation of large polar motion path shifts in BIH data. He also concludes that "The direct observation of the effect of a large earthquake on the path of the Earth's rotation pole will not be possible until some way is found to reduce the noise contamination in the observed polar motion path by at least a factor of ten." VLBI data is more precise than the BIH data of 1968 by at least a factor of five to ten, so kinks in polar motion paths due to large earthquakes might be observed presently.

Dahlen (1973) next examines the cumulative effect of many large earthquakes on Chandler wobble power P, which is computed via the formula

$$P = \frac{Q}{\omega_0} \langle R^2 \rangle \qquad (V.5)$$

where Q is the Chandler wobble quality factor, ω_0 is the characteristic oscillation frequency of the wobble, and

$\langle R^2 \rangle$ "... is the mean squared polar shift per unit time associated with the earthquake sequence." Since Q and $\langle R^2 \rangle$ are not accurately known, any power estimated using (V.5) is only of limited accuracy. Dahlen accounts for this in some fashion by considering several values of Q in his power calculations, and he also compares the magnitude-moment relations of Brune (1968), and Aki (1967, 1972) and the effect of each on the power calculations. The magnitude-moment relations are displayed in Figure 7 (from Dahlen, 1973).

It appears that the Aki ω^2 model (1967, 1972) provides a better fit to observed surface wave and field data than Brune's (1968) magnitude-moment relationship, if the Sanriku (1933) datum is not included in the fitting process. There is some justification for not including the Sanriku earthquake in forming a general magnitude-moment relation. O'Connell and Dziewonski (1976) state that it is difficult to assign a source mechanism to Sanriku since the event occurred near the junction of the Eurasian, Pacific and Philippine plates, and its moment is somewhat low for large, shallow, subduction-zone events. In any event, use of Aki's (1967, 1972) ω^2 moment-magnitude relation gives a more favorable outlook (by power comparisons) of earthquake excitation of the Chandler wobble than does the Brune (1968) relationship.

For the calculated Chandler power values as a function of Q and moment estimation process, please refer to Dahlen

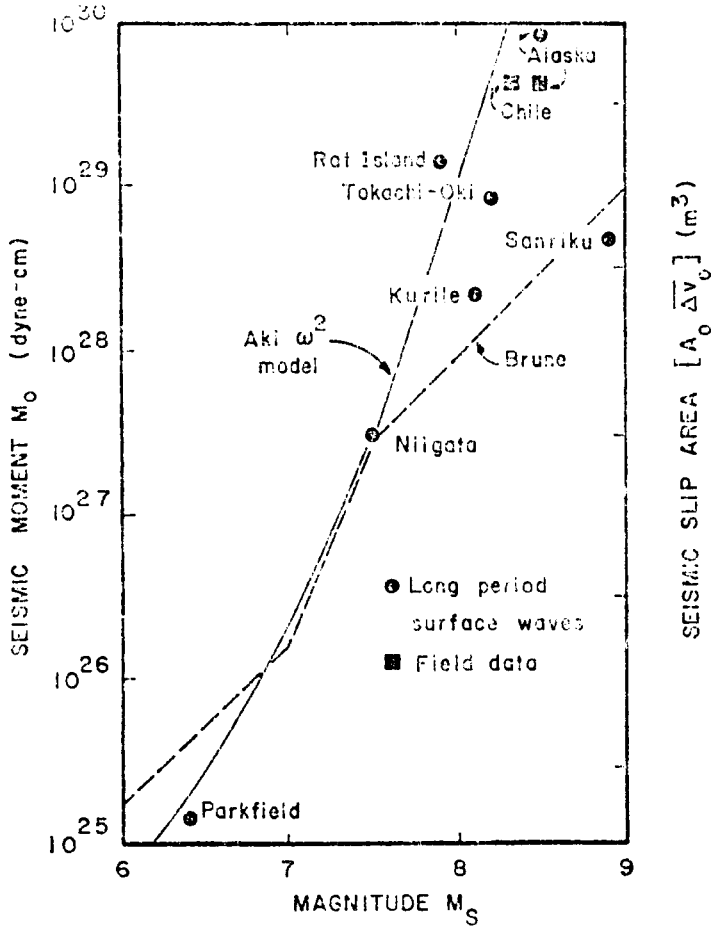

Fig. 7. Seismic moments M_0 vs. earthquake magnitude, as proposed by Brune (1968) and Aki (1967, 1972). (From Aki, 1972 and Dahlen, 1973).

(1973). Dahlen (1973) ultimately decides "... that the Earth's seismic activity can account for no more than 10 percent (for Q = 100), and probably even significantly less, of the observed level of excitation of the Earth's Chandler wobble." But since the value of the quality factor, Q, is ill-constrained, it is difficult for anyone to know if such a conclusion is valid, or certainly final.

In a much different vein, evidence was found by Kanamori and Cipar (1974) to support the hypothesis that earthquake events are accompanied by large, slow, aseismic deformations. The foundation for their study comes from a long-period strain seismogram recorded during the Chilean earthquake of 22 May, 1960. On the seismogram, accompanying the P wave arrival from a M_S = 6.8 foreshock, which occurred fifteen minutes prior to the main Chilean event, Kanamori and Cipar (1974) observe a long-period wave of period 300-600 seconds. That such a signal is real may be a valid question, but Kanamori and Cipar (1974) respond to this by stating that the seismogram shows a quiet, noise-free trace prior to the foreshock, and also note that such a long period precursor may be evident for the Chilean 1960 event, but not for other earthquakes because the Chilean earthquake is one of the largest events ever recorded using "modern" seismographs. They do admit, however, that the long-period precursor signal could be due to instrumental instability.

Next, Kanamori and Cipar (1974) determine fault parameters for the 1960 main Chilean earthquake and the long-

period precursor by matching synthetic seismograms to the observed strain seismogram traces. They find a moment of 2.7×10^{30} dyne-cm for the main shock and 3.5×10^{30} dyne-cm for the aseismic long-period precursor. The aseismic moment is of the same order as the moment of the elastic main shock. Kanamori and Cipar (1974) postulate that the Chilean sequence occurred as follows: "About fifteen minutes before the main shock a gradual slip having time constant of about 450 sec started taking place at the boundary between the downgoing oceanic lithosphere and the relatively weak asthenosphere beneath the [South American] continent. This slip caused a stress concentration at the lithosphere-lithosphere boundary above. The large foreshock may represent a brittle fracture caused by such a stress concentration. Eventually this stress concentration exceeded the breaking strength of the lithosphere-lithosphere boundary causing a major catastropic failure, the main shock." They also suggest that the Chilean aseismic slip may have occurred for hours or days before the main shock and feel that precursory long-period phenomena, even if only observed ten to fifteen minutes before a main shock, may be useful in preparing human populations near the epicenter for an impending event. Obviously, further study of aseismic stress releases is warranted.

Press and Briggs (1975) find correlations between Chandler wobble and earthquake activity through a pattern recognition analysis, the details of which are too many to be included here. They conclude that earthquakes of certain

positions (latitude, longitude, slip and fault orientation) are associated with years of increasing Chandler wobble amplitude, and hypothesize that large preseismic and post-seismic deformations (over hours or days) play a part in Chandler wobble forcing, in addition to the slip occurring during the main earthquake shocks. Press and Briggs (1975) also note that earthquakes along the Kurile-Japan-Marianas seismic belt and in China do not show a correlation with increasing Chandler wobble amplitude, and suppose that "...; perhaps slow deformation occurs in these belts during aseismic periods many years before or after major earthquakes." For the most part, Press and Briggs (1975) conclude that Chandler wobble excitation is due to large mass displacements associated with earthquakes.

Synthetic curves which mimic ILS polar motion data (with annual wobble removed) have been generated by O'Connell and Dziewonski (1976) for the time period 1901-1970, by the superposition of polar motion shifts from 234 large earthquakes of $M_S \geq 7.8$. The polar motion shifts are found from changes in the earth inertia tensor, ΔC_{ij}, which are related to the earthquake moment tensor M_{kl} via the following equation (O'Connell and Dziewonski, 1976)

$$\Delta C_{ij} = D_{ijkl} M_{kl}. \qquad (V.6)$$

where D_{ijkl} is a tensor with components determined by choice of earth model, and latitude and longitude of a

given earthquake epicenter. For details, see O'Connell and Dziewonski (1976). The source moments M_{kl} for the 234 earthquakes are approximated using simple double couple moments (of scalar moment M_0) in unison with plate tectonic information (O'Connell and Dziewonski, 1976).

The seismic moments M_0 are calculated from surface wave magnitudes M_s reported by Duda (1965), and other sources, using the relation (O'Connell and Dziewonski, 1976)

$$\mathrm{Log}_{10}\, M_0 = 8.8 + 2.5\, M_s . \qquad (V.7)$$

Once the pole shifts are calculated, the synthetic wobble m(t) is found with the expression (O'Connell and Dziewonski, 1976)

$$m(t)=m(t_0)\exp\{i\omega(t-t_0)\}+ \qquad (V.8)$$
$$+ \sum_k s_k H(t-t_k)\ \{1-(1+\omega_0/\Omega)\exp[i\omega(t-t_k)]\},$$

where $m(t_0)$ is the reference (starting) position of the Chandler wobble pole at time equals t_0, $\omega = \omega_0(1 + i/2Q)$, ω_0 is the Chandler wobble frequency, Q is the Chandler wobble quality factor, $H(t-t_k)$ is a step function, s_k is the pole shift due to an earthquake at the epoch t_k, Ω is the diurnal rotation frequency, and t is the time for which the synthetic signal m(t) is produced. The real and imaginary parts of m(t) are the Chandler wobble components, x_1 and $-x_2$ respec-

tively.

Synthetic polar motion curves for the x_1 wobble component (for various Q values) and smoothed ILS data with annual wobble removed are presented in Figure 8. The curve for $Q_s = Q_{synthetic} = 100$ resembles the ILS curve in general form, but the match is by no means exact. O'Connell and Dziewonski (1976) then compute power spectra of the various synthetic and ILS curves and compare the Chandler wobble peaks. In general, the agreement of ILS and synthetic data is fair. O'Connell and Dziewonski (1976) conclude that earthquake-associated mass movements may account for about fifty per cent of Chandler wobble excitation.

There is a major problem with the work of O'Connell and Dziewonski (1976). Kanamori (1976) points out that the surface wave magnitude used in Duda (1965) and by O'Connell and Dziewonski (1976) is not the same as the M_s referred to in the relation $Log_{10} M_0 = 8.8 + 2.5 M_s$. The net effect of this error is that O'Connell and Dziewonski (1976) overestimate the scalar moment M_0 of many of the earthquakes used in their study by a factor of 5.6 (Kanamori, 1976), and thereby overestimate many of the Chandler wobble shifts due to these earthquakes. This casts doubt upon the results of O'Connell and Dziewonski (1976). Another problem with O'Connell and Dziewonski's work is that their comparison was made in the time domain, as opposed to the excitation domain; Chao (1985) addresses this problem in detail. Kanamori (1976) also states that the direct effect of earthquakes on Chandler

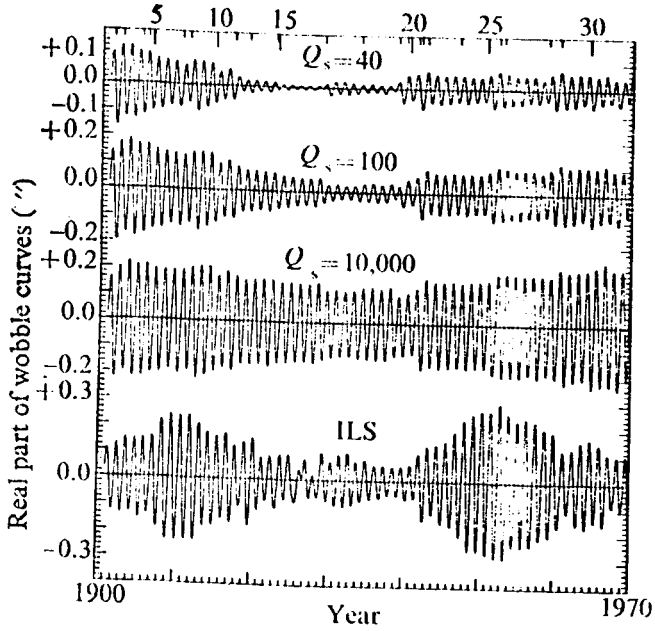

Fig. 8. Simulated polar motion curves resulting from excitation by large earthquakes; the damping for each is determined by Q_S. ILS is smoothed observed polar motion with annual term removed. Only the component along the Greenwich meridian is shown. (From O'Connell and Dziewonski, 1976).

wobble as calculated in a correct manner (using proper M_S values) is probably an order of magnitude too small to give observed wobble amplitudes. He does acknowledge that large aseismic deformations accompanying earthquakes may indeed be responsible for driving the Chandler wobble, and proposes that these deformations may be detected in the future with global arrays of ultra-long period seismological instruments.

In his 1977 article, Kanamori asserts that the Gutenberg and Richter (Gutenberg, 1956) magnitude-energy relation $\log E = 1.5M + 11.8$ is of questionable applicability to earthquakes of rupture length of 100 km or more (but works well for smaller rupture lengths). E is the energy released from an earthquake and M is the magnitude determined from seismic records. "This [problem] arises from the fact that for such a great earthquake the magnitude M which is determined at the period of 20 s (or converted from m (body wave magnitude) determined at shorter periods) does not represent the entire rupture process of an earthquake. In fact, there is little correlation between M and the rupture length for great earthquakes." (Kanamori, 1977).

Kanamori then derives, following laborious and rigorous analysis of large earthquakes, an alternate energy-magnitude relation for great events

$$\log W_0 = 1.5\ M_W + 11.8. \qquad (V.9)$$

M_W is the new magnitude for great earthquakes and W_0

is the minimum strain energy drop for great earthquakes. According to Kanamori (1977), the minimum strain energy drop is equal to the seismic wave energy. Also he states that W_0 can be calculated using the approximation

$$W_0 \approx M_0/(2\times10^4), \qquad (V.10)$$

where M_0 is the seismic moment of an earthquake (CGS units).

The minimum strain energy drop W_0 (and seismic wave energy released) is then calculated for (shallow) great earthquakes from 1904 to 1976 (Kanamori, 1977) and the results (5-year running averages) as a function of time are presented in Figure 9. In addition to W_0, the Chandler wobble amplitude; N, the annual number of earthquakes of $M_S \geq 7.0$ (a five-year running average); and a five-year running average of E (explained earlier) are included in the figure. The correlation between W_0 and wobble amplitude is high, and it appears that the wobble amplitude leads W_0. N seems to lead the Chandler wobble amplitude.

Kanamori (1977) proposes one explanation for the results in Figure 9. "One possible mechanism that accounts for the correlation between the wobble, W_0, and the activity of moderate to large earthquakes [as indicated by N] is that an increase in wobble amplitude triggers worldwide seismic activity and accelerates plate motion,

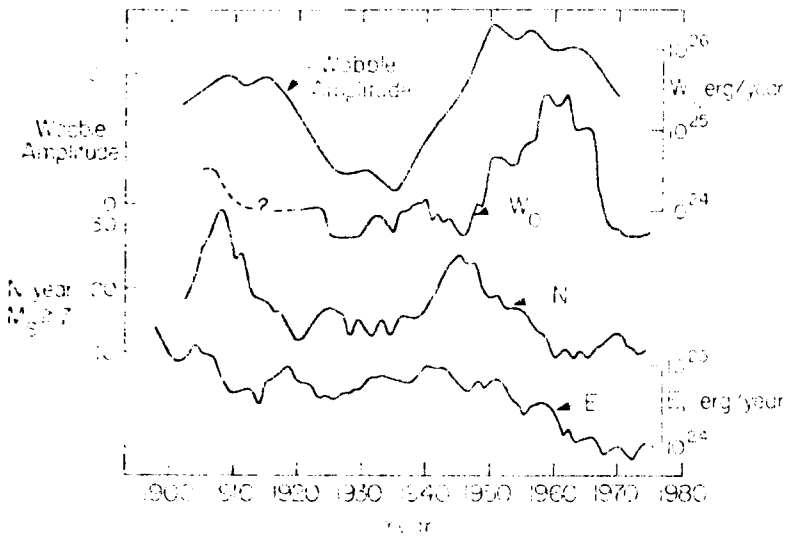

Fig. 9. Correlation between the amplitude (envelope) of the Chandler wobble, W_0 (5-year running average), annual number N of earthquakes of $M_S \geq 7.0$ (5-year running average), and the Gutenberg-Richter energy E (5-year running average). (from Kanamori, 1977).

which eventually leads to great decoupling earthquakes [i.e. decoupling along major plate boundaries]. This decoupling causes the decline of moderate to large earthquake activity."

Kanamori's (1977) analysis is straightforward. An alternate magnitude scale to describe the magnitude-energy relationship of great earthquakes is necessary. The correlation of wobble amplitude and energy released by great earthquakes is striking. The data do indicate that a Chandler wobble amplitude peak does precede a maximum in the seismic wave energy (1950 to 1965). The paper does not include the effects of aseismic slip. Kanamori's (1977) work suggests that the Chandler wobble triggers earthquakes, as opposed to vice versa.

It was mentioned earlier in this work that the Chandler wobble is a long period normal mode of the earth. It is because of this long periodicity that the Chandler wobble is of geophysical interest; few geophysical phenomena have been observed (or exist) at this frequency. Smith (1977) looks at the excitation of the Chandler wobble by seismic events by treating wobble as a normal mode. He uses his (1974) equations describing "... the infinitesimal free elastic-gravitational oscillations of a rotating, slightly elliptical Earth ... " to compute polar shifts due to the 1960 Chilean (modelled as a two-event source) and 1964 Alaskan earthquakes, which are two of the largest seismic events in recent history. The details of Smith (1974) are not fully described here.

Smith's (1977) normal mode calculation of Chandler wobble shifts differs from elastic dislocation methods typically applied to the excitation problem; it also avoids difficulties encountered in equations of motion describing the static deformation of the fluid core of an earth which is not rotating, which are used in such elastic dislocation calculations (Smith, 1977). Thus, Smith's (1977) analysis might be used to determine which of the many quasi-static Chandler wobble excitation studies is most correct.

Smith (1977) represents the particle displacement field, s(r), of the Chandler wobble normal mode by a truncated series of spheroidal vector fields, σ_l^m, and toroidal vector fields, τ_l^m,

$$s(r) = \tau_1^{\pm 1}(r) + \sigma_2^{\pm 1}(r) + \tau_3^{\pm 1}(r) \qquad (V.11)$$

where r is a radius variable. Equation (V.11) is inserted into the differential equations of motion of Smith (1974), and the solutions of these equations approximate normal mode eigenfunctions describing the Chandler wobble. The excitation theory developed by Dahlen and Smith (1975) is then applied to the calculated eigenfunctions to find the Chandler wobble shifts due to the aforementioned earthquakes (Smith, 1977).

Smith (1977) argues that the truncated series (equation V.11) is accurate enough for his Chandler wobble study. He bases this on the fact that "... the principle response of

an elastic solid body to rotational disturbances was characterized by l=2 spheroidal distortion." (Smith, 1977). Also Smith (1977) suggests use of equation (V.11) is valid because (to first order in ellipticity) equation (V.11) is of the correct form "... which represents the response of an incompressible, homogeneous, inviscid rotating fluid core to slight rotations of a rigid mantle...." Equation (V.11) does include an l=2 spheroidal term. However, it is probably more realistic to conclude that Smith used the truncated particle displacement series (V.11) so that the computations and analysis could be carried out with reasonable effort. Smith's (1977) calculations should be performed again using more terms in the particle displacement series.

Smith (1977) presents the polar motion shift results in terms of a magnitude and a direction, in degrees East of Greenwich, rather than by two wobble components. For comparison, values found by Dahlen (1973) using a quasi-static calculation are given in parentheses. For the first event of the 1960 Chile source model (Chile (1)) the magnitude is 0".02116 (0".0210) and the direction is 114.3^{o} (116^{o}). For the second event (Chile (2)) the values are 0".02803 (0".0280) and 117.7^{o} (118^{o}). Finally, the shift magnitude and direction for the 1964 Alaska earthquake are 0".00723 (0".0073) and 201.3^{o} (202^{o}); (Smith, 1977).

Obviously the agreement of the polar shifts and associated directions between Smith (1977) and Dahlen (1973)

is very good, implying that the quasi-static calculation of Dahlen (1973) is among the better attempts to determine polar shift magnitudes using a dislocation source on a non-rotating earth. No conclusion is made in Smith's (1977) paper as to whether earthquakes are the primary source of Chandler wobble excitation.

Mansinha, Smylie and Chapman (1979) revisit the Chandler wobble, and again conclude that earthquakes are the major driving mechanism of the Chandler wobble. They correct the static dislocation theory of Smylie and Mansinha (1971) for errors made in transforming planar dislocation models to a more realistic spherical geometry. These corrections bring pole path shift amplitudes and directions (degrees East of Greenwich) of Smylie and Mansinha (1971) into better agreement with the estimates of Smith (1977), with the resulting amplitudes being different by no more than a factor of one-half to two. Mansinha, Smylie and Chapman (1979) use the SNREI model of Dahlen (1971, 1973) in their computations of the shifts, and speculate that pole shifts observed (astronomically) in the future may be used to constrain focal mechanisms of earthquakes.

The cumulative effects of earthquakes on wobble is then studied by Mansinha, Smylie and Chapman (1979). They characterize the root-mean-square (rms) Chandler wobble amplitude using the relation

$$\text{RMS amplitude} = s_m \left\{ \frac{b}{2c-b} (s_0/s_m)^{b/c} \frac{N_0 \tau}{2} \right\}^{1/2}, \quad (V.12)$$

"... where s_m is the average polar shift due to the largest magnitude considered, s_0 is that due to the smallest magnitude considered (with N_0 the corresponding frequency), and τ is the damping time of the Chandler wobble." "b" and "c" are constants derived from frequency-magnitude and pole path shift-magnitude relations respectively. Mansinha, Smylie and Chapman (1979) then use the 30 largest earthquakes from 1901 to 1964 as taken from O'Connell and Dziewonski (1976), to form a plot (Figure 10) of rms Chandler wobble excitation as a function of the constant "c" mentioned previously. They assume a damping time of 20 years (Q = 52).

Mansinha, Smylie and Chapman's (1979) calculations as shown on Figure 10 surely support the view that earthquakes are, at worst, a large contributor to Chandler wobble excitation and, at best, the primary excitation source. Mansinha, Smylie and Chapman (1979) continue to use BIH data as the observational standard of comparison for their theoretical results, and base cumulative earthquake excitation conclusions on their magnitude-moment of choice.

Research which indirectly supports the hypothesis that earthquakes primarily excite the Chandler wobble was done by Wahr (1983) in an attempt to determine the level at which atmospheric phenomena drive the Chandler wobble. Wahr (1983) considers earthquakes and the atmosphere as the most plausible means of exciting the Chandler wobble, but

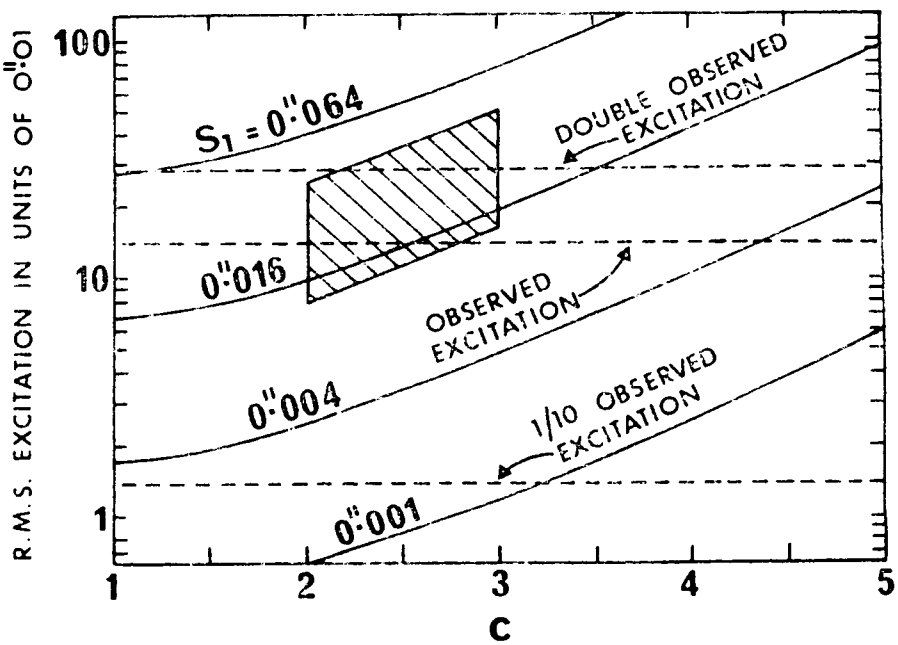

Fig. 10. Cumulative Chandler wobble excitation by earthquakes. Shaded area indicates domain of possible excitations (boundaries are extremes). Range is from 0.08 to 0.50 while observed level is 0.15. Some of the more extreme values of seismic moment would provide too much Chandler excitation. S_1 is a reference pole shift associated with a reference magnitude M_1; see reference for details. (From Mansinha, Smylie and Chapman, 1979).

concludes that the atmosphere is not the main source of excitation. Atmospheric data and models are used by Wahr to compute power, coherence and phase spectra of atmospheric excitation sources such as atmospheric pressure, the pressure-driven ocean, mountain torques due to variations in pressure at different locations on a mountain, and wind drag over the surface of the earth. These spectra are compared to excitation spectra from ILS data for the years 1900-1973 to investigate if atmospheric effects do drive Chandler wobble.

Wahr (1983) considers several ways to look at mechanisms driving Chandler wobble: one way is by examining excitation functions, ψ, and associated derived quantities such as excitation power spectra in frequency space; another is by examining the wobble components (m_1, m_2) in the time domain. Wahr uses the former technique. The ultimate result of Wahr's study is that no more than 20-25 percent of the Chandler wobble observed (ILS) excitation is due to atmospheric and oceanic sources. Wahr (1983) does not take into account the effects of ground water storage or El Nino events.

In more recent work, Gross and Chao (1984) deconvolve LAGEOS (satellite for laser ranging) Chandler wobble polar motion data for the period 21 January, 1977 to 20 January, 1984 to look at the excitation function of the wobble. They observe a shift in the excitation axis by 0".040 in the -54 degrees East longitude direction during the time period

8/13/77 to 9/2/77, and assume the shift is due to the Sumba earthquake of 8/19/77. The correlation in time of the two events is quite good. However, when Gross and Chao (1984) compare their observation with Dahlen's theoretically derived value of the Sumba shift due to elastic dislocation models (0".0003 towards 93 degrees East longitude), they they find little agreement between theory and experiment. Gross and Chao (1984) conclude that the LAGEOS observation may have resulted from some discontinuity in processing LAGEOS data.

Gross and Chao (1984,1985) also consider the possibility that the descending slab associated with the 1977 Sumba earthquake may have broken away from its parent oceanic lithosphere and excited the Chandler wobble in its downgoing motion; but they reach no conclusion about this hypothesis. They (1985) also look for a correlation between polar motion excitation and the 1982-83 El Nino and believe they observe one. The 1982-83 El Nino was particularly strong and may have been involved in Chandler wobble excitation.

Gross (1986) compares Chandler wobble excitation function power spectra derived from theoretical static deformation fields of 1287 large earthquakes during 1977-1983 (a time involving one great earthquake) with power spectra of observed excitations derived from LAGEOS earth orientation measurements. He finds that the earthquake (amplitude) power is about 56 deciBels (dB) less than the power necessary to drive the observed Chandler wobble.

Gross concludes that the static deformation fields of earthquakes during 1977-83 are not the primary excitation source of the Chandler wobble, but also notes that no extremely large earthquakes, such as the 1960 Chilean or 1964 Alaskan events occurred during this time interval. He leaves open the possibility of Chandler wobble excitation by aseismic slip, whose contributions to Chandler wobble have not been currently evaluated.

In another investigation, Robertson (1985) examines IRIS VLBI polar motion components plotted against one another over five-day intervals during 1984 and early 1985. He observes variations in the data similar to the breaks observed by Mansinha and Smylie (1970), but is hesitant to correlate the variations with another large Chilean earthquake which occurred in early 1985. Perhaps it is better to be cautious in interpreting early VLBI results.

Hinnov (1985) takes a much different route to explain the Chandler wobble excitation by water storage and air mass loading. She uses Northern Hemisphere precipitation and temperature observations for the years 1900-1979 to form an excitation series. The air mass and water storage excitation data display almost zero phase lag and significant coherence with ILS polar motion observations near the Chandler frequency. Hinnov (1985) believes that the aforementioned meteorological phenomena can fully explain Chandler wobble excitation.

It is of interest to note that geophysical observers do

do not always see eye-to-eye with theoreticians regarding numerical agreement of strain magnitudes. The following are two early quotes on the subject. "Surface strain observations are at least an order of magnitude greater than predicted by the elastic theory of dislocations." (Mansinha and Smylie, 1970). And from a question at the 1969 NATO Advanced Study Institute about the effects of earthquakes on earth rotation: " Although you [Richard Haubrich, University of California/San Diego] mentioned that the excitation from historical [earthquake] events is at least an order of magnitude too small to maintain the observed wobble, I [M.W. Major, Colorado School of Mines] am not clear as to how one arrives at the magnitude of the excitation. The main problem is that most of us see strain steps at distances which are embarrassingly large compared to those predicted by either the half-space or spherical dislocation theory." (Mansinha, Smylie and Beck, 1970).

Chapter VI.

KALMAN FILTERING OF VLBI DELAY DATA FOR EARTH ROTATION AND ORIENTATION PARAMETERS

A Kalman filter has been designed to make optimal estimates of earth rotation and orientation parameters which are derived from Very Long Baseline Interferometry delay data. Generally the filter will be applied to one to two day long VLBI data sets. Such a data set will have several hundred or more delay observations, and should allow one to estimate polar motion and earth rotation variations over times of a few hours to two days. If one desires observational data of longer duration, one can examine multiple data sets.

Earlier it was mentioned that the derivation of equation (III.5)

$$x_{k+1} = \Phi(k+1,k)\, x_k + \Gamma(k)\, w_k$$

would follow, and this will be handled now. Equation (III.5) describes the dynamical behavior of the state vector x_k in time. Recall $\Phi(k+1,k)$ is the state transition matrix which models deterministic changes in x as one proceeds from time t_k to time t_{k+1}. w_k is a stochastic noise input in the state equation, with $\Gamma(k)$ accounting for proportion-

ality. Equation (III.5), or relations like it, which describe the physical variations of the estimated parameter vector x, are usually found from continuous (as opposed to discrete) differential equations characterizing the physical system.

The continuous differential equation form of (III.5) is typically given as (in notation of Gelb, 1974)

$$\dot{x}(t) = F(t)x(t) + G(t)w(t), \qquad \text{(VI.1)}$$

where x(t) is the state vector, w(t) is the stochastic forcing function and F(t), G(t) are proportionality matrices. Consider, as a first step towards understanding the system represented by (VI.1), that there is no random forcing w(t) and that F(t) is time invariant. The differential equation representing this simplified system is just

$$\frac{dx(t)}{dt} = F\,x(t). \qquad \text{(VI.2)}$$

If one rearranges the above differential equation and integrates from time t_k to t_{k+1}

$$\int_{x_k}^{x_{k+1}} \frac{dx(t)}{x(t)} = \int_{t_k}^{t_{k+1}} F\,dt, \qquad \text{(VI.3)}$$

or one can readily find that

$$x_{k+1} = [\exp\{F(t_{k+1} - t_k)\}]\, x_k, \qquad \text{(VI.4)}$$

where x_k, x_{k+1} are the parameter values at times t_k, t_{k+1} respectively. See also Gelb et al. (1974).

Thus the state vector x_{k+1} is related to the state vector at the previous time x_k by the quantity $\exp\{F(t_{k+1}-t_k)\}$. The matrix exponential is defined by (Gelb et al., 1974)

$$e^A = I + A + \frac{A^2}{2!} + \frac{A^3}{3!} + \ldots, \qquad \text{(VI.5)}$$

where I is the identity matrix. The state transition matrix $\Phi(k+1,k)$ is

$$\Phi(k+1,k) = \exp(F(t_{k+1} - t_k)) \qquad \text{(VI.6)}$$

The state transition matrix depends only on the time interval $(t_{k+1} - t_k)$ as should be the case for a stationary system. Equation (VI.6) relates the continuous matrix F and the discrete state transition matrix, $\Phi(k+1,k)$.

Through a derivation procedure similar to the above, one can find the relationship between state vectors x_k, x_{k+1} for a non-stationary process with no random forcing

$$x_{k+1} = [\{\exp(\int_{t_k}^{t_{k+1}} F(t)\, dt)\}]\, x_k \qquad \text{(VI.7)}$$

Evidently, the state transition matrix now takes the form

$$\Phi(k+1,k) = \exp\left(\int_{t_k}^{t_{k+1}} F(t)\, dt\right). \qquad (VI.8)$$

Using the general form (VI.8) for $\Phi(k+1,k)$ one can readily prove some mathematical facts about the properties of the state transition matrix.

The first small proof is quite simple:

$$\Phi(k,k) = \exp\left(\int_{t_k}^{t_k} F(t)\, dt\right) = e^{0} = I. \qquad (VI.9)$$

In words, a state transition matrix not proceeding in the forward or backward direction in time (and thus remaining at the instant of concern, t_k) is equal to the identity matrix. The proof of a second small fact begins with state transition matrices going the opposite direction in time over the same time interval

$$\Phi(k+1,k) = \exp\left(\int_{t_k}^{t_{k+1}} F(t)\, dt\right)$$

$$\Phi(k,k+1) = \exp\left(\int_{t_{k+1}}^{t_k} F(t)\, dt\right) = \exp\left(-\int_{t_k}^{t_{k+1}} F(t)\, dt\right).$$

From the above equation, it is apparent that

$$\Phi(k,k+1) = \Phi^{-1}(k+1,k) \qquad (VI.10)$$

Equation (VI.10) illustrates the fact that for a physical system of given state transition matrix, the state transition matrix going backwards in time, $\Phi(k,k+1)$ is equal to the

inverse of the state transition matrix going forward in time over the same time interval. Relations (VI.9) and (VI.10) illustrate the properties of the state transition matrix, and may help the reader to become familiar with the dynamic system models used in Kalman filtering/smoothing.

Now that one has found the discrete state transition matrix $\Phi(k+1,k)$ from the continuous matrix $F(t)$, one should consider the case of a dynamical system with random inputs

$$\dot{x}(t) = F(t)x(t) + G(t)w(t).$$

Please observe that $w(t)$ is a continuous variable differing from the discrete noise process, w_k. The subsequent derivation uses the fact that

$$\frac{d}{dt}\Phi(t,t_0) = F(t)\Phi(t,t_0), \qquad \text{(VI.11)}$$

which can be found from equation (VI.8); and also uses the property of the state transition matrix

$$\Phi(t_2,t_0) = \Phi(t_2,t_1)\Phi(t_1,t_0). \qquad \text{(VI.12)}$$

Relationship (VI.12) can be shown to be true in the method of Gelb et al. (1974)

$$x(t_2)=\Phi(t_2,t_1)x(t_1)=\Phi(t_2,t_1)\Phi(t_1,t_0)x(t_0).$$

But $x(t_2) = \Phi(t_2,t_0)x(t_0)$,

so that $\Phi(t_2,t_0)=\Phi(t_2,t_1)\Phi(t_1,t_0)$ Q.E.D.

Or verbally, the state transition matrix over multiple time intervals can be represented as the product of the state transition matrices of each interval (this does not include random inputs).

The original derivation with random forcing follows Gelb et al. (1974). Starting with the fact that $x(t) = \Phi(t,t_0)\, x(t_0)$ is the discrete solution to the homogeneous differential equation (VI.2) with F time dependent, one proposes that the solution to (VI.1) is of the form

$$x(t) = \Phi(t,t_0)\xi(t) \qquad \text{(VI.13)}$$

One then substitutes (VI.13) into (VI.1)

$$\frac{d}{dt}\{\Phi(t,t_0)\xi(t)\}=F(t)\Phi(t,t_0)\xi(t)+G(t)w(t), \qquad \text{(VI.14)}$$

and upon taking the derivative and using the relation (VI.11) one finds

$$F(t)\Phi(t,t_0)\xi(t)+\Phi(t,t_0)\dot{\xi}(t)=F(t)\Phi(t,t_0)\xi(t)+G(t)w(t) \qquad \text{(VI.15)}$$

The time indices t and t_0 (as opposed to t_k and t_{k+1}) are used here for convenience. Eliminating terms in (VI.15) and invoking (VI.10) one obtains the equation (as per Gelb et al., 1974)

$$\dot{\xi}(t) = \Phi(t_0,t)G(t)w(t), \qquad \text{(VI.16)}$$

which can be integrated directly to yield

$$\xi(t) = \xi(t_0) + \int_{t_0}^{t} \Phi(t_0,\tau)G(\tau)w(\tau)d\tau, \qquad \text{(VI.17)}$$

Again following the method of Gelb et al. (1974), one inserts (VI.17) into equation (VI.13), and noting that $\xi(t_0) = x(t_0)$, thereby arrives at

$$x(t) = \Phi(t,t_0)x(t_0) + \int_{t_0}^{t} \Phi(t,t_0)\Phi(t_0,\tau)G(\tau)w(\tau)d\tau, \qquad \text{(VI.18)}$$

which simplifies using relation (VI.12) to

$$x(t) = \Phi(t,t_0)x(t_0) + \int_{t_0}^{t} \Phi(t,\tau)G(\tau)w(\tau)d\tau. \qquad \text{(VI.19)}$$

Most apparently, if $w(\tau)$ is zero (no random forcing!), then equation (VI.19) reduces to the homogeneous solution $x(t) = \Phi(t, t_0)\, x(t_0)$, as should be the case.

The second term on the right-hand side of equation (VI.19) represents the stochastic contribution to the state parameter x(t). Equation (VI.19) can also be written for the time interval t_k to t_{k+1} (Gelb et al., 1974)

$$x(t_{k+1}) = \Phi(t_{k+1},t_k)x(t_k) + \qquad \text{(VI.20)}$$

$$\int_{t_k}^{t_{k+1}} \Phi(t_{k+1},\tau)G(\tau)w(\tau)d\tau,$$

and if one uses the following definition

$$\Gamma(k)w_k \equiv \int_{t_k}^{t_{k+1}} \Phi(t_{k+1},\tau)G(\tau)w(\tau)d\tau, \qquad \text{(VI.21)}$$

one can write (VI.20) as

$$x_{k+1} = \Phi(k+1,k)\ x_k + \Gamma_k w_k, \qquad \text{(VI.22)}$$

using slightly modified notation. Equation (VI.22) is the discrete (difference equation) form of continuous equation (VI.1), and is also equation (III.5), which is what was to be derived in this section. The pair of equations (VI.22) and (III.4) are the models on which one builds a Kalman filter/smoother. In general, one starts filter design with knowledge of the continuous dynamics of a problem as given by equation (VI.1) and then forms more useful discrete equations like (VI.22) to work in combination with discrete measurement data.

Before proceeding further with the polar motion problem, it is proper to describe the two noise covariances, R(k) and Q(k), which are needed in the structure of the Kalman filter. R(k) is the measurement error covariance matrix, while Q(k) is the more inscrutable system (or process) noise covariance matrix. Recall from (III.6) that

$$E\{w_k w_l^T\} = Q(k)\ \delta_{kl} \qquad \text{(VI.23)}$$

$$E\{v_k v_l^T\} = R(k)\,\delta_{kl} \qquad \text{(VI.24)}$$

and $$R(k) > 0. \qquad \text{(VI.25)}$$

where δ_{kl} is a Kronecker delta. R(k) is the more easily explained covariance, so it will be discussed first. The covariances R(k) and Q(k) are used in the Kalman filter as opposed to the noises v_k and w_k.

The measurement covariance R(k) is related to the uncertainties v_k in the measurements y_k. Equation (VI.24) suggests how R(k) is calculated. In the case of VLBI delay measurements, the Kalman filter used herein handles one measurement at a time. Thus $R(k) = v_k^2$ for the scalar case. Also notice that R(k) > 0 for any measurement, which means that no measurement is perfect (i.e. has no uncertainty).

The standard deviation in the delay measurements is equal to v_k and is given by (Ma, 1978; Whitney, 1974)

$$v_k = \frac{1}{\omega_s SNR}, \qquad \text{(VI.26)}$$

where ω_s is the "... standard deviation of the observing frequencies used to sample over the observing bandwidth...", and SNR is the signal to noise ratio of the observation. The signal to noise ratio is found from (Ma, 1978)

$$SNR = \frac{2\rho}{\pi}\,(2BT)^{1/2},$$

where B is the recorded bandwidth, T is the integration time

and $\rho = \gamma(K)^{1/2}$. According to Ma (1978), γ is the fringe visibility and is equal to one "... for a completely unresolved source ..." and

$$K = \frac{T_{a1}\ T_{a2}}{(T_{a1}+T_{s1})(T_{a2}+T_{s2})},$$

where

T_{a1} , T_{a2} = source antenna temperatures

T_{s1} , T_{s2} = system [receiver] noise temperatures.

The 1 and 2 subscripts denote the antennas at either end of the VLBI baseline of interest. Furthermore, the source antenna temperatures are defined by (Ma, 1978)

$$T_a = \frac{FEA}{2k}$$

where F = source flux density

E = antenna efficiency

A = [antenna] collecting area

k = Boltzmann's constant

The VLBI delay uncertainties are typically calculated for use in least-squares analysis and stored in VLBI observation (computer) files, so they are taken directly from these locations for use in Kalman filtering. The measurement covariances R(k) used herein do not include the effect of unknown systematic errors which could introduce biases into the estimates.

The determination of Q(k) is not as straightforward as that for finding R(k). In fact, it is not just Q(k) that is required in the Kalman filtering step (III.9), but rather $\Gamma(k)Q(k)\Gamma^T(k)$. The quantity $\Gamma(k)Q(k)\Gamma^T(k)$ is found using equation (VI.21)

$$\Gamma_k w_k = \int_{t_k}^{t_{k+1}} \Phi(t_{k+1},\tau)G(\tau)w(\tau)d\tau. \qquad \text{(VI.27)}$$

Taking the transpose of the above, and changing the dummy variable from τ to α results in

$$w_k^T\Gamma_k^T = \int_{t_k}^{t_{k+1}} w^T(\alpha)G^T(\alpha)\Phi^T(t_{k+1},\alpha)d\alpha, \qquad \text{(VI.28)}$$

and by multiplying (VI.27) with (VI.28) and taking the expectation (E) of each side of the product, one finds, with the aid of (VI.23)

$$\Gamma_k Q(k)\Gamma_k^T = E\{\Gamma_k w_k w_k \Gamma_k^T\} \qquad \text{(VI.29)}$$

$$= E\left\{\int_{t_k}^{t_{k+1}}\int_{t_k}^{t_{k+1}} \Phi(t_{k+1},\tau)G(\tau)w(\tau)w^T(\alpha)G^T(\alpha)\Phi^T(t_{k+1},\alpha)d\tau d\alpha\right\}.$$

The expectation operation is an integration process, and since the order in which the integrations are done in (VI.29) should not affect the ultimate result, one can write (VI.29) as

$$\Gamma_k Q(k) \Gamma_k^T = \int_{t_k}^{t_{k+1}} \int_{t_k}^{t_{k+1}} \Phi(t_{k+1}, \tau) G(\tau) \qquad \text{(VI.30)}$$

$$\times\ E\{w(\tau) w^T(\alpha)\} G^T(\alpha)^T (t_{k+1}, \alpha) d\tau d\alpha .$$

The expectation of the continuous white noise product $E\{w(\tau)\ w^T(\alpha)\}$ is well known (Gelb et al., 1974) with the value of $Q(\tau)\ \delta(\tau - \alpha)$, where $\delta(\tau - \alpha)$ is a Dirac delta function. Placing $Q(\tau)\ \delta(\tau - \alpha)$ into equation (VI.30) and integrating over alpha, one concludes (Gelb et al., 1974)

$$\Gamma_k Q(k) \Gamma_k^T = \int_{t_k}^{t_{k+1}} \Phi(t_{k+1}, \tau) G(\tau) Q(\tau) G^T(\tau) \Phi^T(t_{k+1}, \tau) d\tau . \qquad \text{(VI.31)}$$

Equation (VI.31) relates the system (process) noise covariance Q(k) to a (continuous) spectral density matrix, $Q(\tau)$. For more details, see Gelb et al. (1974). The term $\Gamma_k Q(k) \Gamma_k^T$ is inserted directly into the Kalman filter equations. In the research performed herein Γ_k is set to identity, I (for convenience), and any proportionality constants are absorbed into Q(k), the system covariance matrix.

While it is relatively easy to estimate the uncertainties in delay measurements v_k, and thereby the measurement covariance R(k), it is not so easy to fix the values of the system noise w_k and its associated covariance, Q(k). People are sometimes critical of Kalman filtering because they don't understand how Q(k) is determined. It is sufficient to say

that there are several methods that can be used to find Q(k), but it should be understood that w_k and Q(k) are strictly related to the physics of the system being modelled, and as such, can be found at least in approximate fashion. For a strictly deterministic system, Q(k) = 0. The topic of w_k and Q(k) determination will arise at several subsequent points in this work. An example should help highlight one method of how w_k can be arrived at. More exact methods are available.

Let one consider, as is done in VLBI, how time is kept by a maser. Conventional hydrogen masers presently keep time to one part in 10^{14} or 10^{15}. This is approximately one nanosecond in one day! This number does not account for deterministic variations in maser time due to expansion of the maser oscillation cavity, electrical problems etc. It makes sense to believe that the stochastic variations in maser time w_k are on the order of one part in 10^{14}. Thus the system covariance matrix can be approximated crudely as $Q(k) \approx (1.0/1.0\text{x}10^{14})^2$. More sophisticated maser time ("clock") models will be discussed later. It should be pointed out that for estimation of some parameters, such as the time kept by maser, the parameter estimates are only weakly dependent on the exact choice of system noise covariance Q(k), and thus approximate values of Q(k) can be used in the Kalman filter. Finally, one does not always know the exact system noise information to use in the filter.

Now that the covariances have been described, the

details of the system equation (i.e. equation III.5) for the various parameters of interest in VLBI-polar motion research will be set forth. Much should be known to the reader already about the measurement equation (III.4), as the delays y_k, the uncertainties in the delays v_k, and the measurement partials M(k) have been described earlier; as such, the measurement equation will not be particularized further. On to the system equation. The vector of parameters to be estimated (x_k) using VLBI delay data in this work is

$$x_k = \begin{pmatrix} \tau_c(1R) \\ \tau_{cr}(1R) \\ L_{z1} \\ \tau_c(2R) \\ \tau_{cr}(2R) \\ L_{z2} \\ . \\ . \\ . \\ x \\ y \\ UT1\text{-}TAI \\ \Delta\psi \\ \Delta\epsilon \end{pmatrix} \qquad \text{(VI.32)}$$

where x, y and UT1-TAI are the polar motion and rotation components of primary interest, and $\tau_{clock/rate}(iR)$ are "clock" parameters for the relative time between VLBI station i and some reference station R. One VLBI observation site is chosen as the reference station in each VLBI data set. $\Delta\psi$ and $\Delta\epsilon$ are adjustments to the nutation series. $\{L_{zj} = L_{z1}, L_{z2}, L_{z3}, \ldots\}$ are the atmospheric (wet zenith) delays as estimated at each station j. The number of clock and atmosphere terms to be estimated depends on the number of antennas participating in the VLBI observations. Also, the position

(declination and right ascension) of the quasars and radio sources observed in the VLBI data runs and the terrestrial coordinates of the stations participating in the observing will not be estimated as a part of x_K. Instead, these positions will be taken from multiple data set, least squares analyses of VLBI data done previously; these solutions are updated periodically by the VLBI personnel at NASA GSFC. While this may not be the best means of fixing the quasar and VLBI station positions, such a procedure is necessary because of computer limitations, and has been shown in the past to be a reliable way to arrive at accurate parameter estimates.

The discrete, system dynamical equations will now be derived for the polar motion components, m_1 and m_2. Recall from equations (II.7) that simple Chandler wobble (with no a priori excitation function forcing; ψ_1, $\psi_2 = 0$) is described by the coupled relations

$$\dot{m}_1 = -\sigma\, m_2 \qquad \text{(VI.33)}$$

$$\dot{m}_2 = \sigma m_1, \qquad \text{(VI.34)}$$

where σ_r has been replaced by the actual Chandler wobble frequency, σ. The excitation functions are being set to zero so that one is assuming no pre-conceived form of the excitation functions which are of geophysical interest. The VLBI astronomical measurements will be used to infer what

may be happening to drive the Chandler wobble of the earth.

Equations (VI.33) and (VI.34) can be written in matrix form as

$$\dot{x} = \begin{pmatrix} \dot{m}_1 \\ \dot{m}_2 \end{pmatrix} = \begin{pmatrix} 0 & -\sigma \\ \sigma & 0 \end{pmatrix} \begin{pmatrix} m_1 \\ m_2 \end{pmatrix} = \begin{pmatrix} 0 & -\sigma \\ \sigma & 0 \end{pmatrix} x, \qquad \text{(VI.35)}$$

an equation which does not account for any stochastic variations in m_1 and m_2. Relation (VI.35) clearly resembles equation (VI.1)

$$\dot{x}(t) = F(t)\, x(t)$$

with no stochastic forcing terms. By comparison of equations (VI.1) and (VI.35), one can conclude that

$$F(t) = F = \begin{pmatrix} 0 & -\sigma \\ \sigma & 0 \end{pmatrix} \qquad \text{(VI.36)}$$

and that F is time invariant. If F is time invariant, one can find the discrete state transition matrix $\Phi(t_{k+1}, t_k)$ from F by equation (VI.5) and (VI.6)

$$\Phi(k+1,k) = \exp\{F(t_{k+1}-t_k)\} = I + F(t_{k+1}-t_k) + \frac{\{F(t_{k+1}-t_k)\}^2}{2!} + \ldots$$

Inserting (VI.36) into equation (VI.6) one finds (with $\Delta t \equiv t_{k+1} - t_k$)

$$\Phi(k+1,k) = \begin{pmatrix} 1 - \dfrac{(\sigma\Delta t)^2}{2!} + \dfrac{(\sigma\Delta t)^4}{4!} - \ldots, & -\sigma\Delta t + \dfrac{(\sigma\Delta t)^3}{3!} - \ldots \\ (\sigma\Delta t) - \dfrac{(\sigma\Delta t)^3}{3!} + \ldots, & 1 - \dfrac{(\sigma\Delta t)^2}{2!} + \dfrac{(\sigma\Delta t)^4}{4!} \end{pmatrix}$$

or in more familiar form

$$\Phi(t_{k+1}, t_k) = \begin{pmatrix} \cos(\sigma\Delta t), & -\sin(\sigma\Delta t) \\ \sin(\sigma\Delta t), & \cos(\sigma\Delta t) \end{pmatrix} \qquad \text{(VI.37)}$$

The discrete form of the polar motion system dynamics with no stochastic inputs can thus be written

$$\begin{pmatrix} m_1 \\ m_2 \end{pmatrix}_{k+1} = \begin{pmatrix} \cos(\sigma\Delta t), & -\sin(\sigma\Delta t) \\ \sin(\sigma\Delta t), & \cos(\sigma\Delta t) \end{pmatrix} \begin{pmatrix} m_1 \\ m_2 \end{pmatrix}_k . \qquad \text{(VI.38)}$$

In VLBI work, Δt is on the order of minutes, thereby making the argument $\sigma\Delta t$ small; thus $\Phi(t_{k+1}, t_k)$ is approximately the identity matrix. The sinusoidal form of the state transition matrix makes sense since the original continuous dynamic relations (VI.33) and (VI.34) model a coupled oscillator.

Equation (VI.38) is incomplete and now requires stochastic input terms. The polar motion process noise is assumed to be a random walk (or integrated white noise) which can be described by the equation

$$\dot{x}(t) = G(t)\, w(t) \qquad \text{(VI.39)}$$

or more explicitly

$$\dot{x} = \begin{pmatrix} \dot{m}_1 \\ \dot{m}_2 \end{pmatrix} = \begin{pmatrix} 1 & 0 \\ 0 & 1 \end{pmatrix} \begin{pmatrix} w_1 \\ w_2 \end{pmatrix} \qquad \text{(VI.40)}$$

where w_1 and w_2 are white noise. G(t) is obviously identity here. The covariance of this integrated white noise process, Q'(k), can be found from equation (VI.31): (Q' is used for notation to represent the process covariance with the factors $\Gamma'_k \Gamma'^{T}_k$ absorbed.)

$$Q'(k) \equiv \Gamma'_k Q(k) \Gamma'^{T}_k = \int_{t_k}^{t_{k+1}} \Phi(t_{k+1}, \tau) G(\tau) Q(\tau) G^{T}(\tau) \Phi(t_{k+1}, \tau) d\tau. \qquad \text{(VI.41)}$$

The components of the system noise spectral density matrix are defined as

$$Q(\tau) = \begin{pmatrix} q_{11} & q_{12} \\ q_{21} & q_{22} \end{pmatrix}. \qquad \text{(VI.42)}$$

With the preceding definitions inserted into equation (VI.41) and $\Phi(t_{k+1}, t_k)$ as defined by equation (VI.37), one finds

$$Q'(k) = \begin{pmatrix} q_{11}' & q_{12}' \\ q_{21}' & q_{22}' \end{pmatrix} \qquad \text{(VI.43)}$$

$$= \int_{t_k}^{t_{k+1}} \begin{pmatrix} \cos\sigma\Delta t, & -\sin\sigma\Delta t \\ \sin\sigma\Delta t, & \cos\sigma\Delta t \end{pmatrix} \begin{pmatrix} q_{11} & q_{12} \\ q_{21} & q_{22} \end{pmatrix} \begin{pmatrix} \cos\sigma\Delta t, & \sin\sigma\Delta t \\ -\sin\sigma\Delta t, & \cos\sigma\Delta t \end{pmatrix} d\tau,$$

where Δt now is $t_{k+1} - \tau$. One can approximate equation (VI.43), with $\Phi(t_{k+1}, \tau) \approx I$, as

$$Q'(k) \approx \int_{t_k}^{t_{k+1}} \begin{pmatrix} q_{11} & q_{12} \\ q_{21} & q_{22} \end{pmatrix} d\tau. \qquad \text{(VI.44)}$$

A further approximation made in the filter model for the polar motion stochastic (process) covariance is that the m_1 and m_2 spectral densities are not correlated, thereby giving

$$Q'(k) = \int_{t_k}^{t_{k+1}} \begin{pmatrix} q_{11} & 0 \\ 0 & q_{22} \end{pmatrix} d\tau. \qquad \text{(VI.45)}$$

If q_{11} and q_{22} are constant over the range of integration, one can further approximate (VI.45) as

$$Q'(k) = \begin{pmatrix} q_{11}(t_{k+1}-t_k) & 0 \\ 0 & q_{22}(t_{k+1}-t_k) \end{pmatrix} \qquad \text{(VI.46)}$$

In general, if one is going to determine the numerical values of q_{11} and q_{22} by a trial-and-error technique during simulations with VLBI data, then the simple form of equation VI.46 is conducive to this task. Eventually it will be demonstrated herein that the polar motion is quite deterministic ($Q'(k) \approx 0$) and thus the form of the covariance found here really doesn't matter. But it is always a good practice to set up a Kalman filter model with all parameters having non-zero process noise covariances.

Now that $\Phi(k+1,k)$ and $Q'(k)$ have been determined for the polar motion parameters, the state transition matrix and process noise covariance will be posed for the earth

rotation parameter m_3. From equation (II.8), again with zero excitation (ψ_3), one has the continuous state equation for rotation with no random inputs

$$\dot{x} = m_3 = 0. \tag{VI.47}$$

Comparison of (VI.47) with equation (VI.1) shows that F(t) = 0 and thus from relationship (VI.6), it is clear that the state transition matrix for m_3 is

$$\Phi(k+1,k) = I, \tag{VI.48}$$

or one in the scalar case. Again, a random walk process is assumed for the stochastic contribution to the rotational component, m_3 (the same as UT1-TAI), and thus

$$\dot{x} = m_3 = w. \tag{VI.49}$$

The process covariance for the rotational component is simply

$$Q'(k) = \int_{t_k}^{t_{k+1}} Q(\tau)d\tau \tag{VI.50}$$

since $\Phi(t_{k+1},\tau)$ and $G(\tau)$ are both identity. The assumption that $Q(\tau)$ is invariant in time is also made and the resulting covariance is

$$Q'(k) = Q(t_{k+1} - t_k). \tag{VI.51}$$

A stochastic equation of the form $\dot{x} = w$ (with $\Phi(t_{k+1},t_k) = I$) represents a parameter x whose value is deterministically constant, but has random variations driving it, in this

case a random walk. According to Gelb et al. (1974), a "... random walk process results when uncorrelated signals are integrated. It derives its name from the example of a man who takes fixed-length steps in arbitrary directions. In the limit, when the number of steps is large and the individual steps are short in length, the distance travelled in a particular direction resembles the random walk process." There are many naturally occurring entities of interest to mankind that are randomly driven by integrated white noise, and the assumption of parameters being uncorrelated is common.

One also has to estimate offsets to the nutation in obliquity and longitude with respect to the (reference value) IAU (1980) theory of nutation (Kaplan, 1981). Recently Herring et al. (1985) have discovered annual variations of several marcsec amplitude from the 1980 IAU model, so these offsets are estimated using crude Kalman filter models here. The state transition matrix is set to identity and the process noise covariance matrix for nutation is similar in form to equation (VI.46)

$$Q'(k) = \begin{pmatrix} q_{11}(t_{k+1}-t_k), & 0 \\ 0 & q_{22}(t_{k+1}-t_k) \end{pmatrix} \qquad \text{(VI.52)}$$

Perhaps better models will be needed in the future, but the ones used here should suffice for the present in dealing with data sets of one day duration or less. Currently, there are insufficient data to make any reliable adjustment to the

precession constant.

It is of interest to examine the system model for VLBI "clock" parameters which were detailed earlier. As stated previously, a VLBI clock is actually not just time as kept by a maser, but rather also bears the influences of the phase injection and cable calibration procedures. It may also be composed of other time-like variations due to unknown physical phenomena and oddities in the VLBI observing system and experiment. It is a rare case when one can fully account for all the sources contributing to the clocks.

In general a constant ramp function dominates the clock signals along a given baseline. This ramp function is due to offsets in frequency of the masers at each end of a baseline, and should be modelled deterministically. The clock behavior along a baseline is modelled using two parameters, a clock offset τ_c (i.e. a bias) and a clock rate τ_{cr} (i.e. a ramp). The continuous system model describing the clock dynamics is as follows

$$\begin{pmatrix} \dot{\tau}_c \\ \dot{\tau}_{cr} \end{pmatrix} = \begin{pmatrix} 0 & 1 \\ 0 & 0 \end{pmatrix} \begin{pmatrix} \tau_c \\ \tau_{cr} \end{pmatrix} , \qquad \text{(VI.53)}$$

and simply indicates that the derivative of the clock offset is the clock rate, and that the derivative (with respect to time) of the clock rate is zero. That is, the clock rate is reasonably constant in time as is true for most masers. The model could be made more general by allowing the clock rate to change in time, but such a model may be too elaborate for

present purposes, especially for the case of single-day VLBI experiments.

Equation (VI.53) can be readily made discrete using equations (VI.5) and (VI.8). The result is:

$$\begin{pmatrix} \tau_c \\ \tau_{cr} \end{pmatrix}_{k+1} = \begin{pmatrix} 1 & t_{k+1}-t_k \\ 0 & 1 \end{pmatrix} \begin{pmatrix} \tau_c \\ \tau_{cr} \end{pmatrix}_k \qquad \text{(VI.54)}$$

This equation may seem overly simple to model all that has been discussed, but the stochastic terms have not yet been included. In addition, because the Kalman filter produces innovations (adjustments) to the clock parameters as it processes (passes through) the measurements, the optimal estimates of the clock parameters $\hat{x}(k+1|k+1)$ will reflect the actual clock variations in the data. So, even though we are limited by our understanding of the "clock" system to simple models, the Kalman filter will account to some extent for the neglected variations.

Now that the state transition matrix has been fixed, the stochastic fluctuations of a VLBI clock must be modelled. Recall that the clock being solved for in VLBI is actually the relative clock behavior at one VLBI station with respect to the clock at some reference station, and as such is proportional to the difference in the maser times at the two stations. The random variation in this time difference at the outputs of the hydrogen masers, on the time scales of interest in VLBI, takes the form of flicker noise (Allan, 1983), which is a noise process with a power spectrum that

is inversely proportional to frequency. Power laws for, and illustrations of the form of, flicker and random walk noise as well as other fundamental noises, are displayed in Figure 11 (taken from Allan, 1983). It has been shown (Brown, 1984) that a flicker noise process can only be handled approximately in a Kalman filter, whereas the cases of white noise and a random walk can be treated exactly. This is due to the fact that the power spectrum S(f) of flicker noise is not inversely proportional to an even power of frequency.

The clock covariances are modified from the work of Jones and Tryon (1982) and Tryon and Jones (1982) and take the form

$$Q'_{clock}(k) = Q_{clock}(t_{k+1}-t_k) \qquad \text{(VI.55)}$$

$$Q'_{clock\ rate}(k) = Q_{clock\ rate}(t_{k+1}-t_k). \qquad \text{(VI.56)}$$

It was felt that these models should be satisfactory for describing maser behavior over a day since Jones and Tryon's study was for a maser intercomparison over several months.

A random walk works well for "clocks" even though maser noise is flicker-like because maser timing variations are dominated by changes in signal path (in the VLBI electronics) rather than by noise in the maser. Thus, one really wants to model these environmental effects, and a random walk model for stochastic clock fluctations is probably as good

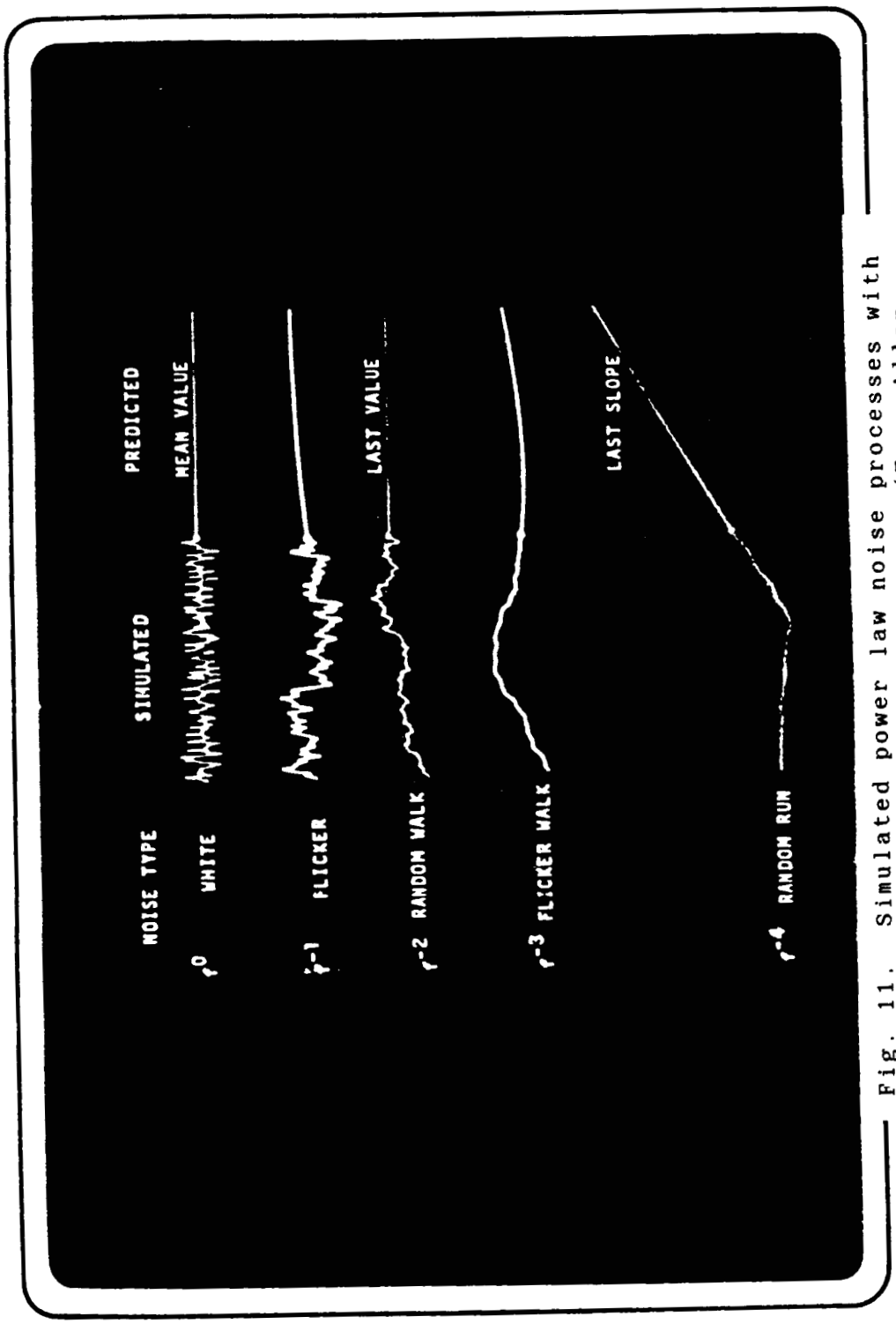

Fig. 11. Simulated power law noise processes with their optimum predicted estimates. (From Allan, 1984).

as any other. It is certainly more physical than a white noise model alone.

Very early on in the research presented here a comparison was made between least squares analysis of a VLBI data set and a crude Kalman filter run estimating a single clock parameter only (no rate was estimated). In actuality what was being solved for was not purely a clock parameter but also included the influences of other parameters not being estimated, such as zenith atmosphere delays etc. The clock model employed an identity state transition matrix and an integrated white noise stochastic model. The results show that the residuals from each technique are comparable and of similar distribution and thus demonstrated that an early version of the Kalman filter was operational. The study is presented here for its instructional value.

The example is a comparison of residuals on the baseline running between Algonquin Park (Ontario, Canada) and Fort Davis, Texas. The VLBI measurement session spanned two days and began on 24 August, 1984. The least squares delay residuals are shown in Figure 12a, while the Kalman filtered clock estimates are presented in Figure 12b.

In Figure 12a, the time during which the VLBI measurements were made (in days) is displayed on the ordinate, while the delay residuals (nanoseconds) are on the abscissa. Each weighted VLBI datum is identified by a capital Roman letter. Data taken, but not used in the weighted least squares solution, are designated by a small Roman letter on

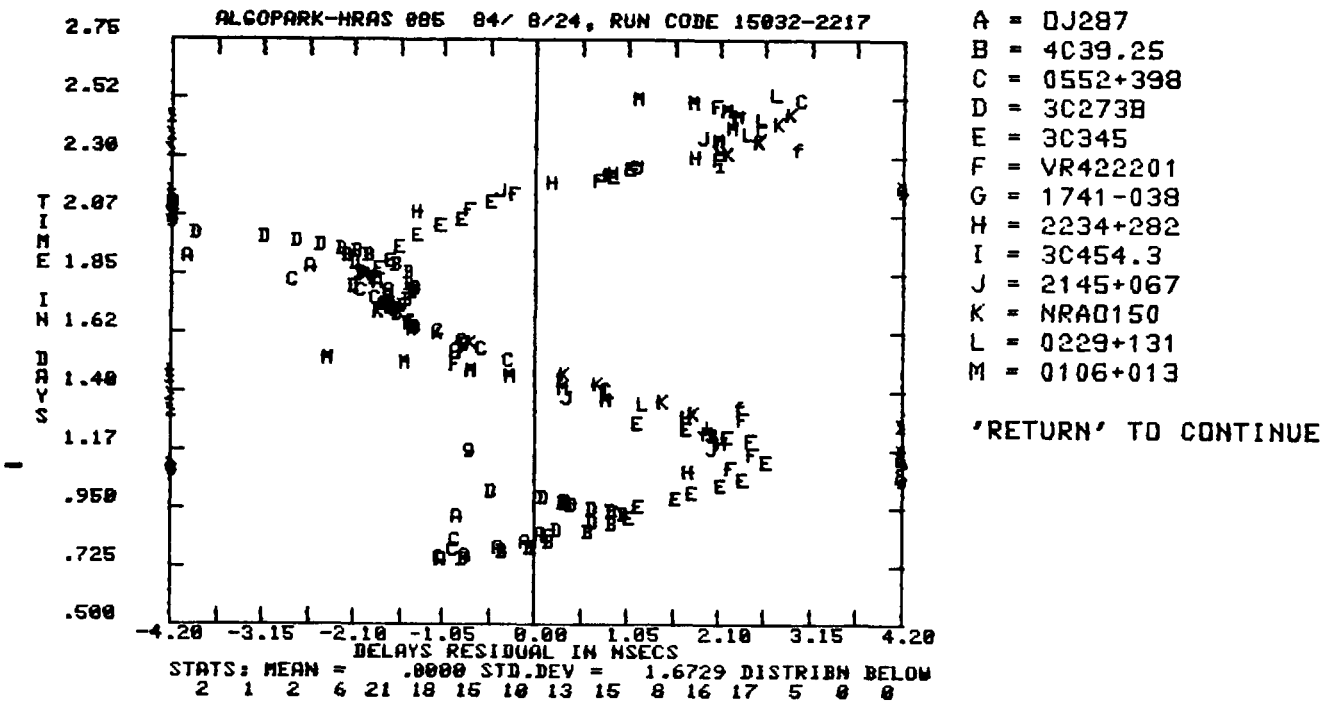

Figure 12a. Detrended (incompletely fitted with only clock offset and rate) least squares (VLBI) group delay residuals. Baseline between Algonquin Park (Canada) and HRAS (Texas). Roman letters indicate (quasar or radio) source being observed during a scan.

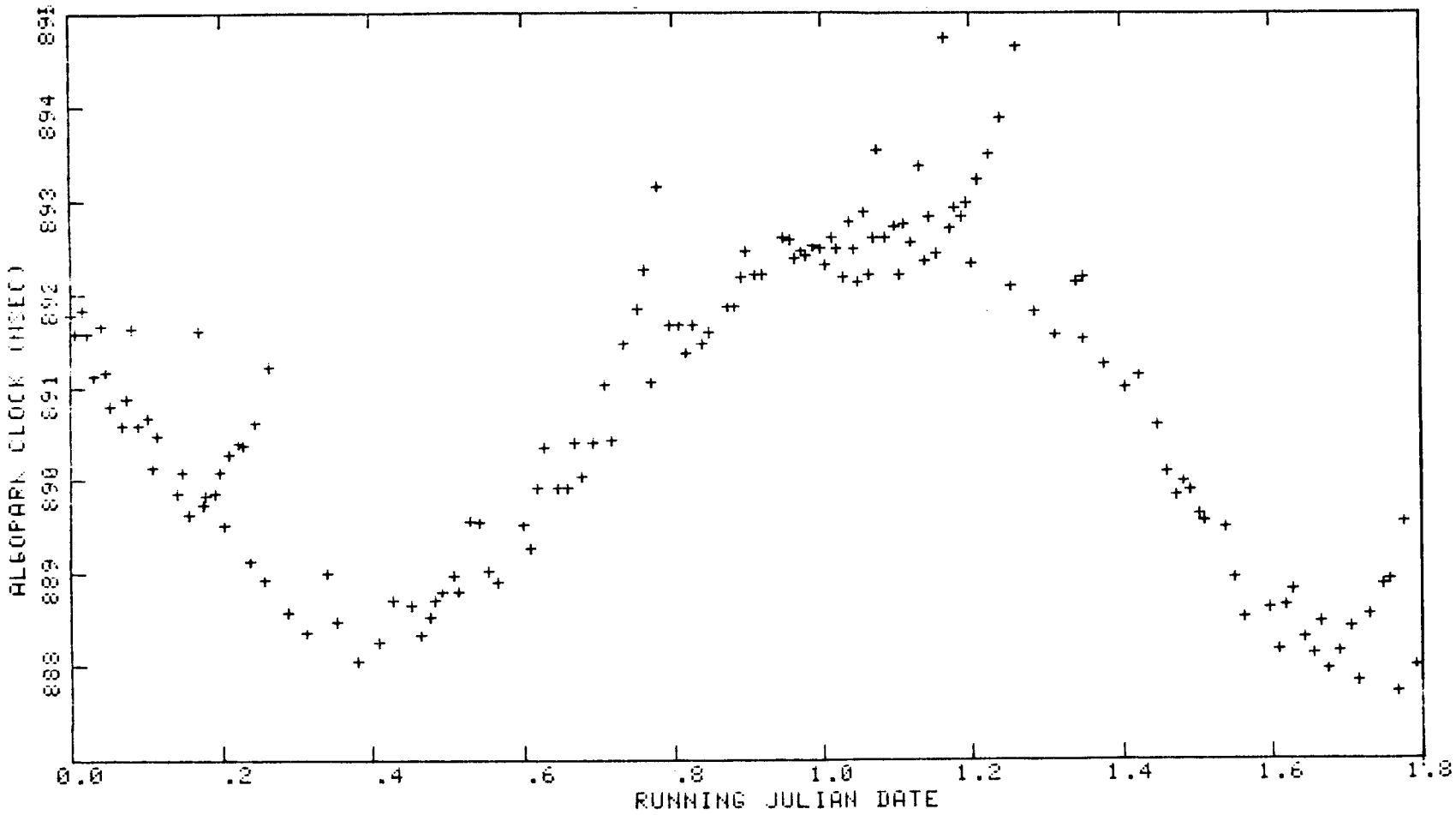

Figure 12b. Kalman filter output for HRAS-Algonquin Park baseline.

the figure. The letters are used to identify the radio source (such as 3C273B, 3C 345, etc.) observed by the VLBI antennas; the key to the right of the least squares plot defines the source associated with each letter. The plot shown has had clock offset and rate contributions removed from the delay residuals by least squares analysis. The resulting delay residual "fine structure" plot is sinusoidal in shape with an amplitude of 6 nanoseconds. The sinusoidal shape may be artificial, and could be due to several "breaks" in the clock behavior. It is the VLBI analyst's job to fit polynomials to the sinusoid; these polynomials would approximate the VLBI clock behavior on the Algonquin-Fort Davis baseline. A very good fit to the clock curve would leave (as a remainder) a linear trend of delay residuals; the residuals would run (in time) along a line centered at 0.0 nanoseconds in the updated delay residual plot. The scatter of the newly fitted delay residuals should be considerably less than 6 nanoseconds, and typically is about 50 - 150 picoseconds.

For comparison, the clock parameter estimates from the Kalman filter are shown as a function of experiment time (a running Julian date - in days) in Figure 12b. In this plot the quasar and radio sources are not designated by letter, but the clock offset estimates are denoted by crosses. The curves of Figures 12a and 12b are visibly alike allowing one to conclude that the Kalman filter estimates match residuals found by the least squares analysis. There

is a time offset in the results of Figure 12b which has been removed (by fitting) in Figure 12a. It would probably be more proper to compare the residuals of each technique, but residual plots from the Kalman filter were not available at this early stage of this work. Producing a Kalman filter which could solve for clock variations as a function of time (with limited analyst intervention) was a primary goal of this dissertation.

The Kalman filtered clock curve of Figure 12b was arrived at using an integrated white noise covariance $Q'(k) = Q(t_{k+1} - t_k)$ as opposed to some flicker noise method. In addition, clock parameter estimates are relatively insensitive to the noise level magnitude of the random walk model, Q, as long as it is in the domain of physical reality for masers (and calibration delays) used in VLBI work.

The clock contributions dominate the measured VLBI group delay residuals, in general, while the second largest VLBI nuisance factor arises from wet atmospheric path delays. The associated parameter being solved for using the Kalman filter is the adjustment to the atmospheric path delay in the zenith direction at each station. The dry part of the atmospheric path delay is usually not solved for but rather is adjusted using the Marini model dry atmosphere calibration which was mentioned earlier.

The choice of the wet zenith delay deterministic model was limited by the fact that only one parameter for each VLBI observing station is set up in the SOLVE analysis

program for atmospheric delay estimation. Thus, the simple model of:

$$\Phi(t_{k+1}, t_k) = I \qquad \text{(VI.57)}$$

is used. In the future, one would anticipate estimation of an atmospheric delay rate term as VLBI data analysis becomes more sophiscated. For now it is assumed that the wet zenith delay adjustment is roughly constant, although again because of its Markov foundation, the Kalman filter can still track non-constant atmospheric changes, even if they are not modelled. The zenith wet delay covariance can be modelled by a random walk process, as has been shown by Davis et al. (1985).

This concludes the derivations of state transition matrices and system (process) noise covariances needed to Kalman filter and smooth VLBI group delay data. The reader is probably wondering how all of the preceding fits together. This will be illustrated . First the measurement equation will be specifically written out (recall that the general form of the equation is $y_k = M(k)x_k + v_k$):

(VI.58)

$$\tau = \left(\frac{\partial\tau}{\partial x}, \frac{\partial\tau}{\partial y}, \frac{\partial\tau}{\partial(UT1-TAI)}, \frac{\partial\tau}{\partial\Delta\psi}, \frac{\partial\tau}{\partial\Delta\epsilon}, \frac{\partial\tau}{\partial\tau_c}, \frac{\partial\tau}{\partial\tau_{cr}}, \frac{\partial\tau}{\partial L_z}, \ldots \right) \begin{pmatrix} x \\ y \\ UT1-TAI \\ \Delta\psi \\ \Delta\epsilon \\ \tau_c \\ \tau_{cr} \\ \cdot \\ \cdot \\ \cdot \\ L_z \end{pmatrix}$$

$$+ \; v_{delay}.$$

Remember that τ is the VLBI group delay and v(delay) is the uncertainty in the delay. The variables x, y, UT1-TAI, $\Delta\psi$, $\Delta\epsilon$, τ_c, τ_{cr} and L_z have been explained earlier (see equation VI.32 and related text). Equation (VI.58) simply relates the group delay τ to parameters x at each observing epoch t_k. The subscripts k have been left out of (VI.58) to avoid clutter.

The discrete system dynamical equation (i.e. equation III.5) is

(VI.59)

$$\begin{pmatrix} x \\ y \\ UT1-TAI \\ \Delta\psi \\ \Delta\epsilon \\ \tau_c \\ \tau_{cr} \\ . \\ . \\ L_z \end{pmatrix}_{k+1} = \begin{pmatrix} \cos(\sigma\Delta t) & -\sin(\sigma\Delta t) & 0 & . & . & . & . & . & . & . \\ \sin(\sigma\Delta t) & \cos(\sigma\Delta t) & 0 & . & . & . & . & . & . & . \\ 0 & 0 & 1 & 0 & . & . & . & . & . & . \\ 0 & 0 & 0 & 1 & 0 & . & . & . & . & . \\ 0 & 0 & 0 & 0 & 1 & 0 & . & . & . & . \\ 0 & 0 & 0 & 0 & 0 & 1 & \Delta t & 0 & . & \\ 0 & 0 & 0 & 0 & 0 & 0 & 1 & 0 & 0 & . \\ . & . & . & . & . & . & 0 & 1 & 0 & \\ . & . & . & . & . & . & . & 0 & 1 & 0 \\ . & . & . & . & . & . & . & . & 0 & 1 \end{pmatrix} \begin{pmatrix} x \\ y \\ UT1-TAI \\ \Delta\psi \\ \Delta\epsilon \\ \tau_c \\ \tau_{cr} \\ . \\ . \\ L_z \end{pmatrix}_k$$

$$+ w_k ,$$

where $\Delta t = t_{k+1} - t_k$. Notice that if Δt is small, the state transition matrix, $\Phi(k+1,k)$ for this problem approximates an identity matrix. If one had no information about the physics or behavior of the VLBI parameters above, one could possibly start with an assumption of $\Phi(k+1,k) = I$ for initial filter runs. Also, the fact that all the VLBI parameters above are given non-zero stochastic noise terms ($w \neq 0$) is only to allow the filter form to be somewhat general. One may find that some of the VLBI parameters are purely deterministic.

Equations (VI.58) and (VI.59) comprise the measurement/system dynamics model employed herein for Kalman filtering/smoothing VLBI group delay data. The previously derived

covariances, R(k) and Q(k), and measurement partials, M(k), in addition to $\Phi(k+1,k)$ from equation (VI.59), are inserted in the Kalman filter/smoother algorithms. The net results of the filtering/smoothing will be the optimal parameter estimates $\hat{x}$ and their associated error covariances P.

Chapter VII.

TUNING THE KALMAN FILTER

To tune a Kalman filter is to define the values of the stochastic noise covariances used in the filter. Generally, one starts with some initial idea of what the variability of a parameter is based on knowledge of the physical system. For instance, one could analyze water vapor radiometer data to discover the stochastic variation in wet atmospheric path delay along zenith. Once one has some inkling of the range of applicable stochastic noise, one can then use some other method to home in on more precise process noise values.

The method employed herein is strictly one of trial and error. This would not be feasible to do if the number of parameters being estimated were large. The tuning of a Kalman filter is usually the most inscrutable facet of its application. Some authors even characterize tuning as being more of an art than a science, although tuning always has a tie to reality in that the process noise level used in a filter must be physically believable.

The ability to tune the Kalman filter used in this study by a brute force technique like trial and error is allowed by its limited realm of applicability. The VLBI data to be analyzed using the Kalman filter are the 1984-1985 IRIS

(International Radio Interferometric Survey) observation set, which consists of single-day VLBI measurement sessions run once every five days. The IRIS radio astronomy antennas are located at Westford, Massachusetts; Fort Davis, Texas (HRAS-Harvard Radio Astronomy Station); Richmond, Florida; Wettzell, Germany; and Onsala, Sweden. Since the Onsala observatory is not a full-time participant in IRIS, data from the Onsala baselines will not be analyzed. Also for the purposes of this study, the observing station at Westford will be the clock reference; that is, it will be the station whose masers other station masers will be compared to along any given baseline. This will simplify the tuning procedure.

The trial-and-error tuning method has a very simple basis -- one adjusts the process covariance values until the Kalman filter residuals $y_{k+1} - M(k+1)\,\hat{x}(k+1|k)$ are minimized. For clarification, the preceding residuals are not the delay residuals $y_k - \bar{y}_k$. Most Kalman filter tuning procedures are based on adjusting process covariances to minimize the Kalman filter residuals and their variances and to make the statistics of the residuals behave in a Gaussian manner. The residuals are examined along each baseline as opposed to all at once in a group.

The IRIS Kalman filter tuning was not done for all parameters at once, but rather was done for the parameters which have the greatest effect on the residuals first, then those parameters having the next greatest effect,etc., until

all tuning was completed. The parameters with greatest impact on VLBI residuals are those of the clock offsets and rates, and the clock offset and rate process covariances along a given baseline were found simultaneously. The clock parameter estimates were made using data from the baselines Westford-Richmond, Westford-Fort Davis(HRAS) and Westford-Wettzell; relative clock behavior along any other baseline in the Westford-Richmond-HRAS-Wettzell system can be found from combinations of clock solutions along the baselines which use Westford as a reference. What is specifically being determined by trial and error are Q(clock) and Q(clock rate) in equations (VI.55) and (VI.56). Once these values are fixed, they will be used in the processing of the 1984-85 IRIS data.

In order to find a Q(clock) and Q(clock rate) that will work in processing all the IRIS data, one would like to tune by examining the residuals of a one-day data set which exhibits behavior typical of most of the IRIS observation dates. A data set $84MAR04XP (version 13) from the IRIS series was arbitrarily selected for the tuning operation, mostly because it was the data set used in constructing much of the filter structure and software. The designation $84MAR04XP means that the data collection started on 4 March, 1984 and that the data set was processed by the NASA Goddard Space Flight Center VLBI analysis group. The least squares analysis residuals of $84MAR04XP (ver. 13) seemed well behaved, which allowed one some confidence in this choice of

a tune-up data set. The tuning results are summarized in Table One.

The tuning procedure along each baseline consisted of at least two steps: first, examine the average residuals (or their standard deviations) as a function of Q(clock), Q(rate) in four-decade intervals over the wide Q ranges Q(clock) = {10^{-31}, 10^{-15} seconds}, Q(rate) = {10^{-38},10^{-22} seconds^{-1}} and choose a subsection of the Q ranges for further study; second, examine average residuals and/or their standard deviations over the subsection until {Q(clock), Q(rate)} are found to the nearest decade in the Q domains. Further specification to better than one power of ten of Q(clock), Q(rate) for each baseline is probably not warranted at this time, unless one would want to Kalman filter phase delay. In general, there are only insignificant changes in the average residual or standard deviation over a decade in either Q value, in the region of minimum average residual.

Figure 13 depicts the results of the coarse clock tuning procedure along the Westford-HRAS baseline. Contours of constant average value are drawn to highlight the structure in the plot. A region of minimal average residuals extends from the center of the graph to the upper right-hand corner along a line in which both Q(clock) and Q(rate) are increasing; the average delay residual varies little along this line.

In Figure 14 a coarse plot of the "average residual"

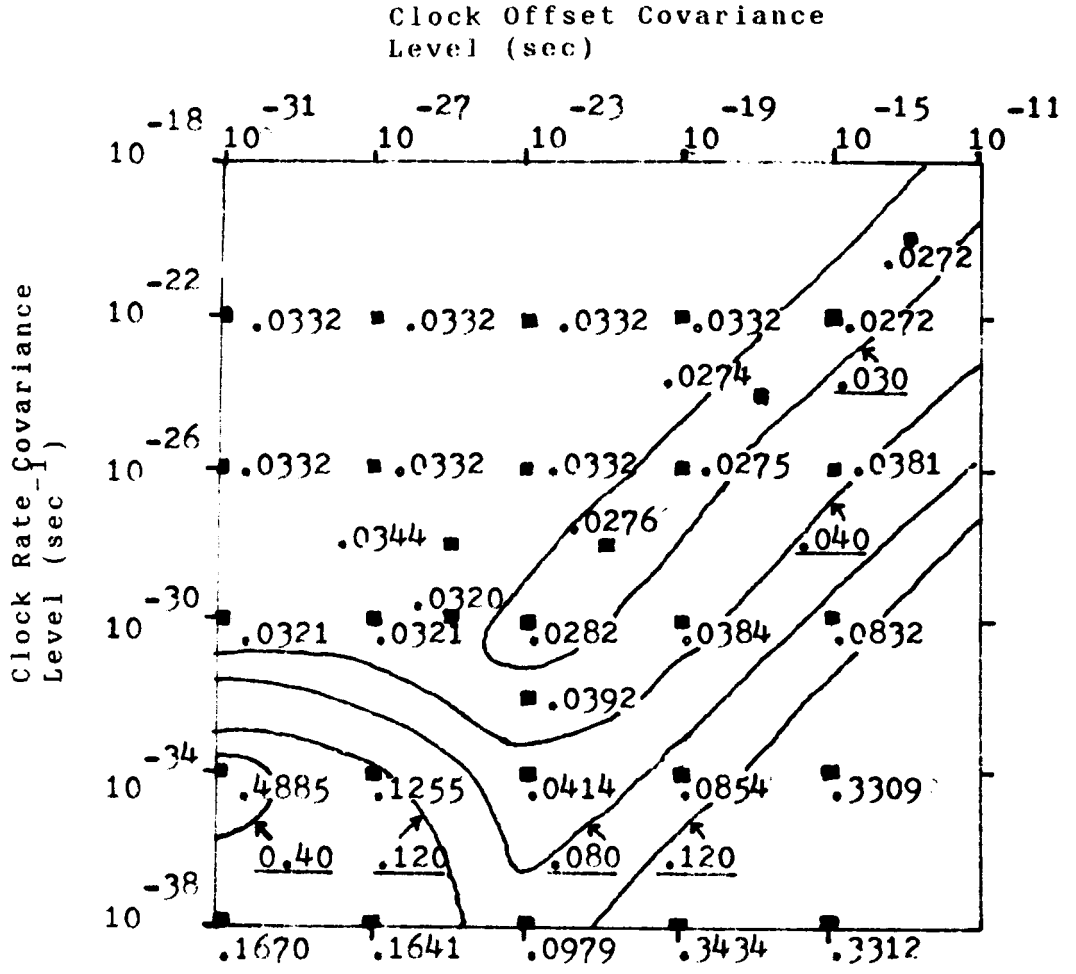

Figure 13. Kalman filter (group delay) residual averages (and contours) plotted as a function of clock offset covariance level and clock rate covariance level. Contour residual values are underlined.

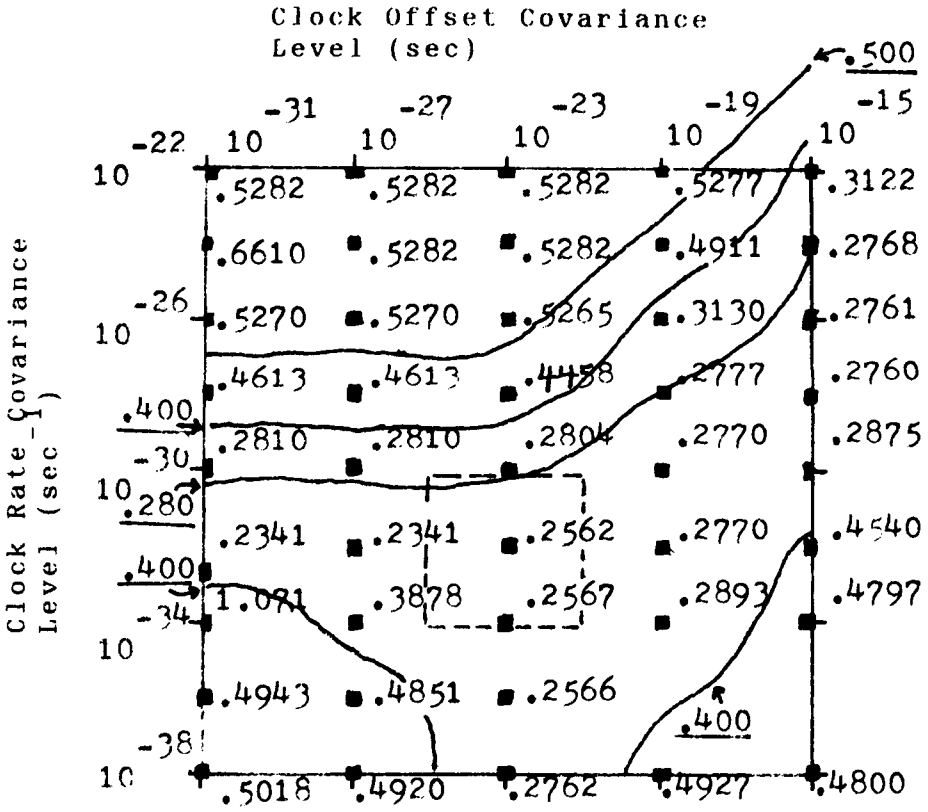

Figure 14. Kalman filter standard deviations of residuals. Contour values are underlined. Plot is for tuning of clock covariance levels.

standard deviations is displayed. The structure is similar to the plot of average residual values, and contours of constant standard deviation are drawn. A region for further tuning is surrounded by a square made up of dotted lines. This area has been chosen for further tuning because the standard deviations of the residuals are close to minimum value and the residual standard deviations don't change much within the region surrounded by the dotted line. Similar plots are made for the finer (single-decade resolution) tuning study and ultimately the best Q(clock) and Q(rate) are chosen from such a graph. This trial-and-error procedure was also followed for the Westford-Richmond and Westford-Wettzell clocks, and it was reassuring to find that the plots used to select Q values for each baseline all resembled one another. In addition, the Q values found in this manner have been applied herein to non-IRIS data with good residual fit results.

The clock tuning done by trial and error yielded process noise standard deviations of about 10 - 100 picoseconds for clock offset and one part in 10^{14} for clock rate, which are both physically reasonable. A part in 10^{14} for the clock rate process noise makes sense because the VLBI masers are supposed to operate at this specification over the period of several hours. The standard deviation of 10 - 100 picoseconds in clock offset agrees with current GSFC VLBI data analysis uncertainties in which the all-inclusive "clock" is a dominant factor.

After the process noise covariances for clock offset and rate were found, the process (or stochastic) noise level for the wet (atmospheric) zenith delays, a set of nuisance parameters, had to be fixed by trial and error. Characterization of these delays at each observing location is important for VLBI data sets in which no (or bad) water vapor radiometer (WVR) data are available, which at present, almost always seems to be the case. The implementation of WVR's is currently in its infancy.

The random walk covariance level at each station (HRAS, Wettzell, Westford, Richmond) was estimated using data from two individual baselines: HRAS-Richmond and Westford-Wettzell. Along the Westford-Wettzell baseline, the previously determined clock models were used in solving for clock parameters in addition to wet zenith delay parameter adjustments at Westford and Wettzell. The wet atmosphere delay covariances were adjusted until the delay residuals were minimized. A similar procedure was followed for HRAS-Richmond. As with the clock tuning, the residuals were estimated using atmosphere delay covariance levels over a coarse range of 10^{-18} to 10^{-30} seconds in four decade intervals. This range was chosen because it is on the order of the square of nanoseconds to picoseconds - the level at which one might expect to see atmospheric delay variations. Figure 15 depicts the delay residual standard deviations as a function of covariance level for each of the stations at the end of the HRAS-Richmond baseline. The dotted line on

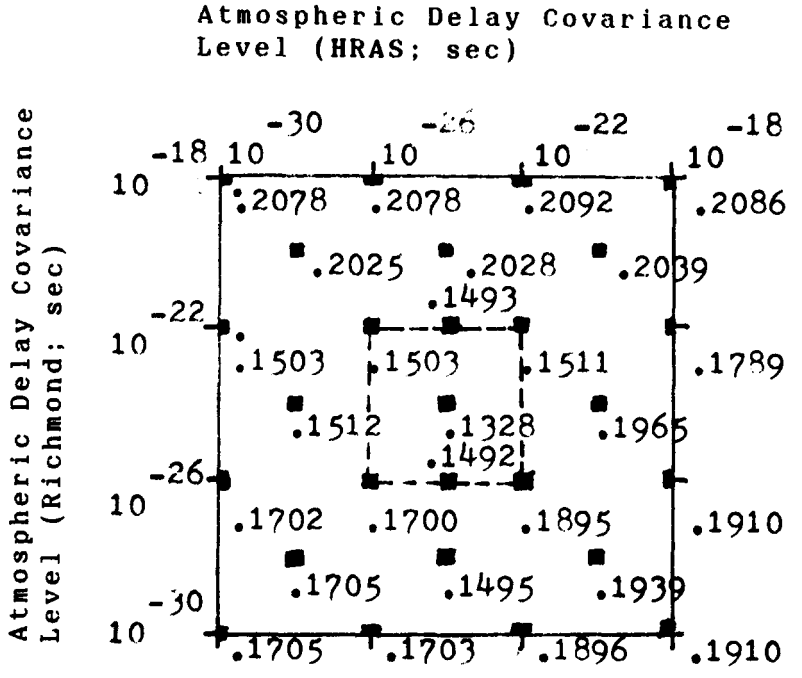

Figure 15. Kalman filter standard deviations of residuals for atmospheric covariance level tuning. VLBI stations are at HRAS (Texas) and Richmond, Florida. Contour values are underlined.

the figure again indicates the region over which fine tuning (at one-decade intervals) took place, and from which the final covariance levels were found.

The standard deviations of wet zenith group delay were found to be on the order of tens of picoseconds, which again agrees with the physical value of what one would expect as the wet delay uncertainty. It should be noted here that estimates of the wet zenith delay adjustment should be directly comparable in magnitude and shape to the delays output by water vapor radiometers. Now that the covariance levels have been set for the clock and atmosphere nuisance parameters one can now turn attention to the more physically important parameters of polar motion, earth rotation and nutation.

The covariance levels for the two components of polar motion were found (simultaneously with clocks and atmospheres) using the method of trial and error for the VLBI triad Westford-Wettzell-HRAS. The Richmond station was not used in order to save time during tuning -- the trial-and-error method becomes somewhat long-winded after a while. Residuals were only examined for the baseline HRAS-Wettzell, which should be sensitive to polar motion. VLBI baselines trending North-South are generally sensitive to at least one polar motion component; for more about this topic, please refer to Lundqvist (1984). The polar motion covariance levels being determined are q_{11} and q_{22} in equation (VI.46).

The results of the polar motion tuning are presented in Figure 16. The covariance level range is 1.0×10^{-18} to 1.0×10^{-30} radians^2/sec for each component of polar motion, and again the area chosen for further fine tuning is marked by the dotted line. The standard deviation of the group delay residuals is sometimes used in the process noise covariance estimation procedure rather than the average residuals because the spread in the residuals seems to be a more useful indicator in tuning than some average residual. The average residual is usually very close to zero. In addition the standard deviation of the average residual is positive in value.

The polar motion process covariance levels are roughly the same for both components and very small in value. The small covariance levels indicate that the polar motion parameters are deterministic to a high degree. The non-zero polar motion process covariances found through trial and error are retained in the filter only so the filter does not "close up" on itself. A filter which closes up is one that no longer modifies parameter estimates even though new data are being processed. It is a condition in Kalman filters that should be avoided, even if by injection of slightly extra artificial noise.

The tune-up of nutation and obliquity was similar to that of polar motion except that polar motion parameters were estimated also, in addition to nutation adjustments, clock terms and atmospheric parameters. The nutation in

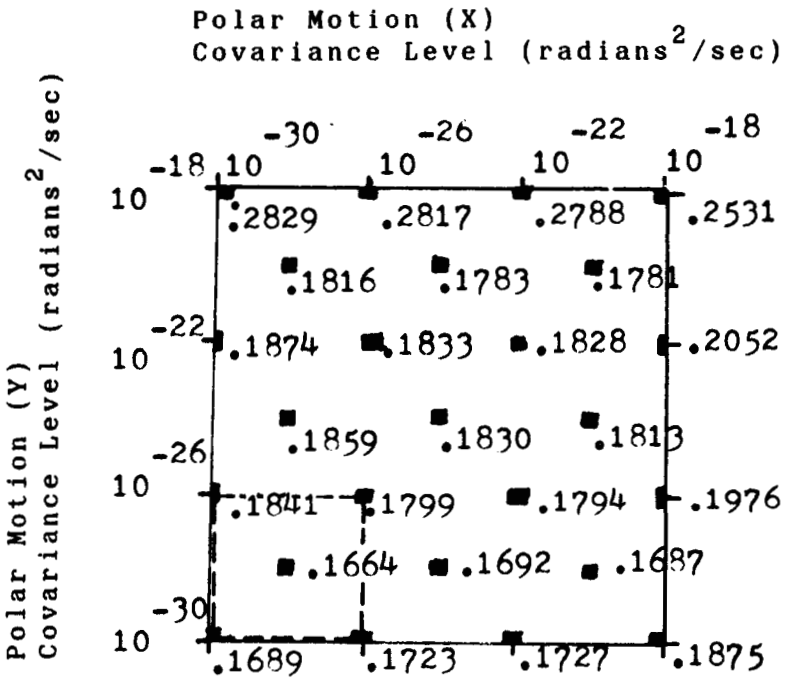

Figure 16. Kalman filter standard deviations of residuals for polar motion covariance level tuning. Baseline is HRAS (Texas) to Wettzell (Germany).

obliquity and longitude adjustments also proved to be very close to deterministic. Better nutation models (deterministic and stochastic) should probably be implemented in the near future.

The last remaining covariance level to be found is for UT1-TAI, length of day adjustments. All previously mentioned parameters were solved for and the residual standard deviation was observed as a function of the process covariance level, Q, in equation (VI.51). The change in length of day is found to be very nearly deterministic. Thus all the parameters of interest (nutation, polar motion, earth rotation) appear to be quite deterministic while the nuisance parameters (clock, clock rate, wet atmosphere zenith delay) bear strong stochastic components. In the future, what is here modelled as stochastic may become deterministic as scientists become more familiar with the physics of clocks and atmospheres.

Table One summarizes the process noise covariance information for the parameters estimated in this work. It is interesting to note that all atmospheric process covariance levels are the same except for the HRAS station at Fort Davis, Texas which appears to be less variable than its eastern U.S. counterparts. It seems that the general lack of water vapor in west Texas is exhibited in a low relative covariance level, at least for the day of data being used to tune the Kalman filter. In addition the Westford-HRAS clock rate covariance level is anomalously

Table One- Kalman Filter Covariance Levels

COVARIANCE LEVELS (Westford = reference station)

CLOCK LEVELS

Baseline	clock offset (sec)	clock rate (sec^{-1})
Westford-Wettzell	10^{-23}	10^{-30}
Westford-Richmond	10^{-23}	10^{-30}
Westford-HRAS(085)	10^{-23}	10^{-32}

ATMOSPHERE DELAY LEVELS

Station	Level (sec)
Westford	10^{-24}
Wettzell	10^{-24}
HRAS (085)	10^{-25}
Richmond	10^{-24}

POLAR MOTION

Each component	10^{-28}	(rad^2/sec)

NUTATION

Each component	10^{-30}	(rad^2/sec)

UT1 - UTC

One component	10^{-28}	(sec)

(but not severely) low, suggesting that the relative maser behavior along the Fort Davis-Westford baseline is better than along other baselines.

It should be stressed that the process covariance levels of Table One should produce good-to-excellent residuals if applied to 1984-85 IRIS data sets for which they were designed. However, as improvements in the Mark III VLBI data-taking systems are made in the future, one may have to modify the Kalman filter deterministic and process covariance models applied here. In addition, finer tuning may be needed if one is to filter phase delay data rather than group delay observations.

Apparently there is some precedent for this trial-and-error approach to Kalman filter tuning. Fitzgerald (1967) uses a trial and error Kalman filter tuning technique for aeronautical guidance problems. There are more sophisticated techniques for determining the process covariances Q and also for the measurement covariances R than the trial-and-error method. For details about these procedures see sections 8.8 through 8.11 of Jazwinski (1970). Simply put, these methods use predicted residuals r(k+1|k) and the constraint that the predicted residuals be consistent with their theoretical statistical properties, to estimate the process covariances used in a Kalman filter. A specific example (for l=1) of a predicted residual is

$$r(k+1|k) = y_{k+1} - M(k+1)\hat{x}(k+1|k). \qquad \text{(VII.1)}$$

An advantage of this technique is that one is using obser-

vational data to tune the Kalman filter. Time considerations and computer limitations prevented implementation of such a filter for this work. The smoother requires no further tuning because it only operates on the output of the Kalman filter.

Chapter VIII.

FILTER OPERATION AND ILLUSTRATIVE EXAMPLES

This chapter explains the manner in which the Kalman filter was used to process VLBI group delay data. Some illustrative examples are presented to clarify what is going on. In general the filter can be set up to automatically generate the estimates, error covariances etc. which are used as input to the smoother. Once the filter run has finished, the smoother is simply turned on. Thus again the filter operation will be emphasized here. The smoother depends on a proper filter run in order to produce optimal results.

So far, much has been described about the state transition matrix $\Phi(k+1,k)$ and the process noise covariance Q, but little has been said about the a priori estimates, x_0, and error covariances, P_0, used to initially start the filter; lack of emphasis on this subject is a distinct shortcoming in most Kalman filter texts. It is very desirable to start a Kalman filter run with the best a priori values possible. The source of such a priori's could be previous Kalman filter end point estimates which stop at the start epoch of the subsequent Kalman filter run, or could be measurements of a priori parameters made just before the

start of data taking.

In parameter estimation of IRIS VLBI data there are usually no prior measurement data since the preceding observing session was five days earlier. The end point estimates from the earlier session could be used as a prioris for the current filter run, but this is not done here because it is thought that the maser time offsets will change greatly in the (four) intervening days due to the clock ramp signals inherent in maser time keeping. Perhaps it is better to start a Kalman filter run with the belief that one has no information about the a prioris. This is the tactic employed in this research.

To utilize the assumption that nothing is known about the a prioris, one sets x_0 (actually, the adjustments to parameters with respect to reference values) to zero and P_0 to infinity. Instead of setting the error covariance, P_0, to infinity, it is sufficient to set P_0 to some large value much larger than the parameter errors are thought to be. For the purpose of IRIS VLBI parameter estimation, P_0 is assumed (for simplicity) to be a diagonal matrix with null values for off-diagonal elements, and with P_0 diagonal elements given in Table Two. It can be seen that some of the initial covariance values are not overly large (i.e. approaching infinity), but the filter seems to quickly recover from this.

Since the amount of VLBI data for single IRIS runs is limited to about one day duration, it was necessary to

Table Two - Kalman Filter Initial Conditions

	Initial Conditions	
Parameter	x_0	P_0
Clock offset	0.0 sec	1.0×10^{-16} sec^2
Clock rate	0.0	1.0×10^{-28}
Atmospheric delay	0.0 sec	1.0×10^{-16} sec^2
Polar motion (each component)	0.0 radian	30.0×10^{-18} $radian^2$
UT1 - UTC	0.0 sec	5.0×10^{-7} sec^2
Nutation (each component)	0.0 radian	30.0×10^{-18} $radian^2$

iteratively Kalman filter the VLBI group delay data. P_0 was set to the values listed in Table Two for all runs. For the first iteration, x_0 was set to zero. The ending estimates x from the first iteration were input as a prioris into the second Kalman filter iteration, and each iteration was repeated in a similar fashion. The iterative procedure was concluded when the estimated residuals showed minimum standard deviation. Usually this occurred after three or four iterations. One would believe that the number of iterations could be reduced by starting with larger P_0 values, but there was no excess programming time to look into this possibility. In general, the standard deviation of the residuals found using the iterative Kalman filtering method matched those arrived at via least squares analysis. This result validates the belief that the Kalman filter method can be used to eliminate analyst intervention necessary in VLBI optimal estimation using batch least squares. Kalman filtering on a "state of the art" computer, as opposed to the antiquated (Hewlett-Packard) HP-1000, would be a dream.

Now that most of the preliminary details have been unravelled, it will be quite useful to familiarize the reader with some examples of Kalman filtering. The initial examples reflect the analysis of IRIS data set $85SEP20XI, version 11. Figures 17 a and b depict the clock (offset) and clock rate (filter) estimates as a function of experiment running time (horizontal scale) for the baseline

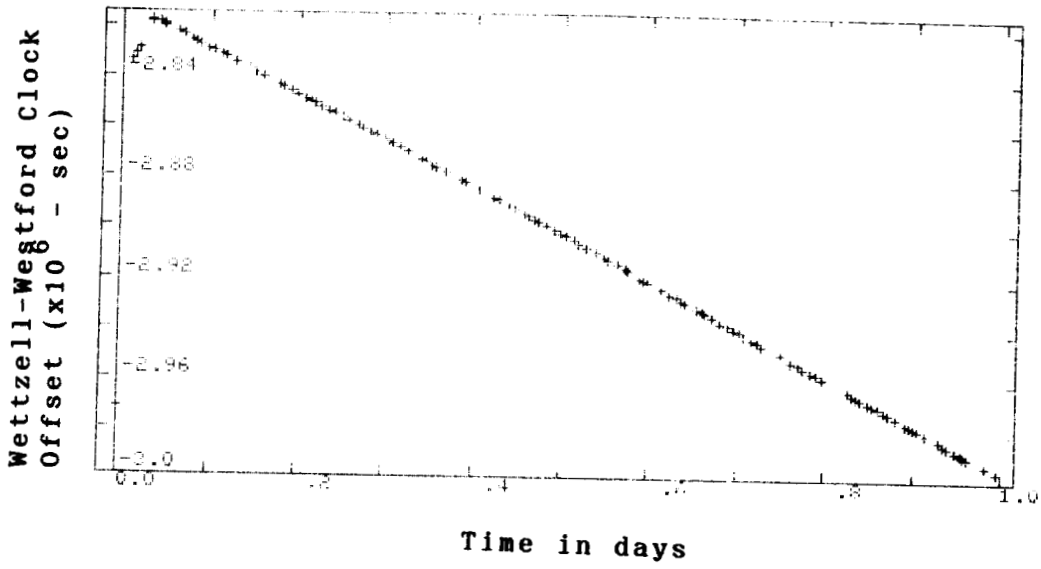

Fig. 17a.

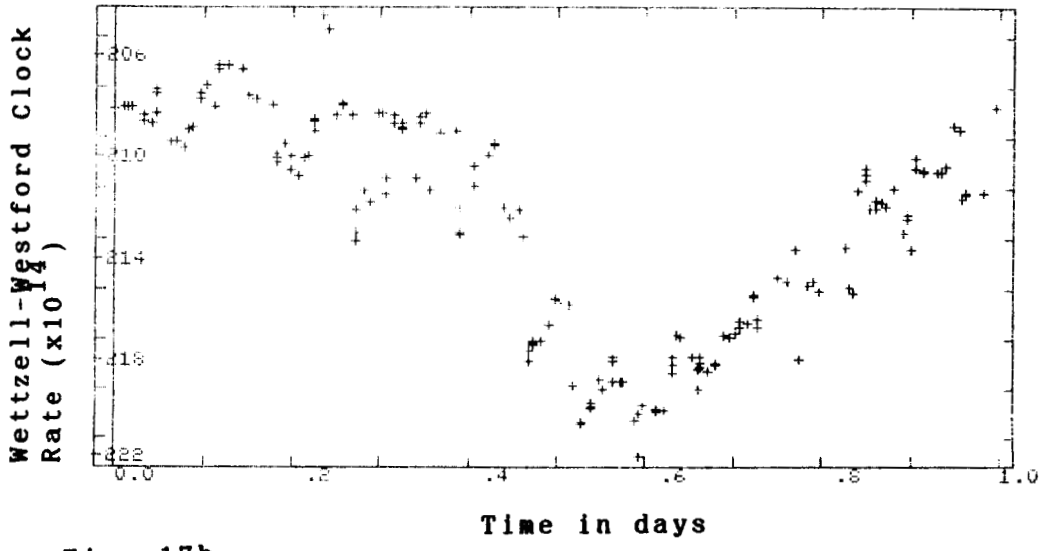

Fig. 17b.

Figure 17. (a) Westford-Wettzell clock offset as a function of time as produced by Kalman filter. Note convergence to actual clock offset at the beginning of the run. (b) Wettzell-Westford clock rate as output by the Kalman filter. Note that the relative clock rate is approximately, but not absolutely, constant as a function of time.

Wettzell to Westford. The clock offset plot is clearly dominated by a ramp function which is actually the relative behavior of the Wettzell maser with respect to the Westford hydrogen maser; an offset in frequency of each maser gives rise to a ramp function in time, and the difference of two ramp functions is the ramp function shown. Notice at the beginning of the clock offset plot that it takes a short time for the Kalman filter to converge on the proper clock offset estimates. The clock rate portion of Figure 17 is not as continuously linear as the clock offset plot, but it can be seen that the clock rate is roughly constant (considering the small vertical scale of the plot) with value between $-206. \times 10^{-14}$ to $-220. \times 10^{-14}$ seconds/second. The approximately constant clock rate estimate again indicates that the masers along the baseline Westford-Wettzell are working well. There are three distinct changes in slope visible in the clock rate plot which can probably be attributed to phase injection delays and/or cable calibration effects. The changes in slope on the clock rate plot suggest that the deterministic "clock" model (of the Kalman filter) which includes clock rates, but no clock acceleration parameter, is approximate. The model will work better in some situations than in others.

Clock offset along Westford-Wettzell with much of the dominating clock offset and rate removed is depicted in Figure 18. That the clock rate has at least three distinct values is now clearly reflected in the finer scale clock

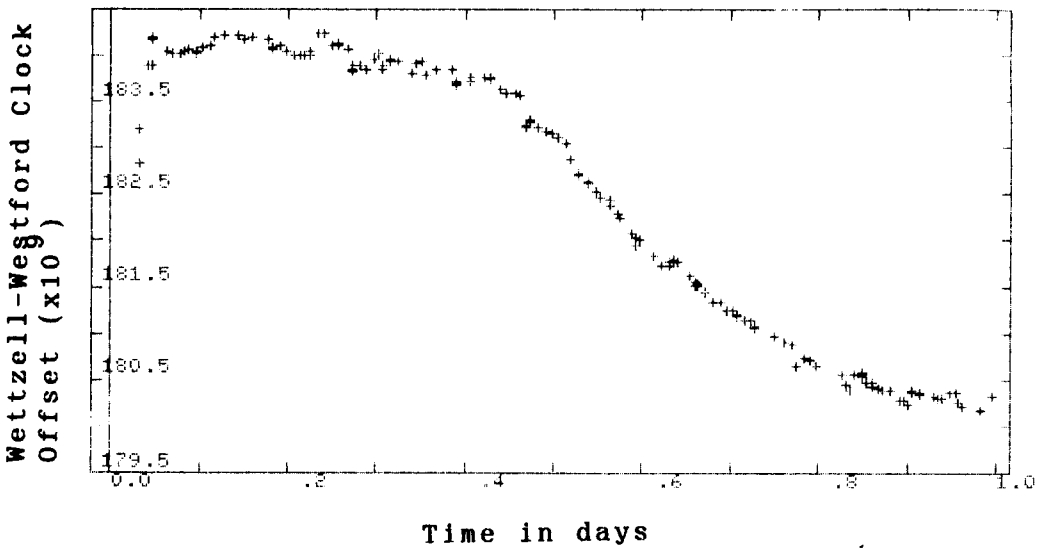

Figure 18. Wettzell-Westford clock offset with primary linear clock trend removed. Variations in clock offset as a function of time can be observed.

offset estimates. This figure is included to remind one that fine structure can be hidden by dominant trends in data.

The other "nuisance" parameters in VLBI optimal estimates are the wet zenith (atmospheric) delays (at Westford and Wettzell) which can be viewed in Figure 19. It is obvious from comparison of the "clock" plots and Figure 19 that the clocks will affect VLBI observations more than the wet zenith delay. However, it should be remarked that the plots of Figure 19 are for a day when variations in wet zenith delay are quite small. The graphs of Figure 19 give the moisture content adjustment in the zenith direction at each station from VLBI data alone; this illustrates the sensitivity of Very Long Baseline Interferometry as a measurement technique.

Now that some examples about the nuisance parameters have been presented, one can examine the polar motion estimates displayed in Figure 20. The Kalman filter standard deviations (from the square root of the relevant error covariance elements) are shown as bars with the polar motion component estimates on the figures. The polar motion and UT1-TAI estimates are made with respect to reference polar motion and UT1-TAI values from BIH (Bureau de l'Heure) publications (BIH Circular D or Rapid Service documents). Since BIH data are only found at five-day intervals, the reference values are determined by fitting a curve to the BIH polar motion data at the epoch of observation and at

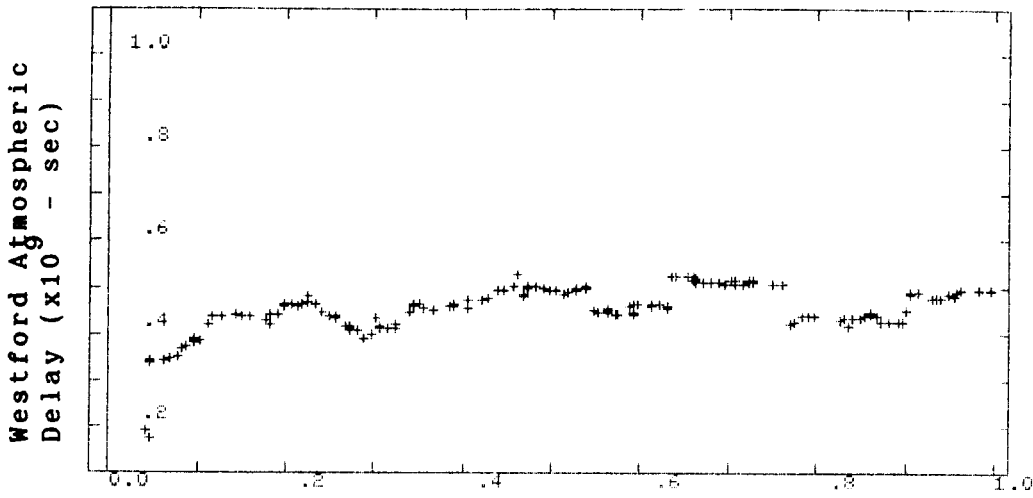

Fig. 19a.

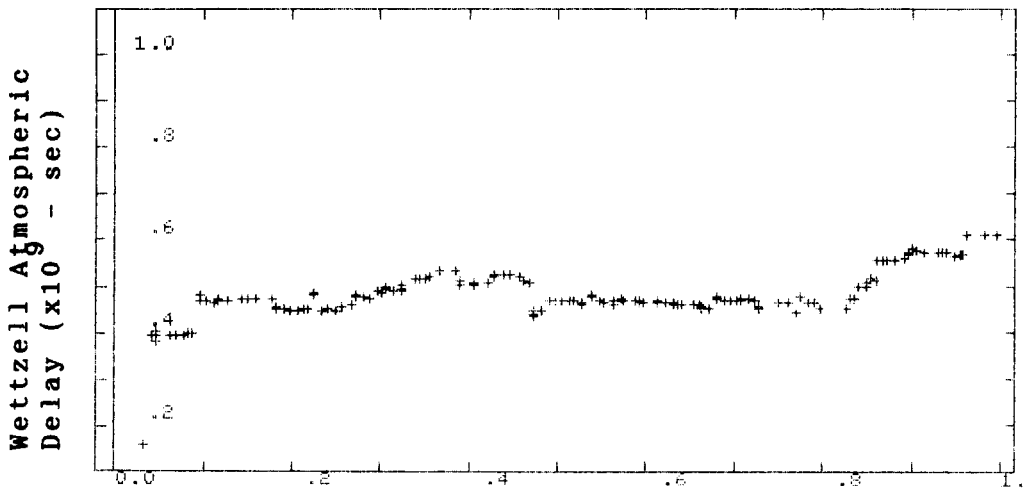

Fig. 19b.

Figure 19. (a) Westford atmospheric (zenith) delay adjustment as a function of time (as output by Kalman filter). (b) Wettzell atmospheric delay.

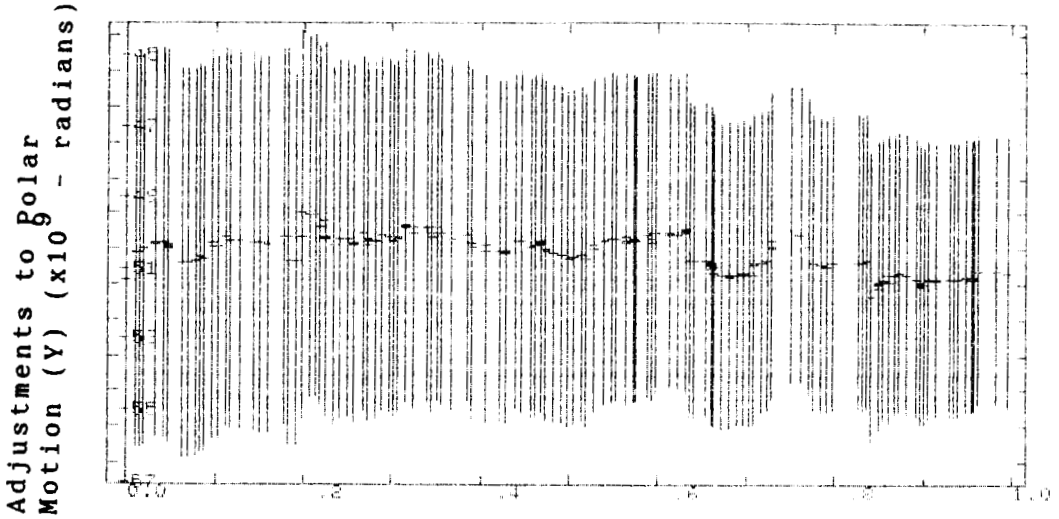

Fig. 20a.

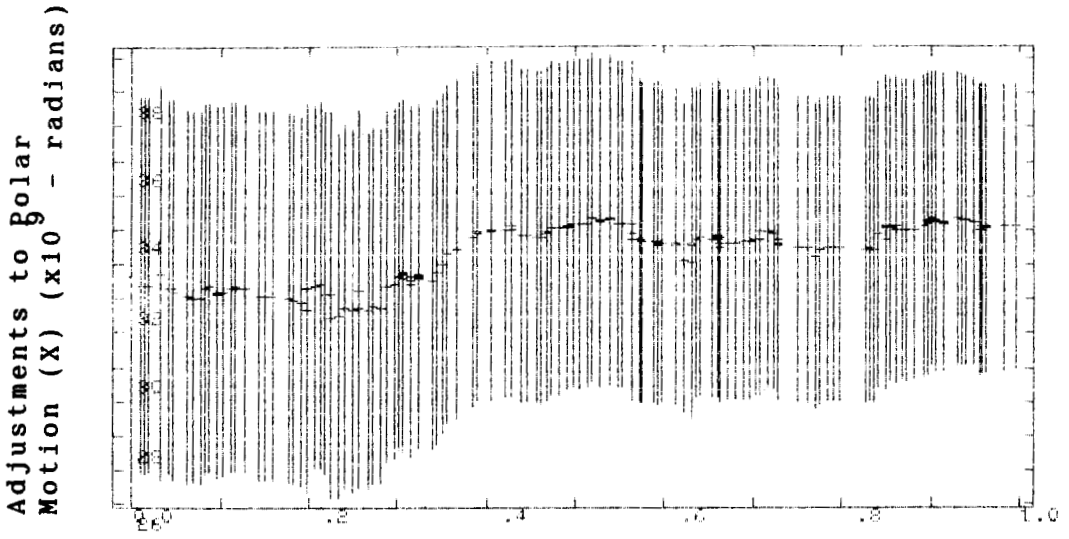

Fig. 20b.

Figure 20. (a) Adjustment of Y-component of polar motion as output by Kalman filter; associated errors included. Error are at the one mas level. (b) Adjustment of the X-component of polar motion and errors.

two BIH values on either side of this IRIS datum; one then interpolates to get polar motion reference estimates (used in the VLBI program CALC) at each VLBI observing epoch.

A look at the general features of Figures 20 a and b reveals that the adjustments in polar motion in time are very nearly constant, especially considering the fine scale of the plots. One can also readily observe the estimates converging as more and more data are processed, as should be the case. The polar motion error bars originally start with amplitudes of about 2.0 milliarcseconds which fall to values of 1.5 milliarcseconds or less at the end of the Kalman filter run. These error bar values lead one to conclude that the Kalman filtered VLBI polar motion estimates are good to the one-milliarcsecond level at best.

In Figure 20 b, one can distinguish a not so gradual change in the x-component (m_1) of polar motion of about 0.4 milliarcseconds from the time 0.3 to 0.4 days. There is no corresponding change in the y-component of polar motion and, of course, a change of 0.4 milliarcseconds in the x-component is not statistically significant. Nevertheless, it is interesting to note that this change in the x-component is well correlated in time with a large aftershock of the Great Michoacan, Mexico earthquake of 19 September, 1985. The aftershock event was of magnitude M_S = 7.6, moment 2.4 x 10^{27} dyne-cm with epicenter at 17.802^o N latitude and 101.647^o W longitude (depth = 31 km) and occurred on 21 September, 1985 at 1:37:13.4 UTC (Preliminary

Determination of Epicenters, USGS, September, 1985). The VLBI experiment started at 17:37 UTC on 20 September, 1985 and ran for about one day, with the 0.3-0.4 day time range (when the change in the x-component of polar motion occurred) lasting from 00:49 UTC to 3:13 UTC on the 21st of September. The time of the aftershock falls well within the time range 00:49 to 3:13 UTC.

It should be remarked that variations in clock and atmosphere parameters did occur from 00:49 to 3:13 UTC, and that these variations could influence the polar motion x-component results. But if this is indeed the case, one would expect such clock and atmosphere contributions to appear in the y-component of polar motion also. Such behavior is not evident and suggests that the change in the x-component of polar motion may be real, even though not measurable to our statistical satisfaction. Future improvements in VLBI measurement precision should allow resolution of whether such an observed variation is real.

A return to the original topic of presenting examples is warranted. The change in length-of-day estimates for data set $85SEP20XI.version 11 appear in Figure 21. The figure shows that UT1-TAI is quite constant over the one-day VLBI session, although a very slight slope is evident in the estimates once the filter has recovered from the UT1-TAI a priori values at a time of 0.07 days. The error bars of the estimates are quite large until a priori recovery, which is what one would expect. Following the recovery, the

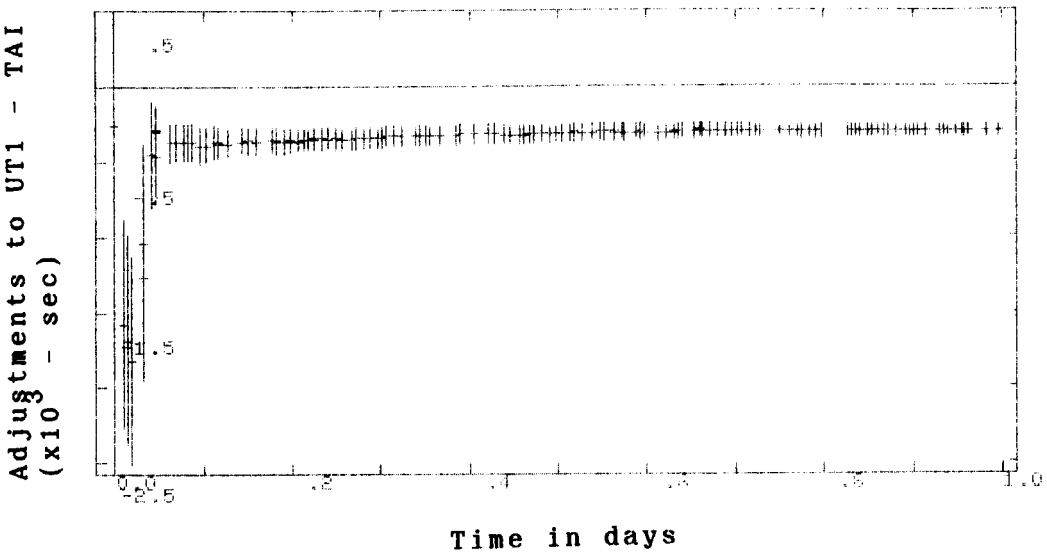

Figure 21. Kalman filtered adjustments to UT1 - TAI (changes in length of day) as a function of time. Note decrease in error size as filter converges on optimal estimates.

estimates converge and the error in the estimates decreases to 0.1 milliseconds or less. The reduction in the UT1-TAI errors over one day is relatively larger than that observed for the polar motion and nutation parameters.

The adjustments to the nutation in obliquity and longitude are revealed in Figure 22. The nutation offsets are estimated with respect to reference values given by the 1980 IAU (Kaplan, 1981) nutation series. Again the nutation in obliquity and longitude offsets are roughly constant, and converge as the filter processes more and more data. The nutation in obliquity estimates are determined to a much higher precision than those of the nutation in longitude; this behavior is commonly repeated in other Kalman filtered VLBI data sets. A step observed in both nutation estimates at time equals 0.84 days is due to influences of "clock" parameters; it is evident that the clocks are responsible because both nutation parameters are affected.

The last items of educational interest are the residual plots for a final run of the Kalman filter, which are given in Figure 23. The residuals are broken up into groups by baseline and, on a given plot, they would ideally be expected to have zero mean and some statistically predictable value of standard deviation. The residuals are displayed versus the running time during the observing session (on the vertical scale) so a VLBI analyst can spot trends in the data. The residuals along the Westford-Wettzell baseline bear some remnants of the "clock" conduct shown

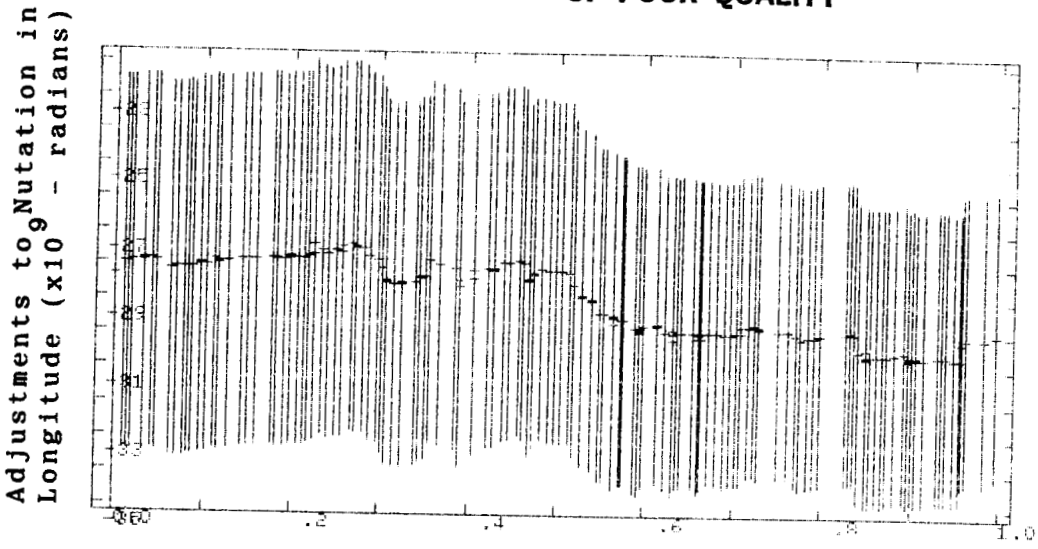

Fig. 22a.

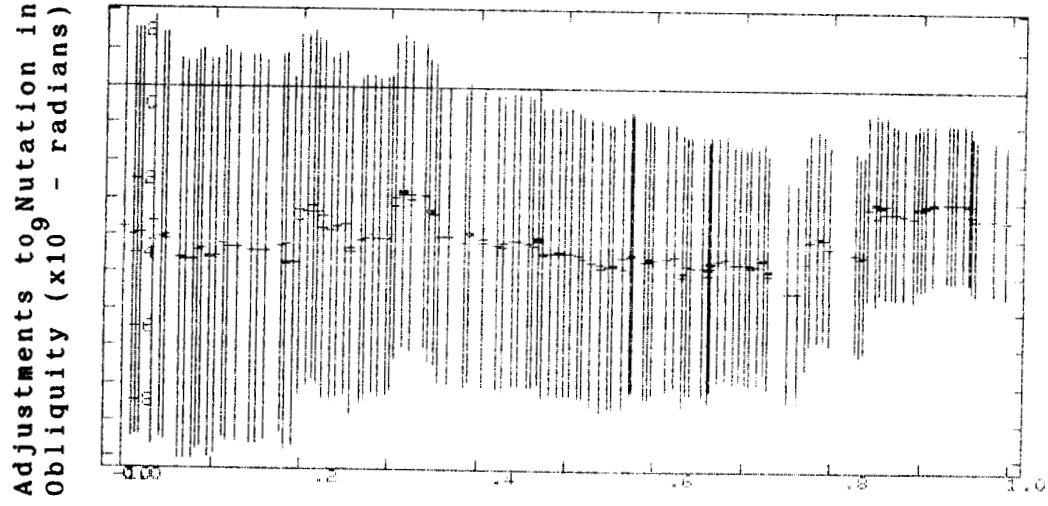

Fig. 22b.

Figure 22. Kalman filtered nutation adjustments and errors. (a) Nutation in longitude (b) Nutation in obliquity.

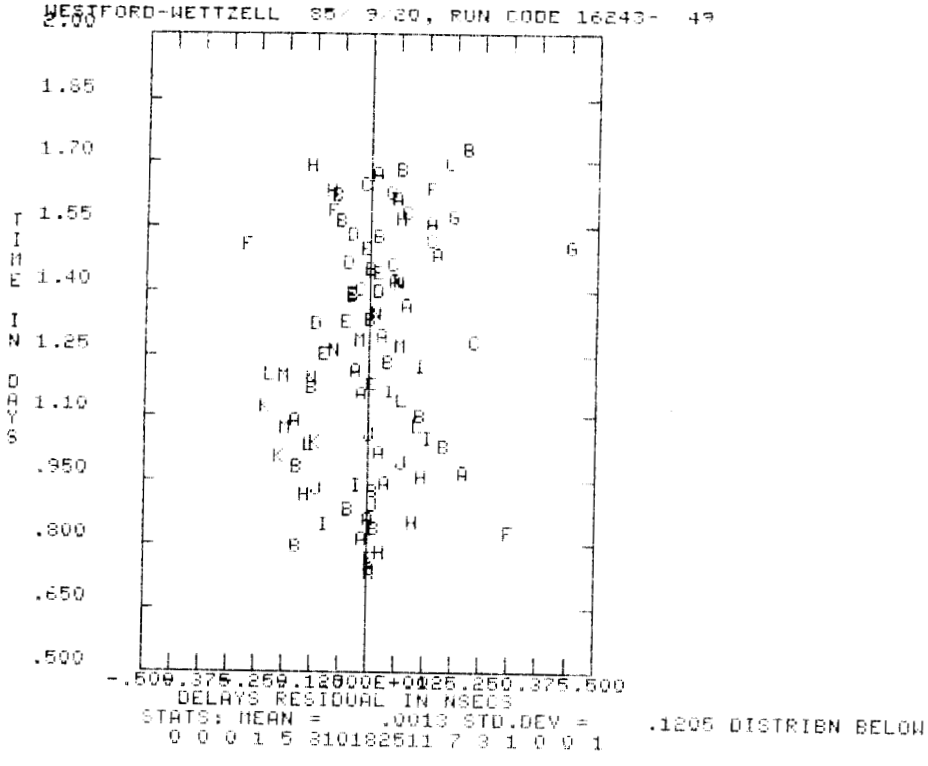

Fig. 23a.

Figure 23. Kalman filter group delay residual plots. Roman letters indicate (quasar or radio) source being observed. (a) Westford-Wettzell baseline. (b) Westford-Richmond (c) Richmond-Wettzell.

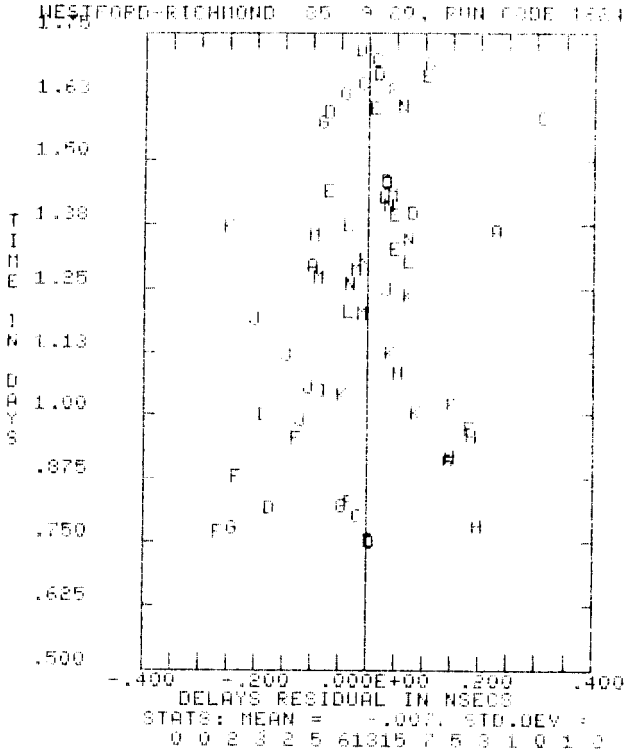

Fig. 23b.

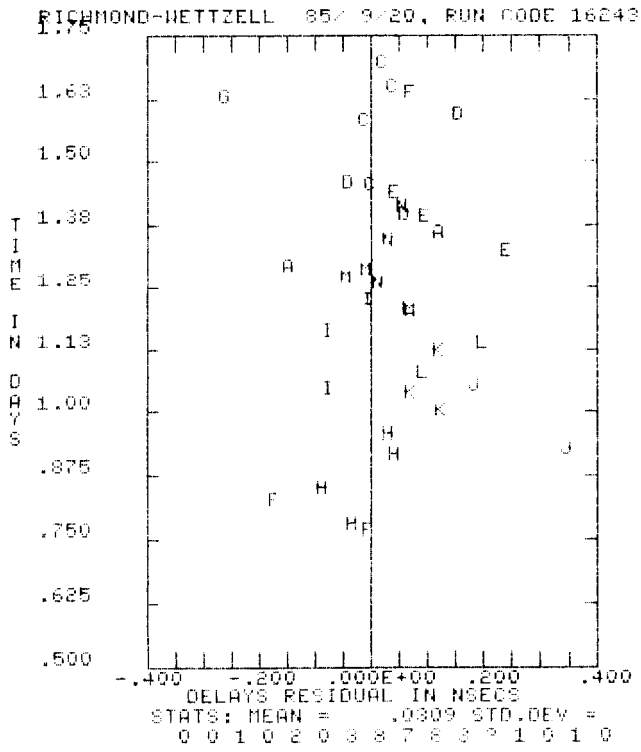

Fig. 23c.

previously, but at a much reduced amplitude. In general, the clock parameters have successfully absorbed such clock-like trends.

Little average bias can be observed in the group delay residuals of Westford-Wettzell and Westford-Richmond, while a somewhat larger offset in average delay is visible for the Richmond-Wettzell baseline. Perhaps the bias could be removed by a slight retuning of the Kalman filter, but in most analyses such time-consuming procedures were avoided. The standard deviations of the group delays are in the 120-picosecond range which is typical for the data handled in this work. No large amplitude trends are evident in the residuals of each baseline, emphasizing that the Kalman filter produces results consistent with those attained via other current VLBI analysis techniques.

A few more illustrative examples involving data sets other than \$85SEP20XI follow. Data from \$84MAR04XP are used to compare filter estimates with Rauch-Tung-Striebel (1965) smoother results. Filter estimates for wet zenith delay at Westford and Wettzell are in Figures 24. The corresponding smoother results are brought out in Figure 25. The rough, discontinuous wet delay fluctuations quite visible in Figure 24 become much smoother and more continuous in Figure 25, as one might expect. The smoother does "smooth" the data in the traditional sense. While the filter and smoother estimates are not very different in amplitude, the smoother uses all the information available

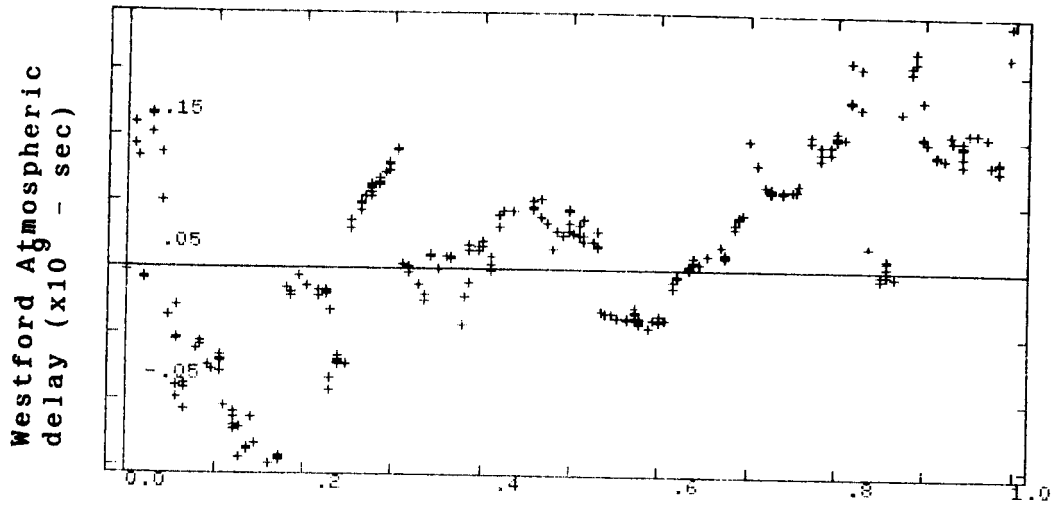

Fig. 24a.

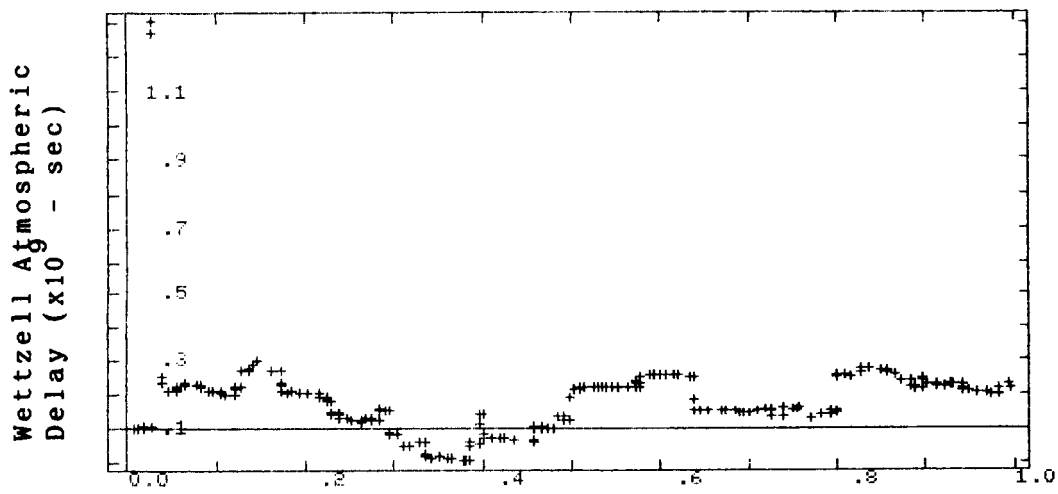

Fig. 24b.

Figure 24. (a) Kalman filtered atmospheric delay adjustments for Westford, Mass. (b) Kalman filtered atmospheric delay for Wettzell, Germany.

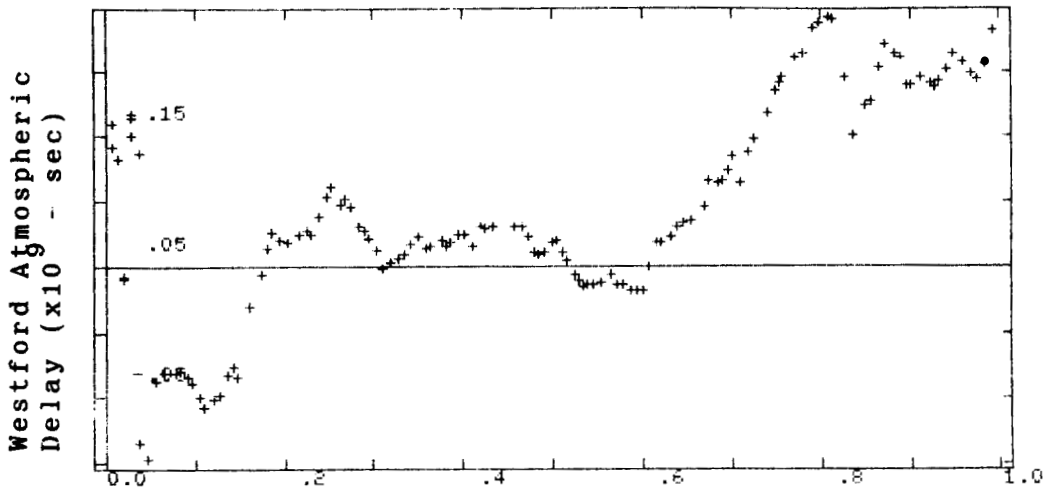

Fig. 25a.

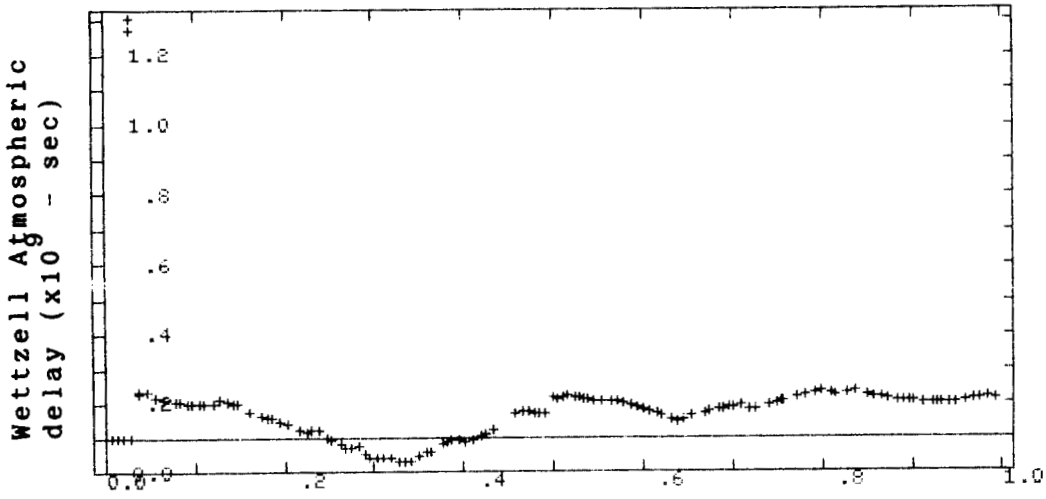

Fig. 25b.

Figure 25. Kalman smoothed atmospheric delay adjustments for (a) Westford, Mass. (b) Wettzell, Germany.

in the VLBI group delay data, and should produce slightly more accurate estimates than the filter.

A comparison is now presented of wet zenith path delay as determined by Water Vapor Radiometer (Figure 26) and Kalman smoothed wet zenith path delay (Figure 27) as estimated using VLBI group delay data. The comparison is intended to be more for instructional purposes than for strict quantitative use. The data set used in the example is $85DEC10X, version 6, with observing antennas at Westford, Wettzell and Onsala. Since the Kalman filter/smoother was not tuned for use with the Onsala station, covariance levels were set to values which seemed to be reasonable, and residuals were examined to make sure they fit well.

In Figure 26 one can see that the WVR data density is quite high, with a gap during the middle of the run, while the data density is less for the Kalman filtered/smoothed zenith delay results. Nevertheless, it is apparent that the WVR and Kalman smoother zenith delays are roughly comparable in form and amplitude. There is a bias of approximately 2.0 centimeters delay between the WVR and Kalman smoother results which is probably due to the method by which the Water Vapor Radiometer measurements (i.e. brightness temperatures) are converted to wet vapor zenith delays. However, some of the bias could be due to somewhat approximate filter tuning.

The Kalman smoother estimates do not have a gap near the middle of the experiment as do the WVR results, which

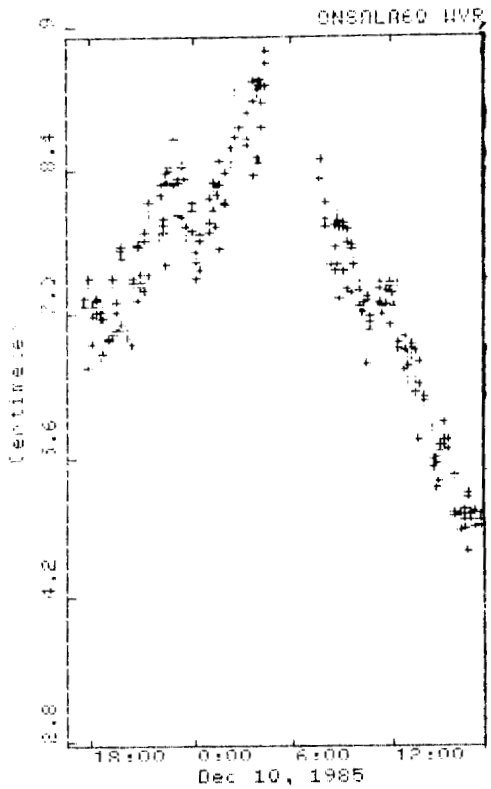

Figure 26. Water Vapor Radiometer (WVR) wet atmosphere path length as a function of time (at Onsala, Sweden; 10 Dec, 1985); (Courtesy of Goran Lundqvist).

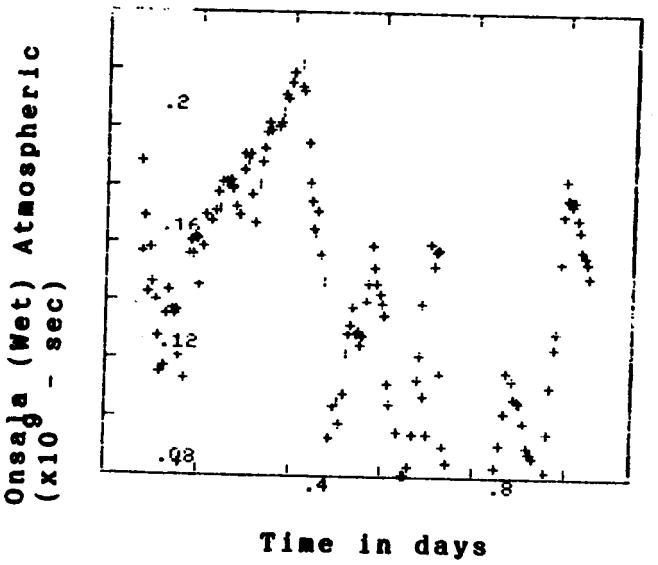

Figure 27. Kalman smoothed wet atmospheric path delay adjustments (Onsala, Sweden - 10 Dec, 1985) as a function of time.

suggests that Kalman smoother wet zenith delays can be available at times when WVR observations may not be. Also one may observe that the smoother and WVR plots "track" one another quite well during the initial half of the VLBI data-taking session, while the match is not so good during the second half of the run. This can easily be explained by the fact that in the filter/smoother, the wet zenith delay is modelled to be deterministically constant as a function of time (with no wet atmospheric rate model). At the start of the VLBI session, the smoother, even with such a limited model, keeps up with the wet zenith delay slope until this slope changes. At this point the filter/smoother has to deal with a change in wet atmospheric delay rate (a zenith delay acceleration!) while it expects the wet zenith delay adjustment to be constant. The result is that the wet zenith delay estimates become poor while the filter/smoother tries to adjust to the new wet zenith delay slope. Still the smoother does produce a descending limb of wet zenith group delays.

The final example in this chapter is included to demonstrate that wet zenith delay adjustments can vary greatly during the single-day period of a VLBI observing session. The results can be viewed in Figures 28, and are from VLBI experiment $86APR06X.version 5. The stations involved in the experiment were at Hatcreek, California; Owen's Valley Radio Observatory (OVRO), California; and Mojave, California. The data are very dense because the

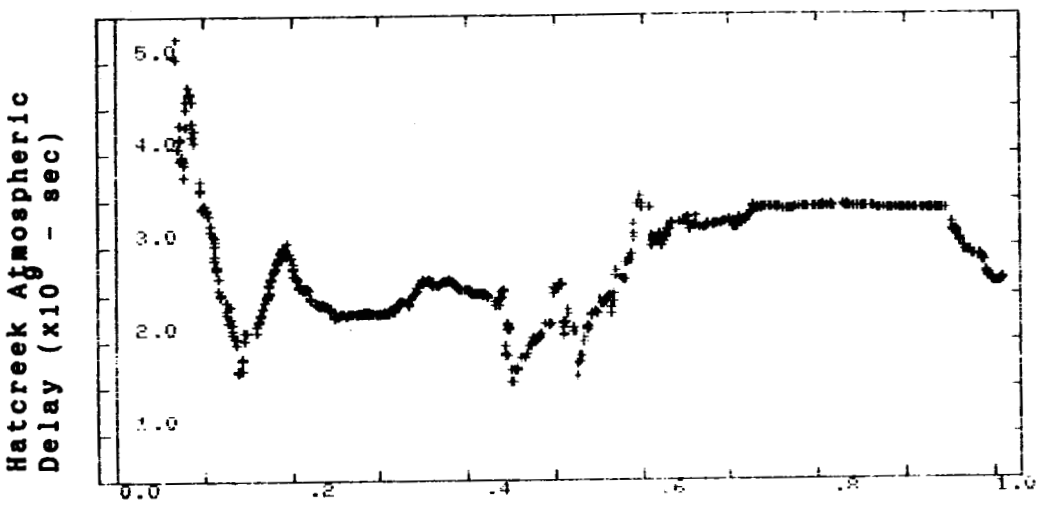

Fig. 28a.

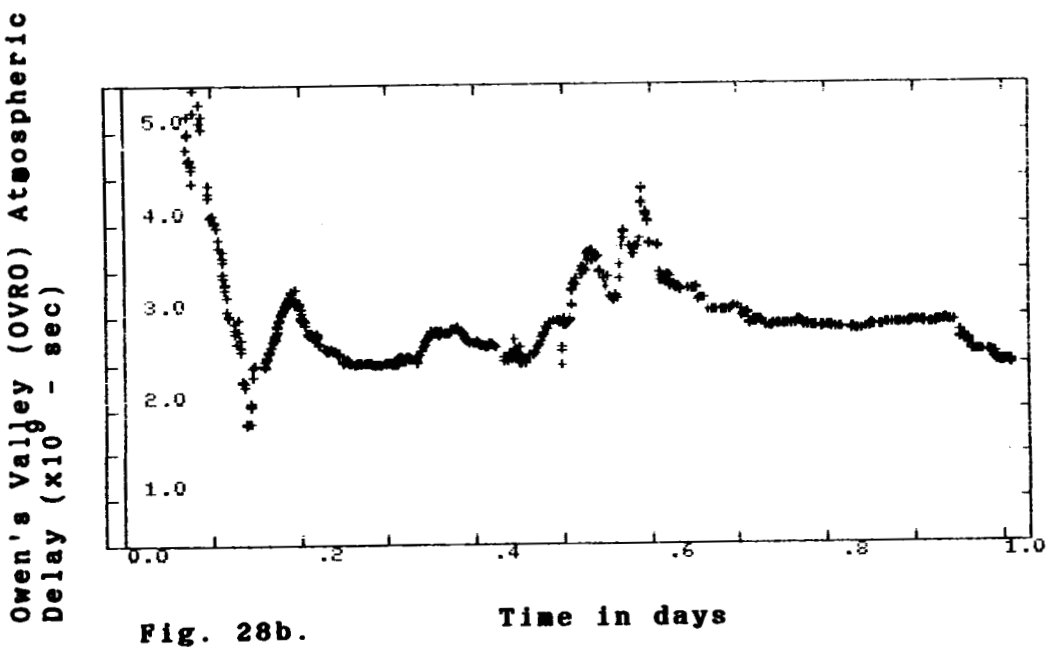

Fig. 28b.

Figure 28. Kalman filtered atmospheric delay adjustments as a function of time for (a) Hatcreek, California (b) Owen's Valley (OVRO), California.

purpose of this experiment was to allow VLBI scientists to use phase delay observations during analysis as opposed to group delays; the former are more precise than the latter but phase delay analysis is more difficult than group delay work.

The OVRO and Hatcreek wet zenith delay estimates from the Kalman filter show some initial recovery from a priori values, then reach a roughly steady state zenith delay, and finally experience a turbulent transition to a second steady state zenith delay which is of larger amplitude than the first delay level. This sequence of events is due to movement of a storm front across California. Some of the wet zenith delay fluctuation observed during the turbulent transition between the (steady state) zenith delay levels is due to use of poor quasar/radio source positions in the solution during this time interval. The wet zenith delay amplitude change during the onset of the storm front is about one nanosecond, which is quite large and should not be ignored for VLBI estimation purposes. The Kalman filter readily includes the change of wet zenith delay as a part of the solution, while current VLBI least squares data analysis usually models the wet zenith delay as being constant over an one-day VLBI experiment.

Chapter IX.

PRINCIPAL RESULTS

This research began with the hope that a large earthquake (magnitude 8.0+) would occur during an IRIS and/or Crustal Dynamics Project VLBI experiment, and thus would allow one to look at the effect of such an earthquake on the earth's polar motion during a single-day IRIS run. Using the Kalman filter one could look at the polar motion estimates as a function of time and thereby examine the influence of an earthquake during the one-day length of data. Some questions to be answered would be: Were there any precursory phenomena to the event?; Is the effect of an earthquake dominated by the main shock?; Is the earthquake signature actually a kink in the polar motion estimates?; and so on.

To the author's chagrin, however, no major earthquake coincided with a 1984-85 VLBI observing session. The largest event occurring during 1984-85 IRIS observing was the Mexican aftershock described earlier; and, as was stated previously, any effect of this earthquake on polar motion was smaller than the polar motion error estimates and (therefore) not significant. It is indeed fortunate only for the purposes of this study that two large earthquakes with moments of about 10^{28} dyne-cm happened at all during

1985. These were the Michoacan, Mexico earthquake of 19 September, 1985 and the event near the coast of central Chile on 3 March, 1985. At the 1986 Spring meeting of the American Geophysical Union, Adam Dziewonski of Harvard University stated that these Chilean and Mexican earthquakes are the first events of moment greater than 1.0 x 10^{28} dyne-cm since 1977.

Since these large events are available for further study, and such events are few and far between, this work has been relegated to determining if the major Mexican and Chilean earthquakes have had any effect on polar motion using the available IRIS data with five-day sampling interval. For both the Mexican and Chilean events, ten IRIS data sets surrounding each shock (see Table 3) were Kalman filtered to determine the polar motion components on each of the ten dates.

The filtering method applied was the iterative approach highlighted in the previous chapter. The use of ten IRIS data sets gives a forty-five day window around each event, and allows an individual scientist the chance to process the data by himself -- the analysis of more data might take too much time, and such heroics are left to the national VLBI analysis teams. The forty-five day time window might allow one to see breaks in polar motion as Mansinha and Smylie (1970) observed, especially since they found that breaks in polar motion typically occurred within ±20 days of an earthquake. But, one should be forewarned that the

Table Three- Data Sets Analyzed Using Kalman Filter

Mexico data interval

Data set	Version
$85AUG26XI	8
$85AUG31XI	8
$85SEP05XI	11
$85SEP10XI	11
$85SEP15XI	8
$85SEP20XI	11
$85SEP25XI	10
$85SEP30XI	11
$85OCT05XI	11
$85OCT10XI	11

Chile data interval

Data set	Version
$85FEB07XB	13
$85FEB12XI	14
$85FEB17XI	11
$85FEB22XI	11
$85FEB27XI	11
$85MAR04XI	11
$85MAR14XI	12
$85MAR19XI	11
$85MAR24XI	11
$85MAR29XI	11

Mexican and Chilean earthquakes of this effort are somewhat smaller than the Alaskan and Chilean earthquakes which took place between 1957.0 and 1968.0, the data interval which Mansinha and Smylie examined. More complete studies of IRIS data should be done in the future when more data are available to test further the hypothesis that large earthquakes signicantly drive the Chandler wobble.

The data sets processed in this study are listed in Table Three. For the Mexico results, 3714 group delay observations were filtered, while 3501 group delays were processed for the Chilean event. No smoothing of the results was done. The outcome of filtering each data set is the adjustment in both polar motion components at the ending epoch of each run. These adjustments are made with respect to BIH reference values.

The Kalman filter (polar motion) adjustments are displayed in Figures 29 through 32. These adjustments are compared with VLBI polar motion adjustment values as produced by least squares analysis. The least squares values were taken from a BIH--VLBI selection option of the SOLVE analysis program from which one can choose either BIH or VLBI polar motion results as reference values for further data analysis. The BIH reference was chosen for the work completed here and is given as the zero amplitude (adjustment) horizontal axis on Figures 29 through 32.

It is apparent from perusal of Figures 29 through 32 that the least squares and Kalman filtered adjustments

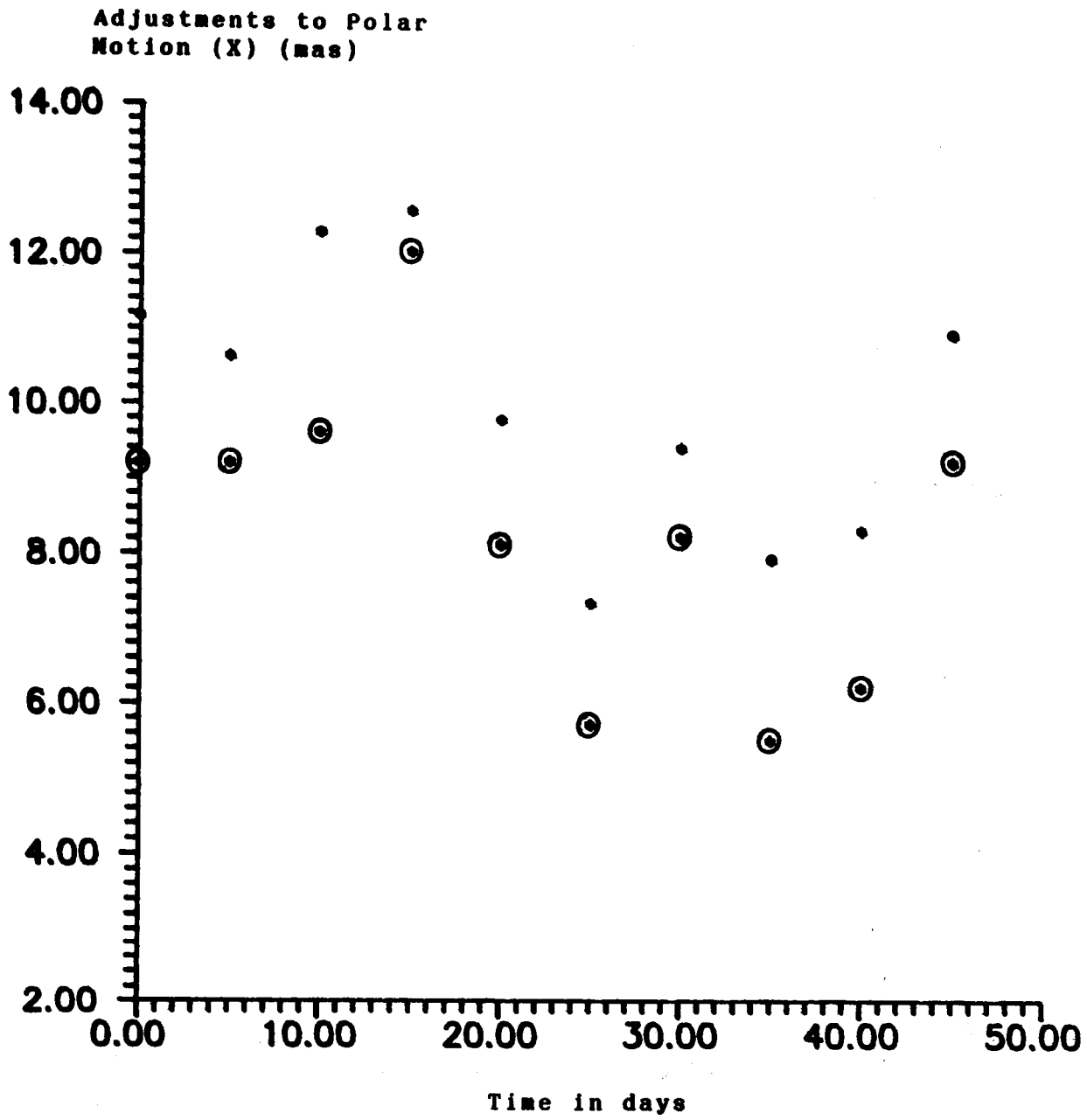

Figure 29. Polar motion (X-component) adjustments (Kalman filtered and least squares estimates) as a function of time. Time interval surrounds epoch of the 1985 great Mexican earthquake. The Kalman filter and least squares adjustments track one another with a slight bias. BIH estimates are at a level of zero mas on this graph. LSQ values circled.

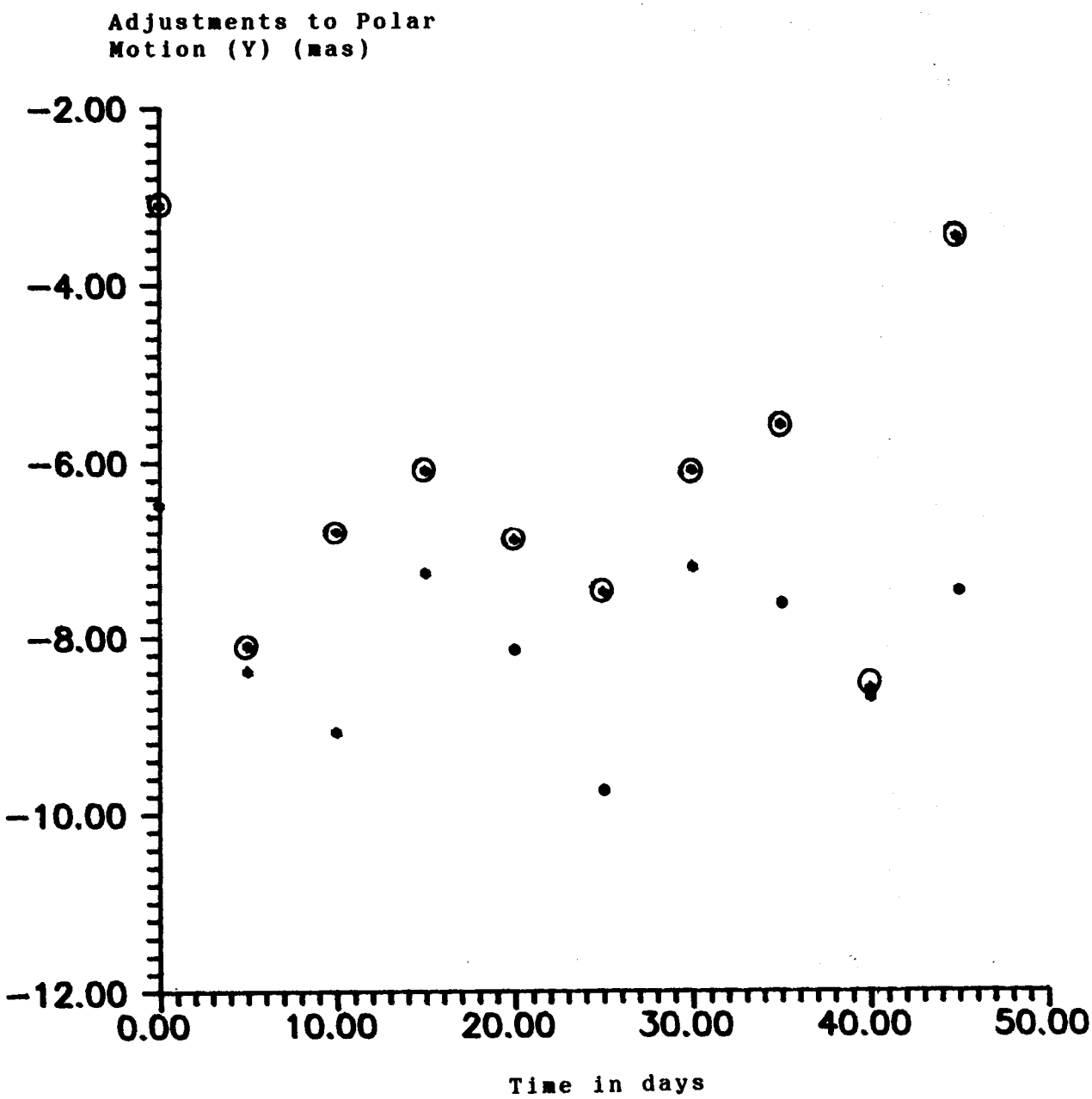

Figure 30. Polar motion (Y-component) adjustments (Kalman filtered and least squares estimates) as a function of time. Time interval surrounds epoch of the 1985 great Mexican earthquake.

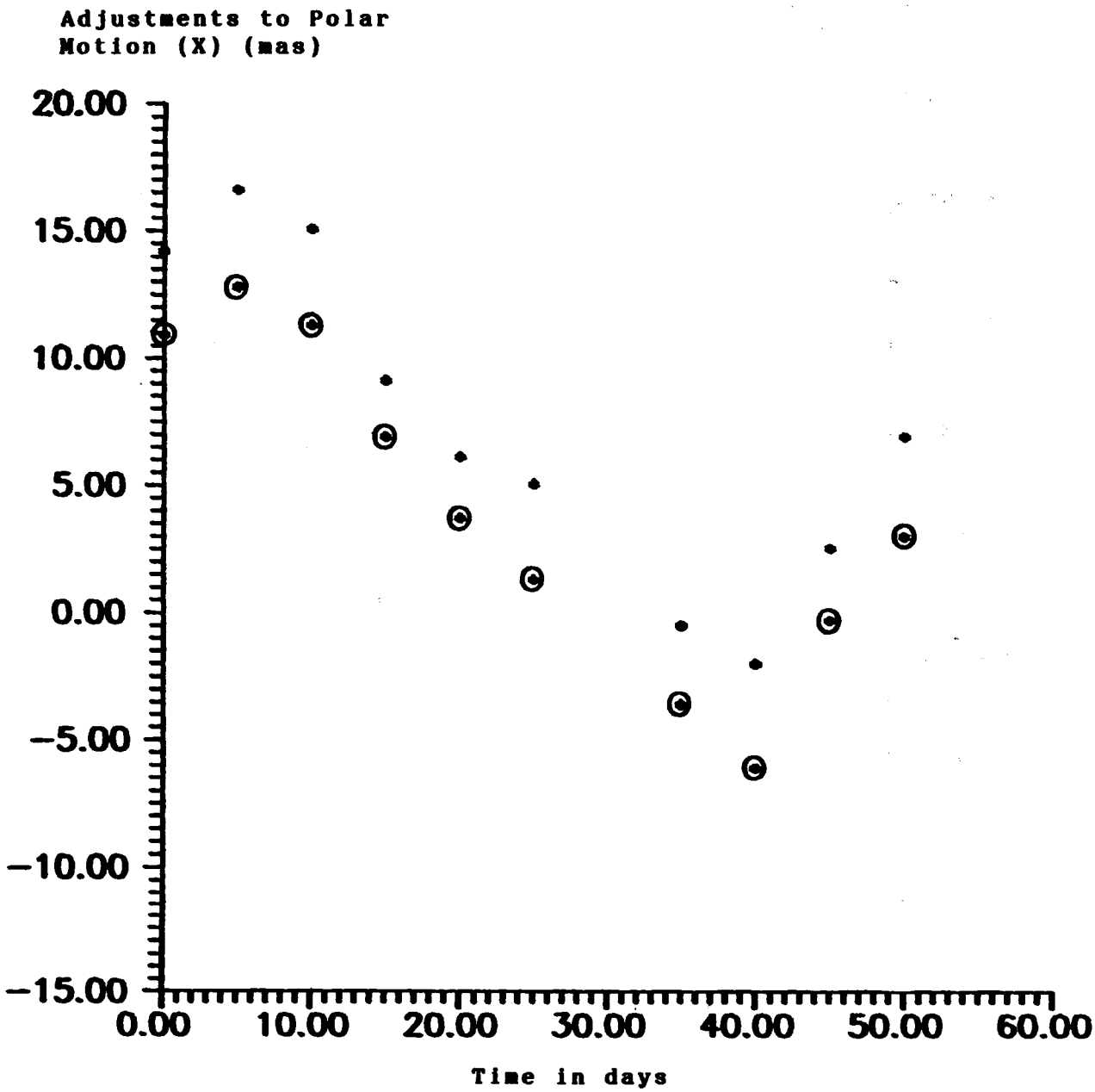

Figure 31. Polar motion (X-component) adjustments (Kalman filtered and least squares estimates) as a function of time. Time interval surrounds epoch of the 1985 great Chilean earthquake.

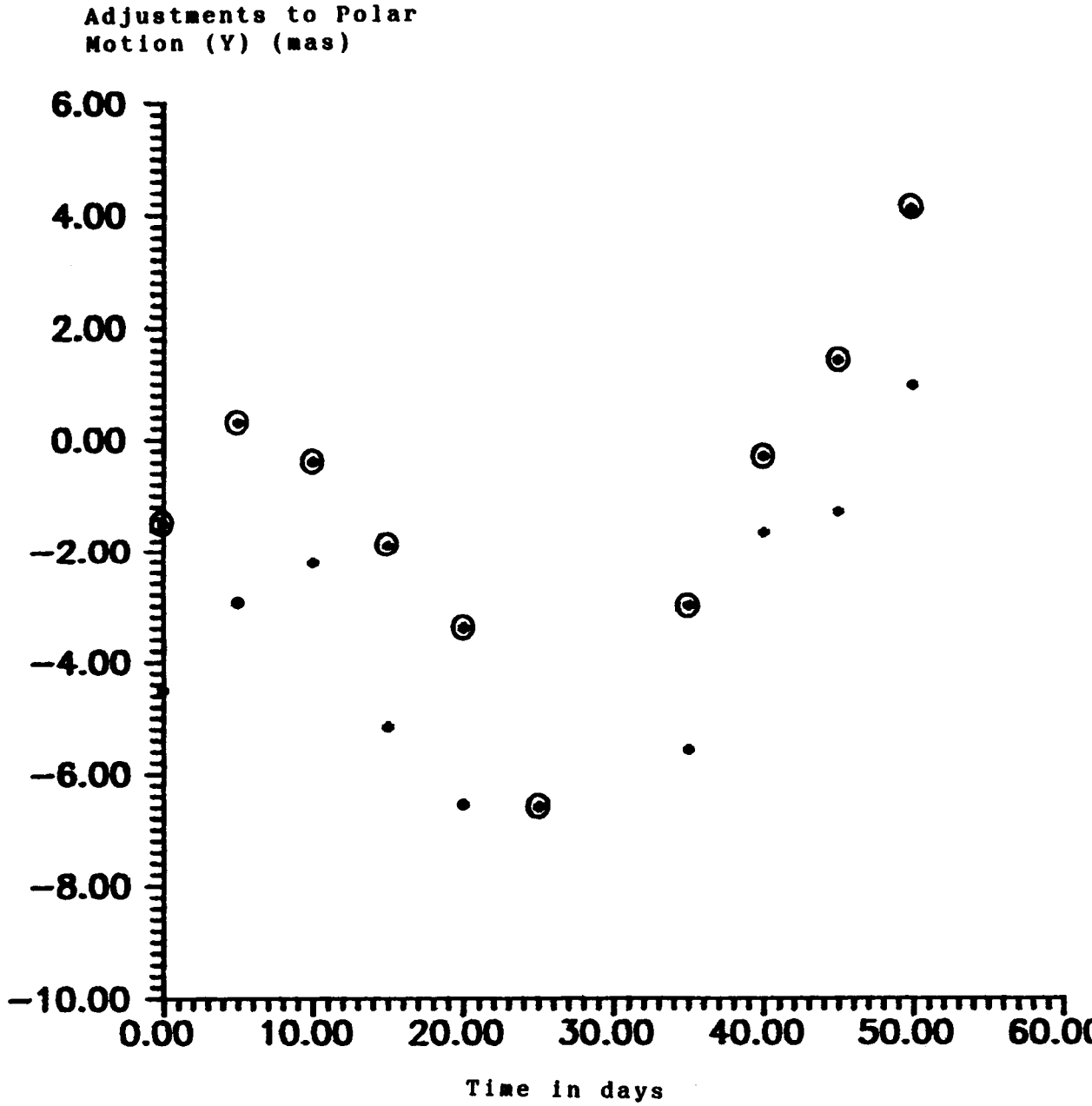

Figure 32. Polar motion (Y-component) adjustments (Kalman filtered and least squares estimates) as a function of time. Time interval surrounds epoch of the 1985 great Chilean earthquake.

track one another quite closely on the plot, as might be expected since they come from the same data sets; only the data analysis differs. Biases between the least squares and Kalman filtered estimates are also evident. In addition, considerable offsets of more than several milliarcseconds can be observed between the VLBI polar motion adjustments and the BIH reference values. Such offsets are expected since the BIH incorporates data from techniques other than VLBI, as well as VLBI, in forming their polar motion estimates. If error bars were indicated with the VLBI estimates, they would be of approximate amplitudes of one milliarcsecond. The error bars are not placed on the figures to facilitate comparison of the adjustments.

Part of the bias between the Kalman filtered and least squares polar motion estimates arises because the Kalman filtered estimates are from the end epoch of the IRIS run, whereas the least squares estimates are for the epoch 0:00 UTC contained in the IRIS run which is usually about eighteen hours earlier. Thus in Figures 29 through 32, polar motion estimates at (slightly) temporally offset epochs are being compared, thereby introducing uncertainty into the intercomparison. The uncertainty could be as much as 4 mas (Dickman, 1987). The comparison is only intended to demonstrate that the Kalman filtered polar motion estimates are reliable as was indicated by the tracking of least squares and Kalman filtered results. The remainder of the bias could be attributed to the fact that nutation adjust-

ments were not made in the least squares analysis or that the Kalman filter is not perfectly tuned. Some of the tuning deficiency may be due to the fact that the VLBI measurement errors are usually larger than the theoretical formal errors. Differences in the way wet atmospheric zenith delays are treated in the two analysis techniques may also contribute to the biases. The average biases in the x and y components of polar motion for the Mexican earthquake results are 1.7 ± 0.6 marcsec and 1.8 ± 1.2 marcsec respectively, and 3.3 ± 0.6 marcsec and 2.4 ± 1.1 marcsec respectively around the time of the Chilean event.

The ultimate results of this dissertation are presented in Figures 33 and 34. Two figures are the climax of this extensive effort? This limited outcome might remind one of high energy physics research in which several years of work are required to set up an experiment which is run in only several weeks or months. In Figure 33 the Kalman filtered polar motion adjustments are added to BIH a priori polar motion values (see equation III.19) to produce the total polar motion estimates in x and y. The total polar motion component estimates are plotted versus one another in the figures. Annual wobble or the secular trend of polar motion have not been removed from these estimates.

Figure 33 depicts a polar motion curve around the time of the Michoacan, Mexican event. The curve is quite circular in general. Straight line segments have been drawn between the polar motion estimate points. The polar

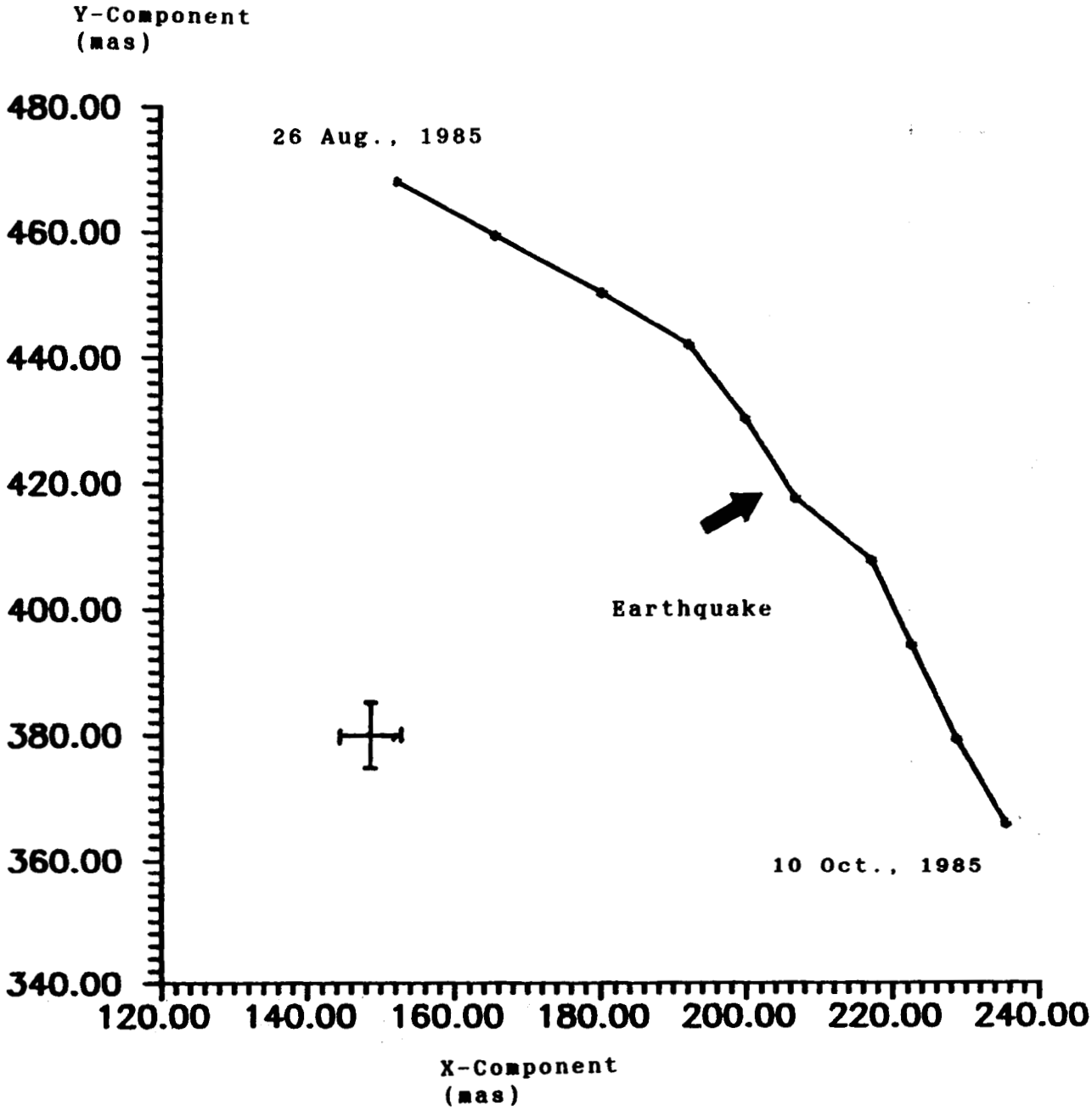

Figure 33. Polar motion (X and Y components) estimates as output by Kalman filter. Estimation interval surrounds epoch of the 1985 great Mexican earthquake. The arrow indicates the time of the main event. Polar motion formal errors are about one mas. Large error bars drawn on graph indicate approximate error level when Mansinha and Smylie (1970- BIH data) studies took place.

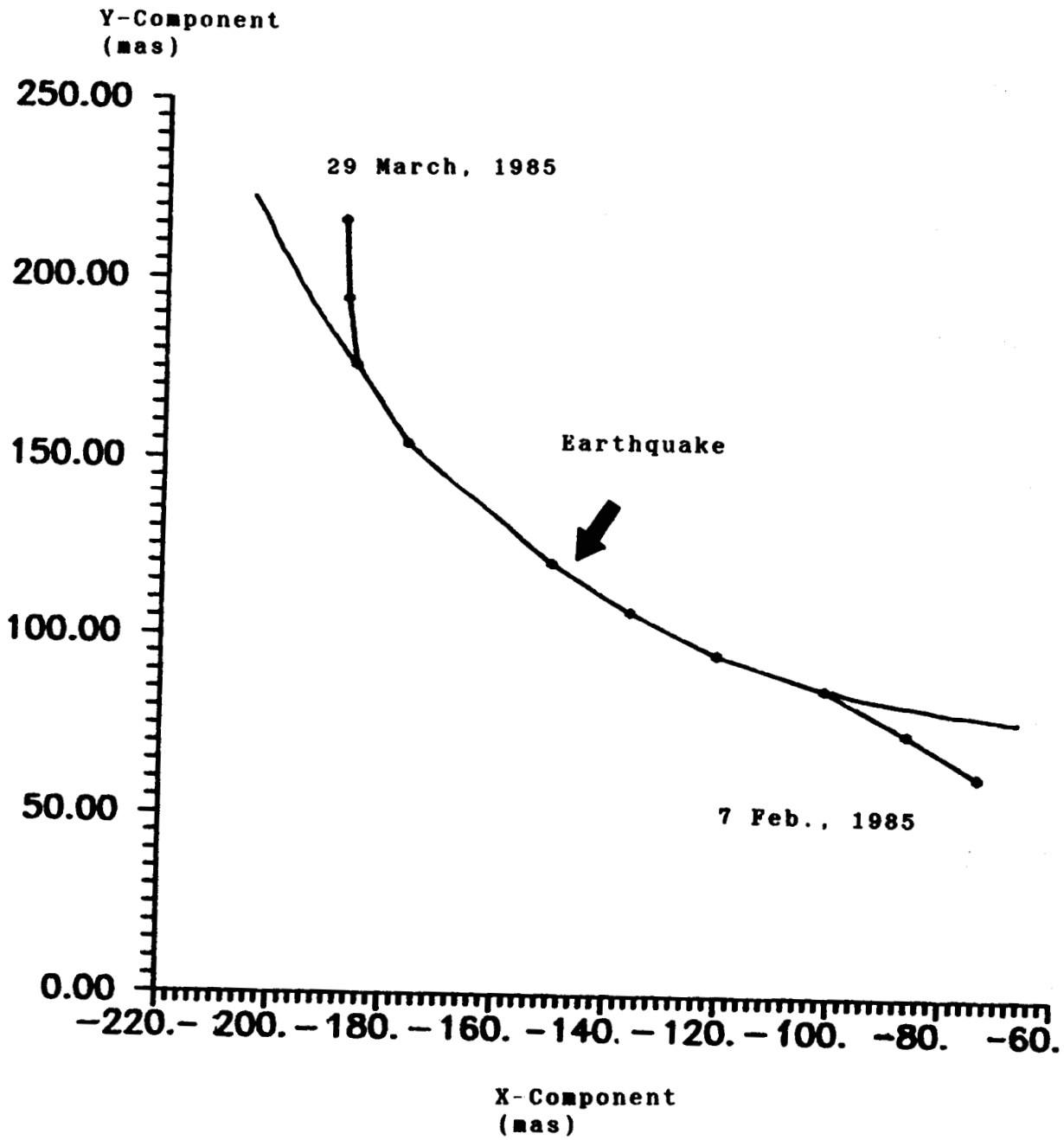

Figure 34. Polar motion (X and Y components) estimates as produced by Kalman filter. Estimate interval surrounds epoch of the 1985 great Chilean earthquake. The arrow indicates the time of the main event. Polar motion formal errors are about one mas.

motion errors in x and y are typically 1 mas. Experiment dates are indicated at the end points of the curve, and an arrow indicates the approximate time of the great Mexican earthquake of 1985. A large pair of error bars of amplitude 10 marcsec by 10 marcsec are drawn on the plot to illustrate the approximate noise level which was prevalent in the (BIH) data Mansinha and Smylie (1970) worked with.

The most striking feature of Figure 33 is the kink in the polar motion curve which is sharply coincident with the time of the 1985 Michoacan, Mexico earthquake. The kink appears to be real and is of amplitude greater than the one-sigma errors (≈1 mas), although it is only a little larger in size than corresponding three-sigma errors (≈3 mas). The time correlation between the main event and kink in polar motion is impressive. One does not even require the curve fitting procedure of Mansinha and Smylie (1970) to see that it exists.

The kink in the polar motion curve of Figure 33 begins prior to the 1985 Mexican event and continues until after the earthquake. This would lead one to believe that large mass movements occur before, during and after the main shock and are responsible for the kink in the polar motion curve and change in polar motion path. One could find the amplitude of the pole shift by a curve fitting procedure. It is doubtful that the observed kink in polar motion is due to the elastic event alone.

The polar motion curve of Figure 34 illustrates the

time period surrounding the 1985 Chilean earthquake. There were a large number of foreshocks and aftershocks associated with the main event, many of which occurred in swarms. The curve of Figure 34 is fairly smooth with no kink evident at the approximate time of the main event (indicated with an arrow). There is no polar motion datum on 9 March 1985, and this hinders the ability to resolve a kink in the curve during the earthquake. It should be pointed out that the Chilean earthquake was of magnitude 7.8 as compared with 8.1 for the Michoacan, Mexico event, and this may be one reason to believe that it is easier to observe a kink in the polar motion at the time of the Mexican event.

One might notice that the ends of the curve in Figure 34 deviate from a true circular (or elliptical) path. This has been emphasized on the plot by adding an approximate path (fit by eye to the interior data) at the ends of the curve. The actual polar motion path begins to diverge from circular form at times of about ±15 days from the Chilean main shock. These deviations may be manifestations of the effect of the Chilean earthquake sequence (and associated mass movements) on polar motion (i.e. kinks in the path). That the breaks occur within ±15 days of the Chilean main shock casts a favorable light on the conclusions of Mansinha and Smylie (1970), for most of their polar motion breaks were within ±20 days of a large earthquake. The author has noticed that the times of the Chilean kinks coincide fairly

well with the epochs at which earthquake swarms (affiliated with the main event) begin to occur and subside (Preliminary Determination of Epicenters, U.S.G.S., February-March, 1985).

IRIS polar motion estimates (source: IRIS Earth Orientation Bulletin A, No. 29, July, 1986) over the intervals of the 1985 Chilean and Mexican earthquakes are displayed in Figures 35 and 36 for comparison with Figures 33 and 34 (Kalman filter results). Aside from small biases, the polar motion path in Figure 36 closely matches that of Figure 34. Figures 33 and 35 are also quite similar in shape except at the endpoints of 26 August, 1985 and 10 October, 1985. A quick look at Figure 30 of the VLBI y-component adjustments will confirm that the end point least squares estimates are quite different from the rest of the Kalman filtered and least squares adjustments. This suggests that these (least squares) end point values should be questioned, since the rest of the group of adjustments are maintaining a relatively constant bias with respect to BIH reference values. In any event, Figure 33 appears to bring out the existence of a kink in the polar motion curve which is not so certain in Figure 35.

The (Kalman filtered) polar motion results of Figures 33 and 34 are deconvolution filtered using the method applied by Gross and Chao (1985; see also Backus and Gilbert, 1970) to LAGEOS polar motion estimates. Deconvolving the VLBI data in this manner produces excitation functions, $\psi(t)$, in which one should be able to directly observe shifts in

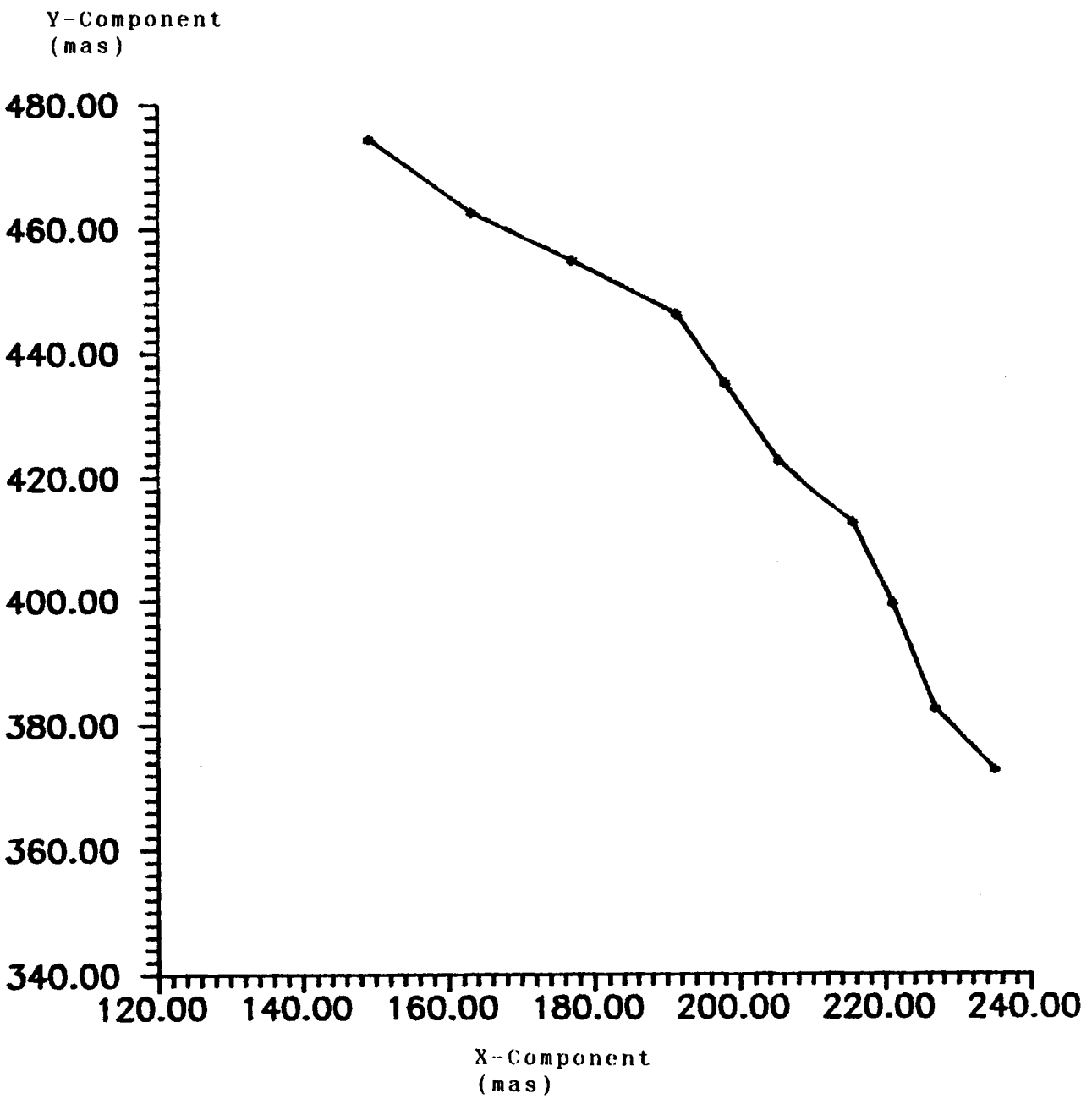

Figure 35. Polar motion (X and Y components) estimates as produced by IRIS. Estimate interval surrounds epoch of the 1985 great Mexican earthquake.

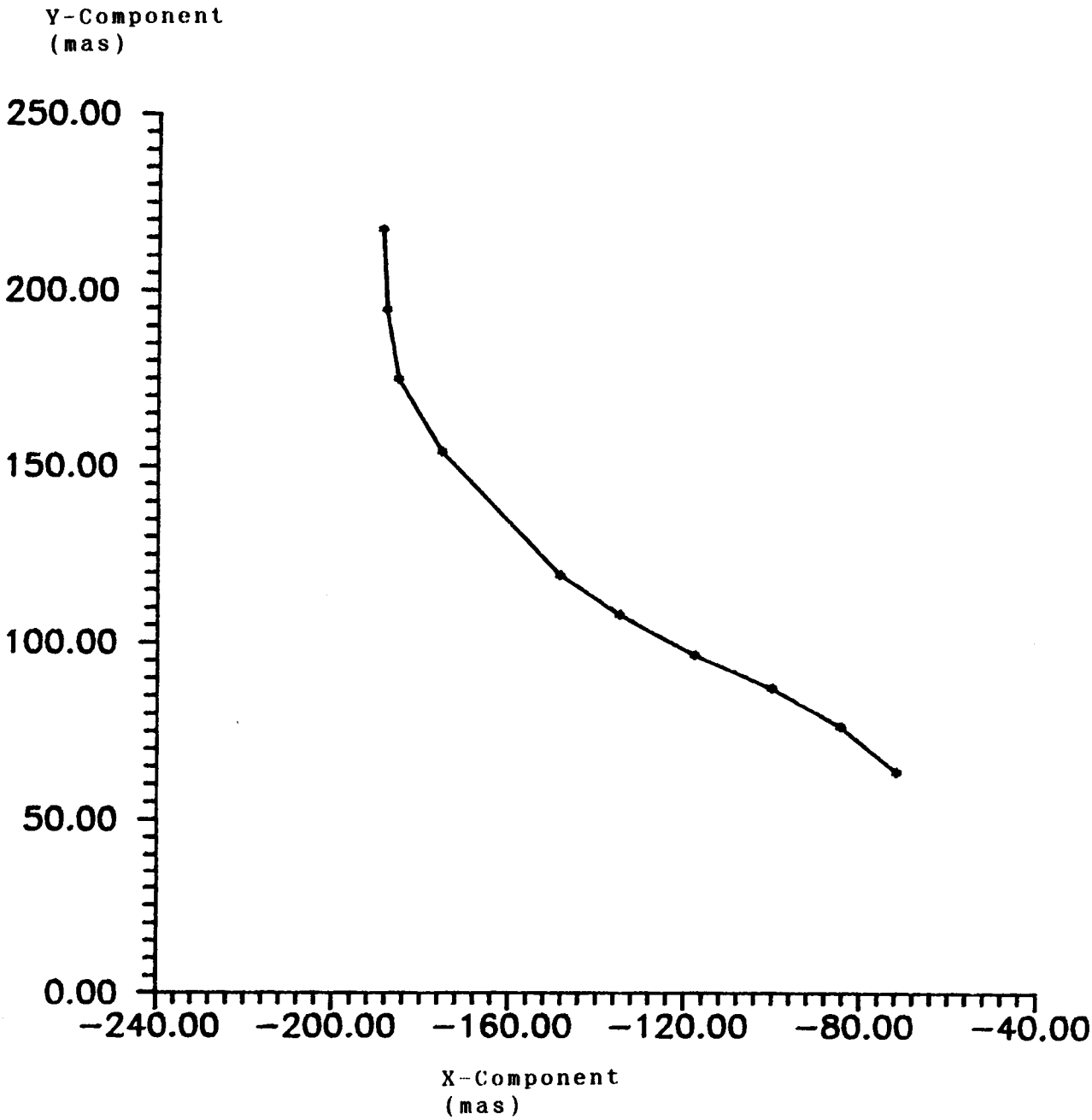

Figure 36. Polar motion (X and Y components) estimates as produced by IRIS. Estimation interval surrounds epoch of the 1985 great Chilean earthquake.

the position of the pole about which polar motion takes place. IT IS STRESSED HERE that the excitation results presented subsequently include polar motion data for the first ten or eleven data points in each time series analyzed; the remaining points in each excitation series are zero padding (i.e. zeroes added to allow fast Fourier transforms to be used in the deconvolution). These points are not based on VLBI data and thus should be ignored in examining the results. They are included here for completeness in data presentation.

Prior to deconvolution, a least squares fit of an offset, trend and sinusoid was made to remove polar motion long term behavior from the optimal estimates, thus leaving data which only bears the effects of earthquake or other short time excitation. A single sinusoid was used to represent the superposed annual wobble and Chandler wobble paths because the data being fit is of short duration. The fits obtained using an offset, trend and a sinusoid for each of the wobble components were as good as those obtained using an offset, trend and two sinusoids.

The deconvolution filter applied to the polar motion data (after fitting and Fourier transformation to the frequency domain) is (Gross and Chao, 1985)

$$V(\omega) = \frac{G^{*}(\omega)}{||G(\omega)||^{2}+(\alpha N)^{2}}, \qquad \text{(IX.1)}$$

where the asterisk indicates complex conjugation, and the

C-3

bars denote the taking of a norm. αN will be discussed shortly. $G(\omega)$ is the earth's transfer function (Gross and Chao, 1985)

$$G(\omega) = \frac{\sigma_0}{\sigma_0 - \omega}, \qquad \text{(IX.2)}$$

where

$$\sigma_0 = (2\pi/T)\ (1 + i/2Q). \qquad \text{(IX.3)}$$

T is the Chandler wobble period, Q is the quality factor of the Chandler wobble and σ_0 is the angular frequency (Gross and Chao, 1985). The Chandler wobble period T was taken as 434 days; Q was taken as 106.

The equation relating the Fourier transformed polar motion $M(\omega)$ and excitation function $\psi(\omega)$ is (Gross and Chao, 1985)

$$M(\omega) = \psi(\omega)G(\omega) + N(\omega) \qquad \text{(IX.4)}$$

According to Gross and Chao (1985) the $N(\omega)$ term represents "... the frequency content of the noise in the measurements of m(t).[polar motion estimates]" If the $N(\omega)$ were missing from IX.4, the equation would relate what is going on in frequency space of a convolution process. To find $\psi(\omega)$ one would simply divide

$$\psi(\omega) = \frac{1}{G(\omega)} M(\omega).$$

and then Fourier transform $\psi(\omega)$ to find $\psi(t)$. In this case, the filter applied to the transformed polar motion data is $1/G(\omega) = G^{*}/||G||^{2}$.

One can observe from equation (IX.1) that the filter actually applied to the transformed polar motion data $M(\omega)$ is somewhat more general. Notice that if αN is set to zero, the general deconvolution filter becomes the simple deconvolution filter. Also if αN becomes very large, $V(\omega)$ approaches zero.

αN is an adjustable parameter which controls how much measurement noise is allowed to remain in the excitation function estimates. For αN small, much noise exists in the excitation functions but temporal resolution is high. For αN large, resolution is lost but the noise level is reduced. The trade-off between noise reduction and achievement of fair resolution can both be reached by choosing some intermediate value for αN in the deconvolution filter. Once the filter has been applied to $M(\omega)$, the results are Fourier transformed to find the excitation functions in time, $\psi(t)$.

The polar motion data of Figures 33 and 34 are handled in the aforementioned manner, and the results are displayed in Figures 37 and 38. The x and y components of excitation, ψ_x and ψ_y, are calculated for the Mexican and Chilean data using αN values of 0.22, 0.5 and 1.0 following the

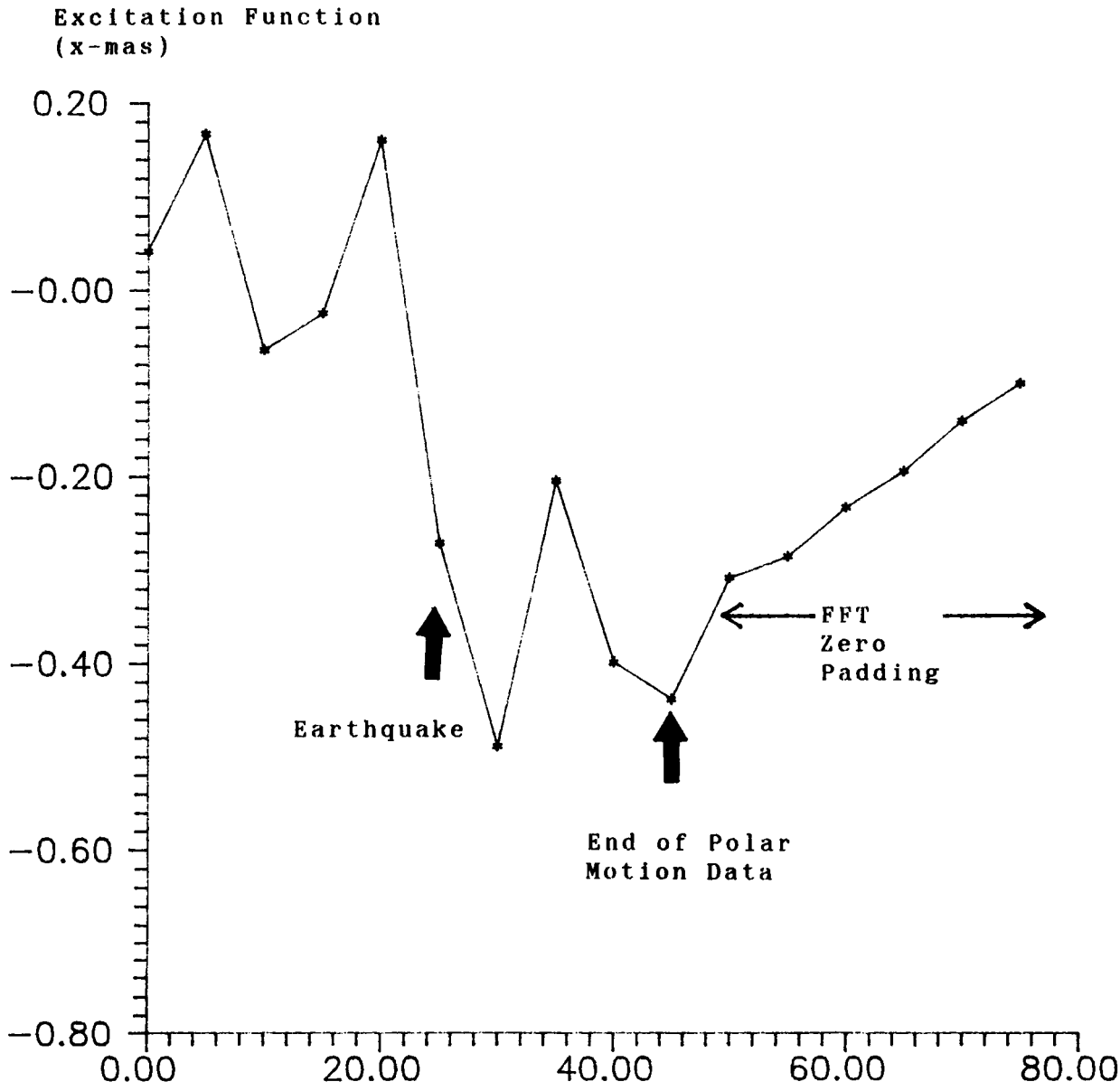

Fig. 37a.

Figure 37. Excitation Function (X-component) versus time. Time interval surrounds epoch of the 1985 great Mexican earthquake. Excitation function errors are about 0.5 mas. (a) $\alpha N = 0.22$ (N is a deconvolution parameter) (b) $\alpha N = 0.5$ (c) $\alpha N = 1.0$. Note changes in scale on the ordinate.

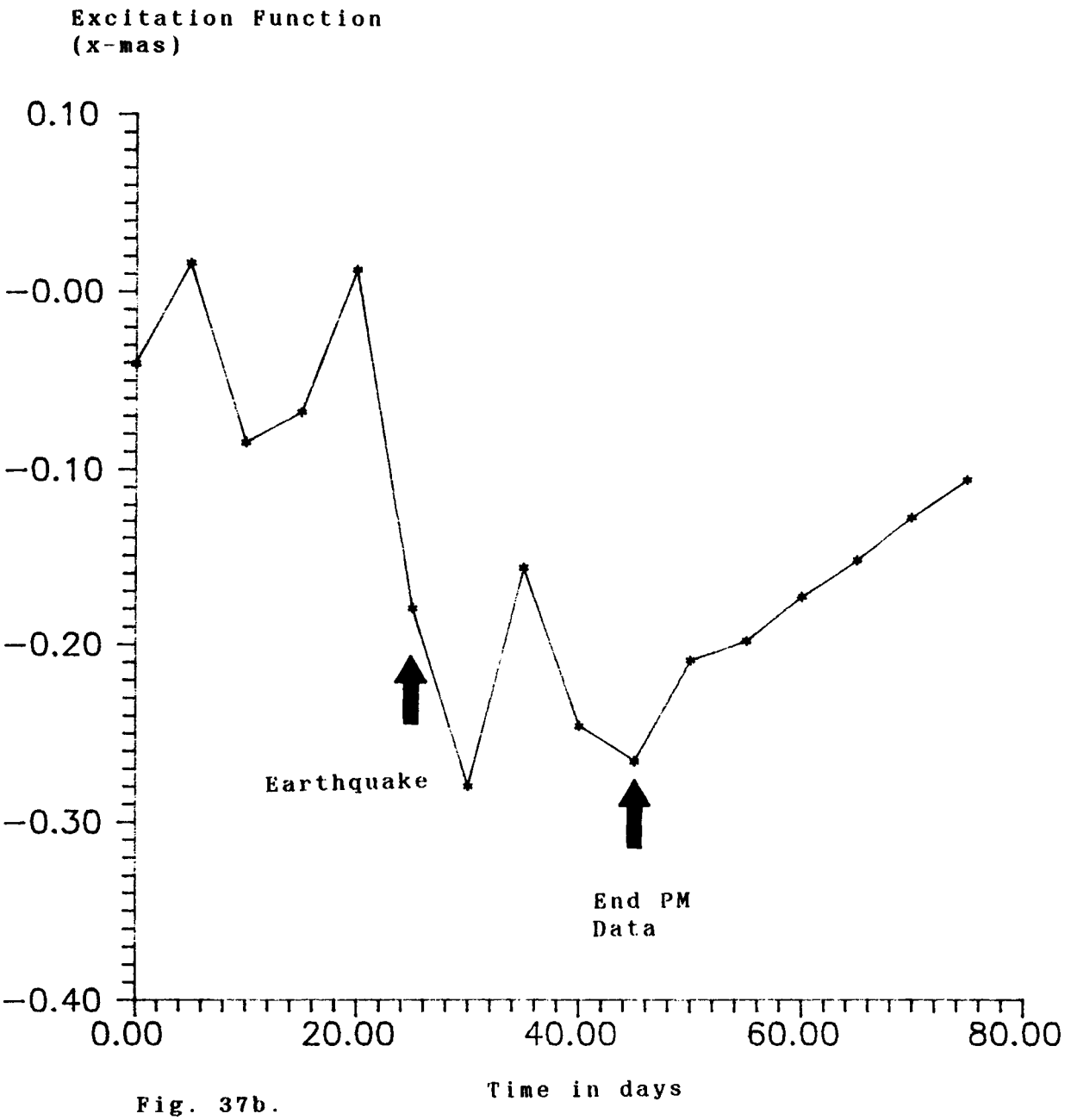
Excitation Function
(x-mas)
0.10
-0.00
-0.10
-0.20
-0.30
-0.40
0.00
20.00
40.00
60.00
80.00
Earthquake
End PM
Data
Time in days

Fig. 37b.

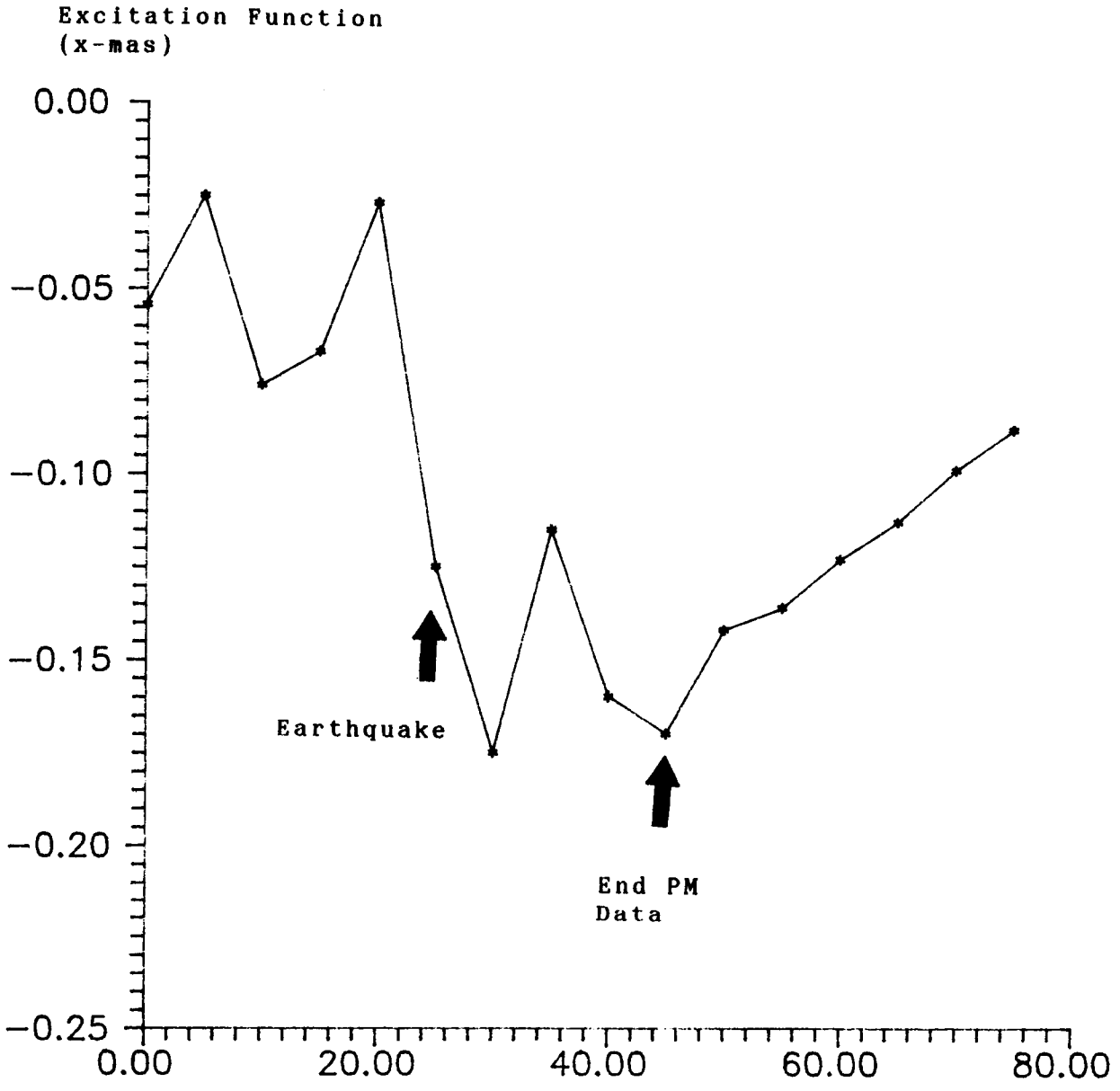
Excitation Function
(x-mas)
0.00
−0.05
−0.10
−0.15
−0.20
−0.25
Earthquake
End PM
Data
0.00
20.00
40.00
60.00
80.00
Time in days

Fig. 37c.

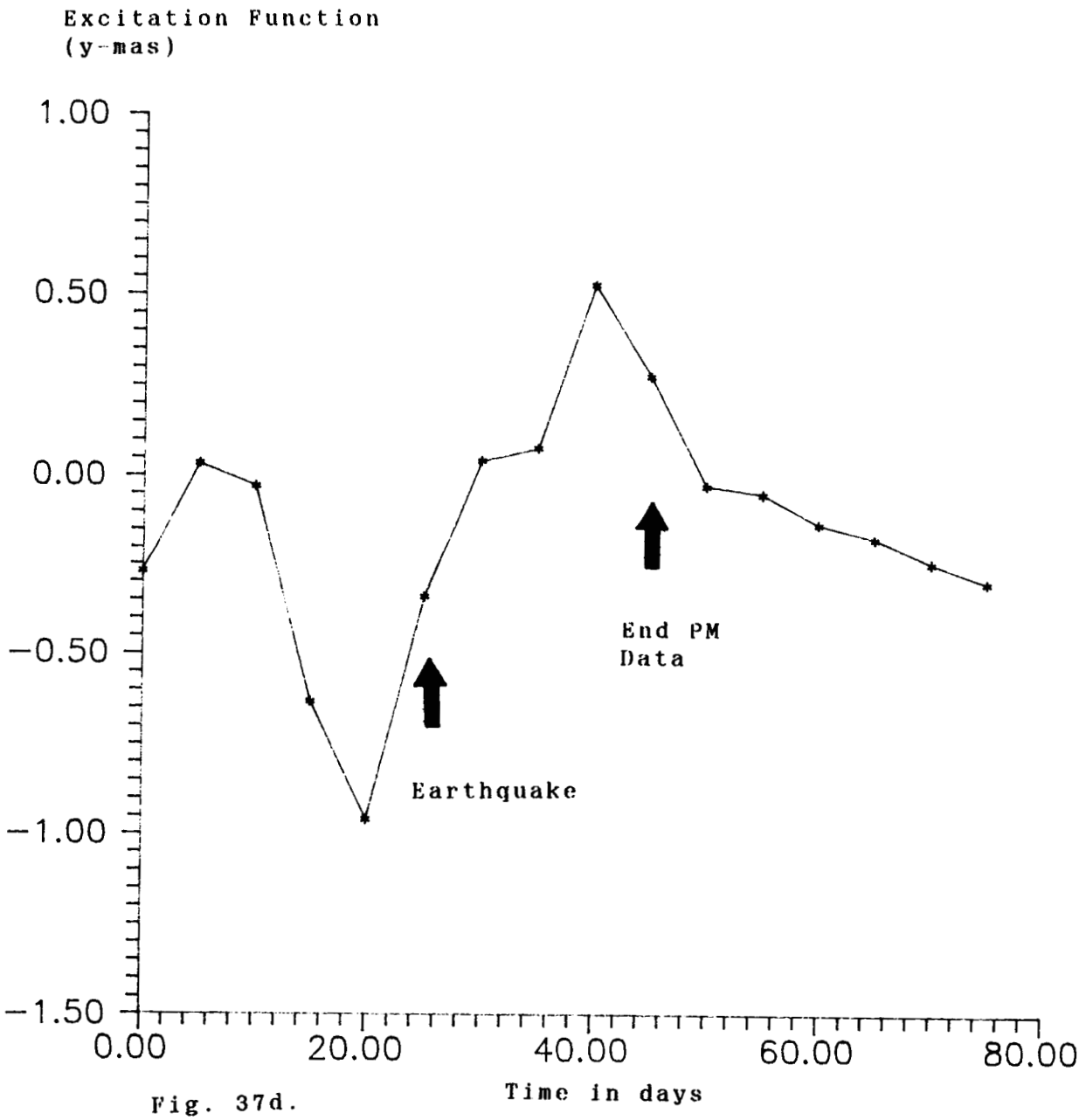

Fig. 37d.

Figure 37. Excitation Function (Y-component) versus time. Time interval surrounds epoch of the 1985 great Mexican earthquake. Excitation function errors are about 0.5 mas. (d) $\alpha N = 0.22$ (e) $\alpha N = 0.5$ (f) $\alpha N = 1.0$.

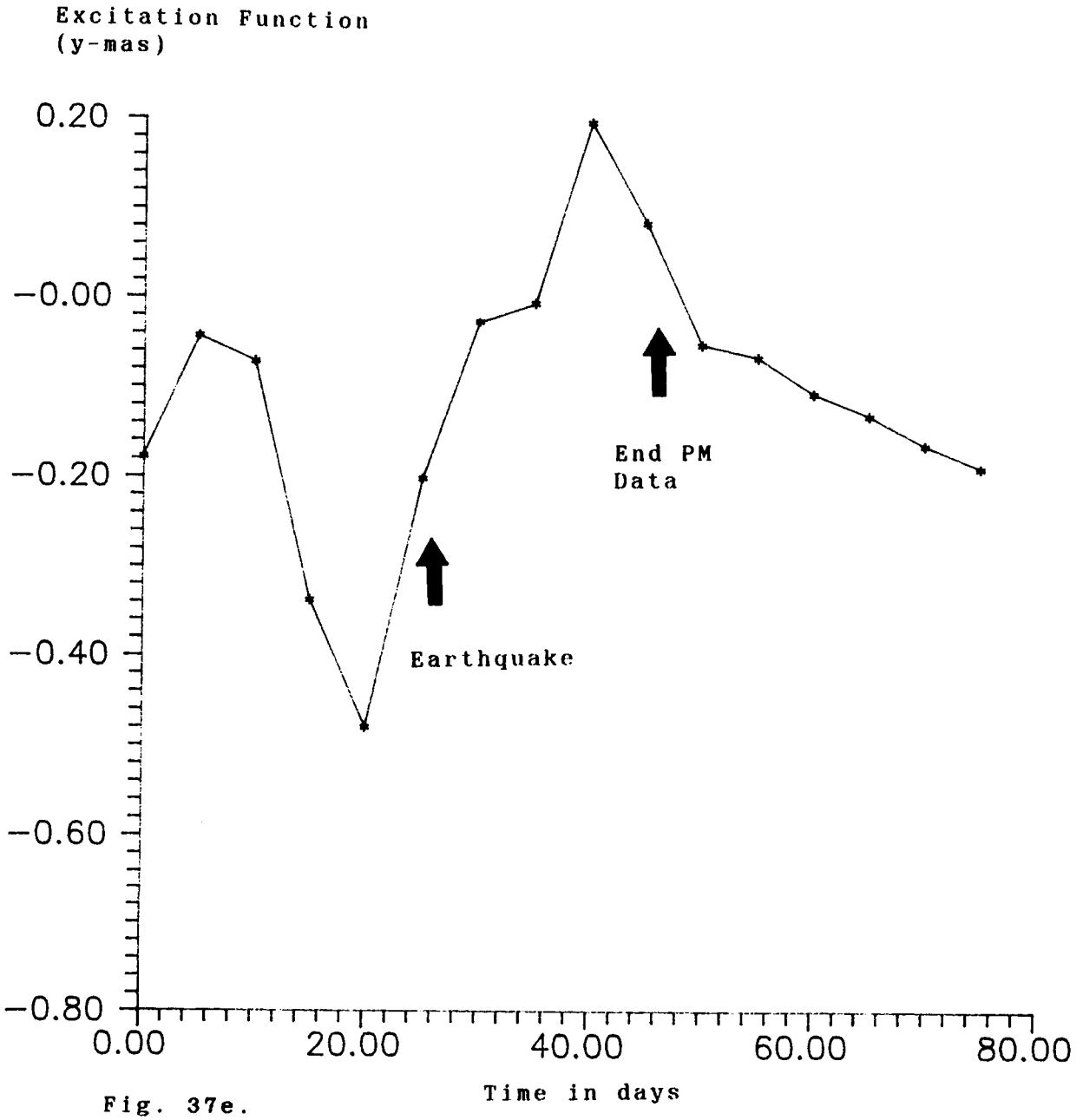
Excitation Function
(y-mas)
0.20
-0.00
-0.20
-0.40
-0.60
-0.80
0.00
20.00
40.00
60.00
80.00
Time in days
End PM
Data
Earthquake

Fig. 37e.

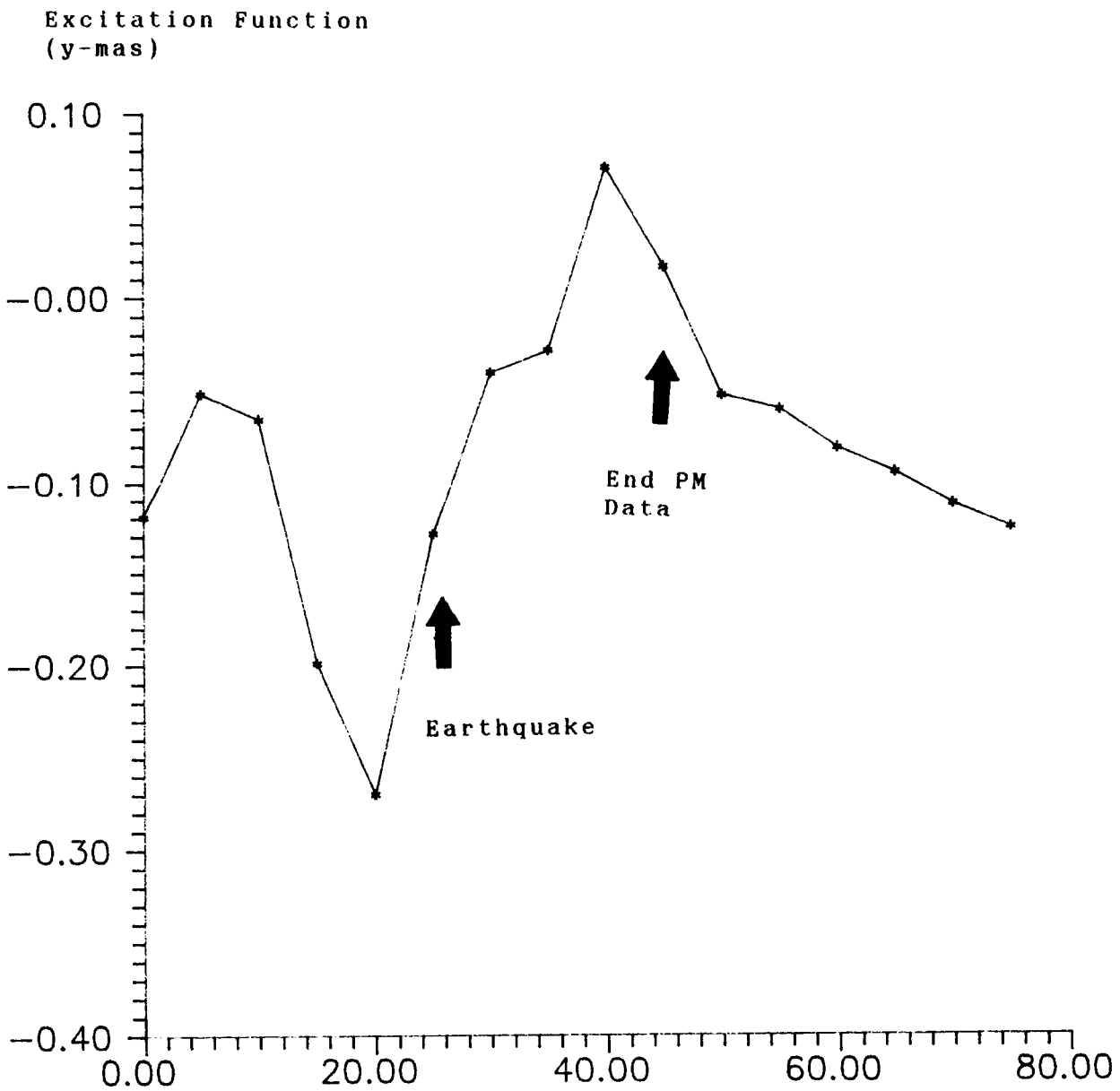
Excitation Function
(y-mas)
0.10
-0.00
-0.10
-0.20
-0.30
-0.40
0.00
20.00
40.00
60.00
80.00
End PM
Data
Earthquake
Time in days

Fig. 37f.

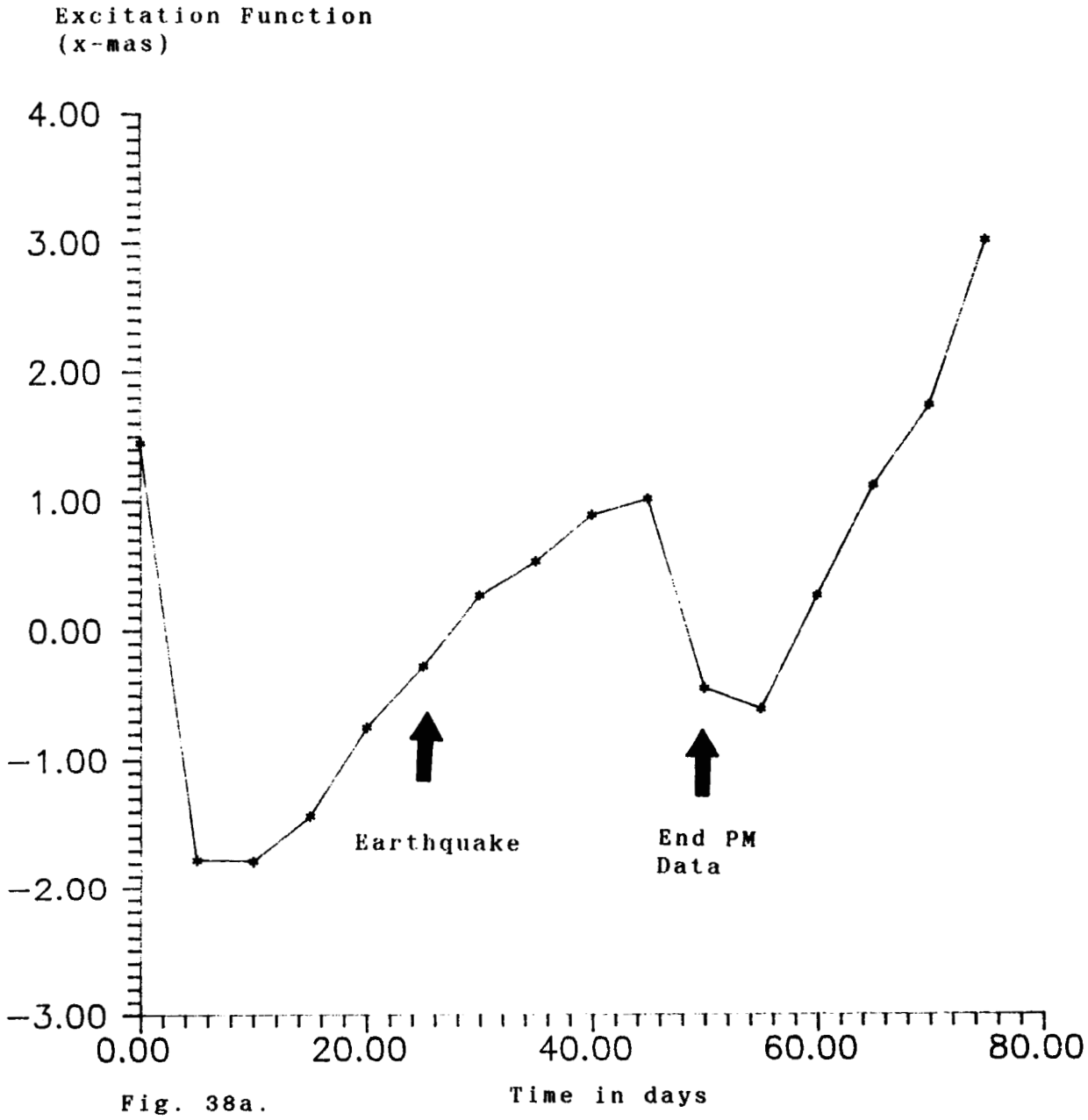

Fig. 38a.

Figure 38. Excitation Function (X-component) versus time. Time interval surrounds epoch of the 1985 great Chilean earthquake. Excitation function errors are about 0.5 mas. (a) $\alpha N = 0.22$ (b) $\alpha N = 0.5$ (this plot has been detrended). (c) $\alpha N = 1.0$.

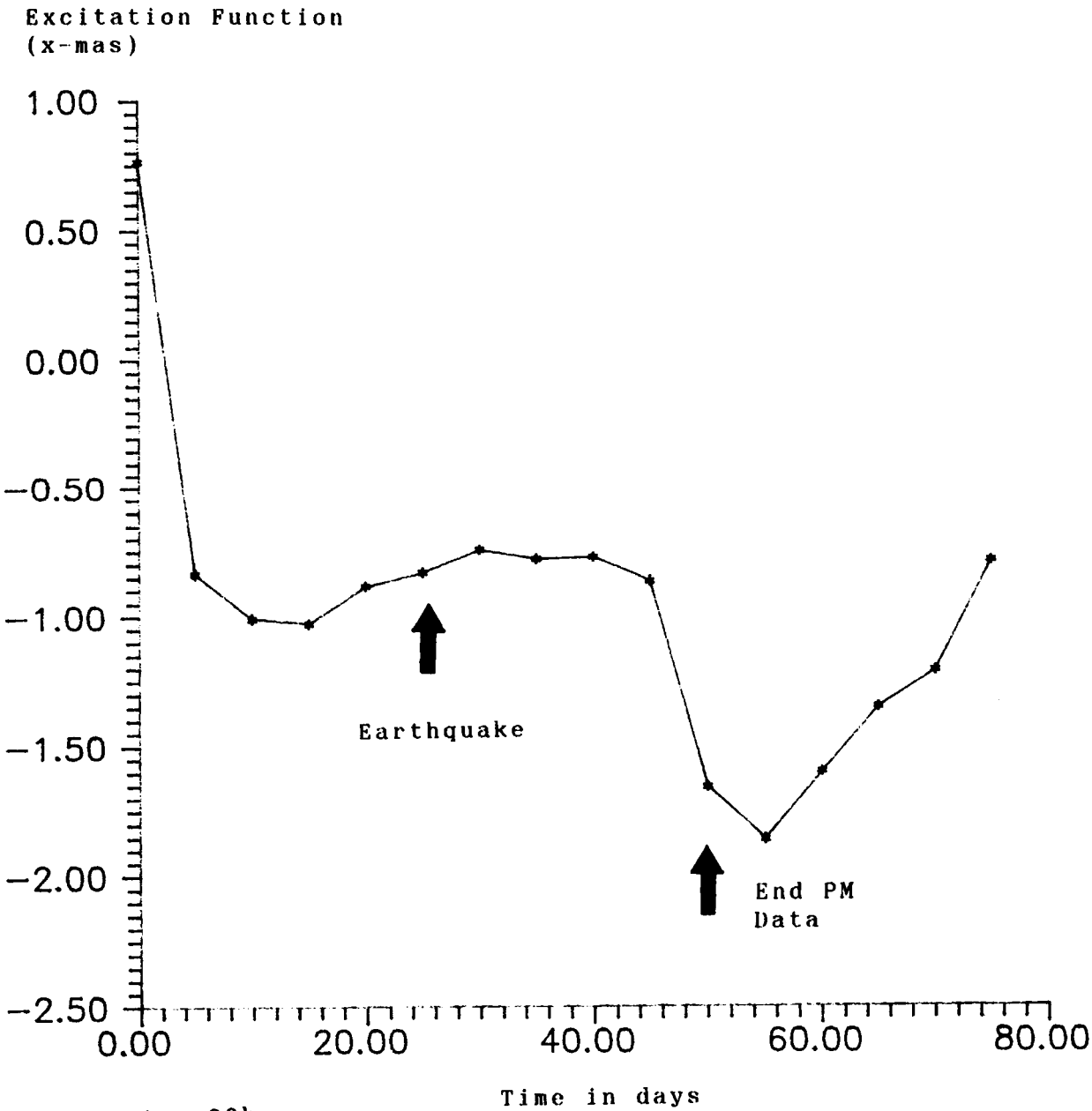
Excitation Function
(x-mas)
1.00
0.50
0.00
−0.50
−1.00
−1.50
−2.00
−2.50
0.00
20.00
40.00
60.00
80.00
Earthquake
End PM
Data
Time in days

Fig. 38b.

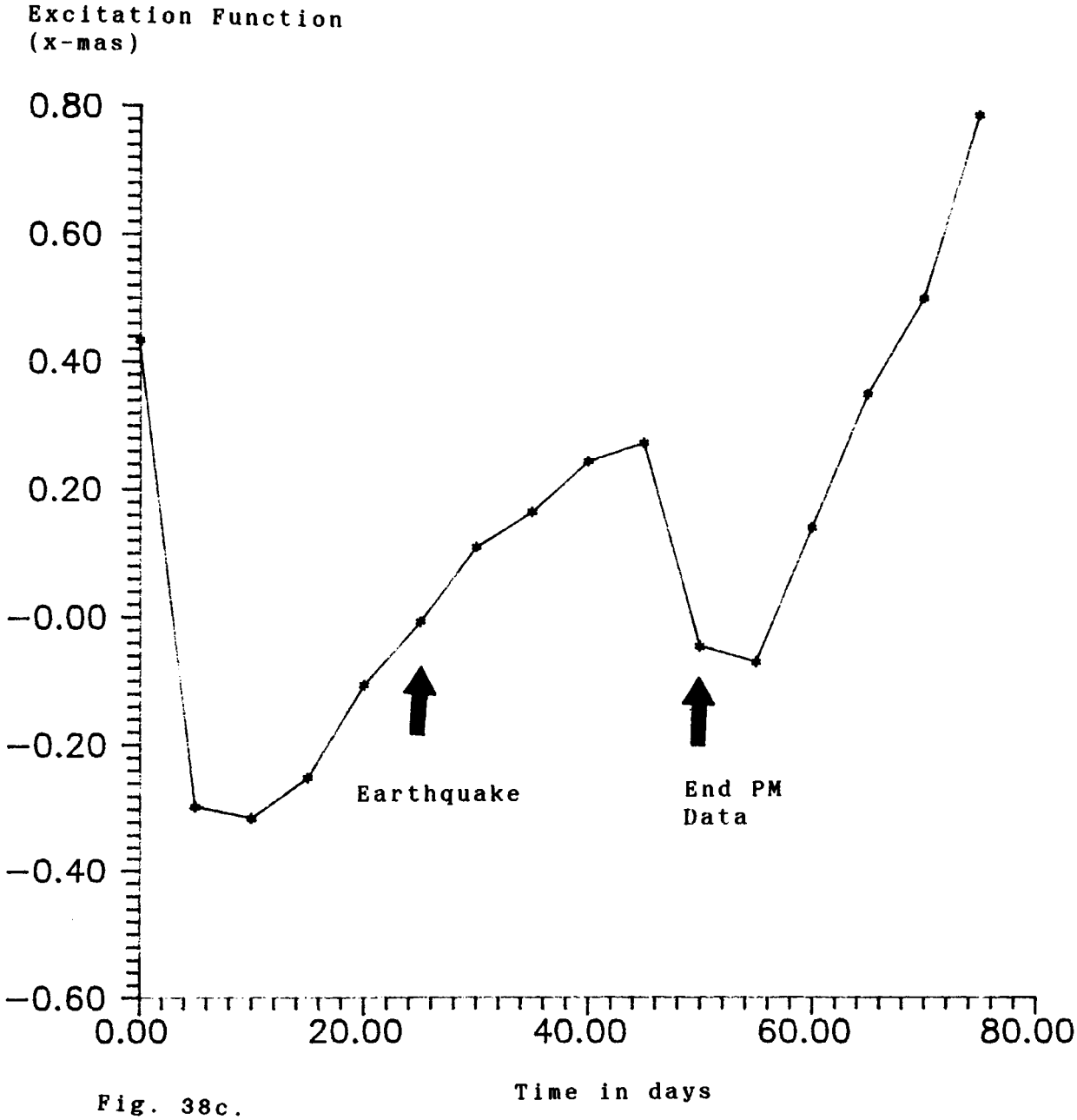
Excitation Function
(x-mas)
0.80
0.60
0.40
0.20
−0.00
−0.20
−0.40
−0.60
0.00
20.00
40.00
60.00
80.00
Earthquake
End PM
Data
Time in days

Fig. 38c.

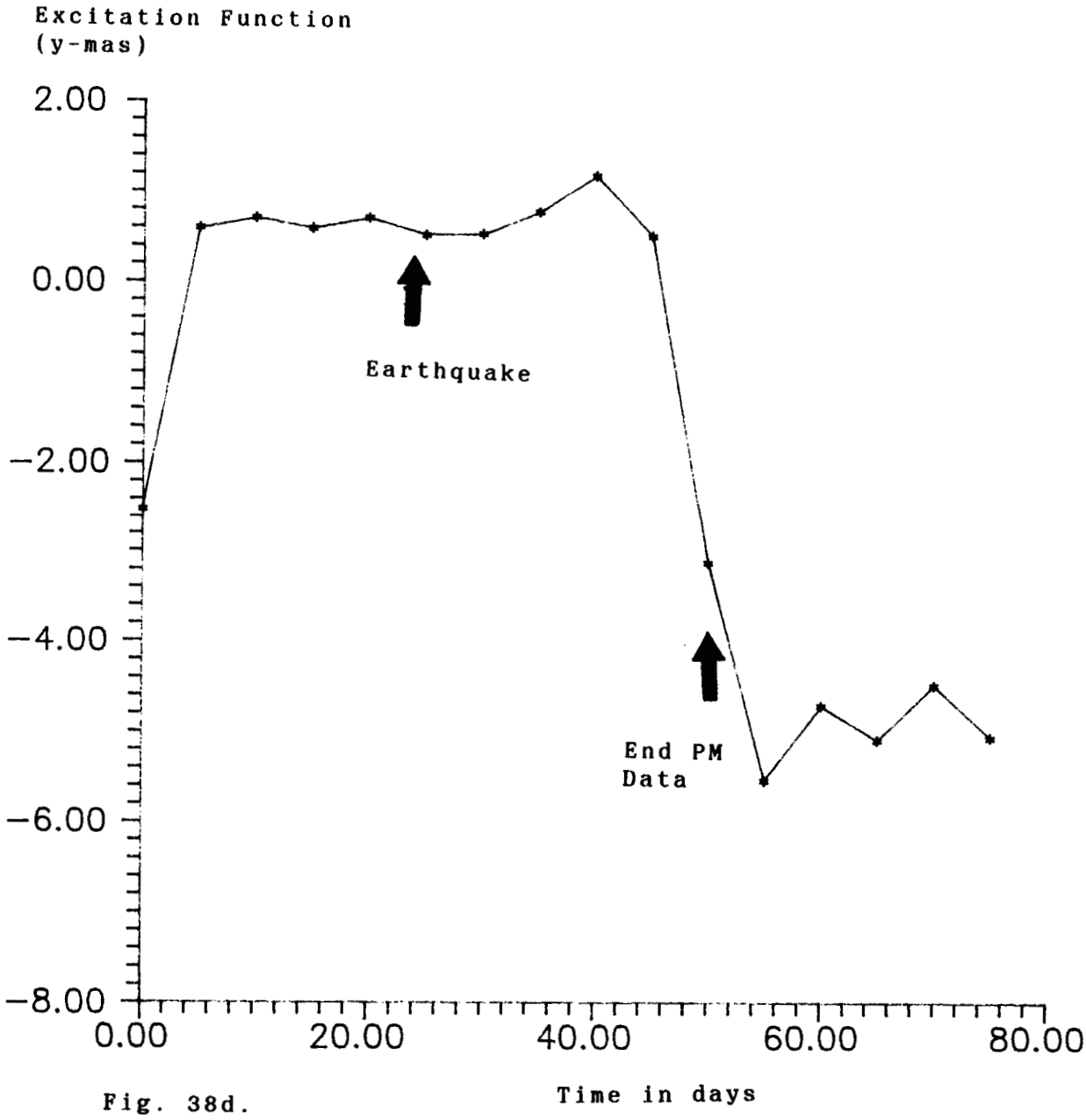

Fig. 38d.

Figure 38. Excitation Function (Y-component) versus time. Time interval surrounds epoch of the 1985 great Chilean earthquake. Excitation function errors are about 0.5 mas. (d) $\alpha N = 0.22$ (e) $\alpha N = 0.5$ (f) $\alpha N = 1.0$.

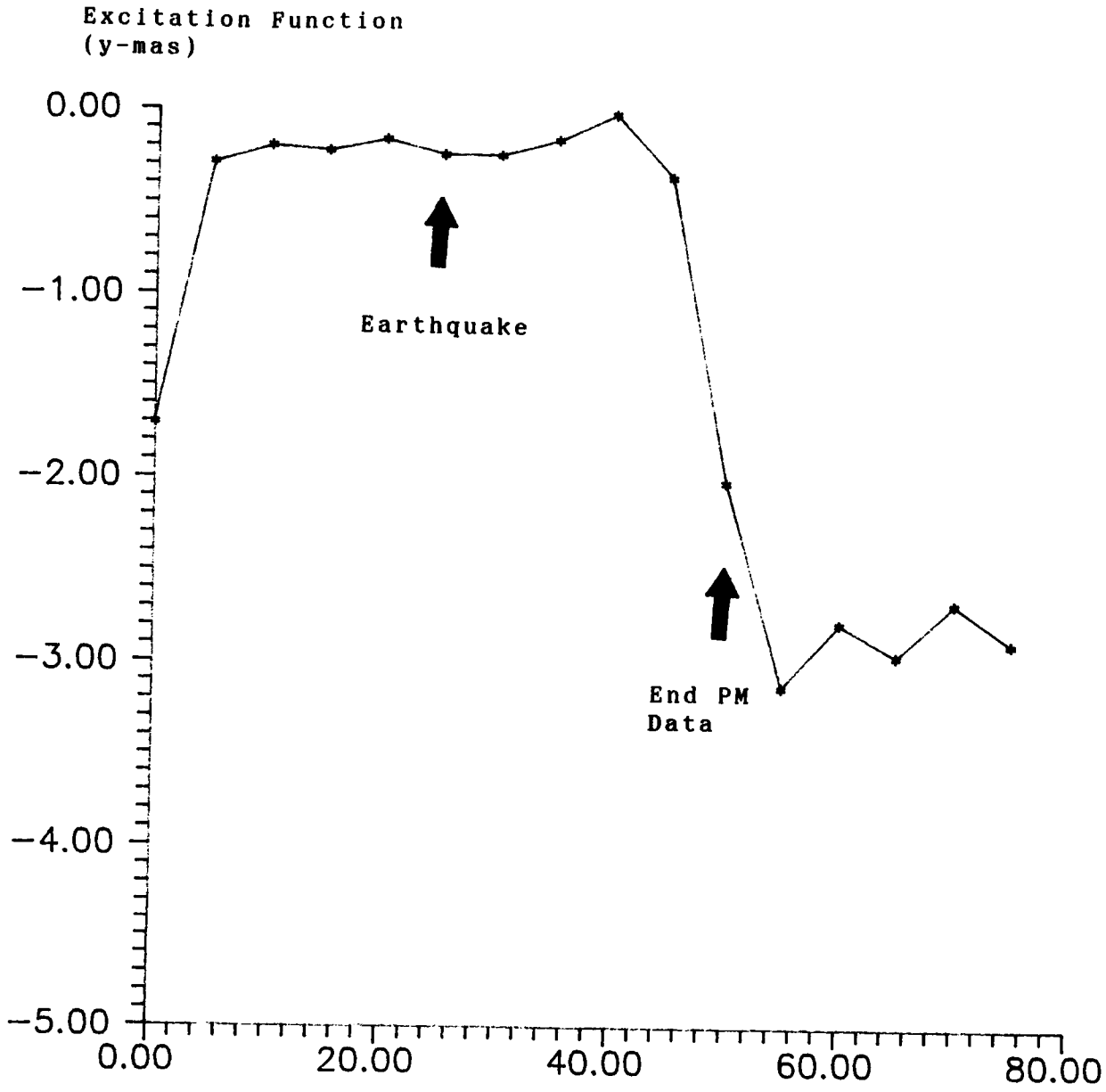
Excitation Function
(y-mas)
0.00
-1.00
-2.00
-3.00
-4.00
-5.00
Earthquake
End PM
Data
0.00
20.00
40.00
60.00
80.00
Time in days

Fig. 38e.

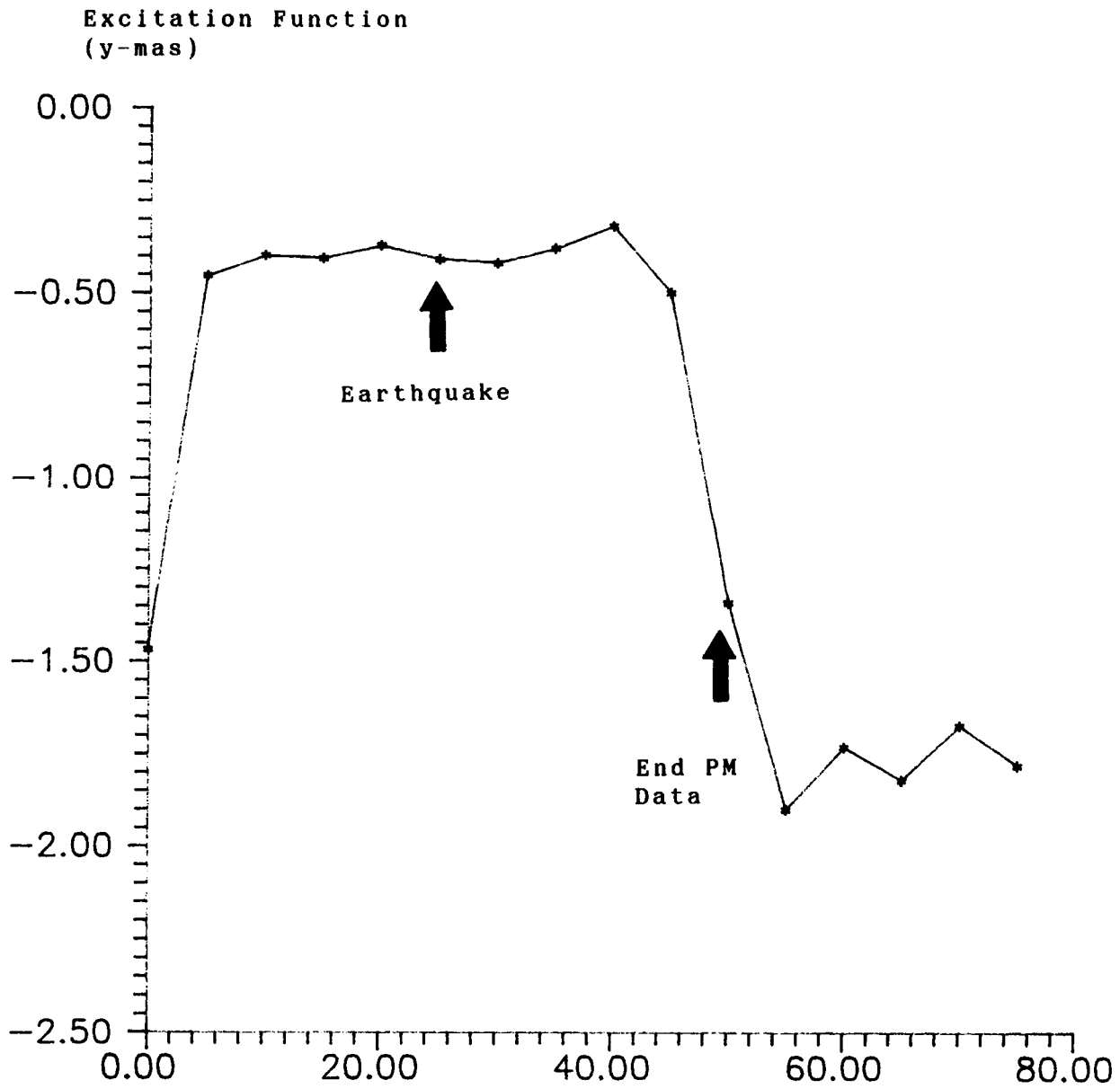
Excitation Function
(y-mas)
0.00
−0.50
−1.00
−1.50
−2.00
−2.50
Earthquake
End PM
Data
0.00
20.00
40.00
60.00
80.00
Time in days

Fig. 38f.

method of Gross and Chao (1985). The Fourier transforms were typically done with 16 data values.

It can be observed in the figures that vertical exaggeration (and thus possibly measurement noise content) is large for αN small ($\alpha N = 0.22$) as was expected. The data from the figures for $\alpha N=0.5$ will be analyzed further here since 0.5 is the value chosen as realistic by Gross and Chao (1985). Please note that all subsequent conclusions are based on this assumption. Also be aware that a linear trend has been removed from $\psi_x(t)$ for the Chile data.

The excitation data for Mexico ($\alpha N=0.5$) show small changes in ψ_x, ψ_y which are more gradual in structure than a step function. Variations in ψ start before the main seismic shock and continue on after the shock. The rates of change in ψ_x, ψ_y seem to be greatest within ±5 days of the main Mexican shock. These changes in ψ are at the sub-milliarcsecond level and are thereby not significant when compared with the formal error level of about 0.5 milliarcsecond in each component of ψ.

The Chile excitation functions bear changes which are much larger than those of the Michoacan, Mexico event. These excitation steps occur within ±25 days of the main shocks and a net change in excitation of about -2.4 milliarcseconds is found in the x-component of ψ. This ψ_x change takes place in two steps. 2.4 marcseconds is significant when compared with a formal error of 0.5 milli-

arcsecond.

Zheng Ying (1986) presents strain results before, during and after large earthquakes. He proposes that strain steps can be observed a few months before a large earthquake and one month after such an earthquake. These observations confirm to a fair degree what is found herein using VLBI data near the epoch of the 1985 great Chilean earthquake.

Since the VLBI polar motion results were deconvolved to produce excitation functions, it is appropriate to also deconvolve polar motion error estimates for comparison with these results. This will only be done for the 1985 Chile polar motion errors. The results are presented in Table Four. The deconvolution changes average polar motion errors of 1.2 and 1.2 mas (in x and y respectively) to average excitation errors of 0.5 and 0.5 mas. The excitation shifts observed (around the time of the 1985 Chilean earthquake) are significant, at least at the one-sigma formal error level.

Theoretically predicted shifts and directions (in degrees East longitude) calculated by Chao and Gross (1987) for earthquake dislocations only are compared with VLBI and LAGEOS observations of excitation shifts and directions in Table Five. The Sumba data are from LAGEOS observations, while the VLBI results are from this study. Observation is not strictly comparable with theory in this instance since the theory only models the effects of the elastic event on polar motion. The ratio of observed excitation to

Table Four- Chile Polar Motion and Excitation Function Errors (mas)

Measurement Date (1985)	Polar Motion x	Polar Motion y	Excitation x	Excitation y
Feb 07	1.05	1.03	0.21	0.77
Feb 12	1.11	1.16	0.26	0.69
Feb 17	1.13	1.11	0.30	0.63
Feb 22	1.07	1.05	0.34	0.56
Feb 27	1.20	1.26	0.39	0.52
Mar 04	1.53	1.48	0.48	0.42
Mar 09	-	-	-	-
Mar 14	1.24	1.18	0.57	0.34
Mar 19	1.32	1.09	0.64	0.26
Mar 24	0.99	0.99	0.69	0.22
Mar 29	1.07	1.11	0.76	0.19

Table Five- Comparison of Observed and Theoretical Excitations

Observed values	Ψ_x	Ψ_y	$\lvert\Psi\rvert$ (marcsec)	Arg(Ψ)
Mexico	-0.2	0.3	0.36	-56.3^{o} E long.
Chile	-2.4	-0.3	2.42	7.1^{o} E long.
Sumba*	-	-	40.0	-54.0^{o} E long.

Theoretical values	$\lvert\Psi\rvert$ (marcsec)	Arg(Ψ)
Mexico	.084	-83^{o} E
Chile	0.18	110^{o} E
Sumba	0.21	160^{o} E

Ratios (Ψ-observed/ Ψ-theory)	
Mexico	4.29
Chile	13.44
Sumba	190.48

* - Sumba event data from Gross and Chao (1985), and Chao and Gross (1987)

theoretical excitation is calculated also. Results are for the 1977 Sumba earthquake and for the 1985 Chile and Mexico earthquakes.

The observed excitation shifts and direction due to the 1985 Mexico earthquake are roughly in agreement with theory. The excitation directions are only rotated 27 degrees from one another and $|\psi|$'s are close in value for theory and experiment. This is especially true when one considers that the formal error in either component of (observed) excitation is less than one mas. One might characterize the Mexico event as one in which polar motion theory and experiment are roughly in accordance.

For the Chilean event the observed and theoretical excitation directions and magnitudes diverge more strongly than for Mexico. The theoretical and observed excitation directions are about 103 degrees apart, and the calculated amplitude ratio is about 13.4. This suggests that more may be taking place geophysically during the great Chilean earthquake of 1985 than is predicted theoretically.

The Sumba (1977) results resemble those of Chile more so than those of Mexico. The observed and theoretical excitation directions are 146 degrees apart (almost oppositely directed from one another). The amplitude ratio is approximately 190. As one might recall from earlier on in this work, Gross and Chao (1985) suggest that the extra (and differently directed) excitation may involve the decoupling (due to slab pull) of a slab segment from the

subducted oceanic lithosphere during the Sumba event, and may be due to subsequent movement of the broken off slab. Independent evidence (tectonic force calculations) that this "slab-pull-and-break" event did occur near the time of the Sumba earthquake is given by Spence (1986). The similarity of excitation results for Chile and Sumba leads one to believe that a slab-pull-and-break event has occurred in Chile also. If so, such slab movements associated with great earthquakes may contribute significantly to the Chandler wobble excitation budget. In addition, unsteady movements of subducting lithosphere may excite polar motion.

Several other earthquakes potentially capable of exciting the Chandler wobble of the earth have occurred in 1985-86: Adak, Alaska; Taiwan; and Kermadec Islands. The Kermadec Islands earthquake is of particular interest since it was a magnitude M_S=8.2 event (EOS, 2 December, 1986), and it compares in size with the Mexican and Chilean great earthquakes. Unfortunately, research into the effects of these events on polar motion was not performed due to lack of resources and facilities. In a related topic, one could check if a decoupled slab of lithosphere was formed during the 1985 Chilean earthquake by making calculations like those of Spence (1986). This would provide some independent confirmation that slab-pull-and-break took place.

Since the author was unable to Kalman filter VLBI data

around the times (Sept.-Nov., 1986) of the Kermadec Islands earthquake (20 Oct., 1986, M_S=8.2; EOS, 2 December, 1986) and of the Taiwan earthquake (14 Nov., 1986, M_S=7.8; EOS, 13 January, 1987), data from the IRIS Earth Orientation Bulletin A (January, 1987) will be examined. These data are polar motion results produced by the National Geodetic Survey (NGS), and they were estimated using least squares analysis. The raw data can be observed in Figure 39 (Pole position 1983-1986). The data of interest are shown near the end of the pole position curve (marked by the Roman letter B). The pole position estimates displayed in Figure 39 includes annual wobble and Chandler wobble components.

The data of interest from Figure 39 are deconvolved using the method of Gross and Chao (1985), and the excitation function estimates are shown in Figure 40. A linear trend (-.062 mas/day) has been removed from the ψ_x component results. The ψ_y plot shows little net change in the excitation as a function of time. The detrended ψ_x component shows a net (maximum) change in excitation of 3.8 mas; this is very significant when compared to a typical excitation function error of about 0.5 milliarcseconds.

The x-component of excitation starts to change directly after the main Taiwan shock, and increases greatly thereafter. Prior to the main Taiwan shock, the x-component of excitation is quite constant. The correlation of the onset of x excitation change with the time of the Taiwanese

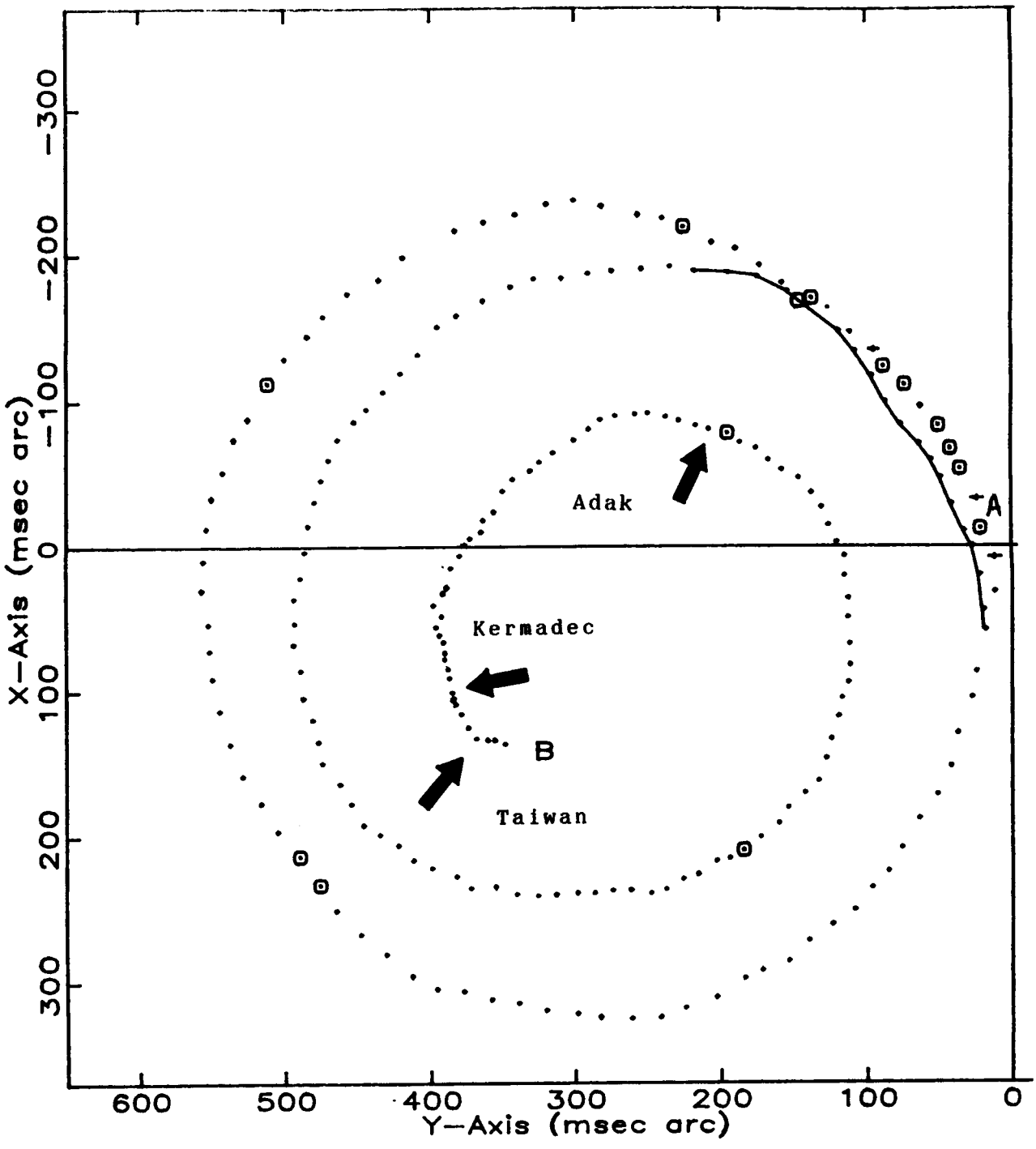

Fig. 39. Pole Position from Nov 17, 1983 (A) to Nov 30, 1986 (B) at 5-day intervals. Circled pts: X,Y = SLR [Satellite Laser Ranging] value; open circles: no value. (From IRIS Earth Orientation Bulletin A, January, 1987).

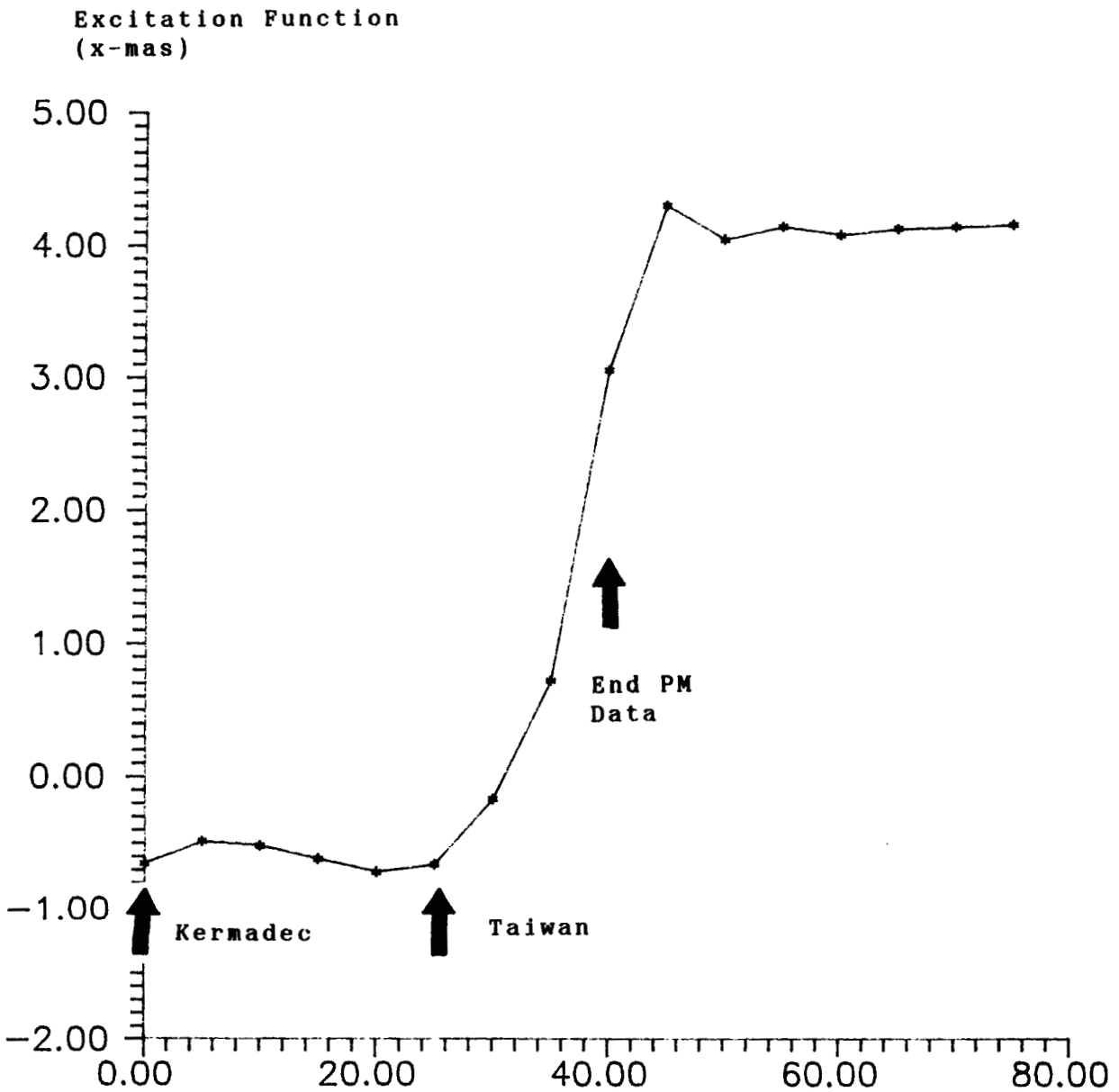

Fig. 40a.

Figure 40. Excitation Function versus time. Time interval is near the epochs of the 1986 great Tonga-Kermadec and Taiwan earthquakes. Excitation function errors are about 0.5 mas. N = 0.5. (a) X-component (detrended) (b) Y-component.

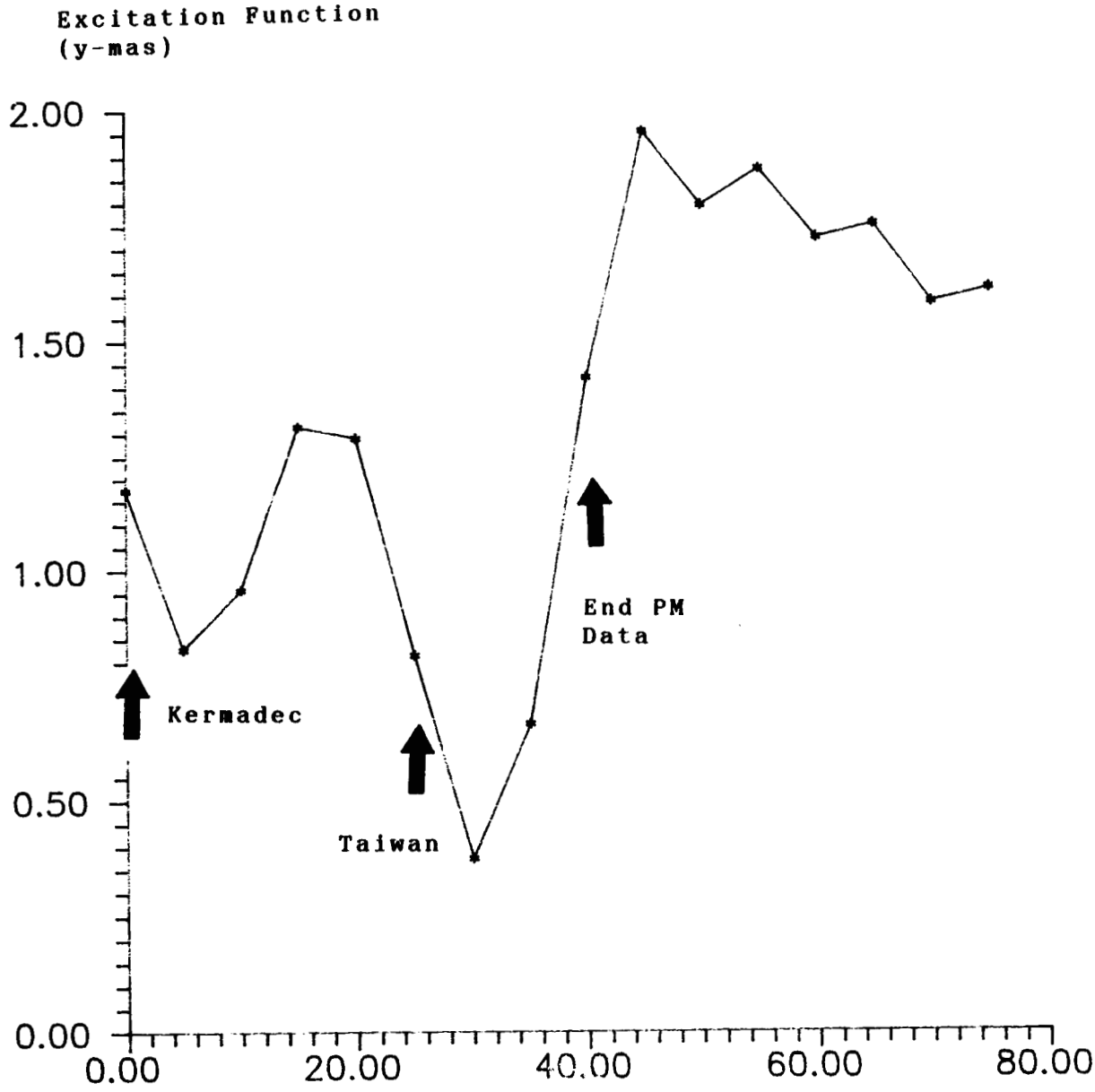
Excitation Function
(y-mas)
2.00
1.50
1.00
0.50
0.00
0.00
20.00
40.00
60.00
80.00
Kermadec
Taiwan
End PM
Data

Fig. 40b.

event is striking. The Taiwanese main shock precedes the change in polar motion excitation, thus inferring that earthquake (and post-seismic mass movement induced) excitation of the Chandler wobble is taking place. The source of such post-seismic excitation might be due to movements of lithospheric slab and/or "...viscous relaxation of the underlying asthenosphere..." around the earthquake zone (Au, 1980; Nur and Marko, 1974; Cohen, 1979; Spence and Turcotte, 1979). In either case, mass movements associated with the main earthquake shock seem to be affecting the Chandler wobble.

Finally some comment should be made about how much aseismic events (and seismic events) associated with the Mexican, Chilean, Taiwan and Sumba earthquakes contributed to polar motion excitation. The sum of the excitations associated with these four events (occurring from 1977-1986) has a maximum value of about 46.6 marcsec. If one then adds in the theoretically determined excitations (Smith, 1977) associated with the Chilean and Alaskan earthquakes of 1960 and 1964, one arrives at a total excitation (related to only six great earthquakes) of about 103 marcsec. If the Sumba results are not included, the excitation level would be 63 marcsec. This excitation level is considerable; examination of an excitation data set of duration similar in length to the Chandler wobble damping time would allow us to draw more valid conclusions about earthquake-associated excitation of polar motion. In addition, the

level of polar motion excitation due to great earthquakes and associated mass movements may vary with time, and other sources of excitation could dominate solid earth mass effects at various times during earth history.

The polar motion results derived in this work can be interpreted in a plate tectonic/geophysical framework. (This is not to say that atmospheric and oceanic phenomena are totally unrelated to Chandler wobble excitation). There is evidence that the Chandler wobble was excited following the 1985 Chilean and 1986 Taiwan great earthquakes. This excitation could be attributed to one or more geophysical phenomena: post-seismic movement of a lithospheric slab (Gross, 1985) and/or (post-seismic) viscous relaxation of the asthenosphere under the earthquake zone (Au, 1980).

For the 1985 Chilean earthquake, there is also (VLBI) evidence of pre-seismic (before the main shock) Chandler wobble excitation. Thus, VLBI could be used as a (temporal and spatial) earthquake prediction tool. If VLBI data could be shipped and processed in a timely fashion, perhaps one could make predictions of seismic main shocks in a range of several days to about one month prior to an event. The pre-seismic changes in wobble seen in the VLBI data would also demonstrate the validity of Kanamori's (1977) work.

A possible source of (pre-seismic) Chandler wobble excitation is the bulging of the lithosphere at a Chilean-like subduction zone prior to a main shock. Such bulging

could change the inertia tensor of the earth, thereby exciting the Chandler wobble. Calculations should be made to determine the theoretical excitation of such bulging. Figures 41 and 42 (Turcotte et al., 1978; Uyeda, 1979) show such (bending and) bulging which may precede great earthquakes such as the 1985 Chilean event. The amount of bulging may increase greatly just prior (several months before) the main shock (thereby driving a great thrust earthquake). Such bulging might not occur at a plate margin such as the one near Taiwan (refer to Figure 42) and thus explain why Chandler wobble excitation steps are not observed prior to the 1986 Taiwan earthquake. Pre-seismic excitation may also be due to aseismic fault slippage. The main emphasis of the preceding lines of thought is that most of the earthquakes of our planet occur at subduction zones, and it appears that a considerable portion of polar motion excitation may be driven by subduction-related phenomena.

More VLBI data are needed during time periods surrounding large/great earthquakes to determine the actual effects of such earthquakes on the Chandler wobble. Kanamori (1977) presents a listing of the great (shallow) earthquakes of 1904-1976; there are roughly nine such earthquakes per decade over this time span. Seismic events, and related major mass movements, are a significant contributor to the to the Chandler wobble excitation budget.

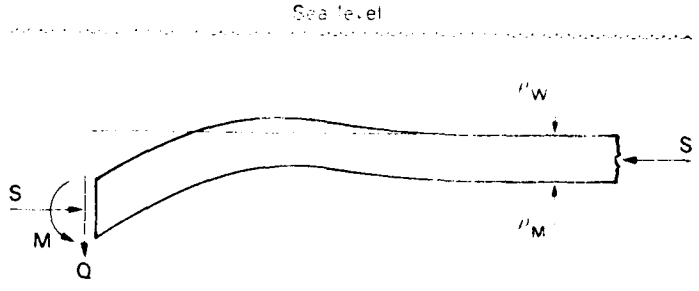

Fig. 41. Bending of an elastic or elastic-perfectly plastic plate in response to applied bending moment M, vertical force Q and horizontal force S, with hydrostatic restoring force applied by the seawater above and assumed fluid mantle below. Redrawn with simplification from Turcotte et al., 1978.

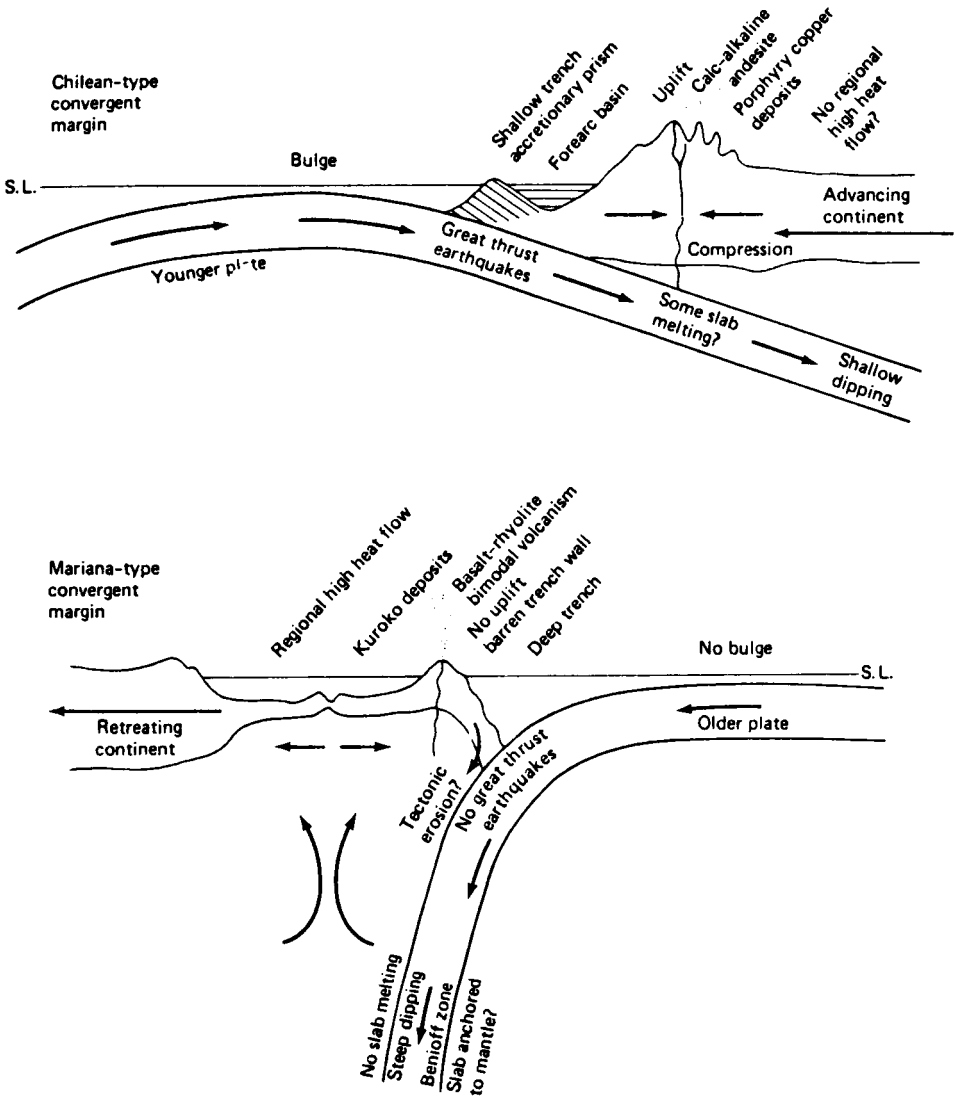

Fig. 42. Diagrammatic sections showing two general modes of subduction and their possible tectonic implications and causes (not to scale). (From Uyeda and Kanamori, 1979).

Chapter X.

CONCLUSIONS

The primary goals of this work were first, to show that a Kalman filter can be used successfully to analyze Very Long Baseline Interferometry group delay data with emphasis on handling clock variability; and second, to shed some light on the problem as to what degree earthquakes excite the Chandler wobble of the earth. The former technological objective has been completed to a reasonable extent while the latter scientific objective continues to elude total resolution as it has so often during the past century. Many more IRIS observing sessions will pass before the latter problem is adequately solved.

The Kalman filter design put forth herein does a satisfactory job of estimating clock terms, wet atmospheric zenith delays, earth orientation and rotation parameters and nutation offsets. The clock models can handle all but very large changes in clock rate. Very large clock rate changes could be accounted for either by making manual adjustments during the data processing or by implementing a clock model which includes clock acceleration parameters. With any luck, most large clock rate changes will be artifacts found only in VLBI data sets of the past.

Wet atmospheric zenith delays estimated using the Kalman filter were found to generally match the zenith delays determined from water vapor radiometer observations, except for slight biases. This confirms work originally performed by Tom Herring and Jim Davis at the Harvard/Smithsonian Center for Astrophysics.

Polar motion estimates from the Kalman filter match the values found via least squares analysis to modest precision, usually better than the agreement of BIH results and VLBI least squares estimates. The sources of biases seen between the least squares values and Kalman filter estimates have not been isolated due to time and funding constraints, but the causes are thought to be differences in analysis methods and assumptions. It could also be that the filter is producing more objective results than least squares methods, since Kalman filtering of VLBI delays requires minimal analyst intervention once the filter has been tuned. Nutation and change in length of day estimates were also made using the Kalman filter, but are not presented here because they were not parameters of interest to this study -- they were estimated in order to produce reliable polar motion results.

The trial and error method of tuning the Kalman filter took much time and computer cycles but did produce good results. More recently discovered tuning methods (than trial and error) based on the adjustment of statistics of filter residuals to meet theoretical expectations should be

employed in future undertakings.

It should be obvious from the last several chapters that the Rauch-Tung-Striebel smoother was only rarely applied to VLBI group delay data. "Why?" would be an appropriate question. The Rauch-Tung-Striebel smoother requires the storage of all parameter error covariance matrices from the forward Kalman filter pass. A typical Kalman filter run could easily generate tens-of-thousands to hundreds-of-thousands of covariance elements which are difficult to store in memory. For this reason the smoother was only used in limited (i.e. small number of estimated parameters) applications. Filtering the data in a backward time direction (back filtering) after forward filtering is probably a better idea than smoothing because storage required for back filtering is minimal.

Some reference is now made to general problems encountered in this research. The largest single cause of grief was having to use an Hewlett-Packard-1000 computer. While the HP-1000 is an excellent machine for computer instruction, it presents a nightmare for number crunching. The ability to load large programs is limited, and one is required to add significant amounts of software to use the extended memory (EMA) features, which is the default operational mode on many modern computers. Unfortunately, most of the NASA VLBI data handling and analysis programs (CALC, SOLVE, Data Base Handler) are written for the HP-1000 and the code is not very transportable.

There were several other forays into the absurd which wasted much time during this research. Several weeks were spent implementing an algorithm called the epsilon technique (Gelb, 1974) in an attempt to make early versions of the Kalman filter operate properly. One should be warned that the epsilon technique is probably not needed in Kalman filter implementation on a modern computer, and at best only offers an additional adjustable parameter with which one can vary filter output. Efforts should be directed at properly setting up the state transition matrices and process noise noise models rather than invoking the epsilon technique. The other major sink of time and effort involved an attempt to use a flicker noise generator for the betterment of Kalman filter clock models. As has been alluded to earlier, the clock noise is probably dominated by changes in signal path rather than by a (flicker) maser noise component, so several months were "spent" on this activity.

Many approximations were made in the course of this research, and it would be prudent to re-emphasize a few of them. In the clock process noise covariance calculation, terms involving the time interval $t_{k+1} - t_k$ of the state transition matrix (see equation VI.29) were not included in the calculation. This is because the clock model applied herein was modified from the work of maser experts (Jones and Tryon, 1982). In retrospect, such an approximation should not be made, but the author was giving in to simplifications which made filter set-up easier.

An approximation forced more by the SOLVE program structure than by anything else was that requiring the wet atmosphere zenith delay to be constant. It would be more accurate to allow for deterministic rate variations in the wet zenith delay, as are actually observed in WVR data. There is a tradeoff in having such extra (rate) parameters in a Kalman filter: the more accurate parameter model will necessitate additional filter tuning. Still, atmospheric rate parameters are part of a more precise VLBI future.

It is obvious that much more IRIS data will be needed before any ultimate conclusions about the effects of earthquakes on the earth's polar motion can be drawn. This may take some time, as no very large events occurred between 1977 and 1985; this lack of activity over long time intervals might lead one to believe that earthquakes are not the only source of Chandler wobble excitation. Still, no conclusion is firm until more is understood about the damping of the Chandler wobble.

One kink observed in the polar motion curve of 1985 appears to be real and extremely coincident with the great Michoacan, Mexico earthquake. Polar motion kinks are also found within ±15 days of the large 1985 Chilean event. The current IRIS one-sigma formal error level is about one milliarcsecond in each component of polar motion. This is a factor of at least ten better than the BIH results studied by Mansinha and Smylie (1970). Thus, while Mansinha and Smylie were able to study the effect of very large

earthquakes (Alaska and Chile of the 1960's) on polar motion with low precision, this study has examined the effects of somewhat smaller events at significantly higher precision. One is forced to conclude that more and better data are needed. Another outcome of this study is that Kalman filters will be available to look at polar motion path fine structure (in time) should a very large earthquake take place during an IRIS observing session.

Excitation functions determined from the optimal estimates of polar motion show statistically non-significant excitation of the Chandler wobble by the 1985 Michoacan, Mexico earthquake. The observed excitation at the time of the Mexican event coincides closely (in amplitude and direction) with theoretical values found. The static deformation field models do not incorporate the effects of aseismic slip or other mass movements.

Significant excitation of the Chandler wobble (at least at the one-sigma level of measurement error) is observed (using VLBI) near the time of the great Chilean earthquake of 1985. The magnitude of the excitation change is about 2.4 milliarcseconds as compared with a formal error of about 0.5 milliarcsecond. Such an excitation is much larger than theoretical seismic models permit. The excitation is also (roughly) oppositely directed from theoretical vectors.

The 1985 Chilean earthquake appears to affect the Chandler wobble in a manner similar to the great Sumba earthquake of 1977, although the effects are not as large.

It may be that lithospheric slabs are being broken off of the subducted lithospheric plate during the main seismic shock of such a large earthquake. Thereby, the decoupled slabs are moving after such an event and change the inertia tensor of the earth. Independent tectonic force studies verify that such a slab-pull-and-break mechanism is realistic. We will need to know the degree of Chandler wobble excitation by such slab movements and the frequency of such events in order to discover to what degree this tectonic phenomenon drives the Chandler wobble. If the excitation step of the 1977 Sumba event is actually forty milliarcseconds, then decoupled lithospheric slabs drive the Chandler wobble at a large percentage of the total observed excitation level.

The IRIS VLBI results around the time of the 1986 Taiwan earthquake show that the time of the Taiwan main event is strongly correlated with polar motion excitation. A change in excitation level directly follows the time of the 1986 great Taiwan event. The excitation is probably due to post-seismic movements of lithospheric slabs decoupled from lithospheric plates, or due to relaxation of the asthenosphere near the fault zone. The preceding mechanisms are likely candidates for post-seismic Chandler wobble excitation. One source of pre-seismic Chandler wobble excitation is posed to be (changes in the inertia tensor due to) lithospheric flexure at subduction zones such as the one near Chile. Aseismic fault creep is

another possibility.

The future of Very Long Baseline Interferometry studies of the earth's polar motion is certainly bright, but every effort should be made to optimize IRIS results. Surely water vapor radiometers will aid in minimizing the effect of wet path delays on VLBI observations. More must be done to improve other calibrations also. Perhaps IRIS observations could be made daily (instead of at 5-day intervals) in the next several years also.

As a final remark emphasizing something which has been pointed out before, the IRIS network of Westford-Wettzell-Fort Davis-Richmond-Onsala is far from the best observing configuration for earth orientation and rotation. A grid utilizing Westford (or Canada), Wettzell, a southern Argentinian station and an antenna in southern Africa would be better. Of course, efforts are being made in this direction and perhaps someday economic and political considerations will permit such an array to exist.

APPENDIX I.

KALMAN FILTER DERIVATION

The discrete Kalman filter will be derived. The abbreviated treatment presented herein follows Gelb et al. (1974). The equations which form the foundation of the Kalman filter are (III.4), (III.5) and (III.6):

$$y_k = M_k x_k + v_k \qquad \text{(AI.1)}$$

$$x_{k+1} = \Phi_k x_k + \Gamma_k w_k \qquad \text{(AI.2)}$$

$$E\{w_k\} = 0, \qquad E\{v_k\} = 0 \qquad \text{(AI.3)}$$

$$E\{w_k w_l^T\} = Q_k \delta_{kl}, \quad E\{v_k v_l^T\} = R_k \delta_{kl}.$$

Equation (AI.1) describes the measurement process, equation (AI.2) models the dynamics of the parameter vector x_k, and equations (AI.3) give the assumed properties of the measurement noise v_k and process noise w_k. y_k is the vector containing the measurement information, and M_k relates the parameters to be estimated to this information. Φ_k is the state transition matrix which models how x_{k+1} is related to x_k, and Γ_k relates

the process noise to x_{k+1}. Q_k and R_k are the process noise and measurement noise covariances. Capital letters usually denote matrices while small letters are reserved for vectors.

The first step of the Kalman filter algorithm to be derived here shows the relationship between optimal parameter estimates in time. Beginning with equation (AI.2) and taking the expectation value of this equation, one finds

$$E\{x_{k+1}\} = \Phi_k E\{x_k\} + \Gamma_k E\{w_k\}.$$

Carets are used to denote optimal parameter estimates (also recall that $E\{w_k\}=0$). The result of taking the expectation is

$$\hat{x}_{k+1} = \Phi_k \hat{x}_k. \qquad \text{(AI.4)}$$

Equation (AI.4) demonstrates how optimal parameter estimates are projected in time. In the notation of Jazwinski (1970), equation (AI.4) is written as

$$\hat{x}(k+1|k) = \Phi(k+1,k)\hat{x}(k|k).$$

The next derivation shows how the error covariance matrix P_k is projected from time t_k to time t_{k+1}. The optimal estimates at times t_k and t_{k+1} are

assumed to be related to the parameter vectors by

$$\tilde{x}_{k+1} = \hat{x}_{k+1} - x_{k+1} \qquad \text{(AI.5)}$$

$$\tilde{x}_k = \hat{x}_k - x_k,$$

where the tilde designates estimation errors. Subtracting equation (AI.2) from (AI.4) leads to

$$\tilde{x}_{k+1} = \Phi_k \tilde{x}_k - \Gamma_k w_k. \qquad \text{(AI.6)}$$

The error covariance at time t_{k+1} is

$$P_{k+1} \equiv E\{\tilde{x}_{k+1}\tilde{x}_{k+1}^T\} \qquad \text{(AI.7)}$$

$$= E\{(\Phi_k \tilde{x}_k - \Gamma_k w_k)(\Phi_k \tilde{x}_k - \Gamma_k w_k)^T\},$$

where the superscript T denotes the transpose operation. Using equations (AI.3), and working through some algebra results (where $P_k \equiv E\{\tilde{x}_k \tilde{x}_k^T\}$) in the covariance update

$$P_{k+1} = \Phi_k P_k \Phi_k^T + \Gamma_k Q_k \Gamma_k^T. \qquad \text{(AI.8)}$$

This is another step in the Kalman filter algorithm, and in the notation of Jazwinski (1974) is

$$P(k+1|k) = \Phi(k+1,k)P(k|k)\Phi^T(k+1,k) + \Gamma(k)Q(k)\Gamma^T(k).$$

How measurements are combined with Kalman filter estimates to yield updated estimates will now be illustrated. It is given that optimal estimates at times immediately before (-) and immediately after (+) a discrete measurement are related to parameter estimates by the equations

$$\hat{x}_k(+) = x_k + \tilde{x}_k(+) \qquad \text{(AI.9)}$$

$$\hat{x}_k(-) = x_k + \tilde{x}_k(-) \qquad \text{(AI.10)}$$

where the tilde again denotes estimation errors. The recursive estimator is assumed to have the form

$$\hat{x}_k(+) = K'_k\hat{x}_k(-) + K_k y_k. \qquad \text{(AI.11)}$$

where K'_k and K_k are Kalman gain matrices (which are yet to be determined). Equation (AI.11) simply means that the optimal parameter estimate (after a discrete measurement) is related to some combination of the optimal parameter estimate (before the discrete measurement is taken) and the measurement itself. The relative contribution of $\hat{x}_k(-)$ and y_k are determined by the gain coefficients K'_k and K_k.

Insertion of equations (AI.1), (AI.9) and (AI.10) into equation (AI.11) produces

$$\tilde{x}_k(+) = \{K_k' - I + K_k M_k\}x_k + K_k'\tilde{x}_k(-) + K_k v_k. \qquad \text{(AI.12)}$$

Taking the expectation of equation (AI.12) and assuming $E\{\tilde{x}_k(-)\} = 0$ (the estimator derived herein produces unbiased results), one finds

$$E(\tilde{x}_k(+)) = \{K_k'-I+K_kM_k\}E(x_k). \qquad (AI.13)$$

For the updated estimates to be unbiased, it is required that $E\{\tilde{x}_k\}=0$; this can be achieved by setting

$$K_k' = I-K_kM_k, \qquad (AI.14)$$

where I is the identity matrix. Placing equation (AI.14) into equation (AI.11) yields equation (AI.15)

$$\hat{x}_k(+) = \hat{x}_k(-) + K_k(y_k-M_k\hat{x}_k(-)), \qquad (AI.15)$$

which is another step in the Kalman filter algorithm. In conditional probability notation the equation is

$$\hat{x}(k+1|k+1) = \hat{x}(k+1|k) + K(k+1)(y_{k+1}-M(k+1)\hat{x}(k+1|k)).$$

The error covariance can also be updated in a manner similar to equation (AI.15). This starts by using equation (AI.9) and a variation of equation (AI.15)

$$\hat{x}_k(+) = \{I-K_kM_k\}\hat{x}_k(-) + K_ky_k \qquad (AI.16)$$

to form $\tilde{x}_k(+) = \hat{x}_k(+) - x_k$

$$= (I-K_kM_k)\hat{x}_k(-) + K_k(M_kx_k+v_k)-x_k.$$

And $x(+)=\{I-K_kM_k\}x_k(-) + K_kv_k$. (AI.17)

The updated error covariance is

$$P_k(+) = E\{\tilde{x}_k(+)\tilde{x}_k(+)^T\}. \quad \text{(AI.18)}$$

Using equations (AI.3), (AI.17) and (AI.18), and the definition $P_k(-) = E\{\tilde{x}_k(-)\tilde{x}_k(-)^T\}$, one finds

$$P_k(+) = (I-K_kM_k)P_k(-)(I-K_kM_k)^T + K_kR_kK_k^T. \quad \text{(AI.19)}$$

The updated error covariance is related to a combination of the prior error covariance and the measurement error covariance. In the notation employed by Jazwinski (1970), the update equation is

$$P(k+1|k+1) = (I-K(k+1)M(k+1))P(k+1|k)(I-K(k+1)M(k+1))^T + K(k+1)R(k+1)K^T(k+1).$$

The last equation to be derived in the Kalman filter algorithm is that determining an optimal gain factor K_k. This is found by minimizing the error in the updated covariance $P_k(+)$ (actually the sum of the $P_k(+)$ diagonal elements) with respect to the undetermined gain factor K_k. The details of this procedure are given in Gelb et al. (1974) and yield the result

$$K_k = P_k(-)M_k^T\{M_kP_k(-)M_k^T+R_k\}^{-1}. \quad \text{(AI.20)}$$

The optimal Kalman filter gain compares the parameter error covariance and measurement error covariance. Notice that if the measurement covariance is very large (i.e. poor data), the Kalman gain will be small, and the updated parameter estimate (see equation (AI.15)) will have a value not much different from the predicted estimate $\hat{x}_k(-)$. Equation (AI.20) in conditional probability notation is

$$K(k+1) = P(k+1|k)M^T(k+1)\{M(k+1)P(k+1|k)M^T(k+1)+R(k+1)\}^{-1}.$$

All of the Kalman filter (algorithm) steps have now been derived.

Appendix II.

EFFECTS OF FAULT PARAMETERS AND LOCATION ON CHANGES IN PRODUCTS OF INERTIA

For completeness, a short discourse is presented here which illustrates the effects of earthquake strike, dip, slip, colatitude, longitude and depth on the changes in the products of inertia ΔC_{13} and ΔC_{23}. This section closely follows the work of Dahlen (1971, 1973).

Equations V.3 and V.4 (presented previously) relate changes in the products of inertia, ΔC_{13} and ΔC_{23}, to strike, dip, slip, colatitude, longitude and depth. Dahlen's (1971, 1973) orientation conventions for strike, dip and slip are as follows: the strike angle α is measured counter-clockwise from North (at the Earth's surface); the dip δ is the angle between the Earth's surface and the fault plane; and the slip angle λ is measured counter-clockwise from horizontal (in the fault plane).

Dahlen (1971) calculates a product of inertia amplitude $\Delta C = (\Delta C_{13}^{2} + \Delta C_{23}^{2})^{1/2}$ for several types of faults, with various combinations of colatitude, strike and dip. Specific test case results (Dahlen, 1971) are presented for a vertical, strike-slip fault (e.g. the San Andreas fault) at a depth of 20 kilometers (Figure AII.1) and a shallow dip ($\delta = 20^{o}$) thrust fault (e.g. Chilean

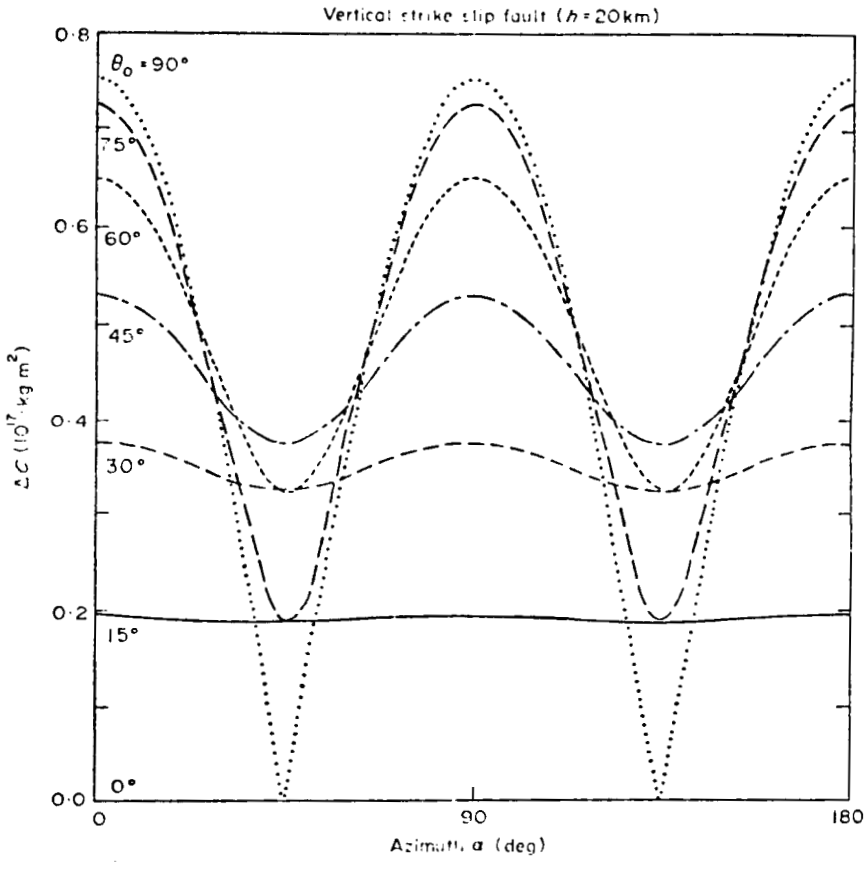

Figure AII.1. Plot showing variation of $\Delta C = (\Delta C_{13}^2 + \Delta C_{23}^2)^{1/2}$ with respect to fault strike α and colatitude θ_0 for a vertical strike slip fault of unit slip area (from Dahlen, 1971)

subduction zone) at a depth of 20 kilometers (Figure AII.2).

It is evident on Figure AII.1 (strike slip fault) that the ΔC amplitude is largest for a colatitude of ninety degrees, ignoring the effects of strike orientation; i.e. a strike slip fault at the equator has the largest relative influence on ΔC when considering the effects of colatitude. The fault strike has maximal effects on ΔC (for a strike slip fault) at integer multiples of ninety degrees (α = 0 degrees, 90 degrees,...). It appears that a North-South trending strike-slip fault has the same effect on ΔC as an East-West trending (strike-slip) fault.

The effects of a shallow angle thrust (dip slip $\lambda = 90^{o}$) fault on ΔC are shown in Figure AII.2 (Dahlen, 1971). ΔC is at a maximum for a colatitude of 60 degrees and for a strike angle of 90 degrees. Thus a shallow angle thrust fault at 60^{o} colatitude and trending east-west has maximal effects on ΔC. It appears from the Figures (AII.1 and AII.2 - for the cases studied here) that a strike-slip earthquake can produce slightly greater changes in ΔC than the shallow angle thrust fault; one may notice that longitude is not varied in Dahlen's (1971) Figures. Knowledge of the symmetry of the earth would dictate that ΔC is not strongly dependent on longitude.

Up until this point, little has been said about the dependence of ΔC on the depth of an earthquake. ΔC is dependent on depth h through the canonical functions, $\tilde{\Gamma}_1(h)$,

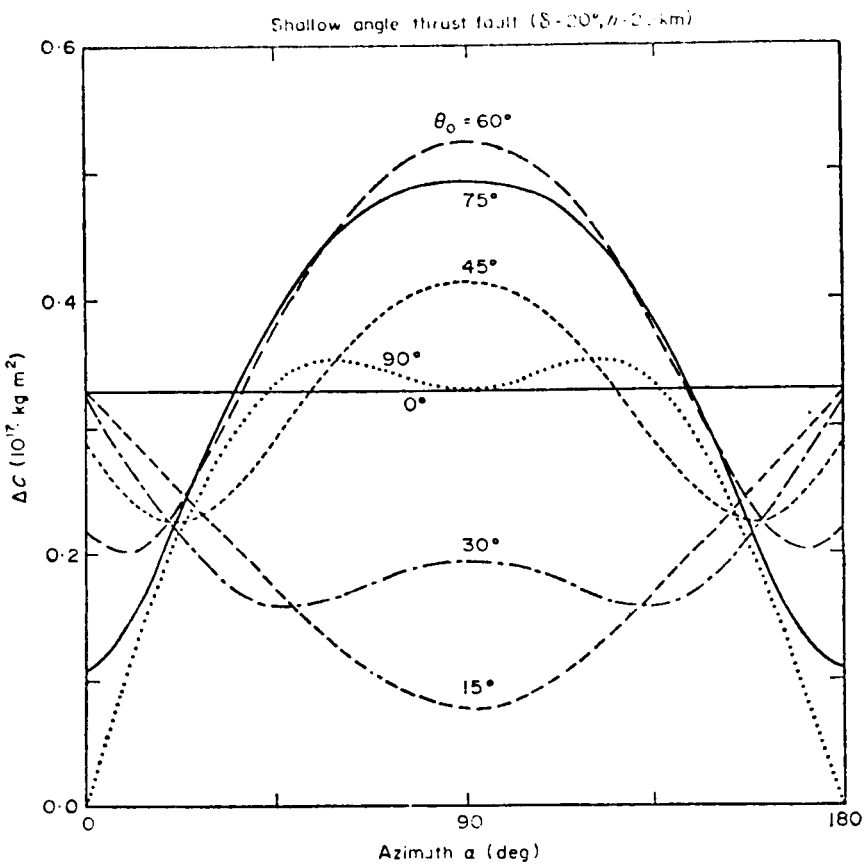

Figure AII.2. Plot showing variation of $\Delta C = (\Delta C_{13}^2 + \Delta C_{23}^2)^{1/2}$ with respect to fault strike α and co-latitude θ_o for a shallow angle ($\delta = 20^o$) thrust fault of unit slip-area (from Dahlen, 1971)

$\widetilde{\Gamma}_2(h)$ and $\widetilde{\Gamma}_3(h)$. The canonical functions are displayed versus depth h in Figure A11.3 (Dahlen, 1973). The canonical functions all increase with increasing depth, with $\widetilde{\Gamma}_1$ and $-\widetilde{\Gamma}_2$ increasing much more linearly than $\widetilde{\Gamma}_3$. The simplest conclusion that can be drawn is (ignoring the other parameters) that ΔC increases with depth h.

However, it should be remarked that subducted (typically dip slip) lithosphere can extend to far greater depths ($\approx$ 700 km) than lithospheric plates typically participating in strike-slip motion ($\approx$100 km). On the basis of this observation, it would be valid to conclude that ΔC would be much larger for subduction-related earthquakes than for strike-slip events.

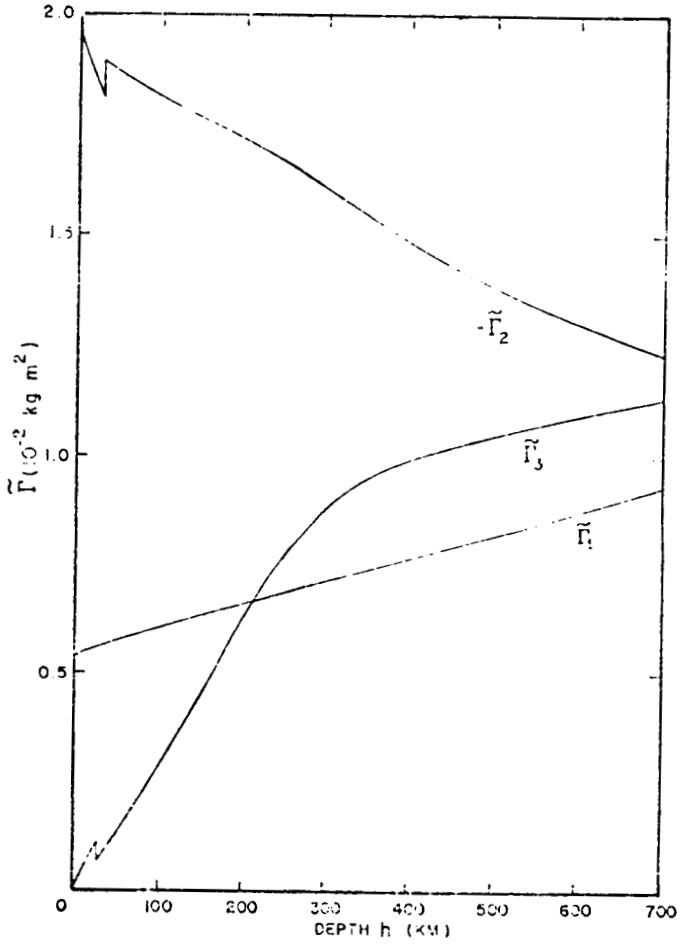

Figure AII.3. Plot of $\tilde{\Gamma}_1(h), -\tilde{\Gamma}_2(h), \tilde{\Gamma}_3(h)$ for SNREI Earth model 8073AW. (from Dahlen, 1973--- for details about 8073AW, see Dahlen, 1973)

REFERENCES CITED

Aki, K., 1967. Scaling laws of seismic spectrum, J. geophys. Res., 72:1217-1231.

Aki, K., 1972. Earthquake mechanism, Proceeding of the Final UMC Symposium, ed. by R. Ritsema, Moscow, 1971.

Allan, David W., 1984. Clock Characterization Tutorial, Proceedings of the Fifteenth Annual Precise Time and Time Interval (PTTI) Applications and Planning Meeting, Naval Research Laboratory, Washington, D.C., 1983.

Aoki, S., B. Guinot, G. H. Kaplan, H. Kinoshita, D. D. McCarthy, and P. K. Seidelmann, 1982. The new definition of universal time, Astron. Astrophys., 105:359-361.

Au, Andrew Y., 1980. Unpublished work (Ph.D. proposal).

Backus, G. and F. Gilbert, 1970. Uniqueness in the inversion of inaccurate gross earth data, Philos. Trans. R. Soc. London Ser. A, 266:123-192.

Barnes, R. T. H., R. Hide, A. A. White and C. A. Wilson, 1983. Atmospheric angular momentum fluctuations, length-of-day changes and polar motion, Proc. R. Soc. London Ser. A, 387:31-73.

Brown, Robert Grover, 1983. Random Signal Analysis and Kalman Filtering. New York: John Wiley & Sons.

Brown, R. G., 1984. Kalman filter modeling, in Proceedings of the Sixteenth Annual Precise Time and Time Interval (PTTI) Applications and Planning Meeting, NASA Goddard Space Flight Center, Greenbelt, Maryland, 27-29 November, 1984.

Brune, J. N., 1968. Seismic moment, seismicity, and rate of slip along major fault zones, J. geophys. Res., 73:777-784.

Chandler, S., 1891. On the variation of latitude, Astron. J., 11:65,83.

Chao, B. F., 1985. On the excitation of the Earth's polar motion, Geophys. Res. Lett., 12:526-529.

Chao, B. Fong and Richard S. Gross, 1987. Changes in the earth's rotation and low-degree gravitational field induced by earthquakes, submitted to Geophysical

Journal of the Royal Astronomical Society, 14 July, 1986.

Chao, C. C., 1970. A preliminary estimation of tropospheric influence on the range and range rate data during the closest approach of the MM71 mars mission, Jet Propulsion Laboratory Tech. Memo 391-129.

Chiu, Mary, 1984. Personal communication. Applied Physics Laboratory/Johns Hopkins University.

Clark, T. A., B. E. Corey, J. L. Davis, et al., 1985. Precision geodesy using the Mark-III very-long-baseline interferometer system, IEEE Trans. on Geoscience and Remote Sensing, GE-23:438-449.

Clark, T. A., G. Lundqvist and C. Moore, 1985. Geodesy by radio interferometry: validation of the water vapor radiometer (WVR) technique, EOS, 66(No.18):243.

Cohen, S. C., 1979. Postseismic surface deformations due to lithospheric and asthenospheric viscoelasticity, Geophys. Res. Lett., 6:129-131.

Dahlen, F. A., 1971. The excitation of the Chandler wobble by earthquakes, Geophys. J. R. astr. Soc., 25: 157-206.

Dahlen, F. A., 1973. A correction to the excitation of the Chandler wobble by earthquakes, Geophys. J. R. astr. Soc., 32: 203-217.

Dahlen, F. A., 1985. Seminar on Chandler wobble held at the Carnegie Institution of Washington/Department of Terrestrial Magnetism -- 10 April, 1985.

Davis, J. L., T. A. Herring, I. I. Shapiro, A. E. E. Rogers and G. Elgered, 1985. Geodesy by radio interferometry: effects of atmospheric modeling errors on estimates of baseline length, Radio Science, 20:1593-1607.

Dickman, S. R., 1982. The pole tide and its geophysical consequences (review article), Geophys. J. R. astr. Soc., submitted.

Dickman, S. R., 1986. The damping of the Chandler wobble and the pole tide, in Earth Rotation: Solved and Unsolved Problems (A. Cazenave, ed.). 203-228.

Dickman, S. R., 1987. Personal communication.

Duda, S. J., 1965. Secular seismic energy release in the circum-Pacific belt, Tectonophysics, 2:409-452.

Elgered, G., 1983. Water vapor radiometry with applications

to radio interferometry and meteorology, Doctoral thesis, Tech. report No. 137, School of Electrical Engineering, Chalmers University of Technology, Gothenburg, Sweden.

Elgered, G. and G. Lundqvist, 1984. Calibration of the excess propagation path for radio waves in the neutral atmosphere, Technical memorandum (unpublished draft), Onsala Space Observatory, Chalmers University of Technology, Onsala, Sweden.

Fitzgerald, R. J., 1967. Error divergence in optimal filtering problems, Second IFAC Symp. Automatic Control Space, Vienna, Austria.

Gelb, Arthur, ed., 1974. Applied Optimal Estimation. Cambridge, Massachusetts: the M.I.T. Press.

Goldstein, H., 1950. Classical Mechanics. Reading, Mass.: Addison-Wesley Publishing Company.

Gross, R. S. and B. Fong Chao, 1984. The observed excitation of the LAGEOS derived Chandler wobble, EOS, 65(No. 16): 187.

Gross, R. S. and B. Fong Chao, 1985. Excitation study of the LAGEOS-derived Chandler wobble, Journal of Geophysical Research, 90(No. B11):9369-9380.

Gross, R. S., 1986. The influence of earthquakes on the Chandler wobble during 1977-1983, Geophys. J. R. astr. Soc., 85:161-177.

Gutenberg, B., 1956. The energy of earthquakes, Quart. J. Geol. Soc. London, 112:1-14.

Haubrich, R. A., 1970. An examination of the data relating pole motion to earthquakes; in Earthquake Displacement Fields and the Rotation of the Earth; Mansinha, L., D. E. Smylie and A. E. Beck, eds. Dordrecht, Holland: D. Reidel Publishing Company.

Herring, T. A., B. E. Corey, C. C. Counselman III et al., 1981. Geodesy by radio interferometry: inter-continental distance determinations with subdeci-meter precision, Jour. Geophys. Res., 86(No. B3): 1647-1651.

Herring, T. A., 1983. Precision and Accuracy of Intercontinental Distance Determinations Using Radio Interferometry. Dissertation, Massachusetts Institute of Technology.

Herring, T. A., C. R. Gwinn and I. I. Shapiro, 1985.

Geodesy by radio interferometry: corrections to the IAU 1980 nutation series, Proceedings of the International Conference on Earth Rotation and the Terrestrial Reference Frame, Columbus, Ohio, 31 July - 2 August, 1985.

Hinnov, L. A. and Clark R. Wilson, 1985. The role of water storage in the excitation of the Chandler wobble, EOS, 66(No. 18):245.

Jazwinski, A. H., 1970. Stochastic Processes and Filtering Theory. New York: Academic Press.

Jones R. H. and P. V. Tryon, 1983. Estimating time from atomic clocks, Journal of Research of the National Bureau of Standards, 88:17-24.

Kalman, R. E., 1960. A new approach to linear filtering and prediction problems, Trans. ASME, Ser. D: J. Basic Eng., 82:35-45.

Kalman, R. E. and R. S. Bucy, 1961. New results in linear filtering and prediction theory, Trans. ASME, Ser. D: J. Basic Eng., 83:95-108.

Kanamori, H. and J. J. Cipar, 1974. Focal process of the great Chilean earthquake May 22, 1960, Physics of the Earth and Planetary Interiors, 9:128-136.

Kanamori, H., 1976. Are earthquakes a major cause of the Chandler wobble?, Nature, 262:254-255. 22 July, 1976.

Kanamori, H., 1977. The energy release in great earthquakes, Journ. Geophys. Res., 82(No. 20):2981-2987.

Kaplan, G. H.,1981. The IAU Resolutions on Astronomical Constants, Time Scales, and the Fundamental Reference Frame; U. S. Naval Observatory Circular No. 163, Washington, D. C.: U. S. Naval Observatory.

Kinoshita, H., K. Nakajima, Y. Kubo, I. Nakagawa, T. Sasao, and K. Yokoyama, 1979. Note on nutation in ephemerides, Publ. International Latitude Observatory, XII:71-107.

Lambeck, K., 1980. The Earth's Variable Rotation: Geophysical Causes and Consequences. Cambridge University Press.

Lieske, J. H., T. Lederle, W. Fricke, and B. Morando, 1977. Expressions for the precession quantities based upon the IAU (1976) system of astronomical constants, Astron. Astrophys., 58:1-16.

Lundqvist, G., 1984. Radio Interferometry as a Probe of Tectonic Plate Motion, Doctoral Thesis, Technical Report No. 150, School of Electrical and Computer Engineering, Chalmers University of Technology, Gothenburg, Sweden.

Ma, Chopo, 1978. Very Long Baseline Interferometry Applied to Polar Motion, Relativity and Geodesy. Dissertation, University of Maryland/College Park.

Mansinha, L. and D. E. Smylie, 1970. Seismic excitation of the Chandler wobble; in Earthquake Displacement Fields and the Rotation of the Earth; Mansinha, L., D. E. Smylie and A. E. Beck, eds. Dordrecht, Holland: D. Reidel Publishing Company.

Mansinha, L., D. E. Smylie and A. E. Beck, 1970. Earthquake Displacement Fields and the Rotation of the Earth. Dordrecht, Holland: D. Reidel Publishing Company.

Mansinha, L., D. E. Smylie and C. H. Chapman, 1979. Seismic excitation of the Chandler wobble revisited, Geophys. J. R. astr. Soc., 59:1-17.

Marini, J. W., 1974. Correction of radio range tracking data for atmospheric refraction at elevation above 10 degrees; Internal NASA Memorandum.

Milne, J., 1893. On the mitigation of earthquake effects and certain experiments in earth physics, Seism. J. Japan, 17:1-19.

Morabito, D. D. and T. M. Eubanks, 1985. UTPM Filter Implementation: Smoothing of ILS Data, Jet Propulsion Laboratory Engineering Memorandum 335-60.

Moran, J. M., P. P. Crowther, B. F. Burke, A. H. Barrett, A. E. E. Rogers, J. A. Ball, J. C. Carter, and C. C. Bare, 1967. Spectral line interferometry with independent time standards at stations separated by 845 kilometers, Science, 157:676.

Moran, J. M. and H. Penfield, 1976. Test and Evaluation of Water Vapor Radiometers and Determination of their Capability to Measure Tropospheric Propagation Path Length, NASA Goddard Space Flight Center report.

Mueller, I. I., 1969. Spherical and Practical Astronomy as Applied to Geodesy. New York: Frederick Ungar Publishing Co.

Munk, W. H. and G. J. F. MacDonald,1975. The Rotation of the Earth: a Geophysical Discussion. Cambridge: Cambridge University Press.

Nur, A. and G. Mavko, 1974. Postseismic viscoelastic rebound, Science, 183:204-206.

O'Connell, R. J. and A. M. Dziewonski, 1976. Excitation of the Chandler wobble by large earthquakes, Nature, 262:259-262.

Preliminary Determination of Epicenters, 1984-1986 (issued monthly). U. S. Geological Survey.

Press, F., 1965. Displacements, strains and tilts at teleseismic distances, J. Geophys. Res., 70:2395.

Press, F. and P. Briggs, 1975. Chandler wobble, earthquakes, rotation, and geomagnetic changes, Nature, 256:270-273.

Rauch, H. E., F. Tung and C. T. Striebel, 1965. Maximum Likelihood Estimates of Linear Dynamic Systems, AIAA J., 3:1445.

Resch, G. M., D. E. Hogg and P. J. Napier, 1984. Correction of interferometer phases using water vapor radiometers, Radio Science, 19 (No. 1): 411-422.

Robertson, D. S., 1975. Geodetic and Astrometric Measurements with Very-Long-Baseline Interferometry. Dissertation, Massachusetts Institute of Technology.

Robertson, D. S. and W. E. Carter, 1985. Earth orientation determinations from VLBI observations, Proceedings of the International Conference on Earth Rotation and the Terrestrial Reference Frame, Columbus, Ohio, 31 July - 2 August, 1985.

Rogers, A. E. E., 1970. Very-long-baseline interferometry with large effective bandwidth for phase-delay measurement, Radio Science, 5:1239-1248.

Ryan, J. W., 1984. Personal communication.

Seidelmann, P. K., 1982. 1980 IAU theory of nutation: the final report of the IAU working group on nutation, Celest. Mech., 27:79-106.

Shapiro, I. I. and Curtis A. Knight, 1970. Geophysical applications of long-baseline radio interferometry; in Earthquake Displacement Fields and the Rotation of the Earth; Mansinha L. et al., eds.; Dordrecht-Holland: D. Reidel Publishing Company.

Smith, M. L., 1974. The scalar equations of infinitesimal elastic-gravitational motion for a rotating, slightly

elliptical earth, Geophys. J. R. astr. Soc., 37:491-526.

Smith, M. L., 1977. Wobble and nutation of the earth, Geophys. J. R. astr. Soc., 50:103-140.

Smith, M. L. and F. A. Dahlen, 1981. The period and Q of the Chandler wobble, Geophys. J. R. astr. Soc., 64: 223-281.

Smylie, D. E. and L. Mansinha, 1968. Earthquakes and the observed motion of the rotation pole, J. geophys. Res., 73:7661-7673.

Smylie, D. E. and L. Mansinha, 1971. The elasticity theory of dislocations in real earth models and changes in the rotation of the earth, Geophys. J. R. astr. Soc., 23:329-354.

Spence, W., 1986. The 1977 Sumba earthquake series: evidence for slab pull, J. geophys. Res., in press.

Spence, D. A. and D. L. Turcotte, 1979. Viscoelastic relaxation of cyclic displacements on the San Andreas fault, Proc. R. Soc. Lond., A365:121-144.

Stacey, F. D., 1977. Physics of the Earth. New York: John Wiley & Sons.

Sullivan, Walter, 21 August, 1984. Wind plays surprising role in spin of earth, The New York Times.

Tryon, P. V. and R. H. Jones, 1983. Estimation of parameters in models for cesium beam atomic clocks, Journal of Research of the National Bureau of Standards, 88(No.1): 3-16.

Turcotte, D. L., D. C. McAdoo and J. G. Caldwell, 1978. An elastic-perfectly plastic analysis of the bending of the lithosphere at a trench, Tectonophysics, 47:193-205.

Uyeda, S. and H. Kanmori, 1979. Back-arc opening and the the mode of subduction, J. Geophys. Res., 84:1049-61.

Wahr, J., 1981. The forced nutations of an elliptical, rotating, elastic and oceanless earth, Geophys. J. Roy. Astr. Soc., 64:705-727.

Wahr, J. M., 1983. The effects of the atmosphere and oceans on the earth's wobble and on the seasonal variations in the length of day - II. results, Geophys. J. R. astr. Soc., 74:451-487.

Wilson, C. R. and R. A. Haubrich, 1976. Meteorological excitation of the earth's wobble, Geophys. J. R. Astron. Soc.,46:707-743.

Zheng, Ying, 1986. The effect of earthquake on polar motion, in IAU Symposium #128: The Earth's Rotation and Reference Frame for Geodesy and Geodynamics (abstract), Coolfont, West Virginia, 20-24 October, 1986.

NASA
National Aeronautics and Space Administration

Report Documentation Page

1. Report No.	2. Government Accession No.	3. Recipient's Catalog No.
NASA TM-100711		

4. Title and Subtitle

Relationships of Earthquakes (and Earthquake-Associated Mass Movements) and Polar Motion as Determined by Kalman Filtered, Very-Long-Baseline-Interferometry Group Delays

5. Report Date

October 1988

6. Performing Organization Code

621

7. Author(s)

Joseph R. M. Preisig

8. Performing Organization Report No.

88B0254

10. Work Unit No.

9. Performing Organization Name and Address

Goddard Space Flight Center
Greenbelt, Maryland 20771

11. Contract or Grant No.

13. Type of Report and Period Covered

Technical Memorandum

12. Sponsoring Agency Name and Address

National Aeronautics and Space Administration
Washington, D.C. 20546-0001

14. Sponsoring Agency Code

15. Supplementary Notes

16. Abstract A Kalman filter was designed to yield optimal estimates of geophysical parameters from Very-Long-Baseline-Interferometry (VLBI) group delay data. The geophysical parameters are the polar motion components, adjustments to nutation in obliquity and longitude, and a change in the length of day parameter. VLBI clock (and clock rate) parameters and atmospheric zenith delay parameters are estimated simultaneously. Filter background is explained. IRIS (International Radio Interferometric Surveying) VLBI data are Kalman filtered. The resulting polar motion estimates are examined. There are polar motion signatures at the times of three large earthquakes occurring in 1984-1986: Mexico, 19 September, 1985 (Magnitude M_S=8.1); Chile, 3 March, 1985 (M_S=7.8); and Taiwan, 14 November, 1986 (M_S=7.8). Breaks in polar motion occurring about 20 days after the earthquakes appear to correlate well with the onset of increased regional seismic activity and a return to more normal seismicity (respectively). While the contribution of these three earthquakes to polar motion excitations is small, the cumulative excitation due to earthquakes, seismic phenomena, etc. over a Chandler wobble damping period may be significant. Mechanisms for polar motion excitation due to solid earth phenomena are examined. Excitation functions are computed, but the data spans are too short to draw conclusions based on these data.

17. Key Words (Suggested by Author(s))

Polar Motion, Earth Rotation, Kalman Filtering, Very-Long-Baseline Interferometry, Geodesy (physics), and Geophysics

18. Distribution Statement

Unclassified - Unlimited

Subject Category 46

19. Security Classif. (of this report)	20. Security Classif. (of this page)	21. No. of pages	22. Price
Unclassified	Unclassified		